UNIVERSITY OF CATANIA

PHD IN CHEMICAL SCIENCES

XXXVIII CYCLE

Maria Teresa ARMELI IAPICHINO

Photocatalytic sustainable processes for the H_2 production by photoreforming of green organic substrates

Laboratory of Industrial & Environmental Catalysis
Department of Chemical Sciences

PHD COORDINATOR: Prof. S. Scirè
TUTOR: Prof. S. Scirè

PHD THESIS

ABSTRACT

In the 21st century, the increasing demand for energy, possibly produced in renewable ways, has made it necessary to find alternative energy sources in place of the use of fossil fuels. In particular, the energy produced from non-renewable sources have caused serious environmental issues, especially a considerable increase in the CO_2 emissions. To address these problems, research is now focused on an efficient utilization of renewable energy, including the exploitation of sustainable and green energy as the hydrogen. Currently, most of hydrogen is produced with processes that required the use of fossil fuels, leading to have a considerable portion in the market of the so-called grey or brown hydrogen. Only a little part of the hydrogen production was obtained with sustainable processes, i.e., the green hydrogen.

Contextually, another critical problem of today is the large amounts of plastic and biomass wastes that are neither properly disposed of recycled. This issue is having a severe impact on marine environments, biodiversity, and human health.

The solar photoreforming of plastics or biomass-derived compounds is a promising process that utilizes the solar radiation (a renewable energy source), a catalyst (typically a semiconductor), and an organic sacrificial agent derived from plastic materials or biomass. This process offers a way to address multiple issues through a single reaction. In particular, it enables the production of green hydrogen with the simultaneous photocatalytic oxidation of the employed sacrificial agent.

The photocatalysts for this reaction require continuous improvements, and the post-pandemic global crisis has highlighted the urgent need to develop new, efficient and not-critical materials for this purpose.

On the above considerations, the focus of this thesis is the investigation of the green hydrogen production using carbon-based photocatalysts for the solar photoreforming of plastics and biomass-derived compounds.

This work presents key studies on the photocatalytic behaviour of materials such as silicon carbide (SiC) combined with the graphitic carbon nitride (g-C_3N_4), originally used for the solar photoreforming of plastic-related materials including bisphenol A (BPA) and polyethylene terephthalate (PET).

Moreover, the influence of the addition on the SiC-g-C_3N_4 of a noble metal-free co-catalyst as the titanium carbonitride (TiCN) was here investigated. This original photocatalytic composite was tested for the solar photoreforming of low-density polyethylene (LDPE), polystyrene (PS), and polylactic acid (PLA).

An in-depth study was carried out on the pre-treatment step of the plastic materials. This process allowed the plastics to be treated and brought into water solution, favouring their depolymerization, enabling also the identification and optimisation of the experimental conditions that enhanced hydrogen production reducing at the same time the environmental impact.

The biomass-derived compounds solar photoreforming was instead studied on g-C_3N_4-based photocatalysts. In particular, the

addition of a very small amount of Pt, lead to effective performance in the visible-light glucose photoreforming also employing different water matrices, such as seawater and wastewater.

This thesis is divided into eleven chapters. **Chapters 1, 2**, and **3** address key aspects of environmental pollution, with a particular focus on plastic waste, the properties of hydrogen, and the main processes used for its production. **Chapter 4** explains in detail the photocatalysis process, including the specific photoreforming reactions investigated in this work. **Chapter 5** presents the studied photocatalytic materials and discusses their chemical and physical properties**. Chapters 6 and 7** outline the objectives of the thesis and describe the experimental part used in this research. **Chapters 8, 9** and **10** present different studies, highlighting various applications of the solar photoreforming. Finally, **Chapter 11** provides the general conclusions drawn from this work.

TABLE OF CONTENTS

CHAPTER I: Introduction

CHAPTER I: Introduction

1.1 Energy background

Although the 21st century has brought an improved quality of life compared to previous decades, it has also been marked by industrialisation and globalisation, which have contributed to significant climate change, environmental pollution, and a decline in fossil fuel resources. In fact, since the 1800s, human activity has been the main responsible of climate change, mainly due to the burning of fossil fuels (FF) such as coal, oil and gas. The increase in global temperature is caused by FF, which introduce several gases including carbon dioxide (CO_2), methane (CH_4) and nitrous oxide (NO_X), which have the power to trap solar heat. Industrial activities are mainly responsible for greenhouse gas emissions (being the carbon dioxide the most predominant). Less prevalent but very powerful Greenhouse Gases (GHGs) include hydrofluorocarbons (HFCs), perfluorocarbons (PFCs) and sulphur hexafluoride (SF_6). Transport, construction, energy, industry and agriculture are the main industries leading to this problem[1].

Global surface temperatures have increased by 0.13 °C on average per decade since 1950 (Fig.1). By the end of the 21st century, global average surface temperatures might rise from 1.8 to 4 °C, depending on how much GHG emissions increase[2].The current climate changes affect various sectors such as agriculture, public health, water use, energy production and biodiversity. For example, the temperature and the modification of the precipitation patterns influence the crop yields, while changes in ocean chemistry affect marine biodiversity and fisheries. In fact, the

number of natural disasters such as floods, droughts and storms increase exponentially year by year in different countries around the world.

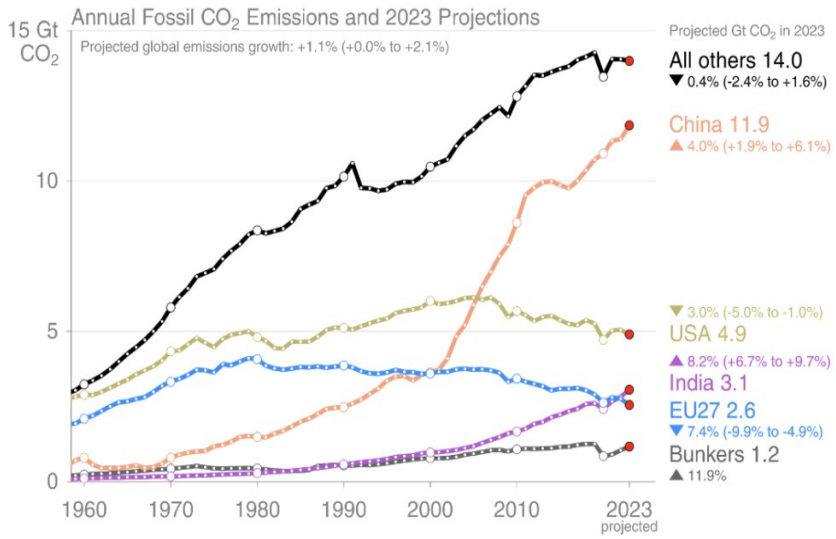

Figure 1 *Annual CO_2 fossil emission since 1960*[3]*. It is observed that there is a significant increase in the case of China and India, instead a decrease in emissions was detected for USA and Europe. For the as-called Bunkers, there is a growth of 11.9% after 2021. This term refers to CO_2 emissions from international transport (international aviation and international shipping). These emissions are excluded from national emission counts, as they occur in international waters or international airspace.*

Therefore, in these years various strategies and plans are programmed, with the support of scientists, in order to reduce the CO_2 emissions and the other greenhouse gases. For example, the European Green Deal aims to make Europe the world's first carbon-neutral continent by 2050 (Fig.2). This goal is supported by the adoption of green technological innovations, clean energy, green finance, and environmental policies, including environmental taxes on CO_2 emissions in 25 European countries[4].

Figure 2 *The European Green Deal plan.*

The growing consumption of fossil fuels and its impact on environmental pollution has encouraged researchers to focus on renewable energy sources, guided by the twelve principles of green chemistry[5] with a special focus on catalysis (Fig.3).

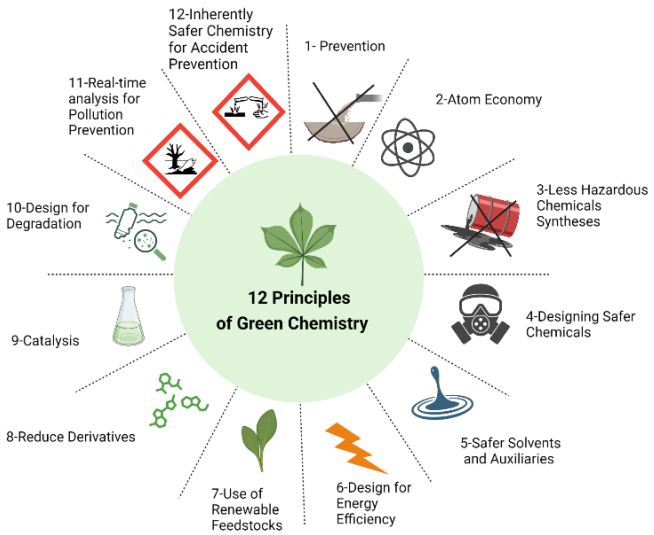

Figure 3 *The 12 Principle of Green Chemistry.*

Renewable energies are defined as all forms of energy that respect the environment, do not pollute and, thanks to their ability to regenerate at the end of their cycle, do not finish. They include solar, wind, hydro, geothermal, and biomass-derived energy. The use of renewable energy sources is steadily increasing due to continuous political investment and the market that, especially in the last years, supports the initial investment. According to the International Renewable Energy Agency (IRENA), renewable energy production has doubled compared to 2010, with most of the growth concentrated in solar energy[6]. Notably, in 2024 alone, global renewable energy capacity grew by 585 GW, marking an annual growth record rate of 15.1%, which exceeded the 2023 growth rate of 14.3% (Fig.4).

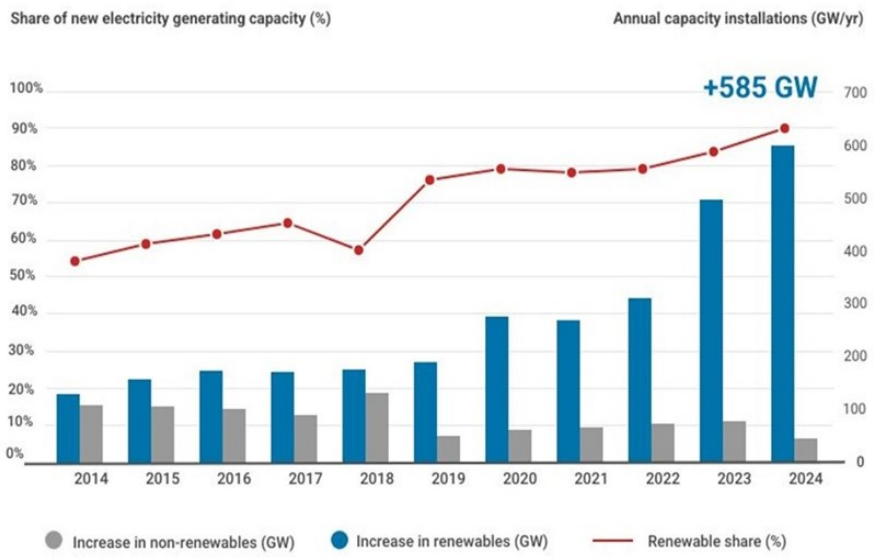

Figure 4 *Renewable share of annual power capacity expansion (2014-2024) IRENA*[7].

Hydrogen can create a synergy between renewable energy resources and the modernisation of energy supply for transport, industry and exports.

Energy demand is increasing by about 2% per year and therefore alternative ways are necessary to cope with their scarcity. The maximum world oil production will occur in a few decades at best, and it will make the price of fuels quite prohibitive. Also, the pandemic (COVID) crisis and the numerous conflicts including the current Russian-Ukrainian war strongly affect its price and availability. Thus, it is fundamental a strong interaction and interconnection between science, techniques, technology and the availability of resources as soon as possible. In this context the use of hydrogen can be considered available alternative as a sustainable energy vector.

1.2 Measures adopted by the European Union

The European Union (EU) is working to sustainable emission targets by implementing strategic plans and promoting clean energy alternatives, such as hydrogen (H_2), to strengthen its position as a leading global competitor, resulting in reduced CO_2 emissions[8].

First of all, an important target that was achieved is the *EU 20-20-20 package*, which aim was to reduce the greenhouse gas emissions by 20% by 2020 compared to 1990, and at the same time increase by 20% the consumption of energy from renewable sources[9].

Today, the best known and the most relevant legislation is the *European Green Deal* (EGD) mentioned above. The EGD was updated in November 2024, with the final approval that has as object the net-zero emission for industries[10]**.**

The goal is to cover 40% of the EU's needs in strategic technology products, such as solar photovoltaic panels, wind turbines, batteries and heat pumps[10].

With these strategies it is expected that the EU's final energy consumption will be reduced by 11.7% within 2030. To date, energy consumption has reached 992.5 million tonnes of oil equivalent (Mtoe). With the implementation of the new reform, this is projected to decline to 763 Mtoe by 2030 [10].

Another important plan is the *REPower* (May 2022), which plans to realise a reduction of at least 55% of greenhouse gas emissions related to energy independence by 2030 and climate neutrality by 2050 with renewable energy (RE)[11]. It provides the production and the importation of 10 million tonnes of renewable hydrogen, a

substantial increase compared to the 5.6 Mton foreseen in the Renewable Energy Directive published in July 2021[11].

The European Hydrogen Strategy plan is that the European electrolyser manufacturing industry will reach at least 40 GW of manufacturing capacity by 2025, representing around 240 GW of the installed capacity in Europe[12].

The EU has also created the Next Generation fund after the COVID crisis. This fund is based on the development of a H_2-based economy (Fig.5), with the valorisation of waste to produce high-added value products. Different projects have been financed. In Italy is still active the PNRR plan (National Recovery and Resilience Plan) with 3.19 billion of resources. It includes research calls and a program agreement with ENEA (Italian National Agency for New Technologies, Energy and Sustainable Economic Development) to produce green and clean hydrogen, innovative technologies for the storage and transport of hydrogen and its transformation into derivatives and the development of fuel cells for stationary and mobility applications[13].

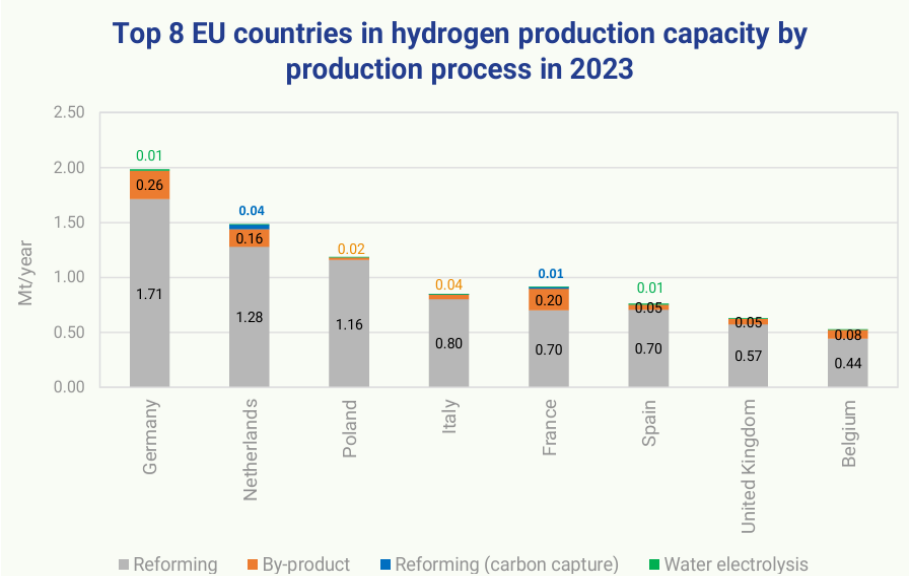

Figure 5 *Top 8 EU countries in terms of hydrogen production capacity by production process (report by The European hydrogen market landscape)*[14].

In Europe, each country has a sustainability indicator defined by Remap. The process consists firstly in collecting data from countries from their national energy plans and targets, while successively it was outlined a national baseline for renewable energy deployment considering the period between 2010 and 2030. In Europe, 11 Member States (Germany, France, Italy, Spain, Poland, Netherlands, Sweden, Belgium, Austria, Romania, Czech Republic), representing more than 80% of the EU's total final energy demand, are part of IRENA's REmap programme[15].

References

[1] G.O. Ofremu, B.Y. Raimi, S.O. Yusuf, B.A. Dziwornu, S.G. Nnabuife, A.M. Eze, C.A. Nnajiofor, Exploring the Relationship between Climate Change, Air Pollutants and Human Health: Impacts, Adaptation, and Mitigation Strategies, Green Energy and Resources. (2024) 100074. https://doi.org/10.1016/j.gerr.2024.100074.

[2] A. Rawat, D. Kumar, B.S. Khati, A review on climate change impacts, models, and its consequences on different sectors: a systematic approach, Journal of Water and Climate Change. 15 (2024) 104–126. https://doi.org/10.2166/wcc.2023.536.

[3] Elena Dusi, Carbon dioxide emissions will increase in 2024. Positive signals in Europe (Italy excluded), (n.d.). https://www.repubblica.it/italia/2024/11/13/news/emissioni_anidride_carbonica_2024_italia-423618332/.

[4] E.S. Obobisa, I. Ahakwa, Stimulating the adoption of green technology innovation, clean energy resources, green finance, and environmental taxes: The way to achieve net zero CO_2 emissions in Europe, Technological Forecasting and Social Change. 205 (2024) 123489. https://doi.org/10.1016/j.techfore.2024.123489.

[5] G. Szekely, The 12 principles of green membrane materials and processes for realizing the United Nations' sustainable development goals, RSC Sustainability. 2 (2024) 871–880. https://doi.org/10.1039/D4SU00027G.

[6] G.T. Reader, The future of renewable energy systems—a long and winding transition pathway, in: Renewable Energy Systems, IOP Publishing, 2025: pp. 1-1-1–86. https://doi.org/10.1088/978-0-7503-6179-8ch1.

[7] Renewable capacity statistics 2025, (n.d.). https://www.irena.org/Publications/2025/Mar/Renewable-capacity-statistics-2025.

[8] D. Vergara, P. Fernández-Arias, G. Lampropoulos, Á. Antón-Sancho, Hydrogen Revolution in Europe: Bibliometric Review of Industrial Hydrogen Applications for a Sustainable Future, Energies. 17 (2024) 3658. https://doi.org/10.3390/en17153658.

[9] 2020 climate and energy package. https://eur-lex.europa.eu/legal-content/EN/TXT/?uri=LEGISSUM:2001_8.

[10] Timeline - European Green Deal, 2024. https://www.consilium.europa.eu/en/policies/european-green-deal/timeline-european-green-deal-and-fit-for-55/?taxonomyId=271842c3-2535-4f5a-a049-bcdab2758865.

[11] REPowerEU: energy policy in EU countries' recovery and resilience plans, (2025). https://www.consilium.europa.eu/en/policies/repowereu/.

[12] P9_TA(2023)0484 – European Hydrogen Bank – European Parliament resolution of 14 December 2023 on the European Hydrogen Bank (2023/2123(INI)). http://data.europa.eu/eli/C/2024/4185/oj.

[13] Energy: Hydrogen, ENEA with research and industry to build a national supply chain, (2024). https://www.media.enea.it/en/press-releases-and-news/years-archive/year-2024/energy-hydrogen-enea-with-research-and-industry-to-build-a-national-supply-chain.html.

[14] European Hydrogen Observatory, The European hydrogen market landscape, Clean Hydrogen Partnership. (2023) 1–95. https://observatory.clean-hydrogen.europa.eu/sites/default/files/2023-11/Report 01 - November 2023 - The European hydrogen market landscape.pdf.

[15] A. Tomassi, A. Caforio, E. Romano, E. Lamponi, A. Pollini, The development of a Competence Framework for Environmental Education complying with the European Qualifications Framework and the European Green Deal, The Journal of Environmental Education. 55 (2024) 153–179. https://doi.org/10.1080/00958964.2023.2259846.

CHAPTER II: Hydrogen Features

CHAPTER II: Hydrogen features

Hydrogen is the lightest and the most abundant element in the universe, accounting for approximately 75% of its mass. Nevertheless, it is not found naturally in its pure form, but rather in combination with other elements, such as in water (H_2O), hydrocarbons, organic molecules, and living organisms. In terms of its properties, hydrogen naturally exists as a diatomic molecule (H_2). It is a flammable, colourless, and odourless gas, which liquefies at -253°C and solidifies at -259°C. Hydrogen has three main isotopes: protium, deuterium, and tritium (Fig.1).

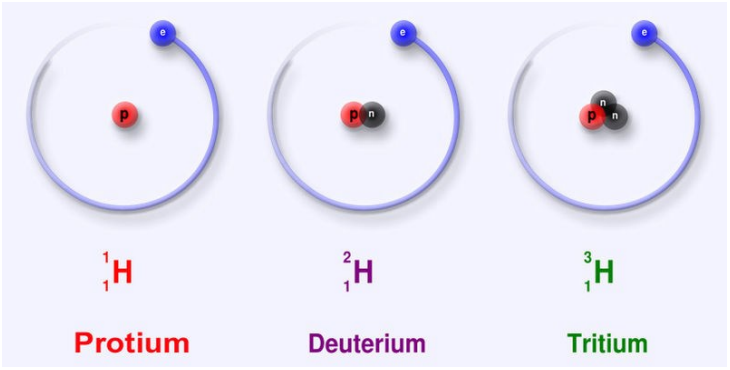

Figure 1 *The isotopic structures of H_2.*

Hydrogen is considered one of the most interesting and complex chemical elements. It has a molecular weight of 2.01594 g/mol and a very low density of 0.071 g/L at 0°C and1 atm. Its relative density compared to air is 0.0695 g/L. Despite its low density, hydrogen is one of the most flammable gases known.

Hydrogen is slightly more soluble in organic solvents than in water and can be readily absorbed by many metals. Under normal conditions, it is relatively unreactive unless activated by a suitable catalyst. However, at high temperatures, it becomes highly reactive[1].

2.1 H_2 Production

Hydrogen is typically found combined with other elements in nature, and therefore it cannot be considered a primary energy source. Instead, it is regarded as an energy carrier, as its extraction requires the input of energy and the use of catalysts.

The first scientist to unintentionally produce hydrogen gas was Philippus Aureolus Theophrastus Bombastus von Hohenheim (known as Paracelsus), through reacting metals with strong acids in his laboratory. In 1761, Robert Boyle produced H_2 from reacting iron filings and dilute acids, while in 1783, Antoine Lavoisier named the material hydrogen (Hydrogenium) from the Greek roots “hydro” (water). This discovery promoted the development of other production methods. Since its combustion only releases water vapour into the atmosphere, it is considered a green renewable energy[2].

The energy content of hydrogen is 142 MJ, which is higher than any other hydrocarbon fuel. It has three times the energy content per unit of weight compared to petrol, but only one-fourth the energy content per unit of volume[3].Therefore, compared to gasoline, hydrogen burns faster. Hydrogen has an energy density 3.2 times lower than that of natural gas and almost 2700 times lower than that of conventional gasoline[4]. Currently, annual hydrogen production is around 0.1 GT, which is mainly consumed on-site, in the refining and treatment of metals and to power cars (but only to a small extent as fuel in fuel cells[5]). Hydrogen demand has been steadily increasing over the past few years, reaching approximately 90 Mt by 2020. Approximately 70 Mt of

hydrogen were used as pure hydrogen, while 20 Mt were combined with other gases to produce methanol and steel[6].
In recent years, there has been increasing international focus on the development of new technologies for hydrogen production, aimed at ensuring both energy and economic security. The system based on the production of this energy carrier consists of a four-corner model (Fig.2) also called “Hydrogen Square (HydS)”[7].

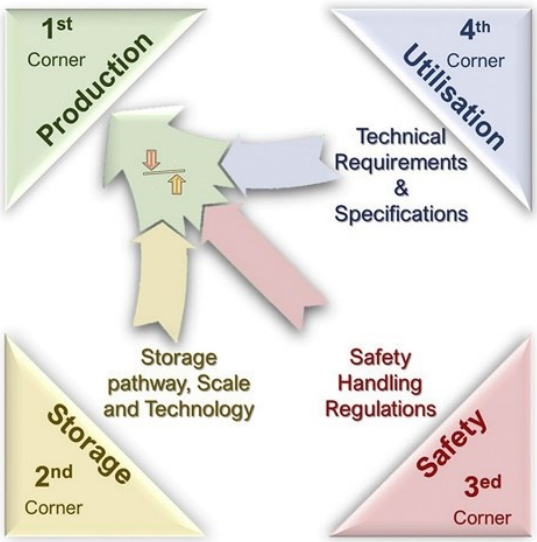

Figure 2 Hydrogen Square (HydS).

Focusing on the first step, the production of H_2 depends on the energy source used (fossil fuels or renewable resources) (Fig.3). Consequently, depending on the particular production method, it is possible to determine cleanliness, effectiveness and inexpensiveness. The implementation of a production process depends on hydrogen-content of the raw materials (hydrocarbons or non-hydrocarbons), the energy source and finally the used catalyst. The efficiency of the processes is evaluated by the

energy value of the produced hydrogen divided by the energy consumed to produce it. Instead, the cost estimations effectiveness ratio is determined by capital investments (CAPEX), but it is necessary to consider also the primary energy requirements and the operational expenses (OPEX), like depreciation and interest on capital investment, utilities and feedstock costs, manpower and maintenance[8].

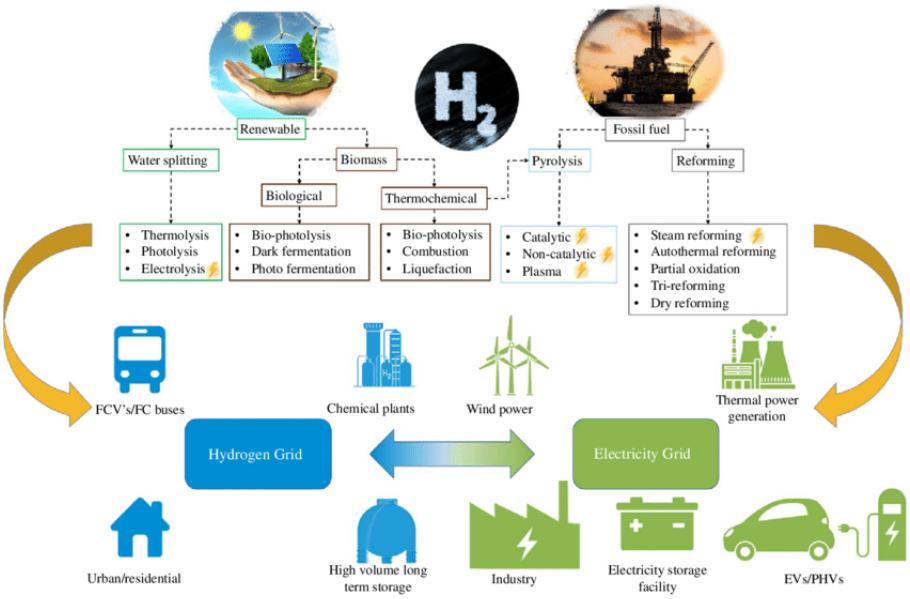

Figure 3 *H_2 production by different energy sources*[9].

2.2 H_2 Production by fossil fuels

Conventional methods able to guarantee a good H_2 production are based on hydrocarbons, i.e. fossil fuels, due to the consolidate technologies. These include steam reforming, partial oxidation of carbon-based materials, dry reforming and gasification, which recently have been improved in order to reduce the carbon emission [10]. Usually, these methods are extensively employed in industrial contexts, particularly for the generation of hydrogen utilized in the petroleum refining and chemical manufacturing sectors[11].

- ***Steam Reforming***

Steam Reforming (SR) is an endothermic process that uses methane (or methanol) in combination with water vapour, leading to the formation of syngas (CO, H_2) at 700°C-1100 °C, 3.5 MPa (react. I.)

I. $C_nH_m + nH_2O \rightarrow nCO + (N + \frac{1}{2} m) H_2 \quad \Delta H_0 = -41\ kJmol^{-1}$

Pressures up to 5 MPa can be used to minimise the energy consumption associated with the compression of large volumes of synthesis gases generated during the process (Fig.4).

The most common industrial catalysts for this process are nickel supported on oxides, generally alumina or magnesium, but one of the most important problems is the carbon deposition with the consequential deactivation of the catalyst. The coke formation led to the blocking of the catalyst active sites, increased the pressure drops and decreased the heat transfers (react. II-IV)

II. $C_mH_n \rightarrow xC + C_{m-x}H_{n-2x} + {}_xH_2$

III. $2CO \rightarrow C + CO_2$ $\Delta H = +172{,}4\ kJ\ mol^{-1}$

IV. $CO + H_2 \rightarrow C + H_2O$

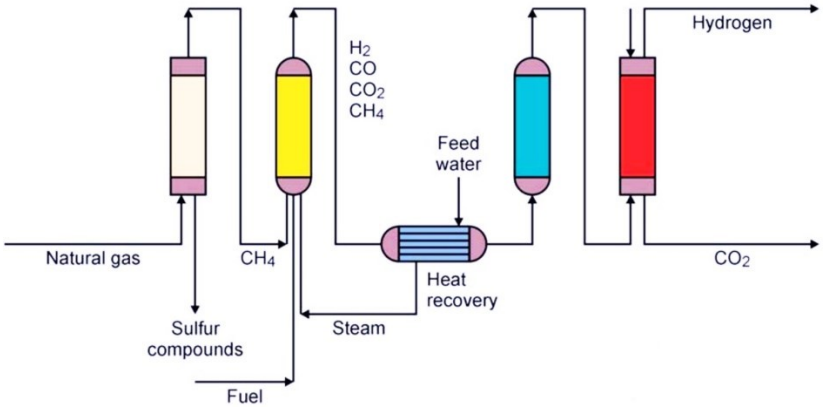

Figure 4 *Process scheme for the methane steam- reforming.*

The industrial steam reformer units are characterised by about 1,000 split pipes, each with a diameter of about 100 mm and a length of 10 m. These units are capable of achieving a production capacity of approximately 130,000 Nm^3/h[12].

❖ *Partial Oxidation of carbon-based materials (POX)*

Catalytic partial oxidation (CPOX) (Fig.5) is a promising natural gas reforming technology for the production of hydrogen/rich syngas. Its development is based on incorporating catalysts into conventional partial oxidation process to favour the exothermic reaction[13]. The major researches of CPOX are directed to the conversion of natural gas to syngas. Natural gas is one of the most abundant carbon sources that nature offers and a key resource for the fuels, chemicals, and fertilizer industries[14]. The non-catalytic

partial oxidation of hydrocarbons in presence of oxygen typically takes place at 1300 -1500 °C to ensure the complete conversion and to reduce the carbon formation (react. V).

V. $C_mH_n + ½\ mO_2 \rightarrow mCO + ½\ H_2$

Generally, the catalysts used are typically based on Ni or Rh.
The advantage of this process is the use of several raw materials such as oil, residues, carbon and biomass. While, the disadvantages are the thermal efficiencies of POX reactors, that with methane as fuel are only 60%-70%, the high energy consumption due to larger reactor sizes compared to steam reforming, high oxygen demand, and catalyst deactivation due to carbon build-up[15].

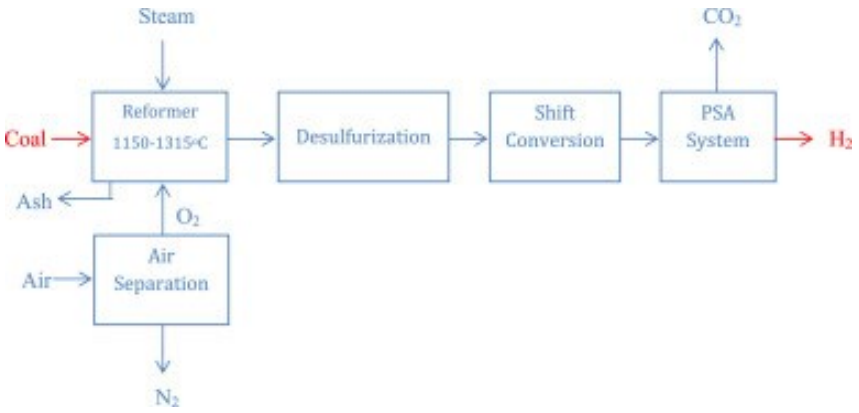

Figure 5 *Partial oxidation process flowchart (coal as raw material).*

❖ *Autothermal Reforming (ATR)*

If steam is added to the CPOX process, this is referred to as autothermal reforming (ATR). ATR can be carried out using catalyst at 800 °C, 25 atm; while, without the catalyst at 1300-1500 °C, 20-30 atm (react. VI). The heat obtained from CPOX, is necessary to avoid the use of an external heating source, simplifying the system and decreasing start-up times.

VI. $C_nH_m + ½\ mH_2O + ¼\ mO_2 \rightarrow mCO + (½\ m + ½\ n)\ H_2$

A significant advantage for this process over SR is that it can be stopped and started quickly while producing more hydrogen than single CPOX process. To work properly, for the ATR both the oxygen/fuel ratio and the vapour/carbon ratio must be accurately controlled, the optimum working temperature depends on the composition of the produced gases, preventing at the same time the formation of coke. This process is particularly used for the gas-liquid industry and for the Fischer-Tropsch synthesis[16].

❖ *Water gas shift (WGS)*

The WGS was first discovered by the Italian physicist Felice Fontana in 1780[17]. The WGS reaction (react. VII) is carried out after steam reforming or gasification, in order to increase the H_2 production efficiency, and to decrease the presence of carbon monoxide (< 5%). This reaction occurs with steam at 450°C.

VII. $CO + H_2O \rightarrow CO_2 + H_2$ $\Delta H = -41\ kJ\ mol^{-1}$

WGS is an exothermic process. To increase the WGS efficiency is possible to use of a membrane reactor (Fig.6). This technology allows to simultaneously produce and separate at the high-pressure side of the membrane the fuels, when they are in contact with the membrane. This permits the improvement of the performance of the reaction in terms of conversion and separation[18]. The reaction can be carried out either in the presence or without catalysts, with supercritical water, or plasma system. In the case of catalytic system, the oxygen vacancies available at the surface of the catalyst, the catalytic activity due to water dissociation and the low adsorption feature of CO are involved in determining the final performance of the overall process[19].

This process can take place at different temperatures.

The high temperature shift reaction (HTSR) at 350-500 °C with Fe-Cr based catalysts.

The low temperature shift reaction (LTSR) at 150-200 °C with Cu-Zn based catalysts.

It is worth mentioning that the medium temperature shift process (MTSR) has recently emerged as a practical strategy for pursuing effective and stable catalytic interfaces, replacing the conventional cascade of high-temperature to low-temperature WGS. The MTSR typically operates within the temperature range of 280–360 °C and predominantly employs noble metals, Cu, and Ni-based catalysts as its primary catalysts[20].

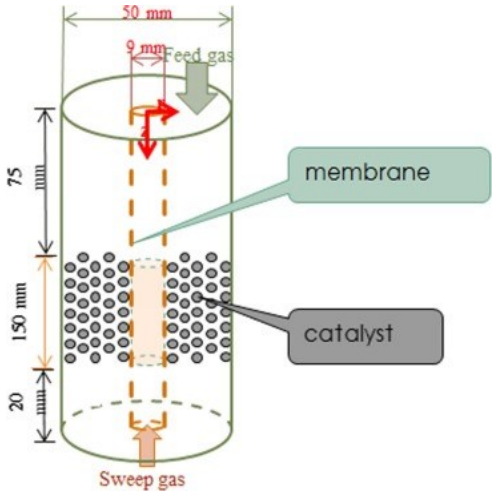

Figure 6 *Representation of a possible fixed-bed membrane reactor used for the WGS reaction.*

Moreover, the WGS reaction is reversible, so it is possible that the thermal equilibrium is reached at higher temperatures. In addition, CO_2 is obtained from the process, which can be stored or captured and injected into geological reservoirs, pre-combustion or post-combustion plants[21]. In more modern plants, the steam produced is used to produce electricity to power the process. The reverse reaction is called reversed water gas shift (RWGS) (react. VIII) and can be exploited to minimize the CO_2 emission.

VIII. $CO_2 + H_2 \rightarrow CO + H_2O \qquad \Delta H = +9\ KJmol^{-1}$

2.3 H_2 Production from renewable sources

In order to reduce the carbon emissions, hydrogen must be extracted, it is therefore possible to obtain it from renewable sources such as biomass through pyrolysis or gasification, or from water (Fig.7).

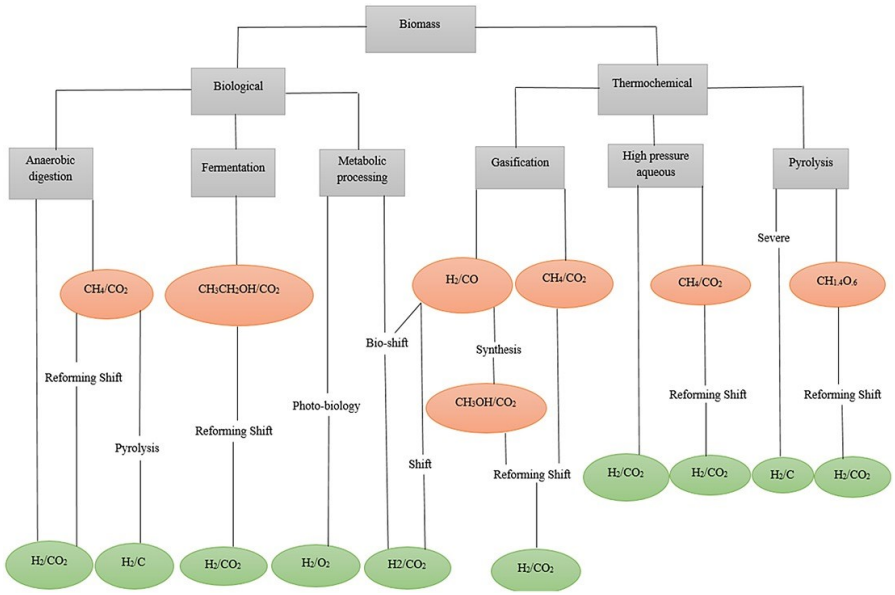

Figure 7 *H_2 production thought different paths.*

- Production from biomass

Obtaining H_2 from biomass is a viable alternative due to their abundant supply. Currently, biomass contributes of about 12% of the world's current energy supply, while in many developing countries it can contribute of about 40-50% of the national energy supply[22]. For example, 150 GT of plant bio-matter generated each year can produce energy equal to approximately 1.08×10^{10} GJ[23].

Furthermore, various resources can be utilized to produce energy, which can be categorized into four main groups:

1. Energy crops: including herbaceous, woody, industrial, agricultural, and aquatic crops.
2. Agricultural residues and waste: such as crop residues and animal waste.
3. Forestry residues and waste: including mill wood waste, logging residues, trees, and shrub residues.
4. Industrial and municipal waste: such as municipal solid waste (MSW), sewage sludge, and industrial waste.

In the case of hydrogen production, it is obtained from biomass gasification or pyrolysis and in combination with CO (syngas stream).

The processes used to generate syngas can be divided into two main categories:

- Thermochemical processes: including combustion, pyrolysis, liquefaction, and gasification.
- Biological processes: such as direct and indirect bio photolysis, biological water-gas shift reaction and photo fermentation.

❖ Production from water

One of the most sustainable methods to obtain H_2 is the use of water[24]..

The main purpose of water electrolysis is to produce hydrogen and oxygen gases from water (H_2O) using electrolytic cells. These cells contain two electrodes, the cathode and the anode, where reduction and oxidation reactions occur at the same time (Fig.8).

Hydrogen is produced at the cathode, while oxygen is formed at the anode. Electrolytes are used to carry the electric current, and they consist of both positively charged cations and negatively charged anions. From an energy perspective, it is required about 5 kWh to produce 1-2 m^3 of H_2 [25]. However, a key issue is the high energy demand, which is still mostly supplied by fossil fuels, raising concerns about sustainability.

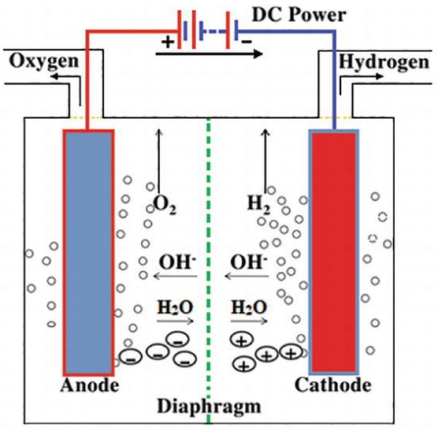

Figure 8 *Set-up for Electrolysis Process.*

Most electrolysis cells are alkaline-based, consisting of aqueous electrolytes containing approximately 30% of KOH; which gives the highest ionic conductivity, at operating temperatures between 70-90 °C, at 30 bar [26].

The half reactions occurring on the cathode and anode, respectively, (react. IX-X):

IX. $\text{Anode: } 2OH^- \rightarrow 1/2\ O_2 + H_2O + 2e^-$

X. $\text{Cathode: } 2H^+ + 2e^- \rightarrow H_2$

To avoid the generation of a potentially explosive mixture, a separator is required to isolate the hydrogen. An alkaline electrolyte allows the use of low-cost, non-precious metal catalysts, such as Nickel, for the electrodes, which helps to maintain capital costs.

In recent years, it was explored the use of an acid electrolyte, such as sulphuric acid. Also the phosphoric acid fuel cells are a promising technology for clean energy generation; however, a significant portion of the fuel's chemical energy is transformed into waste heat, reducing the overall efficiency and potentially affecting the long-term durability[27].

2.4 H_2 Storage

Hydrogen storage remains highly complex and is still under constant development. Hydrogen (H_2) has a very low density; for example, at 25 °C,1 atm, its density under ideal gas conditions is only 0.0824 kg/m^3, compared to 1.184 kg/m^3 of air in the same conditions. This low density leads to a very low volumetric energy content: only 0.01 MJ/L for hydrogen gas at ambient conditions and 8.5 MJ/L for liquefied hydrogen[28]. For comparison, methane and petrol have much higher volumetric energy contents, of 0.04 MJ/L and 32 MJ/L respectively. Notably, 1 kg of hydrogen gas occupies more than 11 m^3 at 25 °C and atmospheric pressure[29]. This low volumetric energy density presents a significant challenge to the economical and efficient storage of hydrogen, which is crucial for the development of a hydrogen-based energy system. Although storing hydrogen remains difficult, current methods include liquefaction, adsorption, and chemical storage (Fig.9).

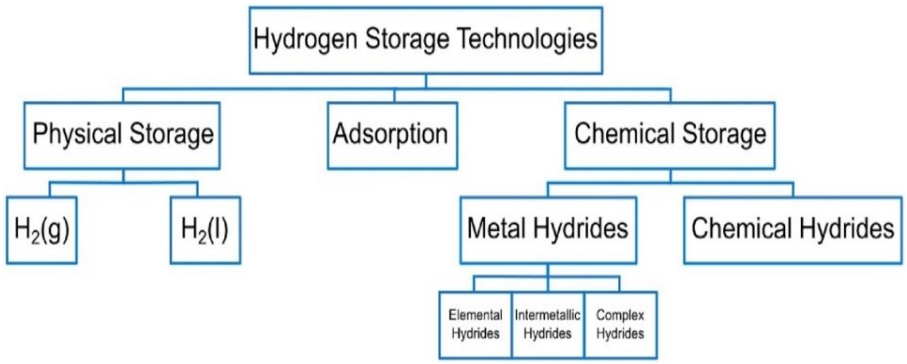

Figure 9 *Summary of the H_2 storage technologies.*

❖ *Physical storage*

Physical storage refers to the liquefaction process, in which case the density of hydrogen is 70 kg/m^3 at 1 bar. The problem with this technology is the high energy required due to the extremely low boiling point of hydrogen (-253 °C at 1 bar), moreover the hydrogen gas does not cool during the adiabatic process at -73 °C. The latter problem requires precooling in the liquefaction process, most often obtained by evaporating the liquid nitrogen.
Next, the hydrogen needs to be stored to minimise evaporation. The problem with this storage, involves not only a loss of energy spent to liquefy the hydrogen, but also, eventually, a loss of quantity as the evaporated gas that must be vented due to pressure build-up inside the storage tank[30].

❖ *Adsorbent*

To achieve adsorption storage, a physical Van Der Waals bond must be formed between the molecular hydrogen and a material with a large specific surface area. Since this is a weak bond, it is sufficient to apply low temperatures and high pressures (10-100 bar). Generally, the used refrigerant is the liquid nitrogen (boiling point: -196 °C). Unlike the storage of gaseous or compressed liquid hydrogen, there is relatively little experience with the application of adsorptive hydrogen storage; most storage tanks based on adsorption are only developed on a laboratory scale. The most successful adsorbents are some activated carbon and MOF, which have achieved the 8-10 wt% of hydrogen adsorption at -196 °C[31]. Thermal stimulation improves the kinetics and reversibility of the storage system and can be used to release hydrogen from

the physiosorbed materials. However, their lack of stability and endurance make these systems unsuitable for commercial applications even if several materials (as for example fullerenes and graphene) demonstrated storage capabilities larger than 6.5 wt%[32,33] (Fig.10).

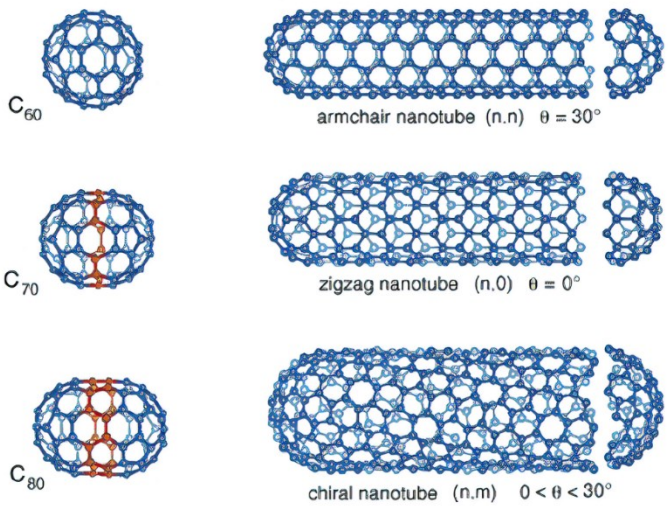

Figure10 *Examples* of carbon-based structures.

❖ *Chemical Storage*

This storage is based on the tendency of hydrogen to chemically bond with various metals and metal alloys, forming hydrides, such as $NaAlH_4$, $LiAlH_4$, LiH boron hydrides and palladium hydrides[34]. Initially, hydrides are formed through hydrogenation reactions, followed by dehydrogenation in which occurs the release of H_2. In this latter case the bond formed between the metal and the hydrogen is broken and pure hydrogen is released, providing heat. It must be considered, however, that all these methods require an input of energy in the form of heat.

Among hydrides, sodium boron hydride ($NaBH_4$) is largely studied and considered as the most promising as it has a gravimetric and volumetric hydrogen density quite high. It reacts with water according to the following (react. XII).

XII. $$NaBH_4 + 2H_2O \rightarrow NaBO_2 + 4H_2$$

This is an exothermic reaction that releases 217 kJ/mol, is simple and occurs without a catalyst. To inhibit, the hydrolysis process, $NaBH_4$ solutions must be kept at pH > 13. At this pH, $NaBH_4$ is very stable, so the release of hydrogen only requires the solution to be in contact with a specific catalyst (Ru/C type), thus enabling the HOD system (Hydrogen On Demand)[35]. An alternative is the use of NH_3BH_3 (ammonia borane), as it exhibits a higher hydrogen storage capacity, lower toxicity and higher stability (pH = 7). This borane can be used with different catalysts, such as silica and zeolites, which cannot be used at pH values above 13 (required with $NaBH_4$)[36].

It must be clear that once hydrogen was stored it is necessary to transport it. At present, there are two methods by which it is transported: via a network of pipelines, or on-site consumption within the industrial complex itself.

2.5 The colours of H_2

Hydrogen can be produced from different energy sources with a different impact of CO_2 release. Depending on the production process and the energy source used, the costs of hydrogen and its emissions can be very different. This is why technologies for generating hydrogen are often classified according to a peculiar colour (Fig.11) as grey, blue, turquoise, black, yellow, green, pink/purple, brown and white.

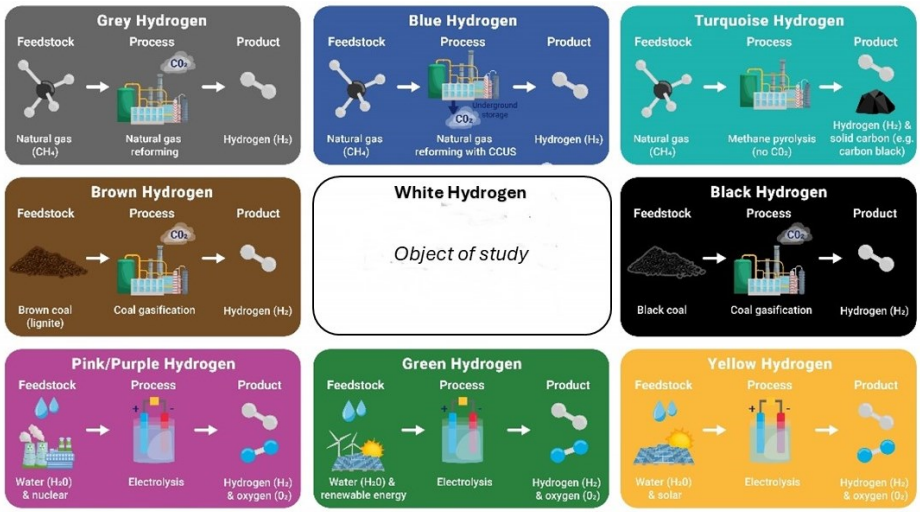

Figure 11 *Summary of the H_2 colours.*

- Grey Hydrogen

Currently, the largest amount of H_2 produced corresponds to grey hydrogen. This production corresponds to *steam methane reforming, partial oxidation or autothermal reforming* [37]. Grey H_2 is mainly used in the petrochemical industry and for the production of ammonia[38]. About 6% of the world's extracted natural gas and 2% of coal are used to produce grey hydrogen. The main

disadvantage of grey hydrogen is the high CO_2 emissions during hydrogen production (830 Mt CO_2/years)[39].

- Brown and Black Hydrogen

The amount of hydrogen obtained from these processes emits an amount of CO_2 comparable to the combustion of the starting fuel. Hydrogen obtained in this case comes from coal. The brown and black colours of the hydrogen refer to the type of coal, lignite (brown) or bituminous coal (black) used for the combustion [40]. These are widely employed methods of hydrogen production, being coal the fossil energy source with the largest reserves in the world. In particular, China produces large quantities of hydrogen through coal gasification due to high natural gas prices and large coal reserves.

- Blue Hydrogen

An important environmental development compared to previous mentioned processes is the blue hydrogen. In this case, hydrogen is still obtained from fossil fuels, but the CO_2 emitted is captured and stored (CCS).

Blue hydrogen currently has lower costs than green hydrogen. It is considered an alternative solution during the energy transition, as it still offers the possibility of consuming fossil fuels, but with a reduced carbon footprint. This provides a sustainable vision for some fossil fuel-producing countries (e.g. Canada, Iran, Norway, Qatar, Russia, USA). The methods used are the same as those for producing grey, brown or black hydrogen.

- Green Hydrogen

Research is today focused on the production of green hydrogen, also referred as ‘clean hydrogen’. This production is obtained from renewable sources using water electrolysis in fact the carbon emissions are almost zero.
Nowadays, green hydrogen only accounts for a small percentage of total hydrogen production due to the high costs involved in its process.

- Turquoise Hydrogen

It is a colour born in 2020; hydrogen is obtained from methane as raw material through a pyrolysis process. In contrast to the methane steam reforming, the formed by-product is solid carbon that appears as filamentous carbon or carbon nanotubes. This type of by-product can be further utilised and is easier to store, thus having a lower carbon footprint[41]. Furthermore, it can be sold for other applications.

- Yello Hydrogen

Yellow hydrogen is produced by electrolysis using electricity from the energy grid. Carbon emissions depend on the energy sources used in the grid. The grid is the result of the injection of electricity from every available energy sources.

- Pink Hydrogen

The production of pink hydrogen is conducted through thermochemical process using electricity from a nuclear power plant. The costs of this process are like those of green hydrogen,

except for the cost of electricity. The cost also depends on the technology used in the hydrogen production process.

- White Hydrogen

To date, white hydrogen, i.e. naturally occurring hydrogen, is not fully recognised. It can be found as a free gas in the layers of the continental crust, stored in the oceanic crust or in volcanic gases, geysers and hydrothermal systems. It appears to be present in a wide range of rock formations and geological regions[42]. The processes involved are not fully understood to date. Some hypotheses are hydrogen outgassing from the Earth's core, reaction of water with ultra-basic rocks or with reducing agents in the mantle, natural radiolysis (i.e. dissociation of water by uranium or plutonium) and decomposition of organic matter. Some of this hydrogen has been found in New Caledonia[42].

Today each countries depending on technology availability and cost is implementing different plans for the H_2 production [40] as shown (Fig.12).

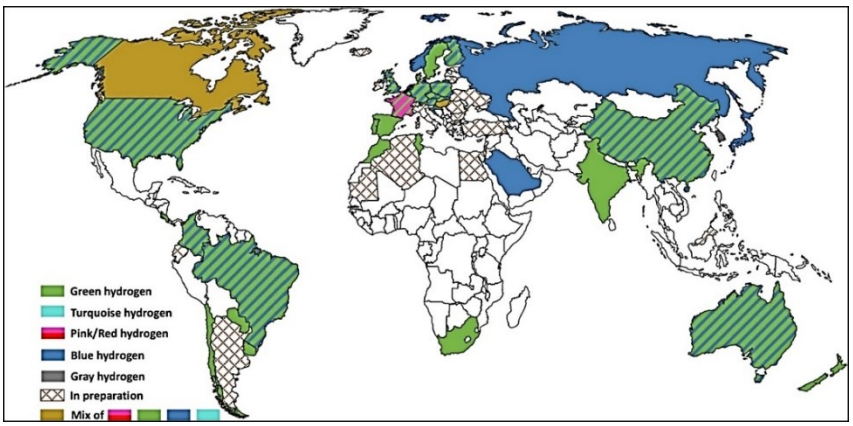

Figure 12 *H_2 Colour classifications on the basis of national hydrogen plans, strategies, or roadmaps across countries*[43].

Currently, the price of each hydrogen production process is highly dependent on the fossil fuel source, and is expected to increase over the years being also influenced by CO_2 taxes or the energy crisis (Fig.13).

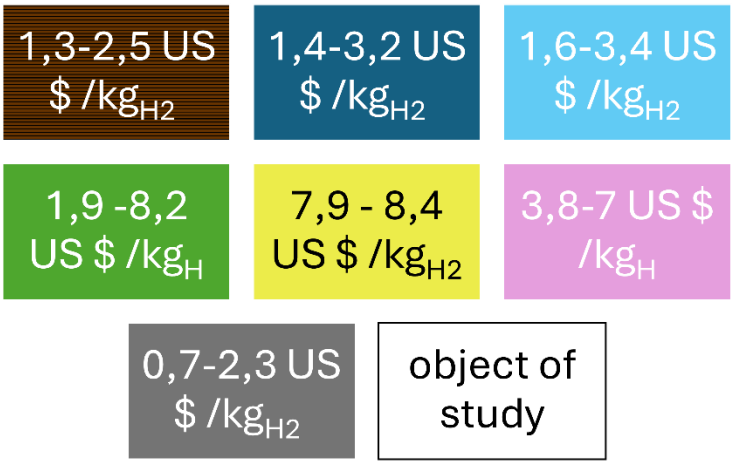

Figure 13 *Production cost comparison for H_2 production* [43].

Each scenario may be different, and it includes the cost of electricity together with the cost of hydrogen production.

References

[1] R.D. McCarty, Hydrogen: Its Technology and Implications, CRC Press, 2019. https://doi.org/10.1201/9780429487170.

[2] I.S. Yakovenko, A.D. Kiverin, Intensification mechanisms of the lean hydrogen-air combustion via addition of suspended micro-droplets of water, International Journal of Hydrogen Energy. 46 (2021) 1259–1272. https://doi.org/10.1016/j.ijhydene.2020.09.234.

[3] T.M.M. Abdellatief, M.A. Ershov, V.M. Kapustin, M. Ali Abdelkareem, M. Kamil, A.G. Olabi, Recent trends for introducing promising fuel components to enhance the anti-knock quality of gasoline: A systematic review, Fuel. 291 (2021) 120112. https://doi.org/10.1016/j.fuel.2020.120112.

[4] D. Tang, G.-L. Tan, G.-W. Li, J.-G. Liang, S.M. Ahmad, A. Bahadur, M. Humayun, H. Ullah, A. Khan, M. Bououdina, State-of-the-art hydrogen generation techniques and storage methods: A critical review, Journal of Energy Storage. 64 (2023) 107196. https://doi.org/10.1016/j.est.2023.107196.

[5] P. Nikolaidis, A. Poullikkas, A comparative overview of hydrogen production processes, Renewable and Sustainable Energy Reviews. 67 (2017) 597–611. https://doi.org/10.1016/j.rser.2016.09.044.

[6] W. Gibbons, D. Peterson, D. Papageorgopoulos, (Invited) DOE EERE Activities in High Temperature Electrolysis and Reversible Fuel Cells, ECS Transactions. 111 (2023) 3–7. https://doi.org/10.1149/11106.0003ecst.

[7] F. Dawood, M. Anda, G.M. Shafiullah, Hydrogen production for energy: An overview, International Journal of Hydrogen Energy. 45 (2020) 3847–3869. https://doi.org/10.1016/j.ijhydene.2019.12.059.

[8] R. Bouckaert, C. Dupont, Assessing the alignment of EU and member states external energy strategies with the European green deal : 2019 – 2024, International Environmental Agreements: Politics, Law and

Economics. (2025) 2019–2024. https://doi.org/10.1007/s10784-025-09671-3.

[9] K.M. Van Geem, B.M. Weckhuysen, Toward an e - chemistree : Materials for electrification of the chemical industry, MRS Bulletin. 46 (2021) 1187–1196. https://doi.org/10.1557/s43577-021-00247-5.

[10] A. M, M.K. V, V.S. Hariharan, T. Narahari, A.K. P, M. K, P.K. G, R. Prabakaran, Fuelling the future: A review of non-renewable hydrogen production and storage techniques, Renewable and Sustainable Energy Reviews. 188 (2023) 113791. https://doi.org/10.1016/j.rser.2023.113791.

[11] C. Zou, J. Li, X. Zhang, X. Jin, B. Xiong, H. Yu, X. Liu, S. Wang, Y. Li, L. Zhang, S. Miao, D. Zheng, H. Zhou, J. Song, S. Pan, Industrial status, technological progress, challenges, and prospects of hydrogen energy, Natural Gas Industry B. 9 (2022) 427–447. https://doi.org/10.1016/j.ngib.2022.04.006.

[12] V. Madadi Avargani, S. Zendehboudi, X. Duan, H. Abdlla Maarof, Advancements in non-renewable and hybrid hydrogen production: Technological innovations for efficiency and carbon reduction, Fuel. 395 (2025) 135065. https://doi.org/10.1016/j.fuel.2025.135065.

[13] R. Ma, Catalytic partial oxidation (CPOX) of natural gas and renewable hydrocarbons / oxygenated hydrocarbons — A review, Catalysis Today. 338 (2019) 18–30. https://doi.org/10.1016/j.cattod.2019.06.025.

[14] Z.R. Chong, S.H.B. Yang, P. Babu, P. Linga, X.-S. Li, Review of natural gas hydrates as an energy resource: Prospects and challenges, Applied Energy. 162 (2016) 1633–1652. https://doi.org/10.1016/j.apenergy.2014.12.061.

[15] I.A. Makaryan, E.A. Salgansky, V.S. Arutyunov, I. V. Sedov, Non-Catalytic Partial Oxidation of Hydrocarbon Gases to Syngas and Hydrogen: A Systematic Review, Energies. 16 (2023) 2916. https://doi.org/10.3390/en16062916.

[16] O. Johnson, Y. He, B. Joseph, J.N. Kuhn, Intensified Biogas-to-Fuels/Chemicals: Optimizing Tandem Bireforming and Fischer-Tropsch Synthesis in a Single Reactor, Energy and Fuels. (2025). https://doi.org/10.1021/acs.energyfuels.5c00551.

[17] D.-W. Lee, M.S. Lee, J.Y. Lee, S. Kim, H.-J. Eom, D.J. Moon, K.-Y. Lee, The review of Cr-free Fe-based catalysts for high-temperature water-gas shift reactions, Catalysis Today. 210 (2013) 2–9. https://doi.org/10.1016/j.cattod.2012.12.012.

[18] A. Yoosefdoost, O. Jazani, S. Liguori, A. Das, R.M. Santos, Toward Carbon-Negative Methanol Production from Biogas: Intensified Membrane Reactor, ChemCatChem. 17 (2025). https://doi.org/10.1002/cctc.202400698.

[19] M.L.T. Triviño, N.C. Arriola, Y.S. Kang, J.G. Seo, Transforming CO2 to valuable feedstocks: Emerging catalytic and technological advances for the reverse water gas shift reaction, Chemical Engineering Journal. 487 (2024) 150369. https://doi.org/10.1016/j.cej.2024.150369.

[20] L. Dehimi, O. Alioui, Y. Benguerba, K.K. Yadav, J.K. Bhutto, A.M. Fallatah, T. Shukla, M.A. Alreshidi, M. Balsamo, M. Badawi, A. Erto, Hydrogen production by the water-gas shift reaction: A comprehensive review on catalysts, kinetics, and reaction mechanism, Fuel Processing Technology. 267 (2025) 108163. https://doi.org/10.1016/j.fuproc.2024.108163.

[21] O.A. Ibigbami, O.D. Onilearo, R.O. Akinyeye, Post-combustion capture and other Carbon Capture and Sequestration (CCS) technologies: A review, Environmental Quality Management. 34 (2024). https://doi.org/10.1002/tqem.22180.

[22] J. Fatema, T. Ahmed, M.M. Islam, M.N. Sakib, A.M.S. Chowdhury, P. Haque, Gasification of kitchen wastes in an updraft fluidized bed gasifier and simulation of the process with Aspen Plus, Journal of Cleaner Production. 371 (2022) 133670. https://doi.org/10.1016/j.jclepro.2022.133670.

[23] A. Jain, A. Sharma, V. Jately, B. Azzopardi, Sustainable Energy Solutions with Artificial Intelligence, Blockchain Technology, and Internet of Things, CRC Press, Boca Raton, 2023. https://doi.org/10.1201/9781003356639.

[24] M. Ahmaruzzaman, S.R. Mishra, V. Gadore, D.K. Sharma, Hydrogen Generation by Photolysis of Water Vis-à-Vis Other Conventional and Advanced Non-conventional Methods of Hydrogen Production—A Review, Journal of Inorganic and Organometallic Polymers and Materials. (2024) 22–45. https://doi.org/10.1007/s10904-024-03272-4.

[25] A.K. Worku, D.W. Ayele, D.B. Deepak, A.Y. Gebreyohannes, S.D. Agegnehu, M.L. Kolhe, Recent Advances and Challenges of Hydrogen Production Technologies via Renewable Energy Sources, Advanced Energy and Sustainability Research. 5 (2024). https://doi.org/10.1002/aesr.202300273.

[26] K. Scoot, Introduction to Electrolysis, Electrolysers and Hydrogen Production, Electrochemical Methods for Hydrogen Production. (2019). www.rsc.org.

[27] H. Li, X. Zhou, Z. Hu, H. Zhang, Waste heat recycling from phosphoric acid fuel cells for desalination with hydrophilic modified tubular stills: Performance prediction and regulation, Energy. 317 (2025) 134572. https://doi.org/10.1016/j.energy.2025.134572.

[28] D.J. Durbin, C. Malardier-Jugroot, Review of hydrogen storage techniques for on board vehicle applications, International Journal of Hydrogen Energy. 38 (2013) 14595–14617. https://doi.org/10.1016/j.ijhydene.2013.07.058.

[29] J. Andersson, S. Grönkvist, Large-scale storage of hydrogen, International Journal of Hydrogen Energy. 44 (2019) 11901–11919. https://doi.org/10.1016/j.ijhydene.2019.03.063.

[30] M.R. Usman, Hydrogen storage methods: Review and current status, Renewable and Sustainable Energy Reviews. 167 (2022) 112743.

https://doi.org/10.1016/j.rser.2022.112743.

[31] R. Moradi, K.M. Groth, Hydrogen storage and delivery: Review of the state of the art technologies and risk and reliability analysis, International Journal of Hydrogen Energy. 44 (2019) 12254–12269. https://doi.org/10.1016/j.ijhydene.2019.03.041.

[32] U.S. Harisankar, S.K. Menon, J.S. Babu, B. Shankar, Exploring Carbon Nanotubes for Enhanced Hydrogen Storage: A Review on Synthesis, Mechanisms, and Evaluation, Korean Journal of Chemical Engineering. 42 (2025) 13–42. https://doi.org/10.1007/s11814-024-00311-1.

[33] Ü. Çakir, M. Doğan, B.K. Kizilduman, Z. Bicil, Functionalized and Schiff base based multi walled carbon nanotubes for hydrogen storage, Journal of Alloys and Compounds. 1010 (2025) 177290. https://doi.org/10.1016/j.jallcom.2024.177290.

[34] A. Z□ttel, Hydrogen storage methods, Naturwissenschaften. 91 (2004) 157–172. https://doi.org/10.1007/s00114-004-0516-x.

[35] T. Fleiter, J. Fragoso, B. Lux, Ş. Alibaş, K. Al-Dabbas, P. Manz, F. Neuner, B. Weißenburger, M. Rehfeldt, F. Sensfuß, Hydrogen Infrastructure in the Future CO 2 -Neutral European Energy System—How Does the Demand for Hydrogen Affect the Need for Infrastructure?, Energy Technology. 13 (2025). https://doi.org/10.1002/ente.202300981.

[36] R. Fiorenza, S. Scirè, A.M. Venezia, Carbon supported bimetallic Ru-Co catalysts for H 2 production through NaBH 4 and NH 3 BH 3 hydrolysis, International Journal of Energy Research. 42 (2018) 1183–1195. https://doi.org/10.1002/er.3918.

[37] R. Yukesh Kannah, S. Kavitha, Preethi, O. Parthiba Karthikeyan, G. Kumar, N.V. Dai-Viet, J. Rajesh Banu, Techno-economic assessment of various hydrogen production methods – A review, Bioresource Technology. 319 (2021) 124175. https://doi.org/10.1016/j.biortech.2020.124175.

[38] E.C. Okonkwo, M. Al-Breiki, Y. Bicer, T. Al-Ansari, Sustainable hydrogen roadmap: A holistic review and decision-making methodology for production, utilisation and exportation using Qatar as a case study, International Journal of Hydrogen Energy. 46 (2021) 35525–35549. https://doi.org/10.1016/j.ijhydene.2021.08.111.

[39] M. Newborough, G. Cooley, Developments in the global hydrogen market: The spectrum of hydrogen colours, Fuel Cells Bulletin. 2020 (2020) 16–22. https://doi.org/10.1016/S1464-2859(20)30546-0.

[40] M. El-Adawy, I.B. Dalha, M.A. Ismael, Z.A. Al-Absi, M.A. Nemitallah, Review of Sustainable Hydrogen Energy Processes: Production, Storage, Transportation, and Color-Coded Classifications, Energy and Fuels. (2024). https://doi.org/10.1021/acs.energyfuels.4c04317.

[41] A.M. Amin, E. Croiset, W. Epling, Review of methane catalytic cracking for hydrogen production, International Journal of Hydrogen Energy. 36 (2011) 2904–2935. https://doi.org/10.1016/j.ijhydene.2010.11.035.

[42] J.M.M. Arcos, D.M.F. Santos, The Hydrogen Color Spectrum: Techno-Economic Analysis of the Available Technologies for Hydrogen Production, Gases. 3 (2023) 25–46. https://doi.org/10.3390/gases3010002.

[43] J. Incer-Valverde, A. Korayem, G. Tsatsaronis, T. Morosuk, “Colors” of hydrogen: Definitions and carbon intensity, Energy Conversion and Management. 291 (2023) 117294. https://doi.org/10.1016/j.enconman.2023.117294.

CHAPTER III: Plastic pollution

CHAPTER III: Plastic pollution

Plastic is one of the most produced solid wastes in our daily lives. For this reason, its exponential growth is a major concern of today due to the connected environmental problems related to its use. Indeed, the applications of the plastic materials are several thanks to their properties such as low cost, a polymeric structure with a low specific weight, low thermal and electrical conductivity, a high durability over the years and excellent mechanical properties[1]. Plastic materials are generated by polymerization of monomers extracts by petrochemical products (Fig.1) in combination with other substances[2].

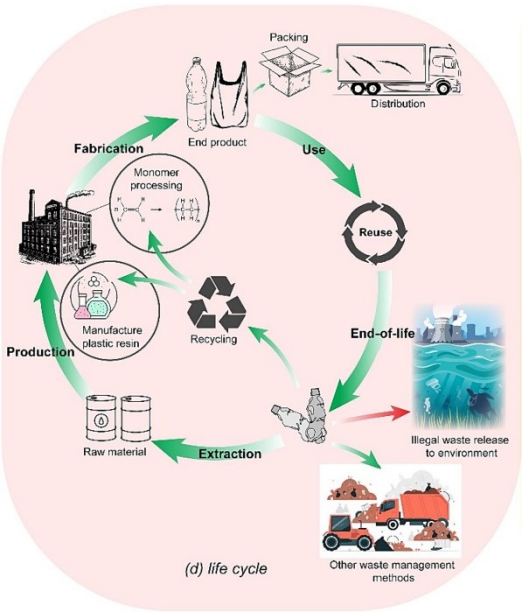

Figure 1 Plastic materials life cycle.

Monomers are the repeating units of long-chain polymers usually composed of carbon, hydrogen and oxygen held together by covalent bonds. On the basis of the particular features of the final products different chemical agents can be added such as fillers,

plasticizers, pigments, foaming agents, processing aids, lubricants, heat stabilizers, acid scavengers, antioxidants, UV stabilizers, flame retardants and antistatic agents, in different amounts, to control different functions such as ease of processing, an increased durability, improved performance and appearance. Plastic materials reached the maximum of production during World War II with the discover of nylon [3], and after they have been used in many fields, including agriculture, construction, transportation, thermal insulation, packaging, manufacturing, electronics, furniture, toys and leisure products, automobiles, and medicine[4]. For this reason, the plastic materials can be classified in different ways as shown in the (Fig.2).

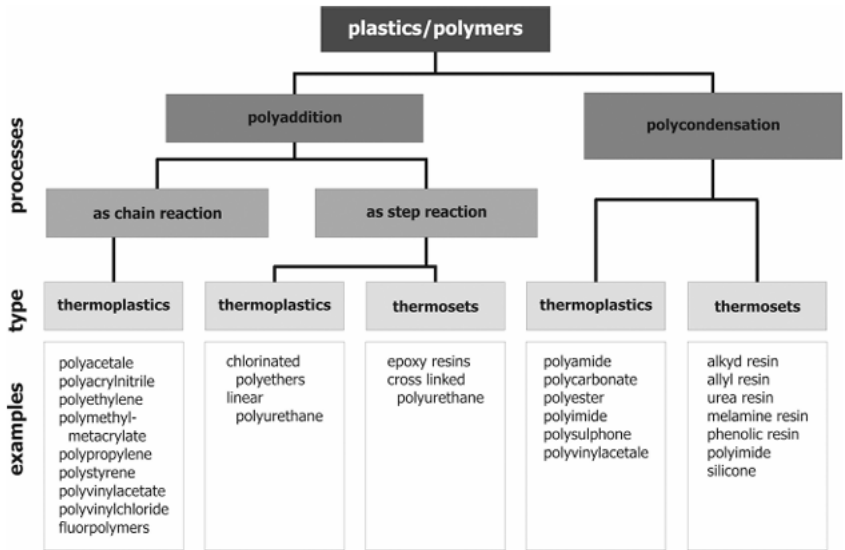

Figure 2 *Classification of polymers on the basis of their preparation* [5].

The Society of the Plastic Industry (SPI) has introduced a numerical coding system for plastics. In this case, numbers from 1 to 7 have been assigned (Fig.3).

Figure 3 *Classification by SPI.*

However, in the last years the exponential use of plastics led to the problem of their disposal at the end of use.

Plastic waste has increased globally for three main reasons: 1) plastics have replaced traditional materials such as ceramics, wood and glass, 2) growth population, 3) low cost. The short life cycle of plastic (i.e. single-use material) increases the accumulation of plastic in the environment. About two-thirds of global plastics have a short life cycle, less than one month[6]. The obvious problem is that plastic degradation rates range from 100 to 1000 years, in fact it is possible that the first invented plastics could still exist in nature[7]. Global plastic waste was estimated in 6.30 billion tons from 1950 to 2015, while in 2016 it was about 242 million tons. Based on the prediction of some researchers[8], the accumulation of plastic waste by 2035 would be equal to the amount of fish in the oceans (Fig.4).

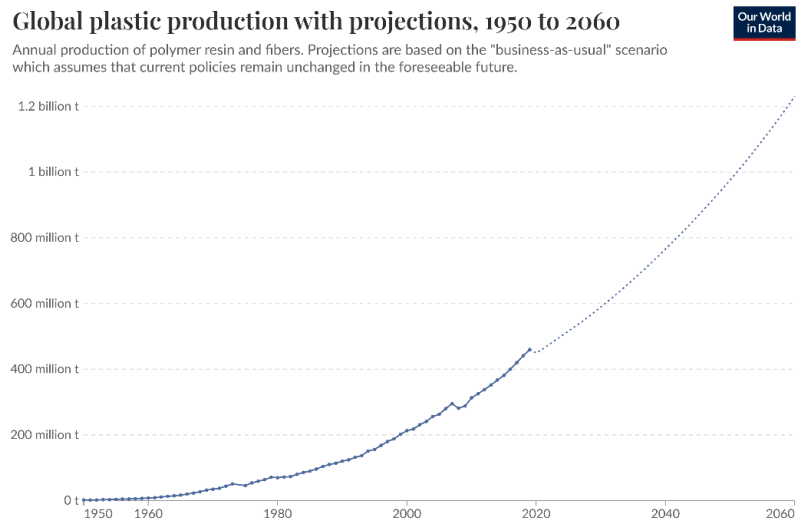

Figure 4 *Trend in the production of plastic waste. Source:*[9].

Plastic causes undoubtedly environmental pollution on global scale. Moreover, the presence of microplastics (plastic particles smaller than 5 mm[10]) can generate dangerous health effects on humans and animals.

Microparticles of plastics have been found in water systems, landfills and even human bodies[11]. During the pandemic COVID-19, the levels of pollutants such as CO_2, NO_X and SO_X decreased, but the crisis has induced an enhanced consumption of the single-use plastics, despite the widespread trend of increasing bans and/or taxes to reduce the plastic utilization[12].

The degradation of plastics can be divided into four categories: physical/mechanical degradation, photodegradation/photo-oxidative degradation, chemical and thermal degradation, and biological degradation.

- *Physical/mechanical processes* (in the presence of waves) involve changes in the bulk structure that occur at the

molecular level, including oxidation of polymers and the formation of short-chain molecules.

- *Photodegradation/photo-oxidative* degradation (under exposure to UV radiation) initiates the breakdown of polymer chains by producing free radicals[13].
- *Chemical degradation* (corrosive chemicals including acids such as nitric, sulfuric, and hydrochloric, and air pollutants) and thermal degradation (chemical changes that affect heat/temperature) can break and oxidize the polymer chains of plastics.
- *Microorganisms* such as bacteria, fungi and yeasts can change the physical and chemical properties of plastics by metabolizing the carbon in the polymer into carbon dioxide or by incorporating biomolecules in a natural degradation. This process is known as biological degradation.

Management solutions encounter constraints and show inefficiency, due to a lack of coordination between local and global levels of governance[14]. It must be made clear that the stages of the plastic life cycle, from oil extraction to production, consumption and disposal, are highly dependent on country policies. In fact, waste management such as recycling and disposal is a national competence, there are many aspects in both production and disposal that cross geopolitical boundaries[15]. Increasing attention is being paid to marine litter, as it directly affects billions of people living in communities because the ocean serves as the main sink for plastic pollution on a global scale.

Numerous studies are being carried out and so are the political challenges, in fact the problem of plastics is also mentioned in the

2015 UN (United Nations) launched 17 SDGs (Sustainable Development Goals) as part of the 2030 Agenda for Sustainable Development[16] (Fig.5).

Figure 5 *Sustainable Development Goals, (2024), United Nations Department of Economic and Social Affairs, https://sdgs.un.org/goal.*

This "Agenda" shows 169 targets associated with 17 objectives, for which 231 unique indicators were proposed. The indicator 14.1.b, mentions the density of plastic debris that should be > 2.5 cm.

Specifically, the objective 14.1, aims to "prevent and significantly reduce marine pollution of all kinds, particularly from land-based activities, including marine debris and nutrient pollution". Indeed, the presence of microplastics and nanoplastics in the seas strongly threaten ecosystems such as the food supply (like fishing) [17]. Since 2000, in order to reduce the amount of CO_2 emitted from the plastics production, the industries started to produce biodegradable plastics using natural and renewable materials such as vegetable fats and oils, gluten, egg white proteins and starch [18].

3.1 Policies adopted for plastic consumption

Europe has committed to limiting plastic consumption by implementing several reforms.

- Com (2018) Strasburg [19]

Goals include reducing marine litter, greenhouse gas emissions and dependence on imported fossil fuels.

- SUPD 2019/904 EU [20]

This directive bans several single-use plastic items, such as cutlery, plates, straws and polystyrene containers. It also sets collection and recycling targets for plastic bottles.

- Packaging and Packaging Waste Regulation 2024 [21]

The EU has reached a provisional agreement to reduce packaging waste by 5% by 2030 and 15% by 2040. All packaging will have to be recyclable by 2030, with bans on some single-use items such as plastic plates and cups.

3.2 Environmental impact caused by plastic pollution

Plastic waste management is a current major issue because it causes a large environmental impact. Plastic is mainly produced, used and disposed on land, resulting in a significant amount of waste accumulating in the global environment. For example, agricultural plastics such as plastic films, wrappers and packaging materials are highly available as plastic waste because they were easily broken down into microplastics and can remain in the soil up to 15 years. Freshwater ecosystems act as magnets for various pollutants released within a river basin, due to their location in valleys and low-lying terrain. According to the United Nations Environment Programme (UNEP)[22], nearly 1,000 rivers are responsible for nearly 80% of annual riverine plastic emissions worldwide. Plastic waste kills more than 100,000 marine species every year, covering all areas from the coast to the ocean depths. Airborne microplastics are made up of natural and synthetic polymers ranging in size from 20 to 500 μm[23]. These airborne microplastics come in a variety of forms, including fiber (the most common), film, fragment, foam, granule, and sphere. Synthetic fabrics are the main carriers (used in clothing). For example, just 1 g of acrylic contained in the clothes can release more than 1,100 airborne microplastic particles during the drying process[23]. These fibres can be released into the atmosphere during activities such as putting on clothes or drying oneself. Airborne microplastics can also have alternative sources, including the degradation of larger plastic items and industrial emissions. In fact, wind acts as a force that lifts microplastics from the soil into the air, facilitating their transport to remote areas causing

contamination in both terrestrial and aquatic ecosystems. Consequently, this dynamic cycle moves plastics between the air, land, and aquatic environments, contributing to their presence in the overall environmental landscape[24]. This cycle strongly influences the food chain causing harm to aquatic and terrestrial animals. For example, reptiles (such as snakes) and birds can be trapped by plastic nets (applied in agricultural fields, in aquatic farms). Furthermore, the transformation into microplastics with consequent ingestion of the animal/human can cause health problems such as blockage of the intestinal tract or gastric enzyme secretion. In marine environments, plastic debris reduces the light and oxygen levels of the water, and this reduces the biodiversity of marine habitats. Chemicals associated with plastic, such as bisphenol A, phthalates and heavy metals, can accumulate on living organisms through food webs and cause negative impacts such as oxidative stress, cancer and endocrine disruption[13]. For example, polychlorinated biphenyls (PCBs) can enter in the food chains leading to reproductive disorders or even death[13].

References

[1] K. Al-Omran, E. Khan, N. Ali, M. Bilal, Estimation of COVID-19 generated medical waste in the Kingdom of Bahrain, Science of The Total Environment. 801 (2021) 149642. https://doi.org/10.1016/j.scitotenv.2021.149642.

[2] A. Torres-Agullo, A. Karanasiou, T. Moreno, S. Lacorte, Overview on the occurrence of microplastics in air and implications from the use of face masks during the COVID-19 pandemic, Science of The Total Environment. 800 (2021) 149555. https://doi.org/10.1016/j.scitotenv.2021.149555.

[3] M. Kedzierski, D. Frère, G. Le Maguer, S. Bruzaud, Why is there plastic packaging in the natural environment. Understanding the roots of our individual plastic waste management behaviours, Science of The Total Environment. 740 (2020) 139985. https://doi.org/10.1016/j.scitotenv.2020.139985.

[4] P.G.C. Nayanathara Thathsarani Pilapitiya, A.S. Ratnayake, The world of plastic waste: A review, Cleaner Materials. 11 (2024) 100220. https://doi.org/10.1016/j.clema.2024.100220.

[5] K.M., The handbook of environmental chemistry, 1982. https://doi.org/10.1016/0143-1471(82)90111-8.

[6] A.K. Panda, R.K. Singh, D.K. Mishra, Thermolysis of waste plastics to liquid fuelA suitable method for plastic waste management and manufacture of value added products—A world prospective, Renewable and Sustainable Energy Reviews. 14 (2010) 233–248. https://doi.org/10.1016/j.rser.2009.07.005.

[7] N.A. Welden, The environmental impacts of plastic pollution, in: Plastic Waste and Recycling, Elsevier, 2020: pp. 195–222. https://doi.org/10.1016/B978-0-12-817880-5.00008-6.

[8] A. Stubbins, K.L. Law, S.E. Muñoz, T.S. Bianchi, L. Zhu, Plastics in the Earth system, Science. 373 (2021) 51–55.

https://doi.org/10.1126/science.abb0354.

[9] and M.R. Hannah Ritchie, Veronika Samborska, Plastic Pollution, (2022). https://ourworldindata.org/plastic-pollution.

[10] J.P.G.L. Frias, R. Nash, Microplastics: Finding a consensus on the definition, Marine Pollution Bulletin. 138 (2019) 145–147. https://doi.org/10.1016/j.marpolbul.2018.11.022.

[11] L.A. Amaral-Zettler, E.R. Zettler, T.J. Mincer, Ecology of the plastisphere, Nature Reviews Microbiology. 18 (2020) 139–151. https://doi.org/10.1038/s41579-019-0308-0.

[12] D. Hantoko, X. Li, A. Pariatamby, K. Yoshikawa, M. Horttanainen, M. Yan, Challenges and practices on waste management and disposal during COVID-19 pandemic, Journal of Environmental Management. 286 (2021) 112140. https://doi.org/10.1016/j.jenvman.2021.112140.

[13] G.M.S.S. Gunawardhana, U.L.H.P. Perera, A.S. Ratnayake, Sources and Fate of Plastics into Microplastics, in: Maritime Accidents and Environmental Pollution - The X-Press Pearl Disaster, CRC Press, Boca Raton, 2023: pp. 155–172. https://doi.org/10.1201/9781003314301-8.

[14] A. Löhr, H. Savelli, R. Beunen, M. Kalz, A. Ragas, F. Van Belleghem, Solutions for global marine litter pollution, Current Opinion in Environmental Sustainability. 28 (2017) 90–99. https://doi.org/10.1016/j.cosust.2017.08.009.

[15] G. Ferraro, P. Failler, Governing plastic pollution in the oceans: Institutional challenges and areas for action, Environmental Science & Policy. 112 (2020) 453–460. https://doi.org/10.1016/j.envsci.2020.06.015.

[16] P. Stoett, V.M. Scrich, C.I. Elliff, M.M. Andrade, N. de M. Grilli, A. Turra, Global plastic pollution, sustainable development, and plastic justice, World Development. 184 (2024) 106756. https://doi.org/10.1016/j.worlddev.2024.106756.

[17] N.S. Zamboni, E.M. Noleto Filho, A.R. Carvalho, Unfolding differences in the distribution of coastal marine ecosystem services values among developed and developing countries, Ecological Economics. 189 (2021) 107151. https://doi.org/10.1016/j.ecolecon.2021.107151.

[18] N.I. Ibrahim, F.S. Shahar, M.T.H. Sultan, A.U.M. Shah, S.N.A. Safri, M.H. Mat Yazik, Overview of Bioplastic Introduction and Its Applications in Product Packaging, Coatings. 11 (2021) 1423. https://doi.org/10.3390/coatings11111423.

[19] COM(2015) 614 final, Closing the loop - An EU action plan for the Circular Economy. https://eur-lex.europa.eu/legal-content/EN/TXT/?uri=CELEX%253A52015DC0614.

[20] Directive (EU) 2019/904 of the European Parliament and of the Council of 5 June 2019 on the reduction of the impact of certain plastic products on the environment (Text with EEA relevance). http://data.europa.eu/eli/dir/2019/904/oj.

[21] Regulation (EU) 2025/40 of the European Parliament and of the Council of 19 December 2024 on packaging and packaging waste, amending Regulation (EU) 2019/1020 and Directive (EU) 2019/904, and repealing Directive 94/62/EC (Text with EEA relevance), (n.d.). http://data.europa.eu/eli/reg/2025/40/oj.

[22] H.L. Chen, S.B. Selvam, K.N. Ting, C.N. Gibbins, Microplastic pollution in freshwater systems in Southeast Asia: contamination levels, sources, and ecological impacts, Environmental Science and Pollution Research. 28 (2021) 54222–54237. https://doi.org/10.1007/s11356-021-15826-x.

[23] P. Li, X. Wang, M. Su, X. Zou, L. Duan, H. Zhang, Characteristics of Plastic Pollution in the Environment: A Review, Bulletin of Environmental Contamination and Toxicology. 107 (2021) 577–584. https://doi.org/10.1007/s00128-020-02820-1.

[24] Y. Wang, J. Huang, F. Zhu, S. Zhou, Airborne Microplastics: A Review on the Occurrence, Migration and Risks to Humans, Bulletin of

Environmental Contamination and Toxicology. 107 (2021) 657–664. https://doi.org/10.1007/s00128-021-03180-0.

CHAPTER IV: Green H_2 Production

CHAPTER IV: Green H_2 Production

4.1 Photocatalysis

Photocatalysis is one of the more recent and interesting process investigated preferentially in research, for many technological applications, because it is characterised by low costs, especially when the solar radiation is used, and eco-friendly and mild treatment conditions. The term originates from Greek and is a word composed of 'photo' and 'catalysis', which indicates the degradation (from the Greek verb καταλειν: to break, to dissolve) of compounds in the presence of light. The concept was firstly used by the British chemist Elizabeth Fulhame in 1794, based on her tests in photo-oxidation/reduction experiments[1]. Catalysis is defined as the process of increasing the rate of a chemical reaction by adding a substance known as a catalyst. Photocatalysis can be homogeneous, heterogeneous and finally enzymatic.

In the case of heterogeneous photocatalysis, the medium on which the reaction takes place can be gas phase, pure organic liquid phases or aqueous solutions. The applications can be several as degradation of pollutants, reduction of volatile organic compounds (VOC), CO_2 conversion[1],CO_2 reduction[2] and H_2

[1] The photothermo-catalytic CO_2 conversion/reduction were investigated in two collaborative works of our research laboratory: R. Fiorenza, C. Contarino, V. Spanò, **M. T. Armeli Iapichino**, S. A. Balsamo, "Photothermo-catalytic strategies for the CO_2 valorisation using TiO_2-based composite" *Catalysis Today,423,114251,2023.*

[2] R. Fiorenza, L. Calantropo, E. La Greca, L. F. Liotta, A. Gulino, A. Ferlazzo, M. G. Musumeci, G. Proietto Salanitri, Sa. C. Carroccio, G. Dativo, **M. T. Armeli Iapichino**, S. Scirè, G. Impellizzeri "Solar-promoted photo-thermal CO_2 methanation on SiC/hydrotalcites derivates catalysts *"Catalysis Today,449,115182,2025.*

production. Photocatalysis is based on five independent steps[2–4]:

a. Transfer of the reactants in the fluid phase to the surface.
b. Adsorption on the photocatalyst surface of at least one of the reactants.
c. Reaction in the adsorbed phase.
d. Desorption of products.
e. Removal of products from the interface region.

The main difference from conventional catalysis is the way in which the catalyst is activated, since thermal activation is replaced by photonic activation.

4.2 Photocatalytic H_2 production

One of the challenges for our future, as already mentioned in Chapter 1.1, is the development of a safe, clean and renewable energy source, or in the case of an energy vector as hydrogen the research of efficient and sustainable ways to produce it.

Recently, one of the technologies investigated and developed is the photocatalytic hydrogen production through water splitting (WS). In this case, the use of solar radiation is the most ideal approach to produce this fuel, as solar radiation provides the Earth with approximately 1022 J[5], which is enough to meet ideally the global needs.

The photocatalytic water splitting was firstly investigated by Honda and Fujishima 1972[6], who studied this reaction using a TiO_2 anode(photo-electrolysis).

The photocatalytic water splitting possesses multiple advantages compared to the thermochemical and photobiological water splitting, including:

- low cost (when the solar radiation was used)[7],
- relatively high solar to H_2 efficiency,
- flexible reactor size, which is appropriate for small-scale use[8].

Photocatalytic water splitting is also considered as an artificial photosynthesis process (Fig.1), in fact, light energy is converted into chemical energy while the water splitting reaction promotes the formation of Gibbs free energy (ΔH_0 =238 kJ mol^{-1})[9].

Three basic elements are required to achieve the photocatalytic mechanism: a reagent, a photocatalyst (semiconductor) and luminescent radiation (preferably the solar radiation).

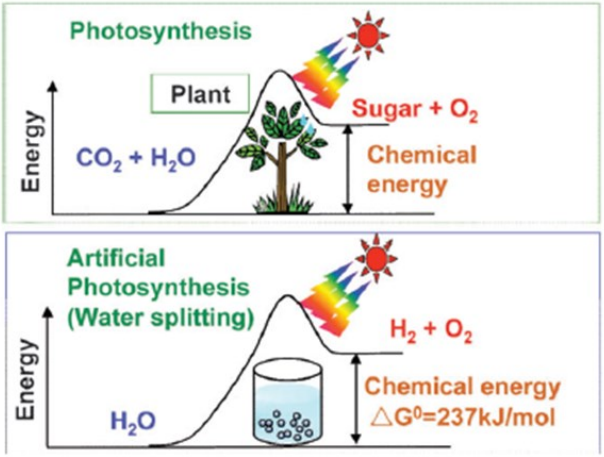

Figure 1 *Photosynthesis by green plants and photocatalytic water splitting as an artificial photosynthesis.*[10]

Photocatalysts (semiconductors) have a non-overlapping valence band and conduction band with an energy gap (E_g) between them. The reaction takes place in the presence of suitable wavelengths (able to cover the E_g). The photons promote the electrons excitation from the valence band to the conduction band, leaving electron gaps (holes) in the valence band and excess electrons in the conduction band. The electron-holes(e^-/h^+) pairs generated play a key role in the redox reactions of water splitting (react. I-II).

$$\text{I.} \quad H_2O + 2h^+_{vb} \rightarrow 2H^+ + \tfrac{1}{2}\, O_2$$

$$\text{II.} \quad 2H^+ + 2\, e^- \rightarrow H_2$$

Electrons are responsible for the reduction of protons in hydrogen molecules whereas water will be oxidised by holes (Fig.2).

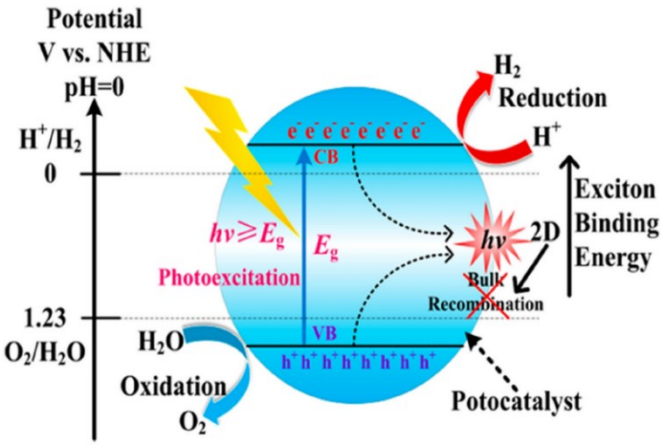

Figure 2 *Water splitting process using semiconductor photocatalyst*[11]**.**

To achieve an efficient hydrogen production and to initiate the redox reaction, the following conditions must be satisfied:

a. The conduction band (CB) reduction potential must be more negative than that of the H^+/H_2 redox couple (-0.41 V vs. NHE at pH 7, 25 °C). (Fig.3)
b. The valence band (VB) potential must be more positive than the oxidation potential of the O_2/H_2O couple (0.82V vs. NHE at pH 7, 25 °C) to enable the oxidation half-reaction. (Fig.3)
c. The theoretical minimum band gap (E_g) required to drive the water splitting reaction is 1.23 V.

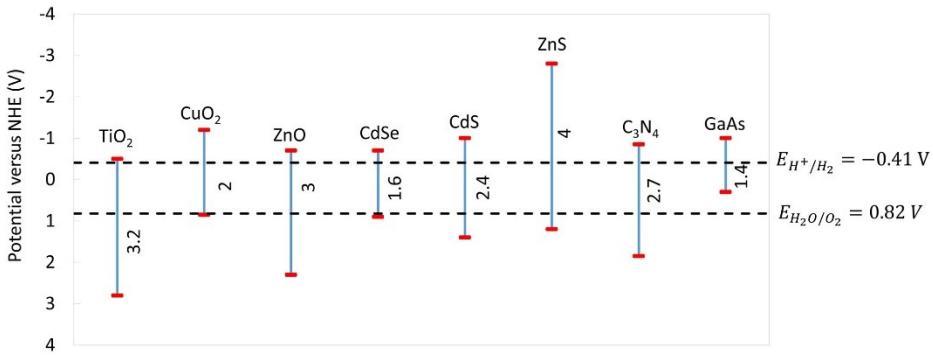

Figure 3 *Band positions of some semiconductor photocatalysts and the redox potentials of water splitting at pH 7 in aqueous solution* [12].

To improve solar energy efficiency, photocatalysts with the ability to operate under visible light are highly desirable, since visible light contributes nearly for half of the incoming solar energy. The band gap of the semiconductor materials must be less than 3 eV to have a response to visible light[13]. Solar-hydrogen efficiency (STH) is a parameter describing the efficiency of direct conversion of solar energy into hydrogen. It is defined as the ratio of the chemical energy stored in the produced hydrogen to the total incident solar energy, typically expressed as a percentage[14–16].

$$STH\ (\%) = \left[\frac{Output\ energy\ of\ H_2\ evolved}{Energy\ of\ incident\ solar\ light}\right] \times 100$$

$$= \left[\frac{(mmol\ H_2\ s^{-1}) \times 273\ (KJ\ mol^{-1})}{P_{in}\ (MW\ cm^{-2}) \times area\ (cm^2)}\right] \times 100$$

Currently, one of the most promising processes to improve the clean hydrogen production is a combined approach as the photo-electrocatalysis (PEC).

PEC involves the application of an external potential to a semiconductor film (photocatalyst) that is supported on a conductive substrate (anode) to prevent the recombination of photogenerated electron/hole (e^-/h^+) pairs[17]. It is possible also to favour the production of H_2 from the degradation of a pollutant organic compound by operating in two separate cells[3].

[3] The photo-electrocatalytic approach for the H_2 production and dye degradation was investigated in a collaborative work of our laboratory:
E. M. Malannata, **M. T. Armeli Iapichino**, A. Auditore, R. Fiorenza, F. Lo Presti, N.Tuccitto and A. Licciardello "Simultaneous H_2 production and water purification with surface-modified nanostructured TiO_2 photoelectrodes*" RSC Advances 15,18, 14273-14281,2025*

4.3 H_2 production by photoreforming

A sustainable method with low environmental impact and extremely low cost recently studied by many researchers both on a laboratory scale with possible applications in industrial scale-up is the *Photoreforming* (PR). With this reaction, there is an increase in the production of H_2 compared to the simple water splitting reaction. The PR reaction takes place in the liquid phase with the presence of a catalyst immersed in an aqueous solution containing the sacrificial agent, an organic compound (react. I). The function of this organic compound is crucial because it limits the recombination of charge couple e^-/h^+ by increasing H_2 production compared to the simple WS reaction. At the same time the sacrificial agent can act as a proton source thanks to intermediate reactions[18,19].

I. $C_xH_yO_z + (2x\text{-}z)\ H_2O \rightarrow (2x\text{-}z+y/2)\ H_2 + x\ CO_2$

The objective of photoreforming is to simultaneously achieve high purity and large quantities of hydrogen gas (reduction) and at the same time to selectively oxidise organic molecules into high-added value products (oxidation).

The efficiency of PR is highly dependent on three basic charge kinetics:

a. excitation/charge generation.
b. charge separation and migration.
c. charge consumption.

In the water splitting reaction, photocatalysts are selected based on the position of their conduction band and valence band, which must have enough energy to carry out both hydrogen reduction

and water oxidation. While, in the photoreforming reaction, photocatalysts can have also a lower valence band energy, depending on the type of organic oxidation reactions involved, which are often easier to achieve compared to the water oxidation (Fig.4).

Moreover, an oxygen-free environment is necessary during PR to avoid the formation of reactive species such as superoxide radicals ($\bullet O_2^-$). These radicals compete with hydrogen production by capturing electrons, which reduces the catalytic efficiency of the reaction[20].

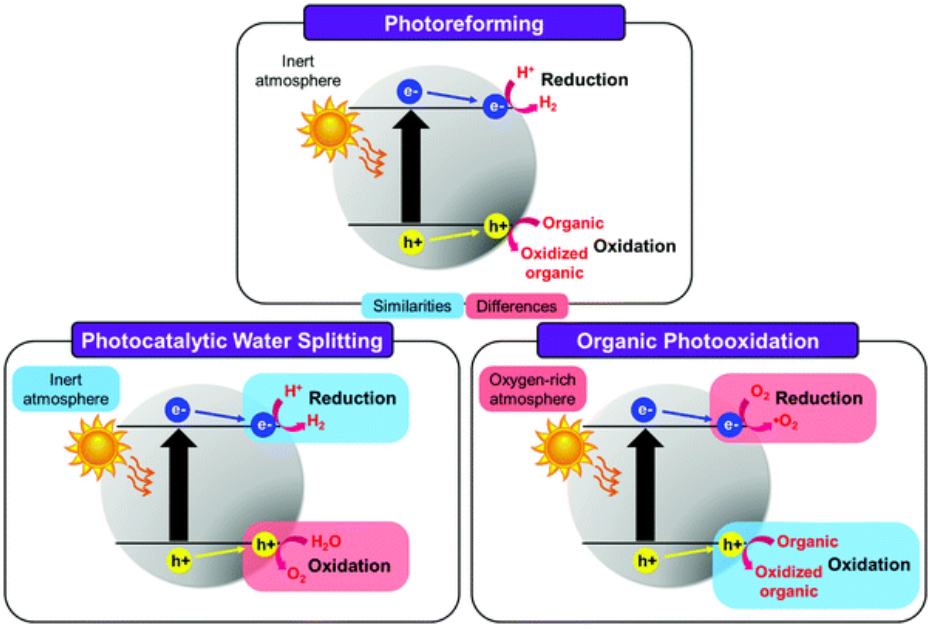

Figure 4 *Photoreforming: comparison with the photocatalytic hydrogen generation by water splitting and organic photooxidation.*[21]

The selective oxidation of the sacrificial agent required that a large number of the active sites present on the catalyst surface interacts with the organic molecules, regulating the formation of the radical species and the surface adsorption/desorption capacity.

For a thermodynamic point of view the photoreforming, is less endergonic compared to the water splitting and overcomes the limits related to the evolution of H_2 by H_2O dissociation and therefore it is more favoured. Indeed, from the energetic point of view the value is almost neutral (ΔE^0= +0.001 V)[22].

It is also important to evaluate the temperature conditions required for the reaction, as a sufficiently intense irradiation flux may be necessary in order to preserve a significant number of photogenerated electron-hole pairs in the semiconductors.

However, it is also possible that an increase in temperature facilitates the solubility of the organic substrate, providing a sufficient supply of electron donors for the photoreforming reaction and promoting the evolution of hydrogen. Therefore, it is necessary to reach the right temperature depending on the examined PR reaction [23].

4.3.1 Plastic photoreforming

The high versatility of the photocatalysis allows to consider a pollutant as a resource, and in this contest, it is possible to use the plastic materials as organic scavenger for the photoreforming reaction. In this way, two nowadays urgent questions as the water pollution by the plastics contaminants and the research of new sustainable sources of energy can be addressed.

Plastic has become extremely popular due to its ease of production, low cost, and strong thermal and mechanical resistance. As mentioned in Chapter 1.3, the main issue is its disposal: a significant portion is incinerated, while only a small amount is recycled[24]. Therefore, using plastics as an organic scavenger of the photoreforming reaction presents a promising method for waste management, particularly in the production of hydrogen fuel and valuable chemicals formation such as acetate, formate, and glycolate[25]. However, the development of plastic photoreforming is still ongoing, with few studies and practical applications [26].

The photoreforming process occurs when solar radiation reaches the photocatalyst surface with an energy greater than or equal to the semiconductor energy bandgap (react. I) Therefore, the light energy must be sufficient to allow the formation of charge carriers (electrons e^-, holes h^+).

The mechanism of plastic photoreforming is carried out in the absence of oxygen rather than in the presence of oxygen, unlike photodegradation and photooxidation [27]. Therefore, the photogenerated holes do not combine with oxygen to form radicals such as superoxide ($O^{2\bullet-}$) and singlet oxygen ($^1O_2$) [28]. However, hydroxyl (•OH) radicals can be formed (react. II). The use of inert

carrier gases, such as argon or nitrogen, for plastic photoreforming is not mandatory but it is often considered advantageous[29]. Decreasing the concentration of oxygen by an inert gas can minimize side reactions which might compete with HER for photo-generated electrons, allowing for a higher yield of hydrogen[30]. It can also help to prevent undesired oxidation reactions, maintaining the stability and effectiveness of the photocatalysts, because oxygen/reactive oxygen species can oxidize the photocatalyst or react with organic products/organic intermediates, reducing the overall efficiency of the process[31].

Since h^+ (holes) move to the catalyst surface and the lifetime of •OH is generally short, mainly •OH radicals bounded to the surface of the catalyst are formed instead of free •OH radicals in the solution [32]. Based on various studies, not only •OH surface radicals (react. III) but also holes act as oxidation agents in the photoreforming process [29,33,34]. Therefore, the plastic degradation is caused by two main agents, photogenerated holes and surface-bounded •OH radicals.

Besides the oxidation of plastic, photo-generated electrons participate in the reduction of H_2O to form H_2 (react. IV).

The simplified reactions for the plastic photoreforming are summarized below[27]:

I. photocatalyst $+h\nu \rightarrow e^-_{(CB)} + h^+_{(VB)}$

II. $h^+_{(VB)} + H_2O \rightarrow \cdot OH + H^+$

III. $h^+_{(VB)}$ or $\cdot OH$ + plastic → intermediates + organic products

IV. $2e^-_{(CB)} + 2H^+ \rightarrow H_2$

From a thermodynamic perspective, a reaction occurs spontaneously when the Gibbs free energy (ΔG°) is negative (Fig.5). For instance, the steam reforming of carbon, ethanol, methane, and ethane have highly positive ΔG° values, meaning that the reactions require a significant energy input. In contrast, some the photoreforming of some synthetic polymers such as polyethylene terephthalate (PET) have a lower ΔG° value (ΔG° = +9.2 kJ mol^{-1}) compared to water splitting (ΔG° = +237 kJ mol^{-1}) (Fig.5). Therefore, hydrogen production from PET can be more efficient than water splitting[35,36].

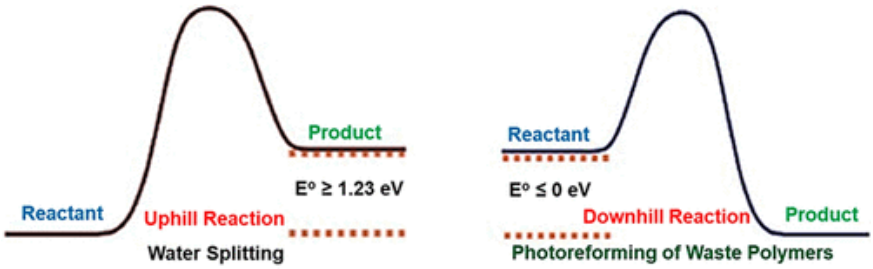

Figure 5 *Water splitting is an endothermic process, while photoreforming of waste polymers is exothermic* [36].

The choice of plastic materials can be done considering these seven categories depending on the best electron promoter (Fig.6).

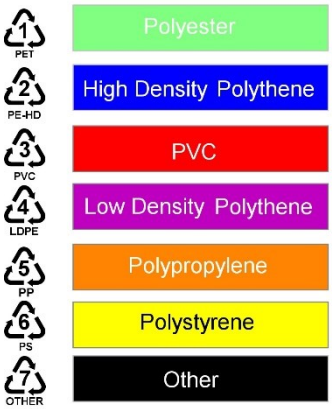

Figure 6 *Plastic materials categories.*

The choice of photocatalyst must be made according to the bands potentials, the conduction band (CB) must exceed the reduction potential of H_2, while valence band (VB) must be more positive than the oxidation potential of the plastic substrate (Fig.7).

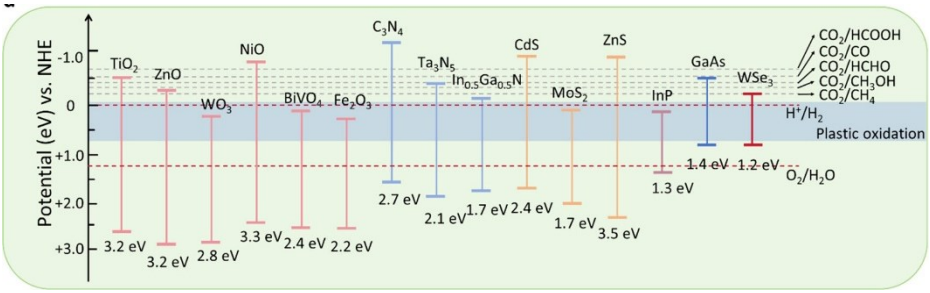

Figure 7 *Bandgaps and band edge positions of various semiconductors on a potential scale versus the normal hydrogen electrode (NHE)* [37].

From a kinetic perspective, the rate of the photoreforming (PR) process depends on the adsorption of the plastic substrate on the surface of the photocatalyst and is improved by the immobilisation of the substrate. Chemisorption facilitates charge transfers within the photocatalyst by shifting the flat-band potential and trapping charge carriers on the substrate. As a result, the oxidation reaction of the plastic occurs on subnanoseconds (ns) timescale through the direct transfer of charge carriers to the chemical substrate, leading to the generation of radicals on the surface-bound substrates[38].

In the photoreforming of plastic material, the pretreatment of the plastic is fundamental because it allows to alter the structure and to reduce the size of waste polymers[39]. This phase is currently under development by numerous researchers, and many aspects remain still unexplored.

The ideal pretreatment process should have the following characteristics:

a. produce monomeric substrates
b. these monomers should be easily hydrolysed for a good solubilisation
c. monomers should be stable to avoid the formation of degradation by products.

The estimation of the costs and the formation of byproducts after the pretreatment process depends mainly on some parameters such as temperature, pH, duration of the process and used solvents. Pretreatment strategies are generally divided into physical, chemical, catalytic, physicochemical, biological and mixed methods (Fig.8).

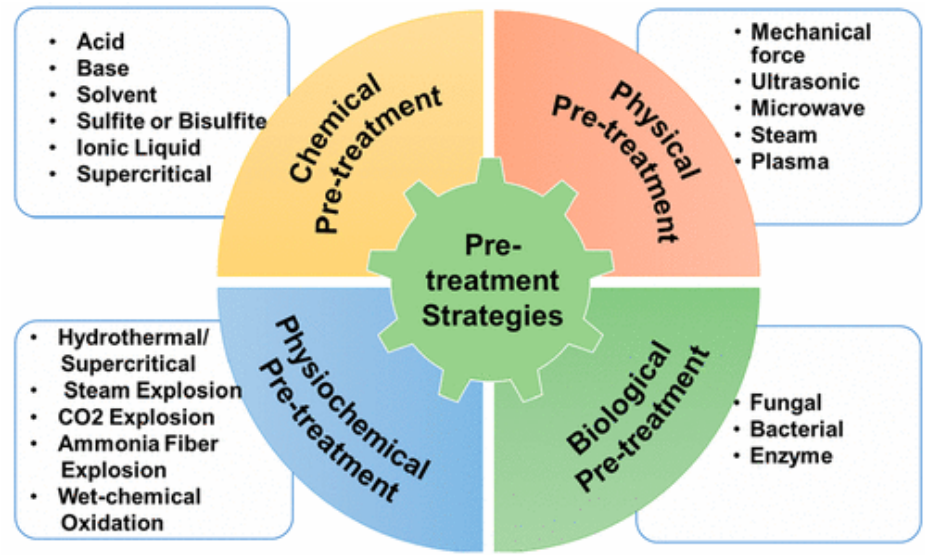

Figure 8 *Schematic illustration of the several pretreatment strategies for the waste polymers utilization in the photoreforming reactions.*

In this thesis, the chemical and physical pretreatments are explored.

- *Chemical strategies*

The most common and effective pretreatment strategy uses chemicals such as acids, alkalis, ionic liquids, organic solvents, and supercritical fluids to remove weak intermolecular forces or to break bonds between waste polymer chains, to reduce the crystallinity of the components, and to improve the degree of depolymerization.

Sulfuric acid (H_2SO_4) and hydrochloric acid (HCl) are among of the most commonly used and extensively studied acids[40,41]. Their use increases the selectivity and efficiency of hydrolyzed polymer fractions or organic substrates into their monomeric units. This process can lead to the recovery of additional solid-phase fractions or enhance their conversion. However, acid pretreatment also has several disadvantages, including the formation of inhibitory compounds, contamination of water sources, generation of wastewater due to acidification, and potential risks for the human health.

Pretreatment with bases or alkalis provides the use of sodium hydroxide (NaOH), potassium hydroxide (KOH), calcium hydroxide ($Ca(OH)_2$) solutions [21]. These bases increase the inner surface area of organic substrates or waste polymers by breaking up or swelling the carbon chains and reducing the degrees of polymerization such as crystallinity[42].

The main limitation of alkaline or base pretreatment is the higher cost of monitoring pH during downstream processing and the possible formation of phenolic inhibitors[43].

An alternative way to pretreat the plastic substrates are the physiochemical treatments[34]. The mixture of physical and chemical modifies leads to break the polymers carbon chains with energy saving process (as for example the hydrothermal methods).

4.3.2 Biomass photoreforming

The biomass conversion into high-added value products together with the sustainable H_2 co-production, by using sunlight as energy source and water, is a fascinating and green way to propose new solutions to both environmental and energy problems[44]. The most abundant biomass is wood with an annual production of about 200 billion tons[45]. It is made up of three basic biopolymers: cellulose, hemicellulose and lignin, together with minerals, phenolic substituents and acetyl groups. The combination of these polymers leads to the formation of cross-linked organic structures that provide resistance against corrosion, degradation and UV damage from the environment. Among them, cellulose $(C_6H_{12}0_6)_n$, is the most abundant polymeric fraction, constituting 40%[46], is made up of glucose units that are linked by intermolecular and intramolecular force bond networks. Thanks to them they maintain stability and prohibit the hydrolysis process.

Glycerol is another biomass-derived byproduct produced in large quantities as waste from the biodiesel industry[47,48]. Moreover, compared to other biomass components, glycerol has attracted significant attention due to its efficiency in hydrogen production[4].

While Glucose, the basic unit of cellulose that accounts for about 40–60 wt% of lignocellulosic biomass in nature, has been widely

[4] The photoreforming of glycerol for the H_2 production was investigated in collaborative works of our laboratory: A, Balsamo, R. Fiorenza, **M. T. Armeli Iapichino**, F. J. Lopez-Tenllado, F. J.Urbano, S.Sciré "H_2 production through glycerol photoreforming using one-pot prepared TiO_2-rGO-Au photocatalysts" *Molecular Catalysis,547,113346,2023*

E. La. Greca, **M. T. Armeli Iapichino**, M. C. Herrera Beurnio, F. J. Urbano, L. F. Liotta, S. Scirè, R. Fiorenza
"Influence of Ni addition on Au/CeO_2 photocatalysts for the solar photocatalytic H_2 production by glycerol photoreforming" *Catalysts,15,555,2025*

chosen to evaluate the feasibility of this biomass-derived photoreforming process[49].

Glucose PR generally involves hydrogen evolution reaction (HER) and glucose oxidation reaction (GOR). HER occurs due to the presence of photocatalyst able to reduce aqueous protons (H^+) by photoelectrons of the CB and to generate h^+ from the VB (react. I-II). GOR may involve direct and/or indirect holes transfer pathways, where direct holes oxidation rather than indirect free radical oxidation is the key to glucose PR selectivity. However, to obtain hydrogen, intermediate oxidation steps of the glucose are required, leading to products such as arabinose, erythrosium, glyceraldehyde and glycolic acid together with formic acid in each oxidation step (react. V-IX)[44]. In most cases not only H_2 and CO_2 are formed, but also formaldehyde and formic acid in the liquid phase. Of course, by-products may vary depending on operating conditions such as solvent temperature, pretreatment.

The process is illustrated as follows[50]:

I. $\text{photocatalyst} + h\nu \rightarrow e^-_{(CB)} + h^+_{(VB)}$

II. $h^+_{(VB)} + H_2O \rightarrow \cdot OH + H^+$

III. $e^-_{(CB)} + 2H^+ \rightarrow H_2$

IV. $C_6H_{12}O_6 + H_2O \rightarrow 12H_2 + 6CO_2 + \text{organic compound}$

V. $C_6H_{12}O_6 + H^+ \rightarrow C_5H_{10}O_5 + HCOOH + CO_2$

VI. $C_5H_{10}O_5 + H^+ \rightarrow C_4H_8O_4 + HCOOH + CO_2$

VII. $C_4H_8O_4 + H^+ \rightarrow C_3H_6O_3 + HCOOH + CO_2$

VIII. $C_3H_6O_3 + H^+ \rightarrow C_2H_4O_3 + HCOOH + CO_2$

IX. $C_2H_4O_3 + H^+ \rightarrow CH_2O + HCOOH + CO_2$

In this thesis cellulose and glucose will be discussed as sacrificial agents.

References

[1] L. Wang, J. Yu, Principles of photocatalysis, in: 2023: pp. 1–52. https://doi.org/10.1016/B978-0-443-18786-5.00002-0.

[2] G. Palmisano, E. García-López, G. Marcì, V. Loddo, S. Yurdakal, V. Augugliaro, L. Palmisano, Advances in selective conversions by heterogeneous photocatalysis, Chemical Communications. 46 (2010) 7074. https://doi.org/10.1039/c0cc02087g.

[3] J.-M. Herrmann, Heterogeneous photocatalysis: state of the art and present applications In honor of Pr. R.L. Burwell Jr. (1912–2003), Former Head of Ipatieff Laboratories, Northwestern University, Evanston (Ill)., Topics in Catalysis. 34 (2005) 49–65. https://doi.org/10.1007/s11244-005-3788-2.

[4] J.-M. Herrmann, Heterogeneous photocatalysis: fundamentals and applications to the removal of various types of aqueous pollutants, Catalysis Today. 53 (1999) 115–129. https://doi.org/10.1016/S0920-5861(99)00107-8.

[5] K.C. Christoforidis, P. Fornasiero, Photocatalytic Hydrogen Production: A Rift into the Future Energy Supply, ChemCatChem. 9 (2017) 1523–1544. https://doi.org/10.1002/cctc.201601659.

[6] T. Hisatomi, J. Kubota, K. Domen, Recent advances in semiconductors for photocatalytic and photoelectrochemical water splitting, Chem. Soc. Rev. 43 (2014) 7520–7535. https://doi.org/10.1039/C3CS60378D.

[7] N.S. Lewis, D.G. Nocera, Powering the planet: Chemical challenges in solar energy utilization, Proceedings of the National Academy of Sciences. 103 (2006) 15729–15735. https://doi.org/10.1073/pnas.0603395103.

[8] A. Kudo, Photocatalysis and solar hydrogen production, Pure and Applied Chemistry. 79 (2007) 1917–1927. https://doi.org/10.1351/pac200779111917.

[9] N. Fajrina, M. Tahir, A critical review in strategies to improve photocatalytic water splitting towards hydrogen production, International Journal of Hydrogen Energy. 44 (2019) 540–577. https://doi.org/10.1016/j.ijhydene.2018.10.200.

[10] A. Kudo, Y. Miseki, Heterogeneous photocatalyst materials for water

splitting, Chem. Soc. Rev. 38 (2009) 253–278. https://doi.org/10.1039/B800489G.

[11] L. Schumacher, R. Marschall, Recent Advances in Semiconductor Heterojunctions and Z-Schemes for Photocatalytic Hydrogen Generation, Topics in Current Chemistry. 380 (2022) 53. https://doi.org/10.1007/s41061-022-00406-5.

[12] J. Corredor, M.J. Rivero, C.M. Rangel, I. Ortiz, Comprehensive review and future perspectives on the photocatalytic hydrogen production, (2019). https://doi.org/10.1002/jctb.6123.

[13] T. Jafari, E. Moharreri, A. Amin, R. Miao, W. Song, S. Suib, Photocatalytic Water Splitting—The Untamed Dream: A Review of Recent Advances, Molecules. 21 (2016) 900. https://doi.org/10.3390/molecules21070900.

[14] J. Chen, D. Yang, D. Song, J. Jiang, A. Ma, M.Z. Hu, C. Ni, Recent progress in enhancing solar-to-hydrogen efficiency, Journal of Power Sources. 280 (2015) 649–666. https://doi.org/10.1016/j.jpowsour.2015.01.073.

[15] Q. Zhang, Y. Shan, J. Pan, P. Kumar, M.J. Keevers, J. Lasich, G. Kour, R. Daiyan, I. Perez-Wurf, L. Thomsen, S. Cheong, J. Jiang, K.-H. Wu, C.-L. Chiang, K. Grayson, M.A. Green, R. Amal, X. Lu, A photovoltaic-electrolysis system with high solar-to-hydrogen efficiency under practical current densities, Science Advances. 11 (2025). https://doi.org/10.1126/sciadv.ads0836.

[16] Y. Li, Z. Ma, S. Hou, X. Li, S. Wang, Z. Du, Y. Chen, Q. Zhang, Y. Li, Q. Yang, Z. Huang, L. Bai, H. Yu, Q. Liu, Y. Xiang, M. Zhang, J. Yu, J. Xie, Y. Zhou, C. Tang, K. Sun, L. Ding, Transition metals-based electrocatalysts on super-flat substrate for perovskite photovoltaic hydrogen production with 13.75% solar to hydrogen efficiency, Journal of Colloid and Interface Science. 677 (2025) 599–609. https://doi.org/10.1016/j.jcis.2024.08.005.

[17] G.G. Bessegato, T.T. Guaraldo, J.F. de Brito, M.F. Brugnera, M.V.B. Zanoni, Achievements and Trends in Photoelectrocatalysis: from Environmental to Energy Applications, Electrocatalysis. 6 (2015) 415–441. https://doi.org/10.1007/s12678-015-0259-9.

[18] R. Liu, H. Yin, P. Guo, X. Liu, Z. Yin, Photoreforming Light Alcohols for Value-Added Resources: A Mini Review, Energy Technology. (2024). https://doi.org/10.1002/ente.202301708.

[19] M. Ding, M. Jia, J. Wang, Insights into performance and mechanism of improving methanol photoreforming on the ternary catalysts with p-n junction, International Journal of Hydrogen Energy. 98 (2025) 67–77. https://doi.org/10.1016/j.ijhydene.2024.12.054.

[20] M.C. Herrera-Beurnio, F.J. López-Tenllado, J. Hidalgo-Carrillo, J. Martín-Gómez, R. Estévez, F.J. Urbano, A. Marinas, Glycerol photoreforming for photocatalytic hydrogen production on binary and ternary Pt-g-C3N4-TiO2 systems: A comparative study, Catalysis Today. 430 (2024) 114548. https://doi.org/10.1016/j.cattod.2024.114548.

[21] C.Y. Toe, C. Tsounis, J. Zhang, H. Masood, D. Gunawan, J. Scott, R. Amal, Advancing photoreforming of organics: highlights on photocatalyst and system designs for selective oxidation reactions, Energy & Environmental Science. 14 (2021) 1140–1175. https://doi.org/10.1039/D0EE03116J.

[22] M.F. Kuehnel, E. Reisner, Solar Hydrogen Generation from Lignocellulose, Angewandte Chemie International Edition. 57 (2018) 3290–3296. https://doi.org/10.1002/anie.201710133.

[23] J. Zou, G. Zhang, X. Xu, One-pot photoreforming of cellulosic biomass waste to hydrogen by merging photocatalysis with acid hydrolysis, Applied Catalysis A: General. 563 (2018) 73–79. https://doi.org/10.1016/j.apcata.2018.06.030.

[24] N. Mohanan, Z. Montazer, P.K. Sharma, D.B. Levin, Microbial and Enzymatic Degradation of Synthetic Plastics, Frontiers in Microbiology. 11 (2020). https://doi.org/10.3389/fmicb.2020.580709.

[25] X. Tang, X. Han, N.H.M. Sulaiman, L. He, X. Zhou, Recent Advances in the Photoreforming of Plastic Waste: Principles, Challenges, and Perspectives, Industrial and Engineering Chemistry Research. 62 (2023) 9032–9045. https://doi.org/10.1021/acs.iecr.3c00809.

[26] J. Chen, J. Wu, P.C. Sherrell, J. Chen, H. Wang, W. Zhang, J. Yang, How to Build a Microplastics-Free Environment: Strategies for

Microplastics Degradation and Plastics Recycling, Advanced Science. 9 (2022). https://doi.org/10.1002/advs.202103764.

[27] T.K. Anh Nguyen, T. Trần-Phú, R. Daiyan, X. Minh Chau Ta, R. Amal, A. Tricoli, From Plastic Waste to Green Hydrogen and Valuable Chemicals Using Sunlight and Water, Angewandte Chemie International Edition. 63 (2024). https://doi.org/10.1002/anie.202401746.

[28] Y. Chen, S. Xu, C. Fang Wen, H. Zhang, T. Zhang, F. Lv, Y. Yue, Z. Bian, Unravelling the Role of Free Radicals in Photocatalysis, Chemistry – A European Journal. 30 (2024). https://doi.org/10.1002/chem.202400001.

[29] S. Chu, B. Zhang, X. Zhao, H. Sen Soo, F. Wang, R. Xiao, H. Zhang, Photocatalytic Conversion of Plastic Waste: From Photodegradation to Photosynthesis, Advanced Energy Materials. 12 (2022). https://doi.org/10.1002/aenm.202200435.

[30] L. Wang, S. Jiang, W. Gui, H. Li, J. Wu, H. Wang, J. Yang, Photocatalytic Upcycling of Plastic Waste: Mechanism, Integrating Modus, and Selectivity, Small Structures. 4 (2023). https://doi.org/10.1002/sstr.202300142.

[31] S. Kang, T. Sun, Y. Ma, M. Du, M. Gong, C. Zhou, Y. Chai, B. Qiu, Artificial photosynthesis bringing new vigor into plastic wastes, SmartMat. 4 (2023). https://doi.org/10.1002/smm2.1202.

[32] H.T.N. Hai, T.T. Nguyen, M. Nishibori, T. Ishihara, K. Edalati, Photoreforming of plastic waste into valuable products and hydrogen using a high-entropy oxynitride with distorted atomic-scale structure, Applied Catalysis B: Environment and Energy. 365 (2025) 124968. https://doi.org/10.1016/j.apcatb.2024.124968.

[33] T.T. Nguyen, K. Edalati, Brookite TiO_2 as an active photocatalyst for photoconversion of plastic wastes to acetic acid and simultaneous hydrogen production: Comparison with anatase and rutile, Chemosphere. 355 (2024) 141785. https://doi.org/10.1016/j.chemosphere.2024.141785.

[34] M. Ashraf, N. Ullah, I. Khan, W. Tremel, S. Ahmad, M.N. Tahir, Photoreforming of Waste Polymers for Sustainable Hydrogen Fuel and Chemicals Feedstock: Waste to Energy, Chemical Reviews. 123 (2023)

4443–4509. https://doi.org/10.1021/acs.chemrev.2c00602.

[35] A. Agosti, Y. Nakibli, L. Amirav, G. Bergamini, Photosynthetic H2 generation and organic transformations with CdSe@CdS-Pt nanorods for highly efficient solar-to-chemical energy conversion, Nano Energy. 70 (2020) 104510. https://doi.org/10.1016/j.nanoen.2020.104510.

[36] K. Shimura, H. Yoshida, Heterogeneous photocatalytic hydrogen production from water and biomass derivatives, Energy & Environmental Science. 4 (2011) 2467. https://doi.org/10.1039/c1ee01120k.

[37] Z. Ya, S. Zhang, D. Xu, H. Wang, M. Li, Coupling Plastic Upgrading and Photocatalysis: Catalytic Mechanisms and Design Principles, ACS Catalysis. (2025) 5339–5369. https://doi.org/10.1021/acscatal.5c00139.

[38] M. Bowker, W. Jones, Methanol photo-reforming with water on pure titania for hydrogen production, Philosophical Transactions of the Royal Society A: Mathematical, Physical and Engineering Sciences. 378 (2020) 20200058. https://doi.org/10.1098/rsta.2020.0058.

[39] X. Wu, N. Luo, S. Xie, H. Zhang, Q. Zhang, F. Wang, Y. Wang, Photocatalytic transformations of lignocellulosic biomass into chemicals, Chemical Society Reviews. 49 (2020) 6198–6223. https://doi.org/10.1039/D0CS00314J.

[40] Y.H. Jung, K.H. Kim, Acidic Pretreatment, in: Pretreatment of Biomass, Elsevier, 2015: pp. 27–50. https://doi.org/10.1016/B978-0-12-800080-9.00003-7.

[41] S. Cao, Y. Pu, M. Studer, C. Wyman, A.J. Ragauskas, Chemical transformations of Populus trichocarpa during dilute acid pretreatment, RSC Advances. 2 (2012) 10925. https://doi.org/10.1039/c2ra22045h.

[42] D. Carta, G. Cao, C. D'Angeli, Chemical Recycling of Poly(ethylene terephthalate) (PET) by Hydrolysis and Glycolysis, Environmental Science and Pollution Research. 10 (2003) 390–394. https://doi.org/10.1065/espr2001.12.104.8.

[43] W. Den, V.K. Sharma, M. Lee, G. Nadadur, R.S. Varma, Lignocellulosic Biomass Transformations via Greener Oxidative Pretreatment Processes: Access to Energy and Value-Added Chemicals, Frontiers in Chemistry. 6 (2018). https://doi.org/10.3389/fchem.2018.00141.

[44] B. Jin, G. Yao, X. Wang, K. Ding, F. Jin, Photocatalytic Oxidation of

Glucose into Formate on Nano TiO_2 Catalyst, ACS Sustainable Chemistry & Engineering. 5 (2017) 6377–6381. https://doi.org/10.1021/acssuschemeng.7b00364.

[45] Y.P. Zhang, S. Ding, J.R. Mielenz, J. Cui, R.T. Elander, M. Laser, M.E. Himmel, J.R. McMillan, L.R. Lynd, Fractionating recalcitrant lignocellulose at modest reaction conditions, Biotechnology and Bioengineering. 97 (2007) 214–223. https://doi.org/10.1002/bit.21386.

[46] X. Xu, L. Shi, S. Zhang, Z. Ao, J. Zhang, S. Wang, H. Sun, Photocatalytic reforming of lignocellulose: A review, Chemical Engineering Journal. 469 (2023) 143972. https://doi.org/10.1016/j.cej.2023.143972.

[47] C.M. Pecoraro, M. Bellardita, V. Loddo, F. Di Franco, L. Palmisano, M. Santamaria, A facile way to synthesize noble metal free TiO2 based catalysts for glycerol photoreforming, Journal of Industrial and Engineering Chemistry. 118 (2023) 247–258. https://doi.org/10.1016/j.jiec.2022.11.010.

[48] S. Çetinkaya, G. Khamidov, L. Özcan, L. Palmisano, S. Yurdakal, Selective Photocatalytic Oxidation of Glycerol and 3-Pyridinemethanol by Nanotube/Nanowire-Structured TiO_2 Powders Obtained by Breakdown Anodization, Frontiers in Chemistry. 10 (2022). https://doi.org/10.3389/fchem.2022.856947.

[49] S.P. Shelake, D.N. Sutar, B.M. Abraham, T. Banerjee, A.V.S. Sainath, U. Pal, Emerging Photoreforming Process to Hydrogen Production: A Future Energy, Advanced Functional Materials. (2024). https://doi.org/10.1002/adfm.202403795.

[50] L. Lan, H. Daly, R. Sung, F. Tuna, N. Skillen, P.K.J. Robertson, C. Hardacre, X. Fan, Lan Lan, * Helen Daly, * Rehana Sung, Floriana Tuna, Nathan Skillen, Peter K. J. Robertson, Christopher Hardacre, * and Xiaolei Fan, (2023). https://doi.org/10.1021/acscatal.3c00858.

CHAPTER V: Critical raw materials and unconventional photocatalysts

CHAPTER V: Critical raw materials and unconventional photocatalysts

Some of the most urgent problems of the 20th century are the sustainable use of the earth's resources and the impact of the consumption of these resources on our atmosphere. The development of functional materials is essential today to address the challenges and the needs of today society. In order to fulfil specific functions, many of these materials require a variety of specific metallic elements, whose total reserves in the planet primary deposits are limited in quantity and unevenly distributed, requiring considerable efforts for both exploration and exploitation of those areas where are present geopolitical and social restrictions. The growing need of advanced materials and components that enable certain functions for a variety of strategic applications, and a crescent world population can clash with the limited earth resources, raising the question of the future supply of some critical materials. Indeed the increasing consumption and the changes in the global economic, financial and political environment have led to disproportions between the supply and the demand of certain raw materials, resulting in price volatility in materials markets and creating uncertainties for the related technologies [1].

The first list of the European Union (EU) critical raw materials was published in 2011, and it was updated regularly. New initiatives have emerged at EU level, such as the EIT(European Institute of Innovation and Technology) Raw Materials Knowledge and Innovation Community and the European Raw Materials Alliance,

and several national agencies dealing with raw material risks have been founded[2].

On 16 March 2023, the European Commission proposed the Critical Raw Materials Act (CRMA), as part of its broader “Green Industrial Plan” and in combination with a “Zero Emission Industry Act” (NZIA), with the intention of reducing the EU's dependence on critical raw materials (CRM) and promoting a sustainable use and development of the EU CRM value chains[3].

The CRMA establishes some important points

- the strategic areas of decarbonisation,
- the strategic areas of digitisation,
- the strategic areas of the defence of the critical raw materials considering the European economy as a whole[3].

These points are important to start to solve related problems such as the insufficient anticipation and mitigation of the supply risks, underutilisation of the national CRM potential and unsustainable supply of CRM.

The CRMA consists of several documents with a several regulations showed in the Fig.1.

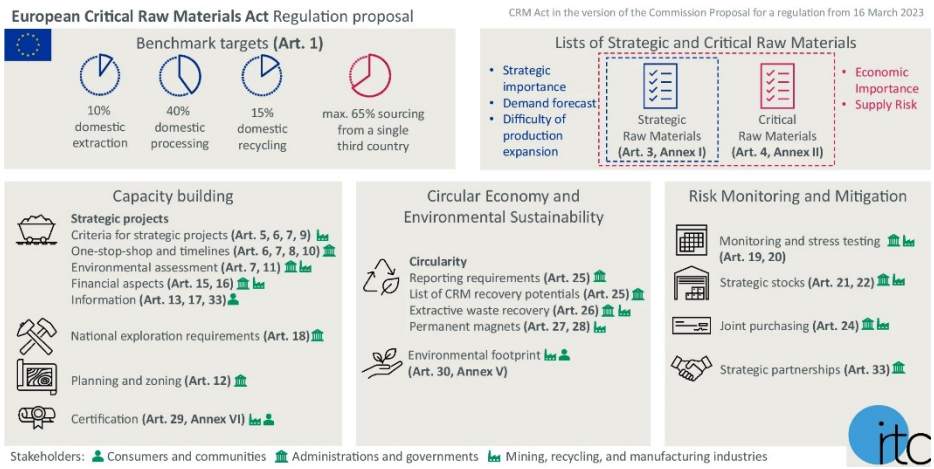

Figure 1 *A thematic overview of the CRMA regulation proposal (March 16, 2023)* [2].

The main indicators on which the EU critical materials list is based can be summarised as follows:

1. Supply risk,
2. Economic importance,
3. Import dependence,
4. End-of-life/recycling input rate.

According to the EU Regulation ((EU) 2024/1252 Art.2), the raw materials include those in unprocessed form and the by-product of other extractions, and of recycling processes. Moreover, they are listed in Annex I, Section 1, the materials that are considered strategic [4]. The regulation aims to: increase and diversify the EU supply of critical raw materials and strengthen circularity. Moreover, it promotes the research of new and efficient methods for the recycling of the CRM and the development of substitutes or of innovative strategies to increase the efficiency of the use of the resources.

The current list (Fig. 2) identifies 34 critical raw materials, 17 of which (highlighted in yellow) are classified as strategic. These

strategic raw materials are expected to exponential increase in demand, being used in complex production processes. Therefore, they are more vulnerable to the supply disruption.

Figure 2 *List of the EU critical raw materials list updated in 2024. In yellow are represented the strategic materials* [5].

Currently, there are many projects focused on the development of technical information and surveys about the deposits, the supply and the demand of the CRM [6]. For example:

- EURARE (Development of a sustainable exploitation scheme for Europe's Rare Earth ore deposits), aiming to set the basis for the development of a European rare earth elements (REE) industry that will safeguard the uninterrupted supply of REE raw materials and products crucial for the EU economy industrial sectors[7].

- FRAME (Forecasting And Assessing Europe's Strategic Raw Materials Needs) and MINDeSEA (Seabed Mineral Deposits in European Seas: Metallogeny and Geological Potential for Strategic and Critical Raw Materials) these two scientific projects are developed in the framework of the GeoERA (Establishing the European Geological Surveys Research Area to deliver a Geological Service for Europe), aiming to expand the strategic and CRM knowledge through a compilation of mineral potential and metallogenic areas of critical raw materials resources in Europe.
- MSP-REFRAM (Multi-Stakeholder Platform for a Secure Supply of Refractory Metals in Europe), the project goal is to create a platform composed of multiple stakeholders for a secure supply of refractory metals in Europe[8].

5.1 Unconventional photocatalysts

In the EU list of critical materials, several of them are used for the synthesis of photocatalysts.

In particular, the titanium metal, are widely extracted from the TiO_2[9].

This material has attracted considerable attention for various applications such as photocatalysis, dye-sensitized solar cells, sensor devices and H_2 production[10–13].

There are four common crystalline phases of TiO_2 (Fig.3): anatase, rutile, brookite, and TiO_2(B)[14].

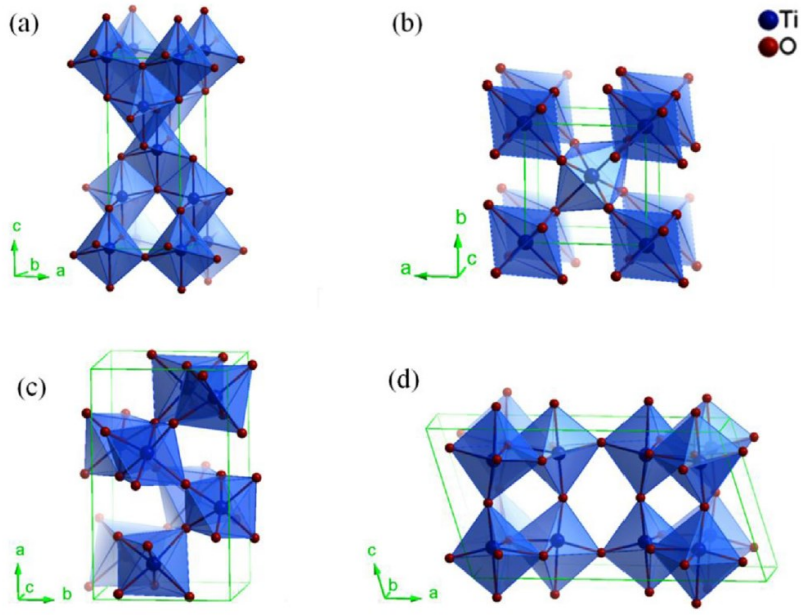

Figure 3 *Crystalline structures of TiO_2 in different phases: (a) anatase, (b) rutile, (c) brookite, and (d) TiO_2(B).*

TiO_2 has been the most widely used semiconductor to perform water splitting(WS) and photoreforming processes(PR), due to its numerous advantages[15]. The enduring interest in TiO_2-based systems stems from their unique combination of chemical stability, cost-effectiveness, low toxicity, and favourable band edge

positions for this reactions[16,17]. Additionally, noble-metal-decorated TiO_2 nanomaterials with an optimized morphology have exhibited a remarkable stability over extended periods while maintaining outstanding hydrogen production rates[18,19].

For this reason, it is necessary to promote the development of new alternatives using not-critical materials or limiting the use of the noble metals co-catalysts in the water splitting/photoreforming reactions[20].

Therefore, the focus of this study is on the performance of not widely used photocatalysts and their composites as the Silicon Carbide (SiC) and the graphitic carbon nitride (g-C_3N_4).

5.2 Silicon Carbide (SiC)

Silicon carbide (SiC), also known as carborundum, consists of a tetrahedral array of covalently bonded silicon and carbon atoms arranged in a three-dimensional crystalline structure[21].

The methods of its synthesis was introduced in 1885 by Cowless[22] and in 1892 by Acheson [23]. Acheson used a reaction between pure SiO_2 and carbon at 1800-2600 °C.

Silicon carbide has different polytypes (two structures that are identical in two dimensions and different in a third). The formation of polytypes depends on temperature, pressure, environment and presence of impurities[24,25]. Also the polytypes differ from one another by the stacking sequence of a double layer formed by two planes of closed-packed Si and C atoms, one Si atom lying directly over one C atom[26]. These double layers are stacked one over the other in a close-packed arrangement. It is possible to obtain 170 polytypes[27], that correspond to cubic, hexagonal or rhombohedral lattice structures, respectively.

Two major polytypes of SiC are α-SiC (non-porous) and β-SiC (porous); they are also the most thermodynamically stable[28]. The characteristics of these polytypes are:

- α-SiC is stable at temperatures higher than 1700°C [29]. It has two hexagonal structures that can be obtained in a simple way called 6H–SiC(1900–2200°C) and 4H–SiC (1500–1800°C) [26].
- β-SiC has a crystal structure similar to the diamond, is formed at temperatures below 1700°C, and has a surface area typically greater than α-SiC[29,30]. It has a cubic structure coded as 3C–SiC.[26].

There are many ways to categorize SiC materials. In the field of catalysis, it is possible to distinguish between porous and non-porous SiC (Fig.4). Non-porous SiC is mainly used as a diluent for highly exo- and endothermic catalytic reactions, and is generally prepared at 1700–2400°C through a solid-state reaction between silicon and carbon. Porous SiC can have ordered or random porosity. Ordered porosity leads to mesoporous or hierarchical structures. Different methods are employed to synthesize these types of SiC materials.

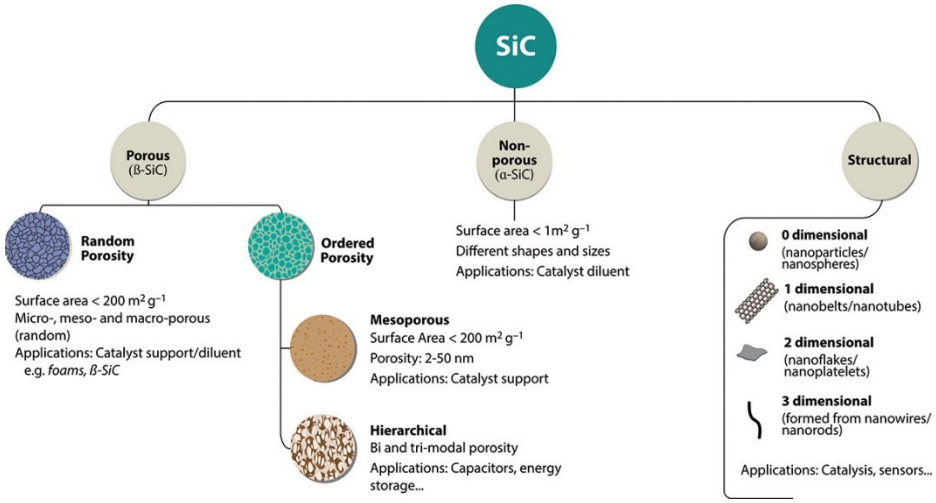

Figure 4 *Classification of different types of SiC based on porosity and structures* [29].

The most interesting properties of SiC are:

a. high thermal conductivity of around 146–270 W m^{-1} K^{-1} (α-SiC) [31]
b. tunable surface properties, [32]
c. mechanical strength [33]
d. surface inertness.

All these features are due to its covalent nature and the electro-neutrality between the silicon and carbon atoms[34]. These

features enable SiC to be used in a wide variety of industrial applications. Within catalysis, SiC is mainly used for its high thermal conductivity to avoid adverse thermal gradients in packed bed catalytic reactors[29]. Its high resistance is also useful in oxidative media[35] and, when used as a support, its high mechanical strength imparts more structural robustness to catalysts against attrition in severe process environments than conventional alternatives.

In addition, due to its tuneable bandgap (2.39–3.33 eV) and high charge-carrier mobility (Fig.5), the SiC is a typical non-metallic semiconductor and various SiC nanostructures were widely explored in different photocatalytic applications under visible-ultraviolet light radiation[35–37].

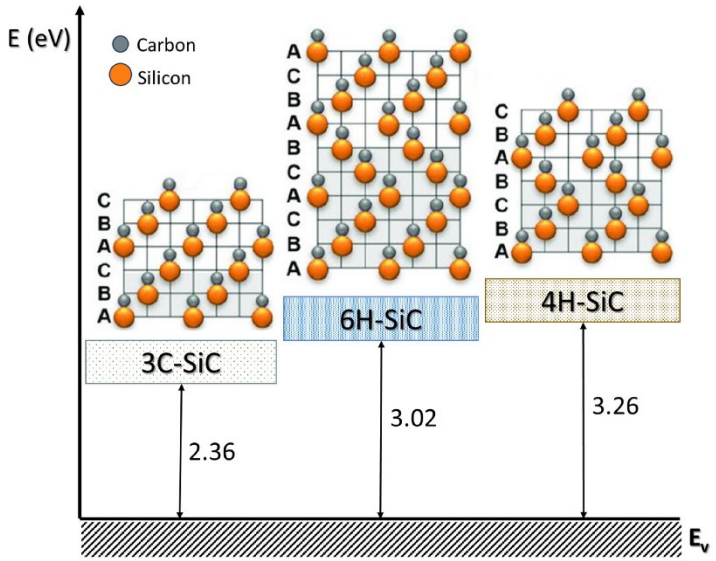

Figure 5 *The crystal structures and the bandgap of 3C-SiC, 6H-SiC, and 4H-SiC*[35].

β-SiC(3C-SiC) has also other uses in the field of solar cells[38], quantum applications[39], biomedical devices and bio-electronics[40].

5.3 Graphitic carbon nitride (g-C_3N_4)

The graphitic carbon nitride (g-C_3N_4) has been largely exploited in various scientific fields including photocatalysis[41]. In fact, its first use in heterogeneous photocatalysis was investigated by Wang[42] in 2009, who produced H_2 by water splitting reaction (Fig.6).

Its structure contains carbon and nitrogen atoms arranged in a two-dimensional conjugated framework. This imparts not only an exceptional chemical stability but also affords a favourable electronic band structure, making it well-suited for photochemical applications[43–45] (Fig.6).

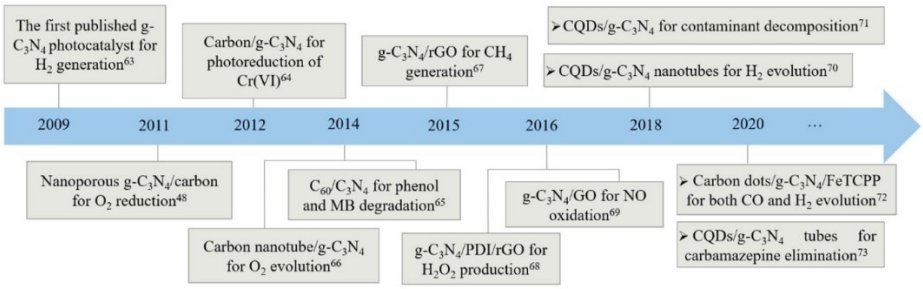

Figure 6 *Schematic illustration for various photocatalytic applications of carbon/g-C_3N_4 photocatalysts* [46].

It was firstly synthetized by Berzelius and named ‘melon’ by Liebig in 1834, and it has been considered one of the first synthetic polymer[47].

Five different phases of CNs were predicted, including α-C_3N_4, β-C_3N_4, cubic C_3N_4, pseudo cubic C_3N_4 and graphitic C_3N_4 (g-C_3N_4)[48]. It consists of stacked layers of carbon and nitrogen atoms arranged in a planar, hexagonal lattice; it is an n-type semiconductor and a π-conjugated system with a sp^2 hybridization. It has been pointed out that the two basic structural

units for the construction of g-C_3N_4 isomers are the triazine (C_3N_3) and tri-s-triazine/heptazine (C_6N_7) rings, respectively (Fig.7).

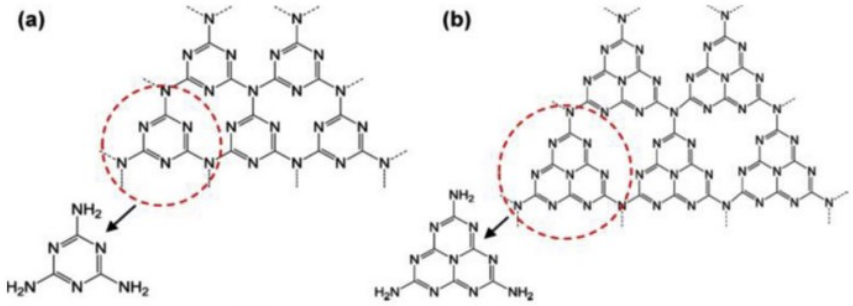

Figure 7 *(a) Triazine, (b) tri-s-triazine (heptazine) structures of g-C_3N_4* [49].

The CNx structures investigated in the evolution of H_2 are the amorphous (ACN) and the crystalline (GCN) phases (Fig.8). In fact, it has been observed that ACN can be used as an effective visible light photocatalyst with an irradiation wavelength beyond 600 nm, owing a bandgap of 1.90 eV[49]. While the band gap of crystalline g-C_3N_4 is about 2.7-2.8 eV, which endows g-C_3N_4 with certain visible light absorption ability and it can suitable for the photocatalytic reactions driven by visible light[50].

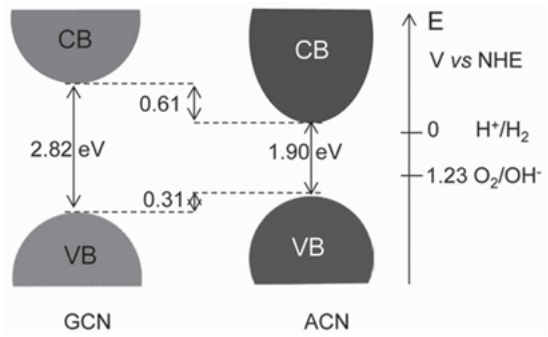

Figure 8 *Band alignments of the two carbon nitride structures referring to the redox potential of water reduction and oxidation for hydrogen and oxygen generation, respectively* [49].

The band gap of GCN (about 2.7–2.9 eV, depending on the synthesis) and the energy levels of its valence and conduction

bands are sufficiently large to overcome the endothermic requirement of the water-splitting reaction[50]. Moreover, carbon nitride possesses the advantages of low cost, non-toxic, thermodynamic stability, and outstanding optical properties[51–53]. Conventional carbon nitride shows the typical absorption pattern of an organic semiconductor with a very strong, stepwise gap adsorption at about 420 nm (Fig.9). This is consistent with its yellow colour[54].

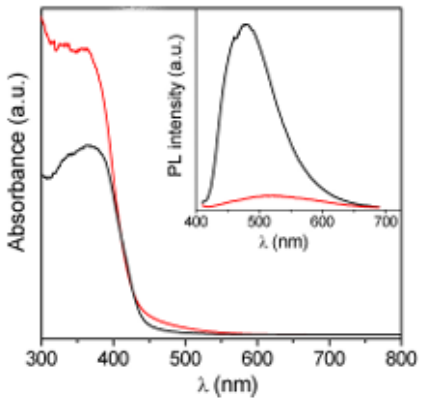

Figure 9 *Diffuse reflectance absorption spectrum and photoluminescence (PL) spectrum (inset) under 420 nm excitation for bulk g-C_3N_4 (black) and mesoporous g-C_3N_4 (red)* [54].

This photocatalyst can be obtained by different synthesis methods such as:

- Thermal polymerization[55]
- Chemical vapor deposition (CVD)[56]
- Solvothermal and hydrothermal processes [57]
- Template-assisted synthesis[58]

On the basis of the peculiar preparation methods, it is possible to change the structural and optical properties of the carbon nitride. The g-C_3N_4 can be simply prepared by the thermal condensation of several low-cost carbon-nitrogen-rich precursors (Fig.10) such

as cyanamide[59] ,dicyandiamide[60], melamine[61], thiourea[62], urea[63], or a mixture of them. In this work, it was used dicyandiamide, melamine and urea.

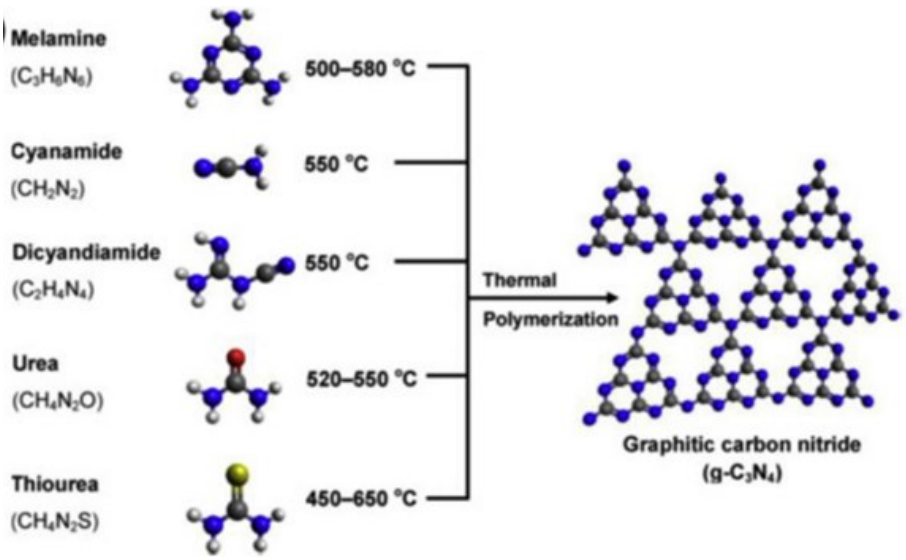

Figure 10 *Thermal polymerization of the different precursors for the g-C_3N_4 preparation.*

5.3.1 Loading of metals on the surface of g-C_3N_4

Graphitic (crystalline) carbon nitride is the most stable allotrope of carbon nitride under ambient conditions[64]. The morphology of g-C_3N_4 can be easily modified to develop high surface area-based samples. Moreover, to increase the photocatalytic performance of g-C_3N_4 in the hydrogen production, the noble-metal deposition is a widely used strategy[65]. The most widely accepted theory attributes the beneficial effects of the presence of a metal on the surface of g-C_3N_4 or in a generic semiconductor is its ability to transfer the photogenerated electrons from the conduction band (CB) of the photocatalyst directly to the metal Fermi level. This process helps to prevent the charge carrier recombination and creates accumulation sites for multi-electrons transfers from the catalyst surface to the reaction substrate. The formation of a Schottky barrier permits the electrons transfer from the CB to the metal and not vice versa as shown in (Fig.11).

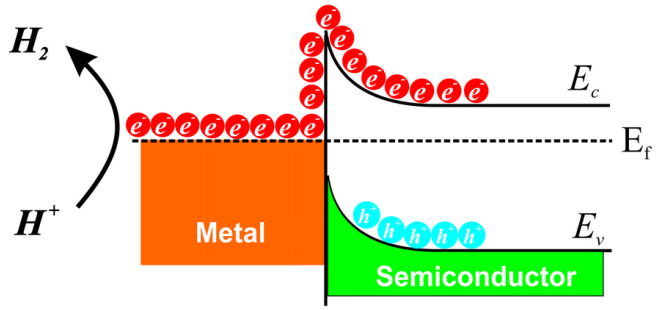

Figure 11 *Scheme of the energy band model of a Schottky junction* [66].

The metal chosen to act as co-catalyst due to its chemical-physical properties such as particle size and valence states influences the overall performance of the photocatalyst [67]. However, a larger amount of co-catalyst provides more active sites for reactions but reduces the absorption capacity of the photocatalyst. Therefore,

the concentration of the cocatalyst must be optimised to achieve maximum activity during water splitting/photoreforming under light illumination.

The most studied and used co-catalysts are platinum, gold or palladium. Among them, Pt seems the most promising due to its easy deposition and dispersion compared to the others one[68]. There are two main techniques to deposit cocatalysts on the surface of photocatalysts: *in situ* photo-deposition and impregnation. Using the impregnation for the Pt/g-C_3N_4 catalyst results in better particle distribution and avoids the formation of agglomerates that lead to a performance decrease in the photoreforming reactions [69]. Also it is considered to be the cheapest and the simplest preparation method, for the deposition of noble metals [70]. Specifically, the impregnation technique consists of bringing the photocatalyst into contact with the metal precursor solution.

The impregnation process can be summarised as follows[71] (Fig.12):

a) Capillarity: the metal solution enters the pores of the catalyst.
b) It then diffuses and adsorption takes place. In the ideal case, the concentration of the solute is the same at all points of the porous solid (incipient wetness impregnation).
c) Drying causes crystallisation of the metal precursor within the pores of the catalyst by supersaturation of the solution.

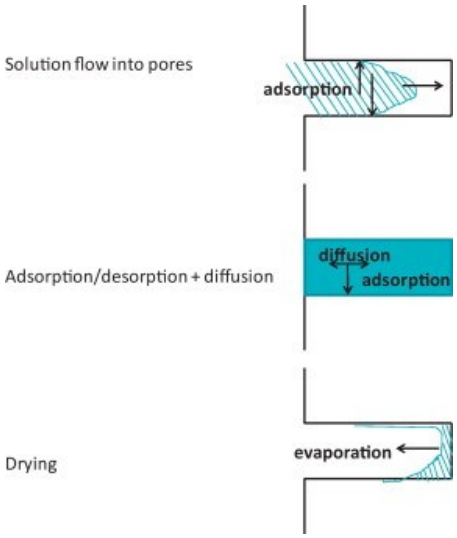

Figure 12 *A schematic picture of the impregnation procedure, showing different steps*[71].

5.4 Titanium carbon nitride (TiCN)

TiCN (titanium carbonitride) belongs to the class of ternary transition metal carbonitrides[72]. They are known for their mechanical applications. In fact, they are widely used in hard coating and cutting tools[73,74], and also appear as enhanced phase in high strength steel[75]. They have hardness, mechanical strength, toughness and wear resistance[76]. Several studies have shown that among these transition metals carbonitrides, the one with the best characteristics in terms of conductivity and porosity is the TiCN[77].

Initially, there were several debates regarding the structure of this material[78], but it was confirmed that it has a centred cubic face (FCC) (Fig.13) [79], with the crystalline planes represented in the Fig.14. The structural similarity of carbides and nitrides makes possible a partial replace of the carbon atoms with nitrogen atoms. In this way a solution of both carbon and nitrogen in the metal is formed and the resulting compounds are named carbonitrides[80]. Depending on the atomic ratio of carbon and nitrogen, carbonitrides of different stoichiometry are produced[80].

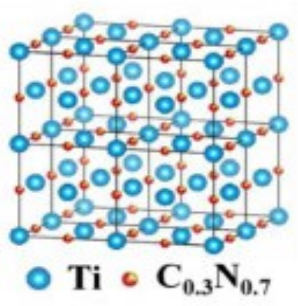

Figure 13 *Structure of TiC0.3N0.7 as TiCN class model sample*[79].

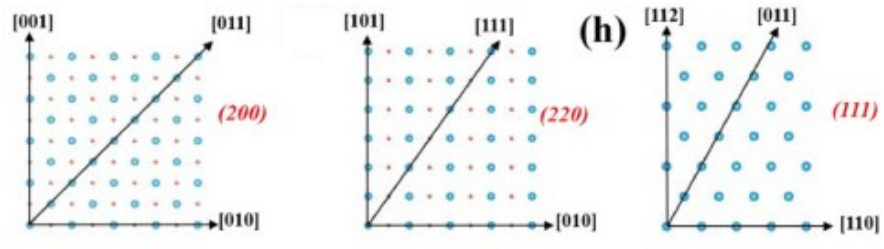

Figure 14 *Crystalline planes of TiCN.*

However, in recent years the TCN has also emerged as a promising material for photocatalytic applications, especially in the field of pollutant degradation and hydrogen production[81]. In fact, the 2D lamellar structure of TCN, obtained after exfoliation, finds application as building-block of the Mxenes [82–84], new 2D materials investigated in photocatalysis, whereas the TiCN bulk structure can be used as co-catalyst.

Transition-metal carbides and nitrides have recently emerged as promising candidates for non-noble metal electrocatalysts due to their excellent electronic properties, structure, and high corrosion resistance[85]. The bonding of transition metals with carbon or nitrogen atoms affects the electronic structure of the d-orbitals of metals by modifying the position of the d-band centre. The position of the d-band relative to the Fermi level determines the strength of the hydrogen binding to the electrocatalyst and controls the adsorption of hydrogen ions and desorption of hydrogen gas molecules[86]. These unique properties of transition-metal carbides and nitrides are helpful in improving the kinetics and thermodynamic parameters.

References

[1] M. Hofmann, H. Hofmann, C. Hagelüken, A. Hool, Critical raw materials: A perspective from the materials science community, Sustainable Materials and Technologies. 17 (2018) e00074. https://doi.org/10.1016/j.susmat.2018.e00074.

[2] A. Hool, C. Helbig, G. Wierink, Challenges and opportunities of the European Critical Raw Materials Act, Mineral Economics. 37 (2024) 661–668. https://doi.org/10.1007/s13563-023-00394-y.

[3] S. Carrara, S. Bobba, D. Blagoeva, A. Dias, P. Cavalli, A. Georgitzikis, K. Grohol, A. Kuzov, T. Latunussa, C. Lyons, G. Maury, T. Somers, Supply chain analysis and material demand forecast in strategic technologies and sectors in the EU - A foresight study, JRC Science for Policy Report, 2023. https://doi.org/10.2760/334074.

[4] Regulation (EU) 2024/1252 of the European Parliament and of the Council of 11 April 2024 establishing a framework for ensuring a secure and sustainable supply of critical raw materials and amending Regulations (EU) No 168/2013, (EU) 2018/858, (EU) 2018/17, (n.d.). http://data.europa.eu/eli/reg/2024/1252/oj.

[5] An EU critical raw materials act for the future of EU supply chains, (n.d.). https://www.consilium.europa.eu/en/infographics/critical-raw-materials/.

[6] M. Girtan, A. Wittenberg, M.L. Grilli, D.P.S. de Oliveira, C. Giosuè, M.L. Ruello, The Critical Raw Materials Issue between Scarcity, Supply Risk, and Unique Properties, Materials. 14 (2021) 1826. https://doi.org/10.3390/ma14081826.

[7] Welcome Eurare. https://eurare.org/.

[8] RESOURCES. https://prometia.eu/resources/.

[9] A.H.J. Sampath, N.D. Wickramasinghe, K.M.N. de Silva, R.M. de Silva, Methods of Extracting TiO_2 and Other Related Compounds from Ilmenite, Minerals. 13 (2023) 662. https://doi.org/10.3390/min13050662.

[10] M. Zhang, X. Liang, Y. Gao, Y. Liu, C60- and CdS-Co-Modified Nano-Titanium Dioxide for Highly Efficient Photocatalysis and Hydrogen Production, Materials. 17 (2024) 1206. https://doi.org/10.3390/ma17051206.

[11] R. Morita, Y. Murakami, X.-F. Shen, D. Yang, M. Watanabe, J.T. Song,

A. Takagaki, T. Ishihara, Enhanced charge mediator properties of photocatalysts with reduced graphene nanoribbons for photocatalytic acceleration of hydrogen production in aqueous media, Journal of Materials Chemistry C. 12 (2024) 1652–1660. https://doi.org/10.1039/D3TC03622G.

[12] P. Jiménez-Calvo, Synergy of visible-light responsive photocatalytic materials and device engineering for energy and environment: Minireview on hydrogen production and water decontamination, Materials Today Catalysis. 4 (2024) 100040. https://doi.org/10.1016/j.mtcata.2024.100040.

[13] S. Shanmugaratnam, P. Ravirajan, Y. Shivatharsiny, D. Velauthapillai, Green hydrogen production through photocatalytic seawater splitting on MS_2/TiO_2 (M=Ni/Co/Sn) nanocomposites over simulated solar irradiation, International Journal of Hydrogen Energy. 91 (2024) 673–682. https://doi.org/10.1016/j.ijhydene.2024.10.091.

[14] Y. Ma, X. Wang, Y. Jia, X. Chen, H. Han, C. Li, Titanium Dioxide-Based Nanomaterials for Photocatalytic Fuel Generations, Chemical Reviews. 114 (2014) 9987–10043. https://doi.org/10.1021/cr500008u.

[15] O.F. Aldosari, Photocatalytic water-splitting for hydrogen production using TiO_2 -based catalysts: Advances, current challenges, and future perspectives, Catalysis Reviews. (2025) 1–38. https://doi.org/10.1080/01614940.2024.2446476.

[16] R. Ghamarpoor, A. Fallah, M. Jamshidi, A Review of Synthesis Methods, Modifications, and Mechanisms of ZnO/TiO_2-Based Photocatalysts for Photodegradation of Contaminants, ACS Omega. 9 (2024) 25457–25492. https://doi.org/10.1021/acsomega.3c08717.

[17] T. Ahasan, E.M.N.T. Edirisooriya, P.S. Senanayake, P. Xu, H. Wang, Advanced TiO_2-Based Photocatalytic Systems for Water Splitting: Comprehensive Review from Fundamentals to Manufacturing, Molecules. 30 (2025) 1127. https://doi.org/10.3390/molecules30051127.

[18] N.R. Reddy, U. Bharagav, M.V. Shankar, P.M. Reddy, K.R. Reddy, N.P. Shetti, F. Alonso-Marroquin, M.M. Kumari, T.M. Aminabhavi, S.W. Joo, Photocatalytic hydrogen production by ternary heterojunction

composites of silver nanoparticles doped FCNT-TiO_2, Journal of Environmental Management. 286 (2021) 112130. https://doi.org/10.1016/j.jenvman.2021.112130.

[19] S.L. Hamukwaya, Z. Zhao, H. Hao, H.M. Abo-Dief, K.M. Abualnaja, A.K. Alanazi, M.M. Mashingaidze, S.M. El-Bahy, M. Huang, Z. Guo, Enhanced photocatalytic performance for hydrogen production and carbon dioxide reduction by a mesoporous single-crystal-like TiO2 composite catalyst, Advanced Composites and Hybrid Materials. 5 (2022) 2620–2630. https://doi.org/10.1007/s42114-022-00545-9.

[20] M. Chaghouri, A. Younis, C. Ciotonea, J. Estephane, S. Aouad, H. Lucette Tidahy, C. Gennequin, E. Abi Aad, Nanomaterials and biomass valorization for hydrogen production, in: Hydrogen Technology, Elsevier, 2024: pp. 35–76. https://doi.org/10.1016/B978-0-443-13547-7.00002-1.

[21] M. Gasik, V. Dashevskii, A. Bizhanov, Metallurgy of Silicon and Silicon Carbide, in: 2020: pp. 35–55. https://doi.org/10.1007/978-3-030-57502-1_4.

[22] E.H. Cowles, A.H. Cowles, C.F. Mabery, Electrical furnace and the reduction of the oxides of boron, silicon, aluminum and other metals by carbon, American Journal of Science. s3-30 (1885) 308–311. https://doi.org/10.2475/ajs.s3-30.178.308.

[23] V.A. Izhevskyi, L.A. Genova, J.C. Bressiani, A.H.A. Bressiani, Review article: silicon carbide. Structure, properties and processing, Cerâmica. 46 (2000) 4–13. https://doi.org/10.1590/S0366-69132000000100002.

[24] R.A. Andrievski, Nano-sized silicon carbide: synthesis, structure and properties, Russian Chemical Reviews. 78 (2009) 821–831. https://doi.org/10.1070/RC2009v078n09ABEH004060.

[25] N.D. Shcherban, Review on synthesis, structure, physical and chemical properties and functional characteristics of porous silicon carbide, Journal of Industrial and Engineering Chemistry. 50 (2017) 15–28. https://doi.org/10.1016/j.jiec.2017.02.002.

[26] C. Codreanu, M. Avram, E. Carbunescu, E. Iliescu, Comparison of 3C–SiC, 6H–SiC and 4H–SiC MESFETs performances, Materials Science in Semiconductor Processing. 3 (2000) 137–142. https://doi.org/10.1016/S1369-8001(00)00022-6.

[27] M. Alsheikh, R. Alsalamah, H. Alshehri, A. Laref, The modulation of photonic band structures of silicon carbide polytype multilayers applicable in optical wave-guiding devices, Journal of Nonlinear Optical Physics & Materials. 34 (2025). https://doi.org/10.1142/S0218863523500650.

[28] V. Haase, G. Kirschstein, H. List, S. Ruprecht, R. Sangster, F. Schröder, W. Töpper, H. Vanecek, W. Heit, J. Schlichting, Si Silicon, Springer Berlin Heidelberg, Berlin, Heidelberg, 1985. https://doi.org/10.1007/978-3-662-06994-3.

[29] S.R. Kulkarni, V.K. Velisoju, F. Tavares, A. Dikhtiarenko, J. Gascon, P. Castaño, Silicon carbide in catalysis: from inert bed filler to catalytic support and multifunctional material, Catalysis Reviews. 65 (2023) 174–237. https://doi.org/10.1080/01614940.2022.2025670.

[30] R. Gerhardt, Properties and Applications of Silicon Carbide, 2011.

[31] K. Broniszewski, J. Woźniak, T. Cygan, M. Kostecki, D. Moszczyńska, M. Chmielewski, K. Dydek, A. Olszyna, Effect of Anisotropy of Reduced Graphene Oxide on Thermal and Electrical Properties in Silicon Carbide Matrix Composites, Nanomaterials. 14 (2024) 555. https://doi.org/10.3390/nano14060555.

[32] S. Alekseev, E. Shamatulskaya, M. Volvach, S. Gryn, D. Korytko, I. Bezverkhyy, V. Iablokov, V. Lysenko, Size and Surface Chemistry Tuning of Silicon Carbide Nanoparticles, Langmuir. 33 (2017) 13561–13571. https://doi.org/10.1021/acs.langmuir.7b02784.

[33] L. Chen, C. Wei, S. Zhang, X. Li, Improved the mechanical properties of silicon carbide fiber reinforced silicon carbide matrix composite joints by short-time diffusion bonding with Nb-Ti-Si alloy filler, Materials Science and Engineering: A. 919 (2025) 147492. https://doi.org/10.1016/j.msea.2024.147492.

[34] G.-Q. Jin, X.-Y. Guo, Synthesis and characterization of mesoporous silicon carbide, Microporous and Mesoporous Materials. 60 (2003) 207–212. https://doi.org/10.1016/S1387-1811(03)00378-0.

[35] A. Deneuve, I. Florea, O. Ersen, P. Nguyen, C. Pham, D. Bégin, D. Edouard, M.-J. Ledoux, C. Pham-Huu, Catalytic growth of silicon carbide composite with nanoscopic properties and enhanced oxidative

resistance as catalyst support, Applied Catalysis A: General. 385 (2010) 52–61. https://doi.org/10.1016/j.apcata.2010.06.043.

[36] C. Teng, Q. Huang, Y. Cheng, Z. Zhang, L. Zhang, J. Zhu, L. Xu, Q. Song, Z. Bian, J. Li, W. Yuan, Waste photovoltaic wafers-derived SiC-based photocatalysts for pharmaceutical wastewater purification: S-scheme, waste utilization, and life cycle assessment, Resources, Conservation and Recycling. 220 (2025) 108332. https://doi.org/10.1016/j.resconrec.2025.108332.

[37] Z. Geng, Y. He, F. Fang, Study on surface integrity of RS-SiC under photocatalysis/vibration-assisted finishing, Journal of Manufacturing Processes. 134 (2025) 384–393. https://doi.org/10.1016/j.jmapro.2024.12.050.

[38] H. Heidarzadeh, Transition metal-doped 3C-SiC as a promising material for intermediate band solar cells, Optical and Quantum Electronics. 51 (2019) 1–11. https://doi.org/10.1007/s11082-019-1742-y.

[39] Y. Wang, Q. Lin, P.X.-L. Feng, Single-crystal 3C-SiC-on-insulator platform for integrated quantum photonics, Optics Express. 29 (2021) 1011. https://doi.org/10.1364/OE.413556.

[40] S. Saddow, Silicon Carbide Technology for Advanced Human Healthcare Applications, Micromachines. 13 (2022) 346. https://doi.org/10.3390/mi13030346.

[41] M.A. Ahmed, A. Mahmoud, A.A. Mohamed, M. Adel, RSC Advances carbon nitride (g-C 3 N 4): a state-of-the-art review, (2024) 25629–25662. https://doi.org/10.1039/d4ra04234d.

[42] X. Wang, K. Maeda, A. Thomas, K. Takanabe, G. Xin, J.M. Carlsson, K. Domen, M. Antonietti, A metal-free polymeric photocatalyst for hydrogen production from water under visible light, Nature Materials. 8 (2009) 76–80. https://doi.org/10.1038/nmat2317.

[43] S. Kumar, S. Karthikeyan, A.F. Lee, g-C3N4-Based Nanomaterials for Visible Light-Driven Photocatalysis, Catalysts. 8 (2018) 74. https://doi.org/10.3390/catal8020074.

[44] V. Srivastava, P.K. Singh, P.P. Singh, Recent advances of visible-light photocatalysis in the functionalization of organic compounds, Journal of Photochemistry and Photobiology C: Photochemistry Reviews. 50

(2022) 100488. https://doi.org/10.1016/j.jphotochemrev.2022.100488.

[45] S.F. Ahmed, M. Mofijur, S. Nuzhat, N. Rafa, A. Musharrat, S.S. Lam, A. Boretti, Sustainable hydrogen production: Technological advancements and economic analysis, International Journal of Hydrogen Energy. 47 (2022) 37227–37255. https://doi.org/10.1016/j.ijhydene.2021.12.029.

[46] L. Cheng, H. Zhang, X. Li, J. Fan, Q. Xiang, Carbon–Graphitic Carbon Nitride Hybrids for Heterogeneous Photocatalysis, Small. 17 (2021). https://doi.org/10.1002/smll.202005231.

[47] M. Kathiresan, Graphitic carbon nitrides: synthesis and properties, in: Nanoscale Graphitic Carbon Nitride, Elsevier, 2022: pp. 1–16. https://doi.org/10.1016/B978-0-12-823034-3.00004-2.

[48] H. Li, B. Cheng, J. Xu, J. Yu, S. Cao, Crystalline carbon nitrides for photocatalysis, EES Catalysis. 2 (2024) 411–447. https://doi.org/10.1039/D3EY00302G.

[49] Y. Kang, Y. Yang, L. Yin, X. Kang, G. Liu, H. Cheng, An Amorphous Carbon Nitride Photocatalyst with Greatly Extended Visible-Light-Responsive Range for Photocatalytic Hydrogen Generation, Advanced Materials. 27 (2015) 4572–4577. https://doi.org/10.1002/adma.201501939.

[50] L. Gudiño, J.J. Rodriguez, C. Belver, J. Bedia, Effect of precursor on the solar photocatalytic production of hydrogen using C_3N_4, Separation and Purification Technology. 365 (2025) 132686. https://doi.org/10.1016/j.seppur.2025.132686.

[51] H. Gao, S. Yan, J. Wang, Y.A. Huang, P. Wang, Z. Li, Z. Zou, Towards efficient solar hydrogen production by intercalated carbon nitride photocatalyst, Physical Chemistry Chemical Physics. 15 (2013) 18077. https://doi.org/10.1039/c3cp53774a.

[52] G. Dong, Y. Zhang, Q. Pan, J. Qiu, A fantastic graphitic carbon nitride (g-C3N4) material: Electronic structure, photocatalytic and photoelectronic properties, Journal of Photochemistry and Photobiology C: Photochemistry Reviews. 20 (2014) 33–50. https://doi.org/10.1016/j.jphotochemrev.2014.04.002.

[53] S.A. Idrees, L.A. Jamil, K.H. Hama Aziz, K.M. Omer, Synergetic Photocatalytic Activity of Metal-Free Boron Nitride Quantum Dots and

Graphitic Carbon Nitride: Harnessing Visible Light for Organic Waste Elimination–A Theoretical and Experimental Approach, Catalysis Letters. 154 (2024) 4201–4217. https://doi.org/10.1007/s10562-024-04628-8.

[54] X. Wang, S. Blechert, M. Antonietti, Polymeric Graphitic Carbon Nitride for Heterogeneous Photocatalysis, ACS Catalysis. 2 (2012) 1596–1606. https://doi.org/10.1021/cs300240x.

[55] A. Hayat, A.G. Al-Sehemi, K.S. El-Nasser, T.A. Taha, A.A. Al-Ghamdi, Jawad Ali Shah Syed, M.A. Amin, T. Ali, T. Bashir, A. Palamanit, J. Khan, W.I. Nawawi, Graphitic carbon nitride (g–C3N4)–based semiconductor as a beneficial candidate in photocatalysis diversity, International Journal of Hydrogen Energy. 47 (2022) 5142–5191. https://doi.org/10.1016/j.ijhydene.2021.11.133.

[56] B. Yuan, Y. Wang, A.Y. Elnaggar, I.H. El Azab, M. Huang, M.H.H. Mahmoud, S.M. El-Bahy, M. Guo, Physical vapor deposition of graphitic carbon nitride (g-C3N4) films on biomass substrate: optoelectronic performance evaluation and life cycle assessment, Advanced Composites and Hybrid Materials. 5 (2022) 813–822. https://doi.org/10.1007/s42114-022-00505-3.

[57] L. Kunhikrishnan, K. Vishal, S. Palaniyappan, Mechanical and Thermal Characterization on Synthesized Silane-Treated Graphitic Carbon Nitride (g-C3N4) Reinforced 3D Printed Poly (Lactic Acid) Composite, Journal of Inorganic and Organometallic Polymers and Materials. 33 (2023) 1234–1245. https://doi.org/10.1007/s10904-023-02579-y.

[58] M. Hao, Y. Li, L. Gao, C. Ji, R. Qu, Z. Yang, C. Sun, Y. Zhang, In-situ hard template synthesis of mesoporous carbon/graphite carbon nitride (C/CN-T-x) composites with high photocatalytic activities under visible light irridation, Solid State Sciences. 109 (2020) 106428. https://doi.org/10.1016/j.solidstatesciences.2020.106428.

[59] K. Maeda, X. Wang, Y. Nishihara, D. Lu, M. Antonietti, K. Domen, Photocatalytic Activities of Graphitic Carbon Nitride Powder for Water Reduction and Oxidation under Visible Light, The Journal of Physical Chemistry C. 113 (2009) 4940–4947. https://doi.org/10.1021/jp809119m.

[60] X. Song, H. Tao, L. Chen, Y. Sun, Synthesis of Fe/g-C_3N_4 composites with improved visible light photocatalytic activity, Materials Letters. 116 (2014) 265–267. https://doi.org/10.1016/j.matlet.2013.11.043.

[61] S.C. Yan, Z.S. Li, Z.G. Zou, Photodegradation Performance of g-C 3 N 4 Fabricated by Directly Heating Melamine, Langmuir. 25 (2009) 10397–10401. https://doi.org/10.1021/la900923z.

[62] G. Zhang, J. Zhang, M. Zhang, X. Wang, Polycondensation of thiourea into carbon nitride semiconductors as visible light photocatalysts, Journal of Materials Chemistry. 22 (2012) 8083. https://doi.org/10.1039/c2jm00097k.

[63] F. Dong, Z. Wang, Y. Sun, W.-K. Ho, H. Zhang, Engineering the nanoarchitecture and texture of polymeric carbon nitride semiconductor for enhanced visible light photocatalytic activity, Journal of Colloid and Interface Science. 401 (2013) 70–79. https://doi.org/10.1016/j.jcis.2013.03.034.

[64] Z. Chen, S. Mitchell, E. Vorobyeva, R.K. Leary, R. Hauert, T. Furnival, Q.M. Ramasse, J.M. Thomas, P.A. Midgley, D. Dontsova, M. Antonietti, S. Pogodin, N. López, J. Pérez-ramírez, Stabilization of Single Metal Atoms on Graphitic Carbon Nitride, 1605785 (2017). https://doi.org/10.1002/adfm.201605785.

[65] N.F.F. Moreira, M.J. Sampaio, A.R. Ribeiro, C.G. Silva, J.L. Faria, A.M.T. Silva, Metal-free g-C_3N_4 photocatalysis of organic micropollutants in urban wastewater under visible light, Applied Catalysis B: Environmental. 248 (2019) 184–192. https://doi.org/10.1016/j.apcatb.2019.02.001.

[66] M. Reza Gholipour, C.-T. Dinh, F. Béland, T.-O. Do, Nanocomposite heterojunctions as sunlight-driven photocatalysts for hydrogen production from water splitting, Nanoscale. 7 (2015) 8187–8208. https://doi.org/10.1039/C4NR07224C.

[67] V. Subramanian, E.E. Wolf, P. V. Kamat, Catalysis with TiO_2/Gold Nanocomposites. Effect of Metal Particle Size on the Fermi Level Equilibration, Journal of the American Chemical Society. 126 (2004) 4943–4950. https://doi.org/10.1021/ja0315199.

[68] W. Zheng, L. Xu, Z. Hu, Y. Zhao, J. Li, M. Ouyang, Dynamic modeling

of chemical membrane degradation in polymer electrolyte membrane fuel cells: Effect of precipitated Pt particles, International Journal of Hydrogen Energy. 56 (2024) 1111–1119. https://doi.org/10.1016/j.ijhydene.2023.12.275.

[69] F. Fina, H. Ménard, J.T.S. Irvine, The effect of Pt NPs crystallinity and distribution on the photocatalytic activity of Pt–g-C_3N_4, Physical Chemistry Chemical Physics. 17 (2015) 13929–13936. https://doi.org/10.1039/C5CP00560D.

[70] L. Jiao, J.R. Regalbuto, The synthesis of highly dispersed noble and base metals on silica via strong electrostatic adsorption: I. Amorphous silica, Journal of Catalysis. 260 (2008) 329–341. https://doi.org/10.1016/j.jcat.2008.09.022.

[71] P. Mäki-Arvela, D.Y. Murzin, Effect of catalyst synthesis parameters on the metal particle size, Applied Catalysis A: General. 451 (2013) 251–281. https://doi.org/10.1016/j.apcata.2012.10.012.

[72] Y. Liu, Z. Tan, R. Yu, B. Gao, M. Zhang, X. Zhang, X. Chong, Anisotropic mechanical properties and electronic structures of transition metal carbonitrides M2CN (M = V, Ti, Ta, Nb, Hf and Zr) by first-principles calculations, Applied Physics A. 126 (2020) 699. https://doi.org/10.1007/s00339-020-03887-7.

[73] X. Chong, M. Hu, P. Wu, Q. Shan, Y.H. Jiang, Z.L. Li, J. Feng, Tailoring the anisotropic mechanical properties of hexagonal M7X3 (M=Fe, Cr, W, Mo; X=C, B) by multialloying, Acta Materialia. 169 (2019) 193–208. https://doi.org/10.1016/j.actamat.2019.03.015.

[74] X. Chong, P.-W. Guan, M. Hu, Y. Jiang, Z. Li, J. Feng, Exploring accurate structure, composition and thermophysical properties of η carbides in 17.90 wt% W-4.15 wt% Cr-1.10 wt% V-0.69 wt% C steel, Scripta Materialia. 154 (2018) 149–153. https://doi.org/10.1016/j.scriptamat.2018.05.038.

[75] J.G. Speer, J.R. Michael, S.S. Hansen, Carbonitride precipitation in niobium/vanadium microalloyed steels, Metallurgical Transactions A. 18 (1987) 211–222. https://doi.org/10.1007/BF02825702.

[76] Y. Peng, H. Miao, Z. Peng, Development of TiCN-based cermets: Mechanical properties and wear mechanism, International Journal of

Refractory Metals and Hard Materials. 39 (2013) 78–89. https://doi.org/10.1016/j.ijrmhm.2012.07.001.

[77] M.E. Goshkoderya, T.I. Bobkova, V. V. Savich, Features of Creating Functional and Functionally Gradient Coatings with a Unique Set of Properties from Composite Powders with Titanium Matrix, Metallurgist. 66 (2023) 1430–1435. https://doi.org/10.1007/s11015-023-01457-9.

[78] G. Levi, W.D. Kaplan, M. Bamberger, Structure refinement of titanium carbonitride (TiCN), Materials Letters. 35 (1998) 344–350. https://doi.org/10.1016/S0167-577X(97)00276-0.

[79] H. Li, K. Wang, G. Xu, H. Jiang, Q. Wang, Y. Wang, Effective inhibition of anomalous grain coarsening in cast AZ91 alloys during fast cooling via nanoparticle addition, Journal of Magnesium and Alloys. 11 (2023) 4575–4588. https://doi.org/10.1016/j.jma.2021.10.008.

[80] C.S. Autorzy Dyjak S., Wasilewska M., Combustion Synthesis of Titanium Carbonitrides, Central European Journal of Energetic Materials. 12, no. 2 (2015) 249--259.

[81] H.S. Gujral, M. Fawaz, S. Joseph, C.I. Sathish, G. Singh, X. Yu, M.B.H. Breese, J. Yi, M. Singh, V. Bansal, A. Karakoti, A. Vinu, Nanoporous TiCN with High Specific Surface Area for Enhanced Hydrogen Evolution Reaction, ACS Applied Nano Materials. 5 (2022) 12077–12086. https://doi.org/10.1021/acsanm.2c00488.

[82] S. Rao, C. Zhi, X. Wang, J. Su, Y. Sun, Y. Sun, R. Ma, Q. Liu, J. Yang, Z. Sun, In situ synthesis of graphitic carbon nitride nanosheet/Ti3C2Tx MXene/TiO2 Z-scheme heterojunctions boosting charge transfer for full-spectrum driven photocatalytic sterilization, Journal of Colloid and Interface Science. 659 (2024) 594–602. https://doi.org/10.1016/j.jcis.2024.01.005.

[83] S.R. Kali, M. V, M. R, S.D. K.R., D. Pinheiro, Research progress of MXenes and MXenes-based catalysts for photocatalytic water splitting: A systematic review, Journal of Environmental Chemical Engineering. 12 (2024) 112748. https://doi.org/10.1016/j.jece.2024.112748.

[84] P. Praus, 2D/2D composites based on graphitic carbon nitride and MXenes for photocatalytic reactions: a critical review, Carbon Letters. 34 (2024) 227–245. https://doi.org/10.1007/s42823-023-00634-9.

[85] Y. Zhong, X. Xia, F. Shi, J. Zhan, J. Tu, H.J. Fan, Transition Metal Carbides and Nitrides in Energy Storage and Conversion, Advanced Science. 3 (2016). https://doi.org/10.1002/advs.201500286.

[86] Y. Zhou, J.L. Silva, J.M. Woods, J. V. Pondick, Q. Feng, Z. Liang, W. Liu, L. Lin, B. Deng, B. Brena, F. Xia, H. Peng, Z. Liu, H. Wang, C.M. Araujo, J.J. Cha, Revealing the Contribution of Individual Factors to Hydrogen Evolution Reaction Catalytic Activity, Advanced Materials. 30 (2018). https://doi.org/10.1002/adma.201706076.

CHAPTER VI: Aim of the PhD Thesis

CHAPTER VI: Aim of the PhD thesis

The main aim of this thesis is to investigate the use of unconventional photocatalytic materials (different to the most investigated semiconductors as TiO_2, WO_3, or ZnO) in solar photoreforming processes. In particular, carbon-based materials were chosen as sustainable and green photocatalysts. In recent years indeed, the scientific community has been focused on the study and the use of carbon-based materials for their remarkable electrical, thermal, and mechanical properties. They have minimal toxicity, strong conductivity, excellent stability, and are environmentally friendly[1,2]. Carbon-based nanomaterials also own a high anisotropic heat conductivity, they are non-critical, cost-effective, environmentally friendly, and non-toxic. In particular, the performance of SiC, g-C_3N_4 and TiCN-based photocatalysts were investigated.

On the other hand, photoreforming is currently considered one of the most innovative methods for the green H_2 production, as the reaction is driven by solar radiation. This makes it a low-cost process. Moreover, it allows the use of waste materials as sacrificial agents, which are degraded during the process while simultaneously being exploited to produce hydrogen. This approach may help to address the growing global energy demand, preserving contextually the environment.

Lastly, plastic and biomass are recently studied as sacrificial agents in the photoreforming reactions[3–6] because they are among of the largest sources of human-made waste. Furthermore, for the plastic materials the effective recycling methods are often

lacking. The plastic or the biomass solar photoreforming allows to degrade and contextually to valorise this waste through a green approach, offering a strategic solution to both the problems of the energy depletion and of the environmental pollution.

To achieve this ambitious aim, an extensive literature review was conducted, followed by several experiments and data analysis. The work was divided in 3 main goals:

- **Goal 1:** Investigation of bisphenol A (BPA) and polyethylene terephthalate (PET) solar photoreforming reaction using SiC-g-C_3N_4 photocatalysts.
- **Goal 2:** Investigation of polystyrene (PS), low density polyethylene (LDPE) and polylactic acid (PLA) solar photoreforming reaction using SiC-g-C_3N_4_TCN photocatalysts.
- **Goal 3:** Investigation of glucose (biomass-derived compound) visible-light photoreforming reaction using Pt/g-C_3N_4 photocatalysts.[5]

[5] This part of work was made at the *University of Porto* (Laboratory of Separation and Reaction Engineering – Laboratory of Catalysis and Materials, Faculdade de Engenharia, Department chemistry engineer), under the supervision *of Dr. Maria Sampaio* from February 2024 to July 2024 as visiting PhD student period.

Goal 1

The first step in this study was to investigate the hydrogen production from plastic materials by solar photoreforming reaction. To simplify the process, the monomer bisphenol A (BPA) was initially selected, as it has a simpler molecular structure compared to plastics like polyethylene terephthalate (PET), which are composed of long polymer chains made up of repeating monomer units. By identifying the optimal conditions for a simpler molecule, these are then extended to more complex macromolecules.
The BPA was chosen because it is a key monomer used in the production of polycarbonates and epoxy resins, and its global production is estimated to exceed 5–6 million tonnes per year[7].
The PET was selected due to its wide use, particularly in food packaging (such as bottles) and synthetic fibres. Global PET production has surpassed 55 million tonnes per year, and some data suggest this number is still increasing[8], making urgent the development of effective disposal methods. However, to carry out the photoreforming reaction using these materials as organic scavengers, pre-treatment was required in order to bring them into solution. Before each test, a chemical pre-treatment in strong alkaline conditions was necessary.

The data presented in the following chapter show that it was possible to produce H_2 through this plastic photoreforming. An important aspect of this process was the selection of carbon-based materials, particularly silicon carbide (SiC) and graphitic carbon nitride (g-C_3N_4). Unfortunately, the synthesis of SiC was

not feasible due to the extreme temperature requirements (1800–1900 °C)[9].

For this reason, it was decided to use the commercial SiC making a comparison between micro-sized and nano-sized samples. Furthermore, the research was focused on the choice of the optimal amount of g-C_3N_4, which was synthesized using different monomers.

By optimizing the interaction between the two materials and employing g-C_3N_4 as minor component of the photocatalytic composite, an efficient photocatalyst was developed for this green hydrogen production method.

Goal 2

The second goal of the work was focused on the study of the photoreforming of other plastic materials. The selected polymers are polystyrene (PS), low density polyethylene (LDPE), and polylactic acid (PLA), chosen for the following reasons:

- *Polystyrene (PS):* Approximately 15 million tonnes of PS are produced annually. It is commonly used in take-away food containers, building insulation, electronic components, and toys. PS was chosen because its chemical and physical properties make it difficult to recycle and dispose of, contributing significantly to ocean pollution[10].
- *Polyethylene (PE):* PE is the most widely produced plastic worldwide. It is highly versatile and cost-effective, making it a popular material in numerous everyday applications[11].
- *Polylactic acid (PLA):* PLA is a biodegradable polymer, and its production is rapidly growing (400,000–600,000 tonnes per year), with the potential to replace a significant portion of conventional plastic production[12]. However, PLA has a relatively long recycling time. It cannot be composted at home and requires industrial composting at temperatures above 200°C. For these reasons, PLA was selected to compare hydrogen yields between biodegradable and non-biodegradable polymers, and to explore alternative disposal methods under ambient conditions and solar irradiation.

Another goal of this section was to compare the chemical pretreatment methods of the plastics. In particular, the strong alkaline conditions were compared to milder alkaline one using ethanol as solvent.

Finally, to further enhance the hydrogen generation, the SiC-g-C_3N_4 composite (with the optimal amount of graphitic carbon nitride) was improved by incorporating small amounts of TiCN as co-catalyst. This addition marked a significant innovation, as TiCN is a carbon-based compound rarely used in photocatalysis. However, it showed excellent performance as a co-catalyst based on the experimental data collected.

Finally, the optimized set-up and conditions developed for the plastic photoreforming were also applied to the photoreforming of biomass-derived compound, specifically the cellulose.

Goal 3

The final section focuses on the visible-light photoreforming of glucose, selected because it represents the main waste component of cellulose. For this work, a very small amount of platinum was added to g-C_3N_4 prepared using several precursors and investigating the effects of the exfoliation process of the graphitic carbon nitride.

The presence of platinum was essential due to the very negligible activity of bare g-C_3N_4[13].

Moreover, to increase the applicability of the examined reaction, the photocatalyst was prepared also in the film form, evaluating the difference in the apparent quantum yield between the film and the powder photocatalysts, and different water matrices, such as wastewater and seawater, were investigated.

In the Fig.1 the graphical abstract of this PhD work is shown.

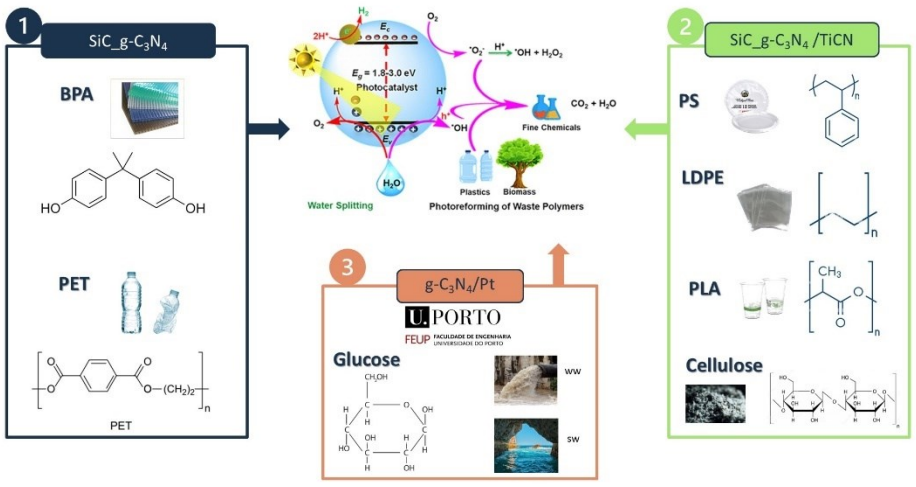

Figure 1 *Graphical Abstract of the thesis.*

References

[1] A.L. Machado, R.A. Oliveira, G. Dražić, J.C. Lopes, C.G. Silva, J.L. Faria, M.J. Sampaio, Producing hydrogen from biomass and seawater using immobilized carbon nitride photocatalysts, Chemical Engineering Journal Advances. 21 (2025) 100697. https://doi.org/10.1016/j.ceja.2024.100697.

[2] M. Moussa, A. Hamrouni, N. Lazaar, M. Ferhi, I. Chérif, H. Lachheb, C.G. Silva, M.J. Sampaio, J.L. Faria, Pt-doped g-C3N4 photocatalyst for simultaneous hydrogen production and value-added chemical synthesis under visible light, Photochemical & Photobiological Sciences. 24 (2025) 247–259. https://doi.org/10.1007/s43630-025-00683-1.

[3] Q.Y. Lee, H. Li, Photocatalytic Degradation of Plastic Waste: A Mini Review, Micromachines. 12 (2021) 907. https://doi.org/10.3390/mi12080907.

[4] Z. Ouyang, Y. Yang, C. Zhang, S. Zhu, L. Qin, W. Wang, D. He, Y. Zhou, H. Luo, F. Qin, Recent advances in photocatalytic degradation of plastics and plastic-derived chemicals, Journal of Materials Chemistry A. 9 (2021) 13402–13441. https://doi.org/10.1039/D0TA12465F.

[5] H. Du, X. Hu, C. Wang, Y. Pu, Y. Huang, T. Tian, M. Yang, Photoreforming for upcycling of plastics into energy, chemicals and materials: a review, Environmental Chemistry Letters. (2025). https://doi.org/10.1007/s10311-025-01850-7.

[6] U. Nwosu, A. Wang, B. Palma, H. Zhao, M.A. Khan, M. Kibria, J. Hu, Selective biomass photoreforming for valuable chemicals and fuels: A critical review, Renewable and Sustainable Energy Reviews. 148 (2021) 111266. https://doi.org/10.1016/j.rser.2021.111266.

[7] O.T. Ologundudu, T.A.M. Msagati, O.E. Popoola, J.N. Edokpayi, Bisphenol A in Selected South African Water Sources: A Critical Review, ACS Omega. (2025). https://doi.org/10.1021/acsomega.4c01686.

[8] C. Duan, Z. Wang, B. Zhou, X. Yao, Global Polyethylene Terephthalate (PET) Plastic Supply Chain Resource Metabolism Efficiency and Carbon Emissions Co-Reduction Strategies, Sustainability. 16 (2024) 3926. https://doi.org/10.3390/su16103926.

[9] L.M. Soltys, I.F. Mironyuk, I.M. Mykytyn, I.D. Hnylytsia, L.V. Turovska,

Synthesis and Properties of Silicon Carbide (Review), Physics and Chemistry of Solid State. 24 (2023) 5–16. https://doi.org/10.15330/pcss.24.1.5-16.

[10] K. Saido, Y. Kodera, H. Kimukai, H. Sato, A. Okabe, K. Koizumi, K. Takatama, B.G. Kwon, S.-Y. Chung, M. Nishimura, S. Mentese, Waste Polystyrene Degradation in the World Oceans: Newly identified sources of Contamination, (2020). https://doi.org/10.21203/rs.3.rs-83390/v3.

[11] L. Chen, Z. Lin, Polyethylene : Properties , Production and Applications, 2021 3rd International Academic Exchange Conference on Science and Technology Innovation (IAECST). (2021) 1191–1196. https://doi.org/10.1109/IAECST54258.2021.9695646.

[12] K.J. Jem, B. Tan, The development and challenges of poly (lactic acid) and poly (glycolic acid), Advanced Industrial and Engineering Polymer Research. 3 (2020) 60–70. https://doi.org/10.1016/j.aiepr.2020.01.002.

[13] H. Sharma, A. Bisht, N. Sethulakshmi, S. Sharma, Catalysis by substituted platinum (ionic Pt) catalysts, International Journal of Hydrogen Energy. 51 (2024) 748–768. https://doi.org/10.1016/j.ijhydene.2023.08.343.

CHAPTER VII: Experimental Set-up

CHAPTER VII: Experimental Set-up

7.1 Photocatalytic H_2 production by solar photoreforming set-up

For the photocatalytic hydrogen production, a home-made Pyrex jacketed reactor thermostated at 30 °C was used (Figs.1-3) [1]. The photocatalytic tests were performed with 50 mg of the photocatalyst, homogeneously suspended in an aqueous solution containing the sacrificial agent (10 ml) inside the reactor. Then the reactor was irradiated for 5 h using a special solar lamp (Osram Ultra Vitalux 300 W, irradiance of 10.7 mW/cm^2)[2] (Fig.2). In the case of plastic substrates, the organic sacrificial agents were pre-treated in order to obtain a solution of them. The measurements were replied three times (3% error).

The reaction gases were analysed using a gas chromatograph (Agilent 6890N) equipped with a thermal conductivity detector (TCD) suitable for the purpose due to its high sensitivity in detecting even small concentrations (μmol/L) of hydrogen (Fig.1). The amount of gas (1 ml) was withdrawn with a syringe (Gastight 1001, Hamilton).

The H_2/CO_2 ratio was evaluated by GC-TCD measurements after the opportune standard calibrations using the same Agilent 6890 N gas chromatograph with a Carboxen 1000 Column.

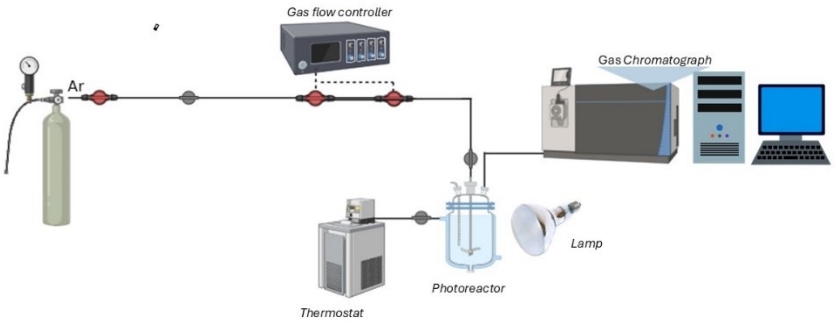

Figure 1 *Experimental set-up for the photocatalytic tests.*

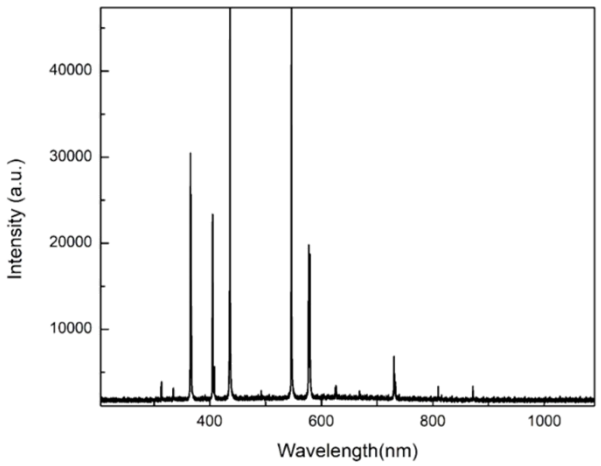

Figure 2 *Experimental emission spectrum of the used solar lamp.*

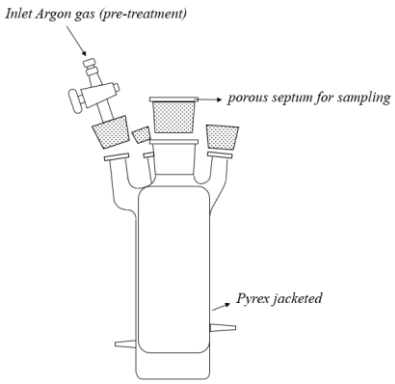

Figure 3 *Pyrex jacketed reactor*

Before the tests, in order to remove the oxygen, present inside the reactor, it was flowed with Argon gas for 1h (4 mL min^{-1}). This step is necessary to avoid the formation of oxygen radicals formed by reaction with the generated electrons, thus subtracting them from the photoreforming reaction. In order to obtain a good reproducibility of the tests, it is necessary that the whole apparatus is thermally controlled, and without gases leaks. The reactor has an insulating jacket to maintain a constant temperature, preventing the reactor overheating due to the heating of the solar lamp. Leak tests were carried out using a flowmeter. The argon flow was constantly monitored using a gas flow regulator (Tylan).

7.1.1 Photocatalytic set-up for the visible-light glucose photoreforming[6]

The photocatalytic hydrogen evolution for the glucose photoreforming was investigated using a borosilicate reactor[3]. The mass of photocatalyst was fixed at 50 mg, and it was dispersed in 100 mL of solution of sacrificial agent. Before the photocatalytic tests, reactor was degassed in the dark for 20 min with a flow of nitrogen (50 mL min^{-1}). After ensuring the total removal of dissolved oxygen, the nitrogen flow was maintained at 7.5 mL min^{-1}. The temperature was set at 25 °C, by water circulation through the photochemical reactor, using a thermostatic bath (Fig.4).

All the photocatalytic reactions were performed under visible-LED irradiation ($\lambda_{exc.}$ = 420 nm, Fig.5) using four visible-LED system placed at 4 cm of distance from the cylindrical glass reactor wall. The average nominal irradiance of each LED was 45 mW cm^{-2}, determined by using a UV–vis spectroradiometer (OceanOptics USB2000+) equipped with an optical fiber located at 4 cm of the irradiation source. The suspensions were irradiated for several hours depending to the type of tests, and the evolved H_2 was measured using an on-line gas chromatograph (Inficon Micro GC 3000, Agilent) equipped with a 5 Å molsieve column and a micro-TCD detector, using argon as gas carrier.

[6] This set-up was used during my period as visiting PhD student at the Faculty of Chemical Engineering at the University of Porto (Portugal) under the supervision of Dr. Maria Josè Sampaio.

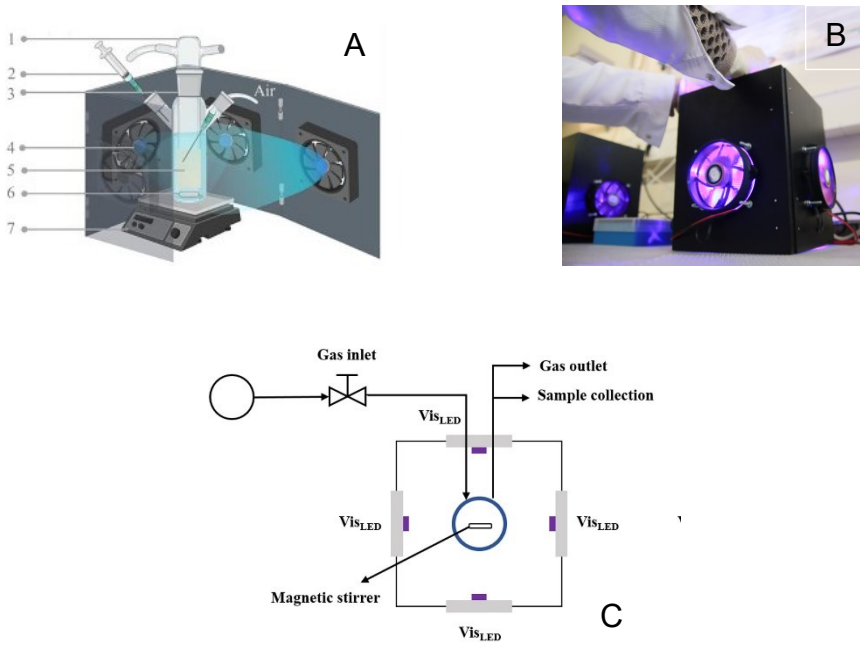

Figure 4 *Photocatalytic experimental systems in batch condition (A), 1. refrigeration system; 2. sample collection; 3. cylindrical glass reactor; 4. LED; catalyst; 6. magnetic bar; 7. stirrer;(B) photo of the system. (C) scheme of the experimental set-up.*

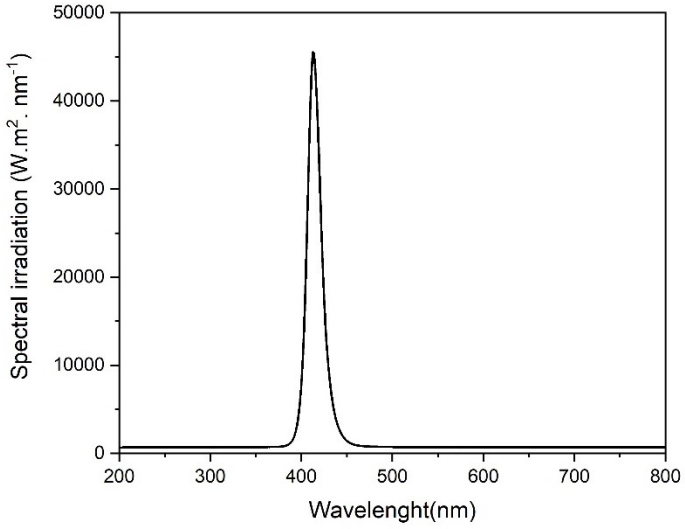

Figure 5 *Emission spectrum of the employed LEDs.*

7.2 Characterization techniques used in this work

7.2.1 Gas chromatography

Gas chromatography (GC) is a chromatographic technique used for analytical purposes, whereby the components of the mixture to be analysed are divided into a mobile phase and a stationary phase according to the different affinities of each substance in the mixture with the phases. Through an injector, the sample to be analysed is conveyed through the column. After a certain time, the separated components reach the detector with the flow of inert gas (He, H_2 or N_2), which signals the arrival, with different retention times. The result is a gas chromatogram in which the analysed mixture is diagrammed according to the various components. Currently, the most widely used system is packed column gas chromatography (PGC). Each gas chromatograph is coupled with a detector of a different nature depending on the physical principle used to detect the release of substances from the column. Detectors can be of two types: destructive (FID) or non-destructive (ECD, TCD) (Fig.6). The most used detectors are the Flame Ionisation Detector (FID) and the Thermal Conductivity Detector (TCD). The latter consist of two filaments that are electrically heated and maintained at a constant temperature. On one flows the pure carrier gas (Ar, He), on the other the gas exiting the column.

As the substance elutes, the second filament will cool or heat up relative to the first due to the heat dissipated by the gas containing the eluted substance. This change in temperature is reflected in a

change in resistance, which is amplified and represents the detector signal. In the FID, the carrier gas leaving the column is mixed with hydrogen and oxygen (or air). The vapours obtained from the combustion of the flame contain ions which are collected on the surface of the detector producing an electric current which, amplified, represents the detector signal.

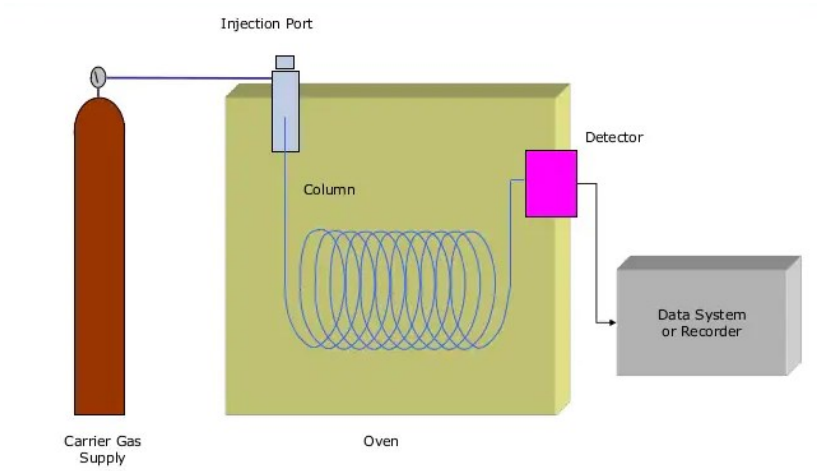

Figure 6 *GC instrumentation.*

7.2.2 UV- Vis DRS spectroscopy

UV-VIS DRS diffuse reflectance absorption spectroscopy is used to obtain molecular spectroscopic information from samples in powder form; it is a non-destructive method. An electromagnetic radiation is reflected off the surface of the sample to be analysed and a spectrum is then obtained that correlates electromagnetic radiation and frequency, called the reflectance spectrum. Due to refraction, the incoming beam also penetrates the interior of the particle and, as it is not absorbed, will leave the surface after many reflections and diffractions. A special device called an integrating sphere is used to carry out the measurements (Fig.7).

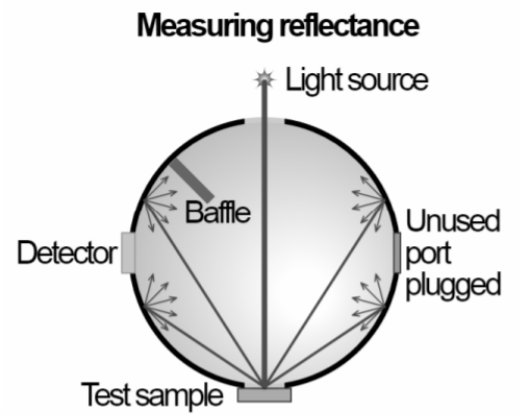

Figure 7 *Mechanism of the integrating sphere.*

It is equipped with a slit that allows light to enter the interior and after being reflected several times, it exits. To make reflectance measurements, it is first necessary to record a spectrum of the blank, i.e. of a substance whose surface is totally reflective, such as barium sulphate ($BaSO_4$) as it has a reflectance close to 100% in the visible range.

The most widely used theory paired with scattered reflectance is the Kubelka-Munk theory where absorption and scattering phenomena are observed together. Assuming that the scattering coefficient is constant over a given energy range, it is possible to derive the absorbance spectrum from the reflectance spectrum (EQ.1).

$$\frac{K}{S} = \frac{(1-Rx\rightarrow\infty)^2}{2Rx\rightarrow\infty} = F(Rx \rightarrow \infty) \quad \text{EQ. (1)}$$

In this equation:

- K represents the absorption coefficient.
- S represents the diffusion coefficient.
- F(Rx→∞) represents the K-M (Kubelka-Munk) function.
- (Rx→∞) represents the reflectance of the sample itself.

In order to estimate the energy band gap, the Tauc plot is used, using the absorption coefficient of the material. However, the function F(R) is usually used instead of α, which does not bring significant changes to the analysis.

7.2.3 Infrared spectroscopy

Infrared or IR spectroscopy is an absorption spectroscopic technique normally used in analytical chemistry, materials characterisation and physical chemistry for the study of chemical bonds. In this technique, an infrared photon is absorbed by a molecule, the latter passing from its fundamental vibrational state to an excited vibrational state. Generally, a spectrum is obtained, the abscissa of which presents a scale of frequencies expressed as a wave number and the percentage of transmittance as the ordinate. When, the material is transparent to infrared radiation, its spectrum will appear as a line parallel to the x-axis. If a material is not transparent, absorption and thus transitions between vibrational energy levels can be observed, with a series of peaks of varying height for each transition. The entire process is generated by the molecular electric dipole moment following the change in position of the atoms. Vibrations can be of two types: stretching of the chemical bond (stretching), deformation of the bond angle (bending).

Stretching is a periodic variation of the interatomic distance and can be symmetrical if the two atoms are simultaneously approaching or receding, or asymmetrical in the opposite case. Stretching can also be symmetrical, if it occurs along the plane and is called scissoring, whereas asymmetrical stretching, which occurs outside the plane, is called rocking; and it can occur along the plane on which the bonding angle lies or outside that plane. Furthermore, asymmetrical deformation out of the plane is called twisting while symmetrical deformation out of the plane is called wagging. A classical dual-beam IR spectrophotometer essentially

consists of a source whose light beam is directed towards the sample and reference. This is followed by the monochromator, whose function is to select a specific wavelength, and a chopper (an optical system in the shape of a half-disk that in dual-beam instruments is also placed after the source to split the light beam) that alternately directs the radiation from the sample and reference respectively to the detector. The detector is the final component that generates a signal depending on the analyte concentration present (Fig.8).

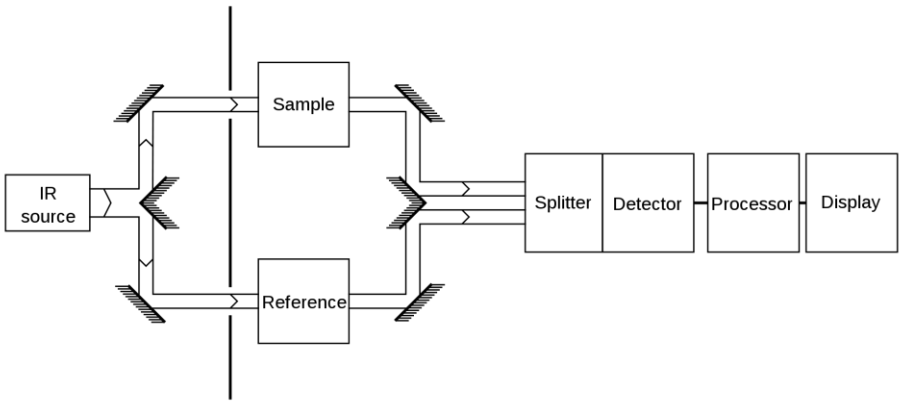

Figure 8 *IR instrument block diagram.*

For the analysis by creating tablets using a special pasteuriser, in which the solid samples to be analysed are finely ground with KBr. The detectors consist of devices capable of converting the thermal content of infrared radiation into an electrical signal.

Fourier-transform IR spectroscopy, or FT-IR for short, is performed using an interferometer to scan all frequencies present in the IR radiation generated by the source.

7.2.4 TEM (Transmission Electron Microscopy)

In the case of TEM, the electron beam, before hitting the sample to be examined, passes through an area where a vacuum has been artificially created, and only then passes through the material to be examined, obtaining information on the structure and morphology of the sample (Fig.9). In fact, the electrons can not only be transmitted but also diffracted.

For the electron beam to pass through the sample, the latter must always be ultra-thin (thickness less than 1 μm) due to the high absorption that electrons undergo when passing through any material and are prepared either as foils, if of metallic consistency, or if non-conductive solids, as thin wedge-shaped margins of a larger granule, or again as deposits on a grid, if organic substances. Transmission electron microscopy makes it possible to highlight individual elementary cells, their repetition in a plane, the presence of extensive structural defects (growth steps and spirals, dislocations and faults etc.) and also, under special lighting conditions, point defects.

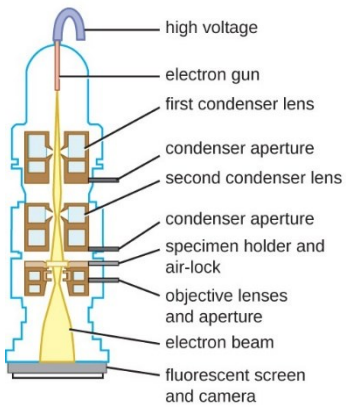

Figure 9 *TEM instrument.*

7.2.5 Xray diffraction (XRD)

X-ray diffraction (XRD) is a powerful non-destructive technique for characterising crystalline materials. It provides information on crystal structures, phases, crystal orientations, average grain size, crystallinity, deformation and defects [34]. X-ray diffraction peaks are produced by the constructive interference of a monochromatic X-ray beam scattered at specific angles dependent on lattice planes in a sample. Peak intensities are determined by the distribution of atoms within the lattice. Consequently, the X-ray diffraction pattern is a fingerprint of the periodic atomic arrangements in a given material (Fig.10).

The interaction of the incident rays with the sample produces constructive interferences, which satisfy Bragg's law:

$$n\lambda=2d\sin\theta$$

This law relates the wavelength of electromagnetic radiation to the diffraction angle and lattice of a crystalline sample. The sample is scanned through a range of two angles θ, all possible diffraction directions of the grating should be reached due to the random orientation of the powder material. X-ray diffractometers consist of three basic elements: an X-ray tube, a sample holder and an X-ray detector.

X-rays are generated by a cathode ray tube heating a filament to produce electrons, accelerating the electrons towards a target by applying a voltage and bombarding the material with electrons.

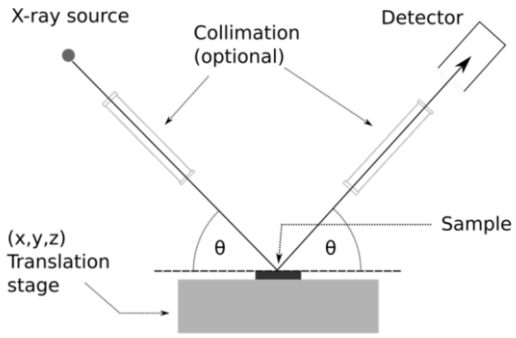

Figure 10 *XRD process diagram.*

When the electrons have sufficient energy to remove electrons from the inner shell of the target material, characteristic X-ray spectra are produced. These spectra consist of several components, the most common of which are Kα and Kβ. These X-rays are collimated and directed onto the sample. When the sample and detector are rotated, the intensity of the reflected X-rays is recorded. A detector records and processes this X-ray signal and converts it into a count rate that is then output to a device such as a printer or computer monitor. Furthermore, from the XRD diffractogram, it is possible to calculate the average crystalline grain size d using Scherrer's formula:

$$d = K\lambda\beta \cos\theta$$

where K is a constant inherent to the source of the instrument used, λ is the wavelength of the X-ray beam used, β is the amplitude at half-height of the most intense peak in the diffractogram, and θ is the angle relative to this peak.

7.2.6 X-ray photoelectron spectroscopy (XPS)

The XPS technique yields quantitative and qualitative information. Quantitative information arises from the element specificity of the binding energies and the relation between the intensity of the photoelectron peaks and the element concentration. Qualitative information is obtained from the energy position of a photoelectron peak with respect to the energy position of the same level in a reference compound (chemical shift).

XPS is based on the photoelectric effect arising when high energy photons (usually in the keV range) hit a material with the consequent emission of electrons (photoelectrons). The photoelectron kinetic energy, E_k, which is the measured quantity in the experiment, is given by Einstein's law:

$$E_k = h\nu - E_b$$

where $h\nu$ is the energy of the incident radiation and E_b the binding energy of the electron in a particular level. If the incident photon is sufficiently energetic, many different levels in the sample may be ionized and thus a spectrum is produced displaying all accessible energy levels as a distribution of photoelectrons with kinetic energies governed by E_k.

Photoelectron peaks are labelled according to the quantum numbers of the level from which the electron originates. The electron is characterized by a total momentum number $j=l+s$, where l is the orbital momentum number and s the spin momentum number which is equal to 1/2 or −1/2. Therefore, whenever $l>0$, the peak is split into a doublet, with an energy difference called *spin-orbit splitting* which increases

with Z roughly as Z^5. The intensity ratio of the two components is determined by the ratio of the multiplicity (2j+l) of the corresponding levels. Additional peaks due to the so-called electron shake-up process sometimes appear on the high binding energy side of a photoelectron peak. These features correspond to photoelectrons emitted from an atom in which a second electron in each orbital goes into an excited state as consequence of the sudden change in the atom central potential produced by the photoelectron ejection. The presence of these types of peaks may be quite useful for chemical state determinations. Because of the primary ionization process, a hole in the core level is created and the excited ion tends to relax by photoemission or by emission of electrons through the Auger decay. The latter is the favourite mechanism for core levels with binding energies below 2 keV. The Auger effect is a multiple ionization process in which an electron from an external level fills the vacancy created in the core level and the difference between the two energy levels is carried away by the ejected Auger electron. The final state is therefore a doubly ionized state with two vacancies in the levels involved in the process. The notation used for the identification of Auger peaks considers all the levels involved in the process.

7.2.7 Photoluminescence

The Photoluminescence (abbreviated as PL) is light emission from any form of matter after the absorption of photons (electromagnetic radiation). It is one of many forms of luminescence (light emission) and is initiated by photoexcitation (excitation by photons). Following excitation various relaxation processes typically occur in which other photons are re-radiated. Time periods between absorption and emission may vary ranging from short femtosecond-regime for emission involving free carrier plasma in inorganic semiconductors up to milliseconds for phosphorescent processes in molecular systems; and under special circumstances delay of emission may even span to minutes or hours. Observation of photoluminescence at a certain energy can be viewed as indication that excitation populated an excited state associated with this transition energy. While this is generally true in atoms and similar systems, correlations and other more complex phenomena also act as sources for photoluminescence in many-body systems such as semiconductors.

PL spectroscopy is then a powerful technique for investigating the electronic structure, both intrinsic and extrinsic, of semiconducting and semi-insulating materials. When collected at liquid helium temperatures, a PL spectrum gives an excellent picture of overall crystal quality. It can also be helpful in determining impurity concentrations, identifying defect complexes, and measuring the band gap of semiconductors. When performed at room temperature with a tightly focused laser beam, PL mapping can be used to measure micrometre scale variations in crystal quality or,

in the case of alloys and super lattices, chemical composition. The information from PL overlaps with that obtained from absorption spectroscopy, the latter technique being somewhat more difficult to perform for several reasons. First, absorption spectroscopy requires a broadband excitation source, such as a tungsten-halogen lamp, while PL can be performed with any above-band-gap laser source. Second, for thin film samples absorption spectroscopy requires that the substrate is etched away to permit transmission of light through the sample. Third, for bulk samples the transmitted light may be quite weak, creating signal-to-noise ratio difficulties. On the other hand, absorption spectroscopy has the advantage of probing the entire sample volume, while PL is limited to the penetration depth of the above-band-gap excitation source, typically on the order of a micrometer. The areas of application of PL also overlap somewhat with Raman spectroscopy, but the latter is much harder to perform because of the inherent weakness of nonlinear scattering processes and because of its sensitivity to crystallographic orientation.

7.2.8 N_2 adsorption-desorption measurements

The specific surface area of a powder is determined by physical adsorption of a gas, usually N_2, on the surface of the solid and by calculating the amount of adsorbate gas corresponding to a monomolecular layer on the surface. Physical adsorption results from relatively weak forces (Van der Waals) between the adsorbate gas molecules and the adsorbent surface area of the powder. The determination is usually carried out at the temperature of liquid nitrogen. The amount of gas adsorbed can be measured by a volumetric or continuous flow procedure. The Brunauer-Emmett-Teller (BET) theory aims to explain the physical adsorption of gas molecules on a solid surface and serves as the basis for the measurement of the specific surface area of a material. Surface area determinations involve creating the conditions required to adsorb an average monolayer of molecules onto a sample. By extending this process so that the gas is allowed to condense in the pores, samples fine pore structure can be evaluated. As pressure increases, the gas condenses first in the pores with the smallest dimensions. The pressure is increased until saturation is reached, at which time all pores are filled with liquid. The adsorptive gas pressure then is reduced incrementally, evaporating the condensed gas from the system. Evaluation of the adsorption and desorption branches of these isotherms and the hysteresis between them reveals information about the size, volume, and area of pores. The BJH (Barrett, Joyner, and Halenda) or the DH (Dollimore and Heal) methods are typical procedure for calculating pore size distributions from experimental

isotherms using the Kelvin model of pore filling. It applies only to the mesopore and small macropore size range.

7.2.9 Zeta Potential measurements

The zeta potential (ζ) is an important physicochemical parameter that provides indirect information about the surface charge of particles and the electrostatic stability of colloidal systems. The concept, first introduced by Smoluchowski in 1903, describes the potential difference between the dispersion medium and the layer of liquid attached to the particle surface. In liquid media, charged particles are surrounded by an electrical double layer (EDL), formed by the attraction of counterions from the solution toward the charged surface. The EDL consists of two regions: (i) the Stern layer, where ions are tightly bound to the surface, and (ii) the diffuse layer, where ions are more loosely associated and extend into the bulk solution. The boundary between these two regions is known as the shear plane, and the electric potential at this point corresponds to the zeta potential. The magnitude and sign of the ζ-potential are influenced by several factors, including pH, ionic strength, temperature, and the chemical composition of the surface. High absolute ζ-potential values (above ±30 mV) indicate strong electrostatic repulsion between particles, resulting in stable dispersions, while values close to zero indicate weak repulsion and a tendency toward aggregation.

Since the zeta potential cannot be measured directly, it is determined through electrophoretic mobility measurements, which evaluate the velocity of charged particles under an applied electric field. The relationship between electrophoretic mobility (μ_e) and ζ-potential is given by Henry's equation, which accounts for the dielectric constant and viscosity of the medium as well as the thickness of the electrical double layer.

7.2.10 1H NMR

Nuclear Magnetic Resonance (NMR) spectroscopy is an analytical method used to determine the molecular structure of organic compounds by studying how atomic nuclei interact with an external magnetic field. Among all NMR-active nuclei, the proton (^1H) is the most commonly studied because of its high natural abundance and sensitivity.

Certain atomic nuclei possess a property called spin, which gives them a magnetic moment. When placed in a strong magnetic field (B_0), these nuclei can align either with or against the field, producing two energy levels. The difference between these levels (ΔE) is small but measurable. When radiofrequency radiation of the correct frequency is applied, nuclei absorb energy and change their spin orientation a process known as resonance. The specific frequency at which this occurs depends on the strength of the magnetic field and the nucleus being observed.

The chemical environment around each hydrogen atom affects its resonance frequency. Electrons surrounding the nucleus create small magnetic fields that oppose the external field, a phenomenon called shielding. Protons with high electron density are more shielded and resonate at lower frequencies (upfield), while those near electronegative atoms or π-systems are deshielded and resonate at higher frequencies (downfield). These variations are expressed as chemical shifts (δ), measured in parts per million (ppm) relative to the standard reference compound tetramethyl silane (TMS), set at 0.00 ppm.

Three main factors influence chemical shift: electronegativity, hybridization and magnetic anisotropy.

In a typical ^{1}H NMR spectrum, each signal corresponds to a distinct set of equivalent hydrogens. The area under each peak (integration) is proportional to the number of protons of that type.

Overall, ^{1}H NMR spectroscopy combines magnetic and quantum principles to provide detailed insight into molecular identity and structure.

References

[1] R. Fiorenza, S.A. Balsamo, M. Condorelli, L. D'Urso, G. Compagnini, S. Scirè, Solar photocatalytic H_2 production over CeO_2-based catalysts: Influence of chemical and structural modifications, Catalysis Today. 380 (2021) 187–198. https://doi.org/10.1016/j.cattod.2021.02.003.

[2] M.T.A. Iapichino, R. Fiorenza, V. Patamia, G. Floresta, A. Gulino, M. Condorelli, G. Impellizzeri, G. Compagnini, S. Sciré, H_2 production by solar photoreforming of plastic materials using SiC-g-C_3N_4composites, Catalysis Communications. 187 (2024) 106850. https://doi.org/10.1016/j.catcom.2024.106850.

[3] M.J. Sampaio, J.W.L. Oliveira, C.I.L. Sombrio, D.L. Baptista, S.R. Teixeira, S.A.C. Carabineiro, C.G. Silva, J.L. Faria, Photocatalytic performance of Au/ZnO nanocatalysts for hydrogen production from ethanol, Applied Catalysis A: General. 518 (2016) 198–205. https://doi.org/10.1016/j.apcata.2015.10.013.

CHAPTER VIII: H_2 production

CHAPTER VIII: H_2 Production

8. H_2 Production by solar photoreforming of plastic materials using SiC-g-C_3N_4 composites[7]

8.1 Introduction

The photoreforming of polyethylene terephthalate and bisphenol A was here investigated using uncommon photocatalysts (SiC-g-C_3N_4 composites). The results showed as the addition of small amounts of g-C_3N_4 on SiC promoted an efficient charge carriers separation and a good interaction between the two materials, leading to a H_2 production rate of 18 and 12 $\mu molH_2/g_{cat}\cdot h$ for the photoreforming of polyethylene terephthalate and bisphenol A, respectively. The accurate selection of different g-C_3N_4 precursors, combined with the appropriate control of the key reaction parameters (pH and plastic materials pretreatments) allowed to optimize the performance of the SiC-g-C_3N_4 composites for the photocatalytic H_2 production.

[7] Most of the data present in this chapter are published in:
"H_2 production by solar photoreforming of plastic materials using SiC-g-C_3N_4composites"
M. T. Armeli Iapichino, R.Fiorenza, V.Patamia, G.Floresta, A.Gulino, M. Condorell, G.Impellizzeri, G.Compagnini, S.Scirè Catalysis Communications V.187, February 2024, 106850

8.2 Material preparation

The SiC-g-C_3N_4 composites were prepared mixing the commercial silicon carbide powder (Sigma Aldrich, 400 mesh, MKCN0364 357391, β-SiC) with diverse amounts of urea (Fluka, BioChemika ≥ 99.5%) to obtain different composites with various weight percentages of carbon nitride. Indeed, one of the easy and green reported methodology for the preparation of the g-C_3N_4 is the urea thermodegradation [1]. Specifically, the SiC and the urea powders were put in a covered alumina crucible and heated in a muffle at 450°C with a ramp of 5°C/min for 5 hours. For the photocatalytic comparison also the bare SiC was treated under the same thermal conditions of the SiC-g-C_3N_4 composites (Fig.1).

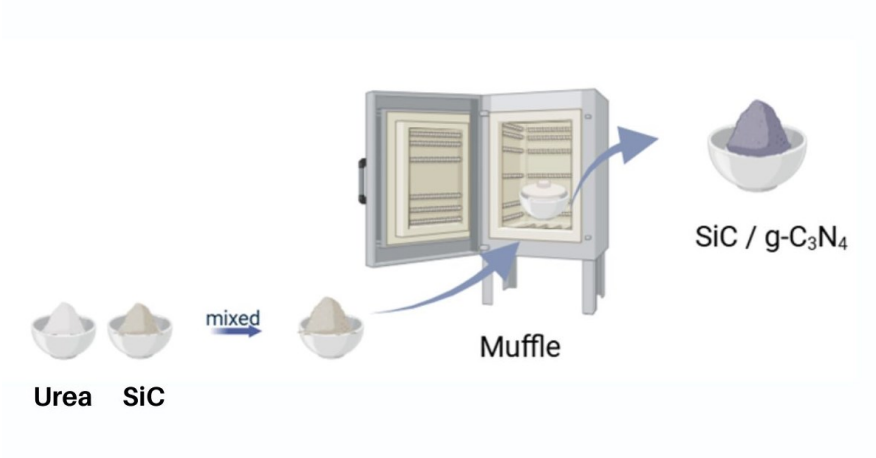

Figure 1 *Photocatalysts preparation.*

8.2 Sacrificial agents pre-treatments

BPA (Sigma Aldrich 98%) and PET (from a commercial bottle) were pre-treated in order to obtain a solution of the sacrificial agent[2]. 50 mg of BPA were solubilized in a 10 M NaOH solution, whereas 50 mg of PET (the PET bottle was previously crushed and transformed in powders of 140-70 mesh) were solubilized in 10 M NaOH solution kept under stirring for 6 days at 40°C (Fig.2).

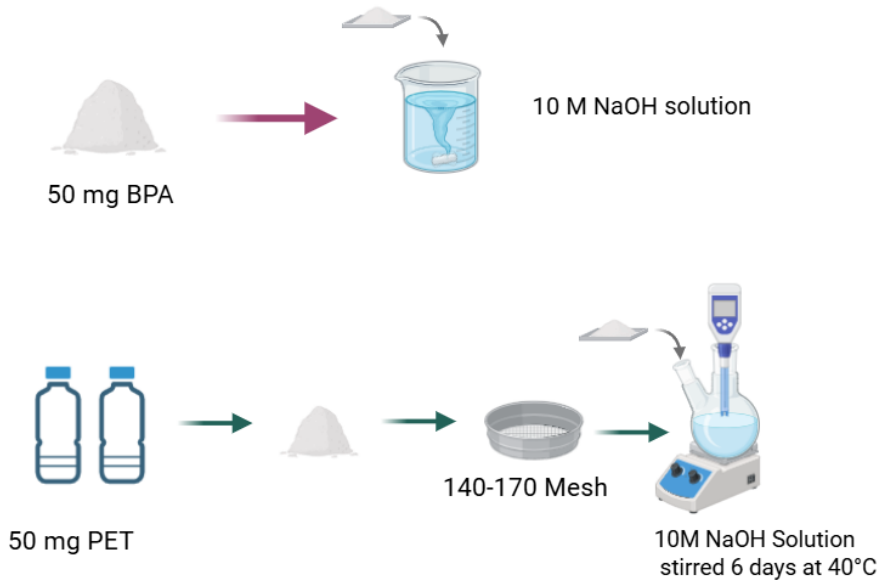

Figure 2 *Pre-treatment plastics sacrificial agents.*

8.3 Experimental Set-up

The measurements conducted in this study were performed using the experimental apparatus described in Section 7.1, under identical conditions. The byproducts detection of the BPA and PET photoreforming was performed by ^{1}H-NMR. The ^{1}H -NMR spectra were recorded at 300 K on a Varian UNITY Inova using D_2O as the solvent at 500 MHz. 128 scans were performed for each sample. The water signal suppression was obtained by applying the PRESAT (WATER) pulse sequence, and the ^{1}H-NMR (PRESAT) optimized acquisition parameters were as follows: relaxation delay (1 s), 128 scans and spectral width from 0 to 11 ppm[3].

8.4 Solar photoreforming of BPA

The Figure 3 illustrates the H_2 production rate obtained by the solar photoreforming of BPA. In these tests the influence of the addition of different amounts of SiC to g-C_3N_4 and the photocatalytic activity both of SiC-g-C_3N_4 and g-C_3N_4-SiC composites were evaluated.

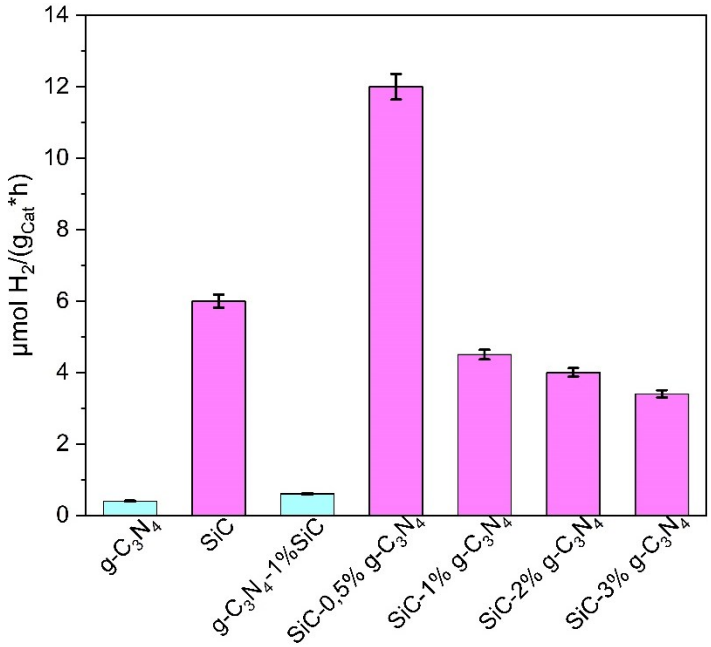

Figure 3 *H_2 production rates for the SiC and the g-C_3N_4-based samples.*

From the reported data it is clear as the SiC-based samples gave the best H_2 production rate whereas the inverse g-C_3N_4-based composites (g-C_3N_4-SiC) gave a negligible evolution of H_2. In accordance with the literature, indeed, due to the high charge carriers recombination of carbon nitride, the photocatalytic features were better exploited when g-C_3N_4 is used as co-catalyst or as minor component of a composite and not as the main one[4,5]. The addition of small amount of g-C_3N_4 increased the production of H_2 from 6 µmol/g_{cat}·h of the bare SiC to 12 µmol/g_{cat}·h

of the SiC-0.5%g-C_3N_4 composite. It is important to highlight that the SiC sample underwent the same thermal treatment of the SiC-based composites, i.e., calcination at 450°C for 5 h, and that the untreated SiC sample (as purchased) gave a slight lower H_2 production (5 μmol/g_{cat}·h, data not showed). A higher amount of carbon nitride on SiC had a detrimental effect with a lower H_2 production, probably because an excess of carbon nitride led to the coverage of the surface-active sites of SiC. The pretreatments of BPA (50 mg solubilized in NaOH 10M) led to a highly basic pH (13) of the reactant solution. Consequently, the influence of the pH on the photocatalytic activity was investigated using the best photocatalyst (SiC-0.5%g-C_3N_4) and the results are reported in the Figure 4A. Interestingly, basic pH (pH = 13) is necessary to both guarantee a good H_2 production with an efficient BPA solubilization/photo-oxidation. Indeed, if the test was carried out at pH= 7 (through neutralization of the BPA basic solution with a solution of HNO_3 10M) the H_2 production rate drastically decreased up to 1 μmol/g_{cat}·h, whereas acidic conditions (50 mg of BPA solubilized in a solution of HNO_3 10M) unfavoured the H_2 evolution. Probably the presence of a high number of OH^- species in the basic environment boosted up the BPA photo-oxidation with a consequent increase of the H_2 production.

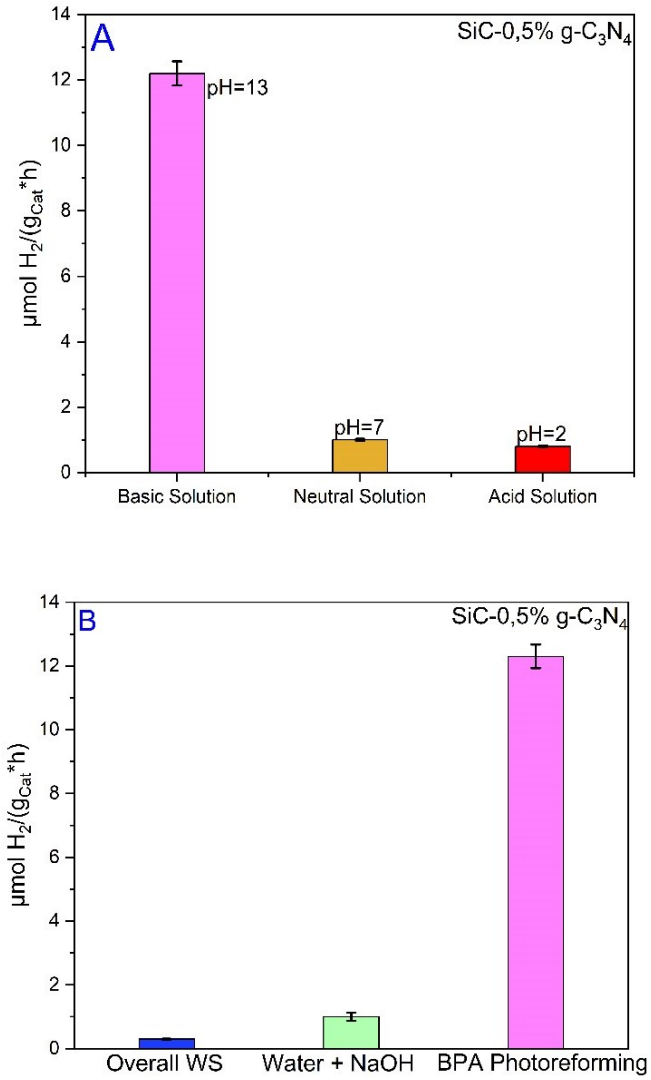

Figure 4 *(A) Influence of the pH on the BPA photoreforming using the SiC-0,5% g-C_3N_4 sample, (B) comparison among the H_2 production rates of the overall water splitting, the water splitting + NaOH and the BPA photoreforming.*

In this contest Fig. 4B compares the H_2 production rates obtained with the SiC-0.5%g-C_3N_4 composite in the overall water splitting test (i.e., without addition of BPA, pure demineralized water, pH = 7) and in water + NaOH solution (40 ml of water + 10 ml of NaOH 10 M, pH= 13). The overall water splitting did not allow to obtain significant H_2 amount, pointing to as the presence of a sacrificial

agent, as the BPA, is necessary for the H_2 formation. The H_2 production rate of the solution containing only water and NaOH solution was also low (1 μmol/g_{cat}·h), thus suggesting that the OH^- ions gave a substantial contribution to the H_2 evolution only with the contextual presence of BPA. Indeed, the hydroxyl species can improve the photo-oxidation of BPA, that acting as holes scavenger, allowed to increase the e^-/h^+ separation on the SiC-0.5%g-C_3N_4 composite[6]. As a result, the solar H_2 evolution increased in the BPA photoreforming test up to 12 μmol/g_{cat}·h.

To get more insight into the mechanism of the BPA photo-oxidation, ^{1}H-NMR spectra were carried out before and after the photoreforming reaction using the SiC-0.5%g-C_3N_4 composite (Fig. 5). Before the reaction it is possible to note the signals related to the aliphatic CH_3 (0.8 ppm) and aromatic protons of BPA (5.78 and 6.29 ppm). After the photoreforming the disappearance of these signals was verified and, in accordance with the literature, the formation of small molecules such as acetaldehyde hydrate (signals at 2.21 and 6.21 ppm) was observed[7]. These small molecules were more reactive towards the photoreforming, allowing to increase the H_2 evolution[8].

In summary, with the best composite (SiC-0.5%g-C_3N_4) and at basic pH, a good BPA photocatalytic degradation was guaranteed with the formation of small organic compounds that boosted the H_2 formation by the contextual photoreforming of both BPA and these intermediate products.

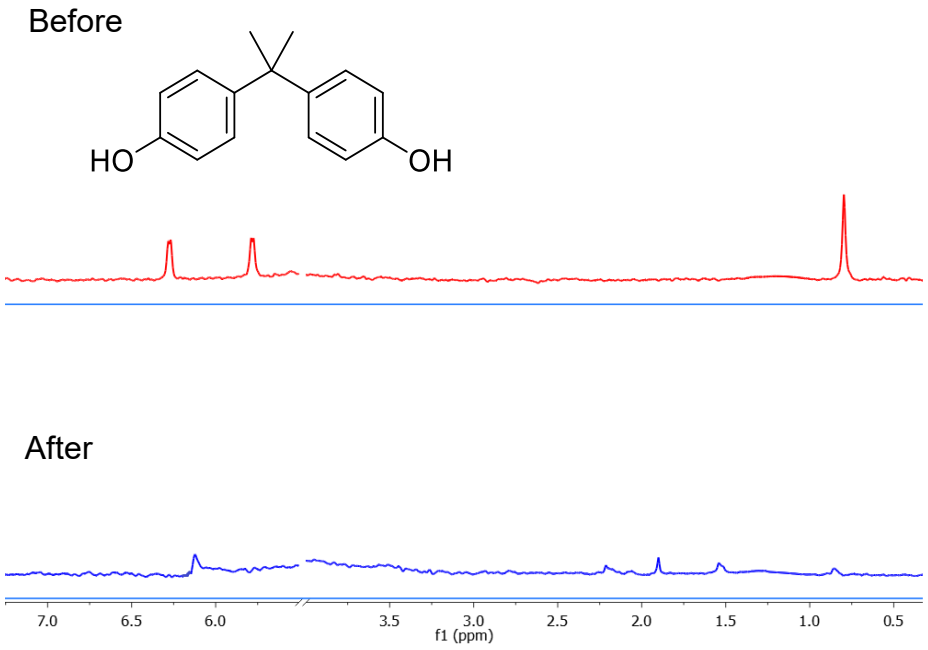

Figure 5 *^{1}H NMR spectra carried out before and after the BPA photoreforming using the SiC-0.5%g-C_3N_4 composite.*

8.5 Solar photoreforming of PET

Figure 6 depicts the comparison among the various investigated samples in the photoreforming of PET and BPA. It is possible to note as the PET photoreforming allowed to obtain a higher H_2 production rate compared to the BPA, with the best composite, in this case the SiC-1%g-C_3N_4, that led to 18 μmolH_2/g_{cat}·h after 5 h of solar PET photoreforming. Due to the employed PET pretreatment also in this case the pH of the reaction mixture was 13. It is important to highlight that a lower amount of 0.5 wt% of g-C_3N_4 was not sufficient to establish a good interaction with SiC, being the H_2 production similar or only slightly higher compared to the bare SiC for both BPA and PET photoreforming.

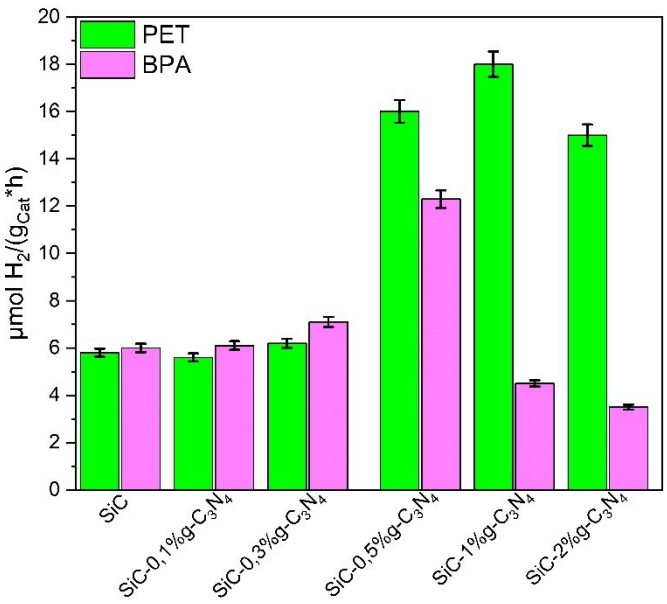

Figure 6 *H_2 production rates of the photoreforming of PET and BPA using the SiC-g-C_3N_4-based samples.*

As reported in the literature [9] the higher H_2 evolution of PET photoreforming compared to the BPA can be related to the byproducts formed during the reaction. Indeed, the ethylene glycol (EG) was the main intermediate formed during the PET photoreforming and its formation was favoured by the hydrolysis under basic conditions[10].The formation of EG was beneficial for the H_2 production by photoreforming due to its tendency to fully decompose into H_2 and CO_2 under mild condition and UV/solar irradiation in the presence of several photocatalysts[11]. The formation of EG was verified by ^{1}H-NMR using the SiC-1% g-C_3N_4 sample (Fig.7). The spectrum of the pre-treated PET before the photoreforming showed signals related to ethylene glycol (2.92 ppm) and terephthalate (7.30 ppm). After the reaction it is possible to note the complete disappearance of these signals and the formation of new peaks attributable to different degradation products such as formate (7.74 ppm) or small carboxylic acids (3.50 ppm)[12].

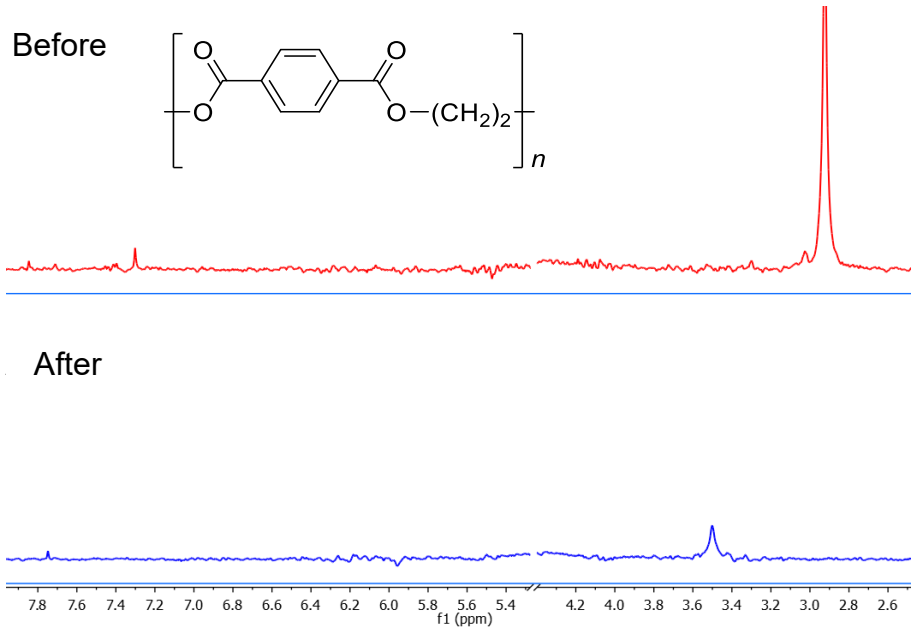

Figure 7 *^{1}H NMR spectra carried out before and after the PET photoreforming using the SiC-1%g-C_3N_4 composite.*

Being the PET photoreforming more efficient than the BPA photoreforming, we tested the influence of the different carbon nitride precursors (urea, thiourea and melamine) to obtain the SiC-g-C_3N_4 photocatalysts (Fig.8). Although in the literature the melamine was the most used precursors for the synthesis of the g-C_3N_4-based materials [13–15], in our experimental conditions, the use of urea led to the best interaction of the formed carbon nitride and the SiC. Consequently, the SiC-g-C_3N_4 samples prepared using urea as carbon nitride precursor gave the best performance in the PET photoreforming. Probably, in the case of thiourea, the formation of sulphur-based impurities during the thermodegradation process affected the photoactivity of the composite[16], whereas in the case of melamine the eventual presence of contaminants or a not complete amine groups

condensation[17] significantly affect the performance of the SiC-based composites. Indeed, the H_2 production rates of the SiC based photocatalysts prepared using melamine were lower compared also to the bare SiC (Fig.8), whereas the samples synthetized from thiourea gave worse results compared to the same ones prepared with urea. It is important to note that on the basis of the literature data, to favour the carbon nitride precursors thermodegradation, the composites synthesized starting from thiourea were treated at 500°C for 5 h (heating ramp of 5°C/min), whereas the samples prepared from melamine at 550°C for 5 h with the same heating ramp[18,19]. These higher thermal treatments compared to the procedures used for the composites prepared starting from urea (heated at 450°C for 5h with a ramp of 5°C/min) can induce the agglomeration of the SiC particles, modifying its structural properties and then the interaction with the in-situ formed g-C_3N_4. As consequence, the H_2 production of the composites synthesized from thiourea and melamine was lower compared to that of analogous samples prepared with urea as g-C_3N_4 precursor. Furthermore, it was recently demonstrated that the use of urea allowed to obtain the ideal C/N molar ratio (0.75) with smaller thickness of the g-C_3N_4 sheets compared to other precursors[17,20,21].

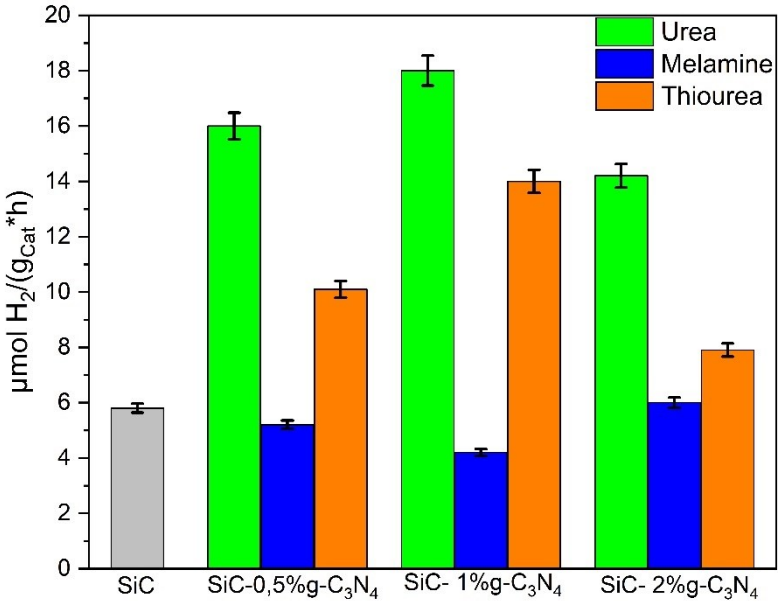

Figure 8 *H_2 production rates for the PET photoreforming using several SiC-g-C_3N_4-based composites prepared with different carbon nitride precursors.*

The influence of the pH was also investigated in the PET photoreforming on the best composite (in this case the SiC-1%g-C_3N_4 prepared from urea), and the results are shown in Fig. 9A. Similarly, to the BPA photoreforming, strong basic pH was fundamental to both guarantee good H_2 production and PET solubilization/photo-oxidation, whereas the neutralization with 10 M HNO_3 solution or acidic conditions (PET pretreatment in a 10 M HNO_3 solution) led to a drastic decrease of the photoactivity of the SiC-1%g-C_3N_4 composite.

Considering also the results obtained in the BPA photoreforming, these data pointed to the importance of the basic environment for the surface charge of the SiC-based samples and the corresponding adsorption of the reaction mixture. In this contest, the Zeta potential on the SiC-1%g-C_3N_4 photocatalyst was measured (Fig. 9B). The sample showed a negative surface

charge independently of the pH. However, at the best condition for both the BPA and PET photoreforming (pH=13) the potential had an intermediate negative value (-46 mV) compared to neutral pH (the most negative value, -63 mV) and to acidic pH (the least negative value, -24 mV at pH= 2). Reasonably, strong basic pH favours a balance between different factors, as the BPA and the PET degradation favoured by the formation of the ideal amount of OH^- ions, that allowed also an efficient interaction between the generated H^+ and the surface negative charge of the SiC-1%g-C_3N_4 photocatalyst. Indeed, it is worth to note that, from a preliminary photocatalytic screening (data not shown), using a more diluted NaOH solution (pH < 13) a strong drop down of the photocatalyst performance was verified with negligible H_2 formation, confirming the importance of a strong basic environment both for PET and BPA photoreforming.

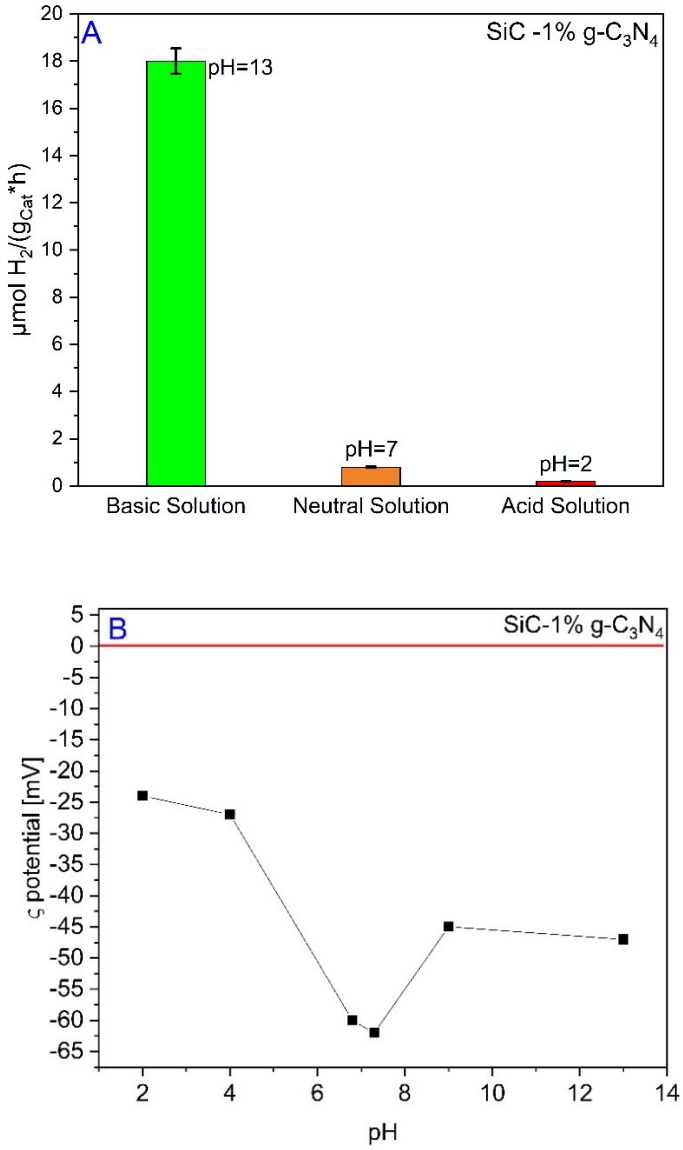

Figure 9 *(A) Influence of the pH on the PET photoreforming using the SiC -1% g-C_3N_4 sample, (B) Z-potential of the SiC 1% g-C_3N_4 composite.*

8.6 Correlation between the photocatalytic activity and the composites characterization

The optical properties of the samples were determined by UV-DRS (Fig. 10) and PL spectroscopies (Fig.11).

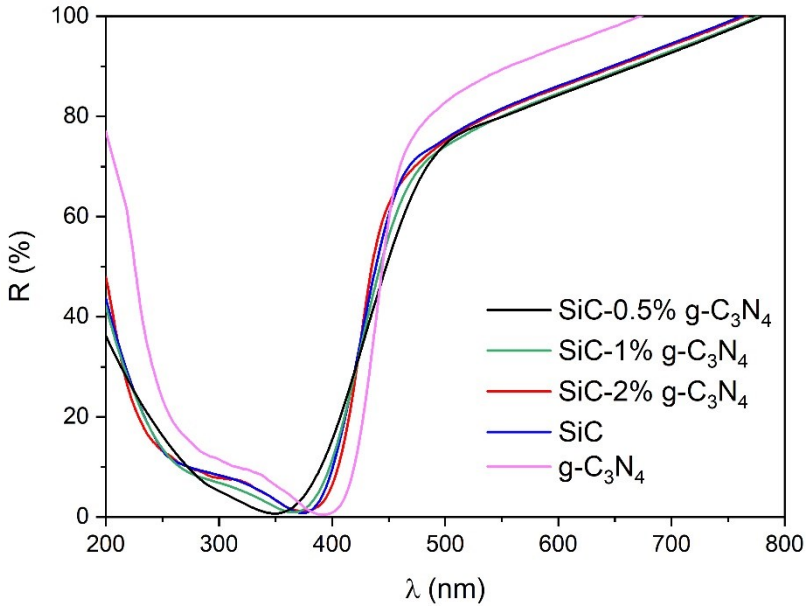

Figure 10 *UV-DRS spectra of the SiC-g-C_3N_4-based samples.*

The estimation of the optical band gap (E_g) was carried out by the modified Kubelka-Munk function [22] and the results are reported in the Table 1, together with the textural properties measured by the N_2-adsorption-desorption measurements

Table 1 *Optical and textural properties of the examined samples*.

Sample	E_g (eV)	S_{BET} (m^2g^{-1})	$P_{diameter}$ (nm)	$V_{diameter}$ (cm^3g^{-1})
g-C_3N_4	2.85	66.8	8.9	0.24
SiC	2.96	17.4	18.6	0.45
SiC 0,5% g-C_3N_4	2.94	17.9	18.4	0.44
SiC 1% g-C_3N_4	2.95	20.5	17.4	0.43
SiC 2% g-C_3N_4	2.95	20.8	15.9	0.39

There are no substantial variations in the E_g values of the SiC-based composites that exhibited a slightly higher E_g compared to the bare g-C_3N_4. The BET surface area values were in accordance with the literature data concerning the as-purchased SiC (in the β form) and the bare g-C_3N_4 prepared from urea[23,24].The addition of a growing amount of carbon nitride on SiC led to a slight increase of the surface area (from 17 m^2/g of the bare SiC to 23 m^2/g of the SiC 2% g-C_3N_4) with a consequent decrease of the mean pores diameter and the pores volume (Tab.1). However, these slight variations did not affect significantly the photocatalytic performance in the examined photoreforming reactions, being the composites with low amounts of g-C_3N_4 the most active ones (SiC 0,5% g-C_3N_4 for the BPA photoreforming, SiC 1% g-C_3N_4 for the PET photoreforming).

The PL spectroscopy was carried out to elucidate the possible electron transfer and the separation efficiency of the photogenerated charge carriers in the as-prepared samples[25,26]. Generally, a relatively weak PL bands intensity is correlated to a low recombination rate in the semiconductors [27].

From the Fig.11 it is possible to note that all samples showed two bands centred at about 487 and 542 nm, usually associated to the excitation/recombination phenomena of the charge carriers of SiC-based materials [28]. The addition of carbon nitride to SiC caused a strong decrease of the PL bands intensity, mainly for the SiC 0.5% g-C_3N_4, and the SiC 1% g-C_3N_4 composites, suggesting that an efficient charge carriers separation occurred on the SiC-low amount of g-C_3N_4 heterostructures[29].

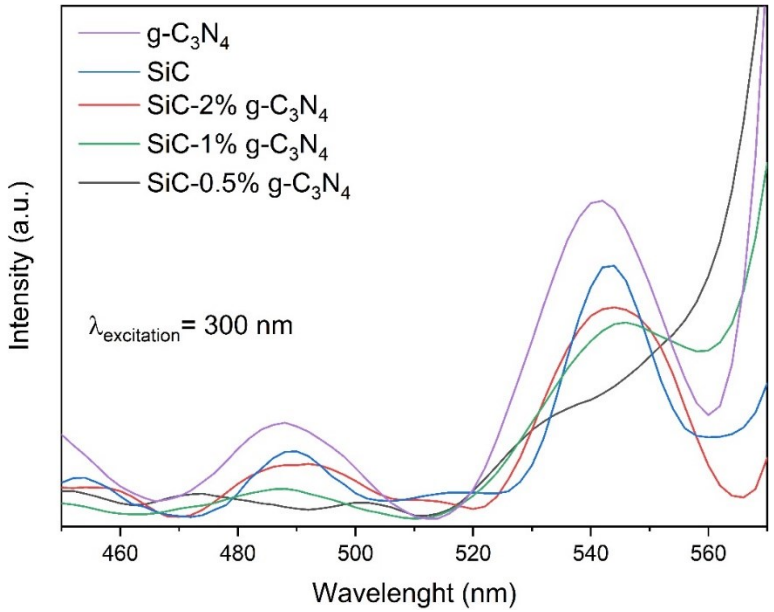

Figure 11 *Photoluminescence spectra of the analysed composites.*

The crystallinity of the as-prepared samples was investigated by XRD (Fig.12). From the XRD patterns it was possible to note that the diffraction peaks of the synthesized C_3N_4, at 2θ=12.9° and 27.4°, correspond to the crystalline planes (1 0 0) and (0 0 2) respectively, associated to the tetragonal C_3N_4 in the graphitic form [30]. The SiC-based samples showed diffraction peaks at 2θ= 37°, 42°, 61.3°, 67° corresponding to the cubic 3C-SiC (β-SiC)

structure and the crystalline planes (1 1 1), (2 0 0), (2 2 0), and (3 1 1) respectively[30]. The peaks in the range 2θ= 33-35° were associated to the spontaneous packing fault related to the SiC growth[29]. In the SiC-based samples the peaks related to the carbon nitride are not present probably due to the low amount of g-C_3N_4.

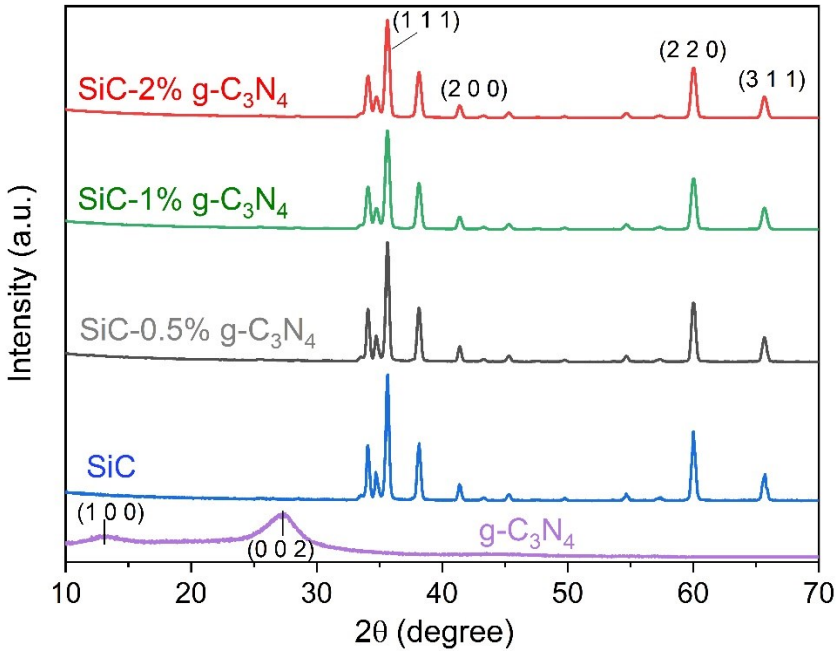

Figure 12 *XRD patterns of the examined samples.*

Furthermore, comparing the TEM images of the bare SiC (Fig.13) and of SiC 1% g-C_3N_4 (chosen at representative sample being the best one for the PET photoreforming, Figs. 14-15) it is possible to verify the interaction between the SiC particles and the g-C_3N_4 sheets.

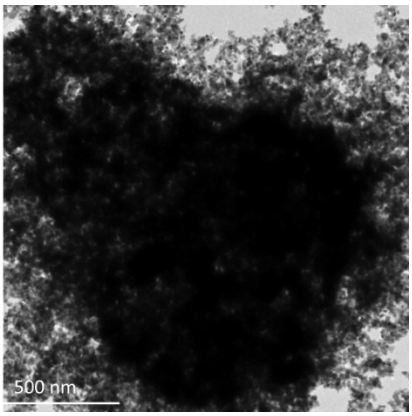

Figure 13 *TEM images of the bare SiC.*

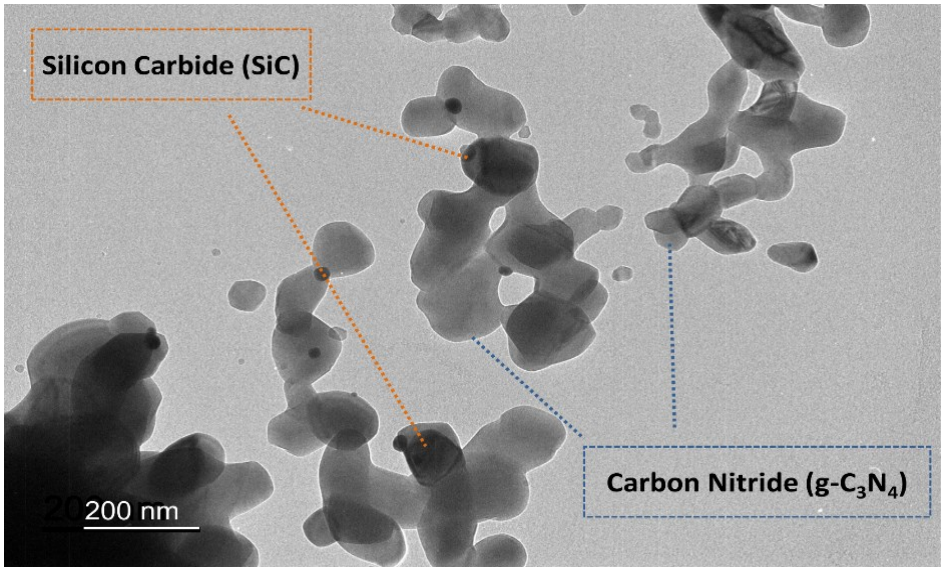

Figure 14 *TEM images of SiC 1% g-C_3N_4.*

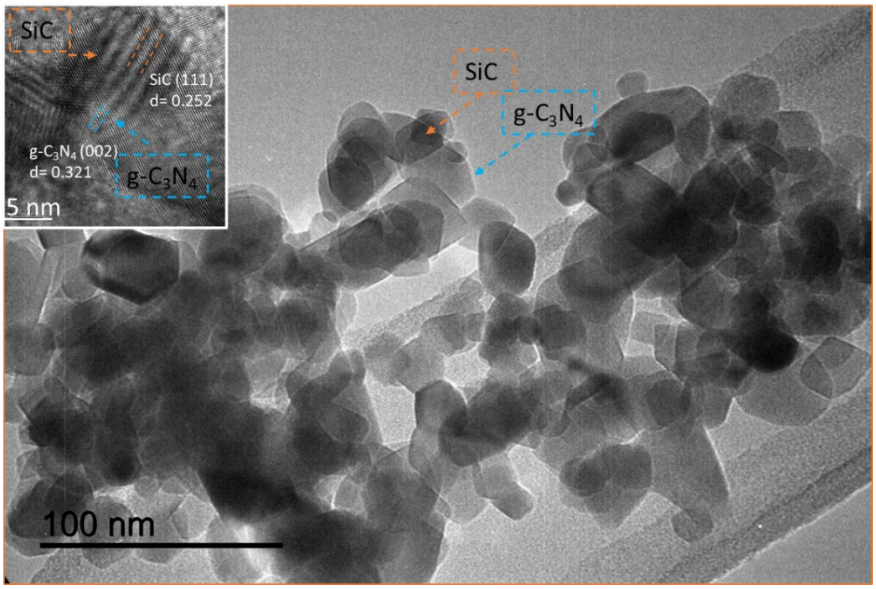

Figure 15 *HR-TEM of the same SiC 1% g-C_3N_4.*

In the Fig.13 it is possible to note the agglomerated SiC particles (dark part) formed due to the employed thermal treatment (calcination at 450°C for 5 h). In the Fig.14 the darker parts (indicated with the orange arrows) show the SiC particles, whereas the g-C_3N_4 sheets where indicate by the blue arrows (the clearest parts) in accordance with the literature data [31,32]. In the Fig.15 it is illustrated the HR-TEM of the same SiC 1% g-C_3N_4 composite at two different magnifications (see inset). It is confirmed the interaction between the agglomerated SiC particles and the g-C_3N_4 sheets, as reported for similar composites [3-6]. The measured interplanar crystal spacing distances are close to the (002) and (111) lattice planes of g-C_3N_4 and SiC respectively, in accordance with the main crystal plans of the two materials detected by XRD.

The surface properties of the as-prepared samples were characterized by XPS (Fig.16). Figure 16A shows the high-resolution XP spectrum of the SiC 1% g-C_3N_4 sample (as representative sample) in the C 1s binding energy region. Two evident signals appear at 282.5 and 285.0 eV due to the carbide states and to the adventitious surface carbon, omnipresent on air thermally-threated materials, respectively[33,34]. In the Si 2p binding energy region (Fig. 16B), the two bands at 100.4 and 103.2 eV are due to the Si states of the carbide and to some SiO_x species [33,34], whose formation was also confirmed by the XP spectrum in the O 1s binding energy region (Fig. 16C), with the unique peak at 532.4 eV, in agreement with the presence of SiO_x species[35]. The same signals are present in all SiC-based materials, including the bare SiC (Figs. 17).

Fig. 18A shows the high-resolution XP spectrum of the bare g-C_3N_4 in the C 1s binding energy region. The two evident signals at 288.2 and 284.7 eV are due to the carbon C-N states of the C_3N_4 and to the adventitious carbon, respectively[36]. Figure 18B shows the high-resolution XP spectrum of the carbon nitride in the N1s binding energy region. A strong signal appears at 398.6 eV with a shoulder at higher binding energy (about 401 eV) and even a very low, but sizeable, band at 404.1 eV. The first signal is due to the expected C=N-C and C_3-N states of the g-C_3N_4 while the B.E. value of the shoulder is compatible with the nitrogen of NH_2-C=O and/or positive N^+ states[36,37]. Finally, the small band at 404.1 eV is due to some negligible nitrite/nitrate [38]. The signal at 398.6 eV of the carbon nitride is present (with low intensity, due to the

low amount added to the SiC) also in the SiC 1% g-C_3N_4 sample (Fig. 16D) and in all SiC-based composites.

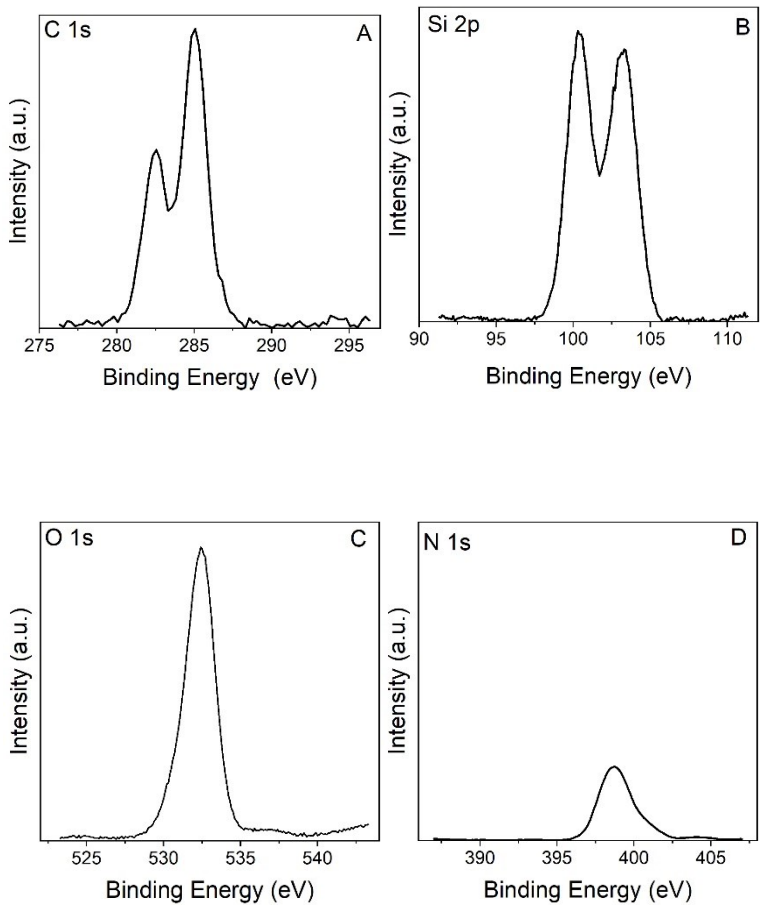

Figure 16 *Al Kα excited XPS of the SiC-1%g-C_3N_4 sample in the (A) C 1s (B) Si 2p, (C) O 1s and (D) N 1s binding energy regions.*

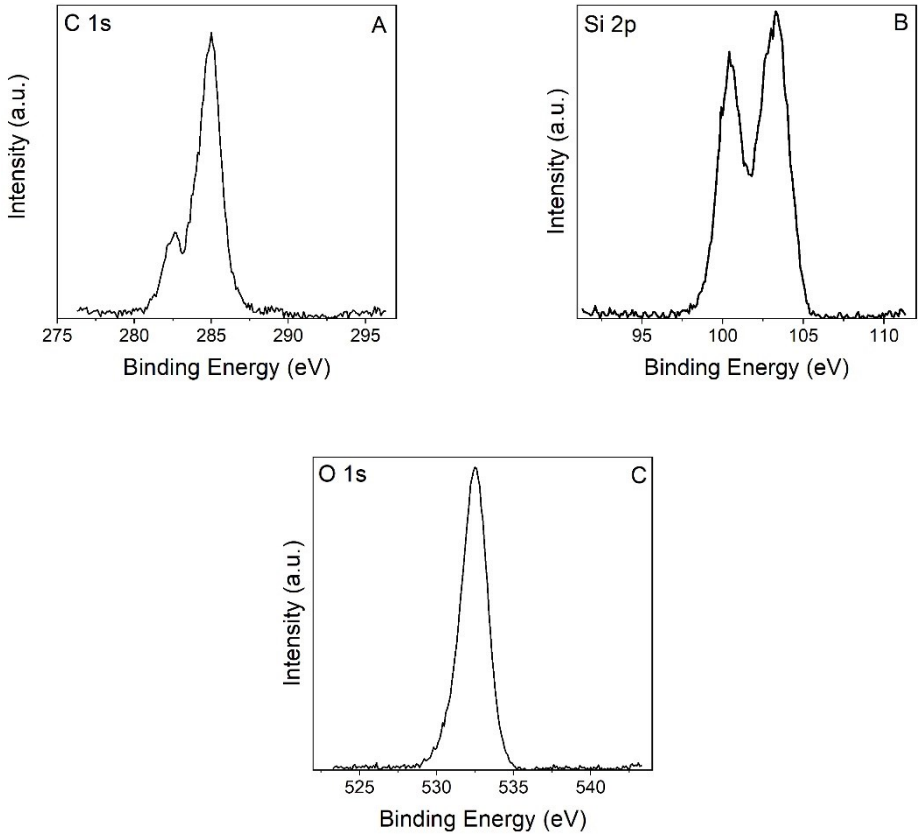

Figure 17 *Al Kα excited XPS of the bare SiC sample in the (A) C 1s (B) Si 2p, and (C) O 1s binding energy regions.*

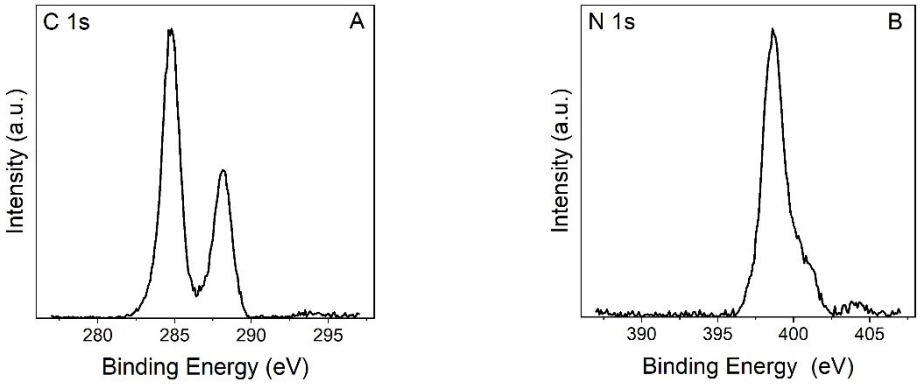

Figure 18 *Al Kα excited XPS of g-C_3N_4 sample in the (A) C 1s and (B) N 1s binding energy regions.*

8.7 Discussion

In summary, the SiC-g-C_3N_4 composites are promising photocatalysts that allowed to obtain H_2 from plastic-related materials. The presence of SiC is fundamental, due to its chemical stability under the extreme basic conditions of the photoreforming reactions, whereas the addition of small amounts of graphitic carbon nitride allowed to increase the charge carriers separation, as confirmed by the PL spectroscopy. The good interaction between the two components of the composites increased the H_2 evolution compared to the bare SiC and g-C_3N_4 samples. In accordance with the literature[29,30,39], this interaction is basically established by van der Waals interfaces formed during the synthesis of the SiC-g-C_3N_4 composite, where the SiC particles were strewn on the as-formed g-C_3N_4 sheets, as verified by TEM (Fig. 14).

Only a low content of carbon nitride (0.5 or 1 wt%) allowed to increase the performance of the bare SiC. Noteworthy, no substantial variations were detected in the optical band gap of the SiC-g-C_3N_4 composites compared to the bare SiC (2.94-2.96 eV, Table 1). On the basis of these data, bearing in mind the reported bands position of SiC and g-C_3N_4 [29,40] and considering that the samples were prepared with simple physical mixture of commercial SiC powders with urea (precursor of carbon nitride), followed by a thermal treatment, a scheme of the proposed photocatalytic mechanism is shown in the Fig.19. The SiC particles were deposited on g-C_3N_4 sheets enabling a good interaction between them. Upon solar irradiation, both SiC and g-C_3N_4 were excited and thus electrons (e^-) and holes (h^+) were

formed in the conduction (CB) and valence bands (VB) of the two materials, respectively. The electrons moved from the CB of g-C_3N_4 to that of SiC and holes migrated from the VB of SiC to that of g-C_3N_4, promoting a good charge carriers separation. In this way, the holes were able to oxidize water to H^+ and to hydroxyl radicals. These latter species were able to degrade the plastic materials with the formation of byproducts that can promote further photoreforming reactions. The generated H^+ species were reduced by the electrons gathered at the CB of SiC, allowing the H_2 evolution.

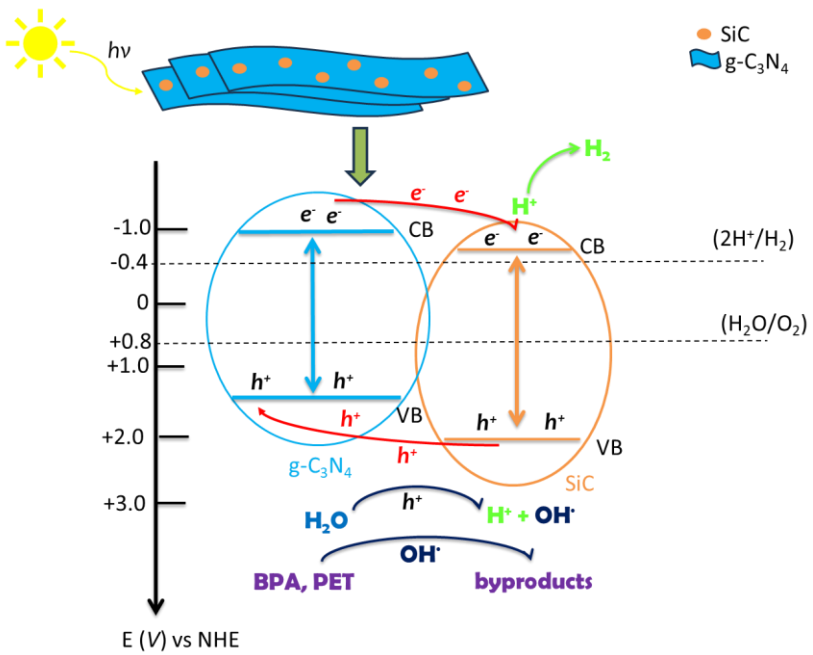

Figure 19 *Schematic illustration of the proposed photocatalytic mechanism.*

The photoreforming of PET led to higher H_2 production rate compared to the bare BPA and this was ascribed to the pretreatment conditions. Indeed, the strong basic environment

favoured, in the case of PET, its hydrolysis with the formation of ethylene glycol (as verified by ^{1}H-NMR) which further undergoes photoreforming thus promoting the H_2 formation. On the contrary the BPA photo-degradation was more difficult with a lower hydrogen production. The pH of the reaction was another key parameter, being pH=13 the best compromise for the optimal interaction among the reactants and the negative charged surface of SiC (Fig. 5B). This pH was also the ideal one for the BPA and PET pretreatments, in accordance with the literature data [41,42]. Neutral, acidic, or less basic solutions (pH < 13) did not allow to obtain sufficient H_2 production both for PET and BPA photoreforming.

Although it is not easy to carry out an accurate comparison with the literature data, due to the different experimental set-ups employed by the various research groups and due to the novelty of the plastic photorefoming reaction, it is noteworthy that the here reported performance of the SiC-1%g-C_3N_4 composite in the simulated solar light driven-PET photoreforming (18 $\mu molH_2/g_{cat}\cdot h$) was better than that of some TiO_2-based samples or carbon nitride porous microtube (CN_xPM) photocatalysts (Table 2), but worse with respect to CN_x-Ni2P or $Cd_{0.5}$ $Zn_{0.5}S$ samples (Table 2).

Samples	*PET pretreatment*	*Irradiation source*	*H_2 production* (μmolH2/gcat · h)	*Ref.*
SiC 1 wt% g-C_3N_4	NaOH solution 10 M at 40° C	solar lamp 10.7 mW/cm^2	18.1	this work
TiO_2 5 wt% Au	KOH solution 10 M at 40° C	high pressure UV mercury vapor lamp 60 mW/cm^2	3.0	[43]
TiO_2-Ni2P	KOH solution 10 M at 40° C	simulated solar light, AM 1.5G	13.8	[11]
CN_xPM	/	300 W Xenon arc lamp equipped with a cut-off filter (λ> 420 nm)	9.4 33.1	[65]
CN_x-Ni2P	KOH solution 10 M at 40° C	simulated solar light AM 1.5G, 100 mW/cm^2	33.1	[11]
$Cd_{0.5}$ $Zn_{0.5}$S	NaOH solution 10 M at 35°C	300 W xenon lamp with a cut-off filter (λ > 420 nm)	74.4	[66]

Table 2 *Comparison among different photocatalysts employed for the PET photoreforming*

Reasonably, we expect that the H_2 production can be further improved by tailoring the interaction and therefore the heterostructures between SiC and g-C_3N_4 or by preparing other more efficient photocatalyst composites. This work, however, shows as it is possible to transform an environmental problem, as

the water pollution by plastic materials, into a sustainable opportunity to produce hydrogen and/or high-added value products from pollutants. This is a relevant and recent topic with several fascinating opportunities as the design of the chemical-physical properties of the employed photocatalysts on the basis of the plastic materials used as organic scavengers. A recent review of *Ashraf et al.* [9] examined the performance of various photocatalysts in the photoreforming of other plastic materials as polyethylene (PE), polystyrene (PS), polyvinyl chloride (PVC), polyurethane (PU) and polylactic acid (PLA), discussing also the byproducts selectivity and the pretreatment conditions. Recently, hybrid catalysis, as the photothermo-catalysis, was applied to accelerate the degradation of biodegradable plastics as the PLA with the contextual H_2 production[44], and chemoenzymatic approaches were used to produce H_2 from the reforming of polyester films and nano plastics [45]. This new data and research, combined with the new technologies related to the photocatalytic degradation of plastics [46,47] can help to find more efficient and performing solutions to the plastic waste disposal and upcycling.

8.8 Effect of the SiC dimension on photoreforming

The influence of the SiC particle size for the PR of the PET was also investigated.

As shown before, using the µSiC the H_2 production rate of µSiC-1% wt g-C_3N_4 was 18 µmolH_2/g_{cat}·h, whereas the same composite prepared with the nanometric SiC (nSiC, Sigma Aldrich, <100nm particle size) gave a H_2 production rate of 5 µmolH_2/g_{cat}·h, similar to the unmodified µSiC (5 µmolH_2/g_{cat}·h, Fig. 6). Probably the size of the nanometric SiC is too small to permit an efficient interaction with the g-C_3N_4.Furthermore, the XRD analysis (Fig. 20) of the two types of SiC showed significant differences between the two samples.

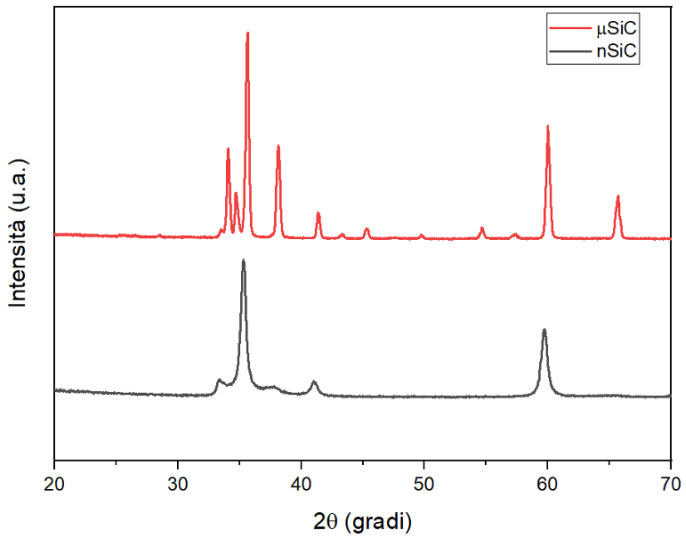

Figure 20 *Comparison XRD of nSiC and µSiC*

In particular, for the nSiC sample (Fig.20), diffraction peaks were observed at 2θ = 37°, 42°and 61.3° always corresponding to the cubic 3C-SiC structure (β-SiC) and the crystal planes (111), (200) and (220) respectively [36]. However, in the case of nSiC, the

peaks are wider and less defined. Probably the nanometric sample has a different distribution of nanoparticles that influenced the crystallinity of the sample and thus its activity.

8.9 Conclusion

The performance of the SiC-g-C_3N_4 composites, prepared with an easy procedure, was investigated in the solar PET and the BPA photoreforming. The addition of small amounts of carbon nitride to SiC resulted in a good SiC/g-C_3N_4 interaction with a negative superficial charge which boosted the H_2 evolution from both reactions. The PET substrate led to the higher H_2 production rate, and this was related to the formation of intermediates (among all ethylene glycol) which further promoted the photoreforming. The strongly basic pH (13) was essential to favour both the plastic materials pretreatment and the interaction between the reactants and the surface of the SiC-g-C_3N_4 composites. Finally, urea was the best carbon nitride precursor for the formation of SiC-g-C_3N_4 composites active for these reactions. The results obtaining in this work pave the way to new photocatalysts for the plastic materials photoreforming, enlarging the future environmental perspectives in which the wastes or the pollutants can be considered new raw materials to obtain H_2 preserving contextually, the water by the emerging contaminants.

References

[1] S. Riaz, S.-J. Park, Carbon quantum dots-embedded graphitic carbon nitride nanotubes for enhancing the power conversion efficiency of sensitized solar cells, Materials Today Chemistry. 24 (2022) 100763. https://doi.org/10.1016/j.mtchem.2021.100763.

[2] Y. Li, S. Wan, C. Lin, Y. Gao, Y. Lu, L. Wang, K. Zhang, Engineering of 2D/2D MoS 2 /Cd x Zn 1− x S Photocatalyst for Solar H_2 Evolution Coupled with Degradation of Plastic in Alkaline Solution, Solar RRL. 5 (2021). https://doi.org/10.1002/solr.202000427.

[3] I.M. Figueiredo, N.R. Pereira, P. Efraim, N.H.P. García, N.R. Rodrigues, A. Marsaioli, A.J. Marsaioli, 1H NMR, a rapid method to monitor organic acids during cupuassu (Theobroma grandiflorum Spreng) processing, Journal of Agricultural and Food Chemistry. 54 (2006) 4102–4106. https://doi.org/10.1021/jf0525176.

[4] K. Qi, S. Liu, A. Zada, Graphitic carbon nitride, a polymer photocatalyst, Journal of the Taiwan Institute of Chemical Engineers. 109 (2020) 111–123. https://doi.org/10.1016/j.jtice.2020.02.012.

[5] J. Wang, Q. Zhou, Y. Shen, X. Chen, S. Liu, Y. Zhang, Carbon Nitride Co-catalyst Activation Using N-Doped Carbon with Enhanced Photocatalytic H2 Evolution, Langmuir. 35 (2019) 12366–12373. https://doi.org/10.1021/acs.langmuir.9b01796.

[6] P. Shandilya, A. Guleria, B. Fang, A magnetically recyclable dual step-scheme Bi2WO6/Fe2O3/WO3 heterojunction for photodegradation of bisphenol-A from aqueous solution, Journal of Environmental Chemical Engineering. 9 (2021) 106461. https://doi.org/10.1016/j.jece.2021.106461.

[7] N. Watanabe, S. Horikoshi, H. Kawabe, Y. Sugie, J. Zhao, H. Hidaka, Photodegradation mechanism for bisphenol A at the TiO2/H2O interfaces, Chemosphere. 52 (2003) 851–859. https://doi.org/10.1016/S0045-6535(02)00837-8.

[8] D. Gunawan, C.Y. Toe, P. Kumar, J. Scott, R. Amal, Synergistic Cyanamide Functionalization and Charge-Induced Activation of Nickel/Carbon Nitride for Enhanced Selective Photoreforming of Ethanol, ACS Applied Materials & Interfaces. 13 (2021) 49916–49926.

https://doi.org/10.1021/acsami.1c14195.

[9] M. Ashraf, N. Ullah, I. Khan, W. Tremel, S. Ahmad, M.N. Tahir, Photoreforming of Waste Polymers for Sustainable Hydrogen Fuel and Chemicals Feedstock: Waste to Energy, Chemical Reviews. 123 (2023) 4443–4509. https://doi.org/10.1021/acs.chemrev.2c00602.

[10] T. Uekert, M.F. Kuehnel, D.W. Wakerley, E. Reisner, Plastic waste as a feedstock for solar-driven H 2 generation, Energy & Environmental Science. 11 (2018) 2853–2857. https://doi.org/10.1039/C8EE01408F.

[11] T. Uekert, H. Kasap, E. Reisner, Photoreforming of Nonrecyclable Plastic Waste over a Carbon Nitride/Nickel Phosphide Catalyst, Journal of the American Chemical Society. 141 (2019) 15201–15210. https://doi.org/10.1021/jacs.9b06872.

[12] B. Cao, S. Wan, Y. Wang, H. Guo, M. Ou, Q. Zhong, Highly-efficient visible-light-driven photocatalytic H2 evolution integrated with microplastic degradation over MXene/ZnxCd1-xS photocatalyst, Journal of Colloid and Interface Science. 605 (2022) 311–319. https://doi.org/10.1016/j.jcis.2021.07.113.

[13] Q. Liang, B. Shao, S. Tong, Z. Liu, L. Tang, Y. Liu, M. Cheng, Q. He, T. Wu, Y. Pan, J. Huang, Z. Peng, Recent advances of melamine self-assembled graphitic carbon nitride-based materials: Design, synthesis and application in energy and environment, Chemical Engineering Journal. 405 (2021) 126951. https://doi.org/10.1016/j.cej.2020.126951.

[14] H.-S. Zhai, L. Cao, X.-H. Xia, Synthesis of graphitic carbon nitride through pyrolysis of melamine and its electrocatalysis for oxygen reduction reaction, Chinese Chemical Letters. 24 (2013) 103–106. https://doi.org/10.1016/j.cclet.2013.01.030.

[15] R.C. Dante, P. Martín-Ramos, A. Correa-Guimaraes, J. Martín-Gil, Synthesis of graphitic carbon nitride by reaction of melamine and uric acid, Materials Chemistry and Physics. 130 (2011) 1094–1102. https://doi.org/10.1016/j.matchemphys.2011.08.041.

[16] A. Sudhaik, P. Raizada, P. Shandilya, D.-Y. Jeong, J.-H. Lim, P. Singh, Review on fabrication of graphitic carbon nitride based efficient nanocomposites for photodegradation of aqueous phase organic pollutants, Journal of Industrial and Engineering Chemistry. 67 (2018)

28–51. https://doi.org/10.1016/j.jiec.2018.07.007.

[17] S. Cao, J. Low, J. Yu, M. Jaroniec, Polymeric Photocatalysts Based on Graphitic Carbon Nitride, Advanced Materials. 27 (2015) 2150–2176. https://doi.org/10.1002/adma.201500033.

[18] Q. Dong, Z. Chen, B. Zhao, Y. Zhang, Z. Lu, X. Wang, J. Li, W. Chen, In situ fabrication of niobium pentoxide/graphitic carbon nitride type-II heterojunctions for enhanced photocatalytic hydrogen evolution reaction, Journal of Colloid and Interface Science. 608 (2022) 1951–1959. https://doi.org/10.1016/j.jcis.2021.10.161.

[19] Y. Hong, E. Liu, J. Shi, X. Lin, L. Sheng, M. Zhang, L. Wang, J. Chen, A direct one-step synthesis of ultrathin g-C3N4 nanosheets from thiourea for boosting solar photocatalytic H2 evolution, International Journal of Hydrogen Energy. 44 (2019) 7194–7204. https://doi.org/10.1016/j.ijhydene.2019.01.274.

[20] Y.-P. Yuan, L.-S. Yin, S.-W. Cao, L.-N. Gu, G.-S. Xu, P. Du, H. Chai, Y.-S. Liao, C. Xue, Microwave-assisted heating synthesis: a general and rapid strategy for large-scale production of highly crystalline g-C 3 N 4 with enhanced photocatalytic H 2 production, Green Chem. 16 (2014) 4663–4668. https://doi.org/10.1039/C4GC01517G.

[21] F. Dong, Z. Wang, Y. Sun, W.-K. Ho, H. Zhang, Engineering the nanoarchitecture and texture of polymeric carbon nitride semiconductor for enhanced visible light photocatalytic activity, Journal of Colloid and Interface Science. 401 (2013) 70–79. https://doi.org/10.1016/j.jcis.2013.03.034.

[22] P. Makuła, M. Pacia, W. Macyk, How To Correctly Determine the Band Gap Energy of Modified Semiconductor Photocatalysts Based on UV–Vis Spectra, The Journal of Physical Chemistry Letters. 9 (2018) 6814–6817. https://doi.org/10.1021/acs.jpclett.8b02892.

[23] H. Yan, Soft-templating synthesis of mesoporous graphitic carbon nitride with enhanced photocatalytic H2 evolution under visible light, Chemical Communications. 48 (2012) 3430. https://doi.org/10.1039/c2cc00001f.

[24] B. Wang, Y. Wang, Y. Lei, N. Wu, Y. Gou, C. Han, S. Xie, D. Fang, Mesoporous silicon carbide nanofibers with in situ embedded carbon for co-catalyst free photocatalytic hydrogen production, Nano Research. 9

(2016) 886–898. https://doi.org/10.1007/s12274-015-0971-z.

[25] S. Chen, Y. Hu, X. Jiang, S. Meng, X. Fu, Fabrication and characterization of novel Z-scheme photocatalyst WO3/g-C3N4 with high efficient visible light photocatalytic activity, Materials Chemistry and Physics. 149–150 (2015) 512–521. https://doi.org/10.1016/j.matchemphys.2014.11.001.

[26] H. Huang, X. Li, J. Wang, F. Dong, P.K. Chu, T. Zhang, Y. Zhang, Anionic Group Self-Doping as a Promising Strategy: Band-Gap Engineering and Multi-Functional Applications of High-Performance CO 3 2– -Doped Bi 2 O 2 CO 3, ACS Catalysis. 5 (2015) 4094–4103. https://doi.org/10.1021/acscatal.5b00444.

[27] N. Tian, Y. Zhang, X. Li, K. Xiao, X. Du, F. Dong, G.I.N. Waterhouse, T. Zhang, H. Huang, Precursor-reforming protocol to 3D mesoporous g-C 3 N 4 established by ultrathin self-doped nanosheets for superior hydrogen evolution, Nano Energy. 38 (2017) 72–81. https://doi.org/10.1016/j.nanoen.2017.05.038.

[28] K.-H. Lee, S.-K. Lee, K.-S. Jeon, Photoluminescent properties of silicon carbide and porous silicon carbide after annealing, Applied Surface Science. 255 (2009) 4414–4420. https://doi.org/10.1016/j.apsusc.2008.11.047.

[29] F. Chang, J. Zheng, X. Wang, Q. Xu, B. Deng, X. Hu, X. Liu, Heterojuncted non-metal binary composites silicon carbide/g-C3N4 with enhanced photocatalytic performance, Materials Science in Semiconductor Processing. 75 (2018) 183–192. https://doi.org/10.1016/j.mssp.2017.11.043.

[30] U. Baig, A. Khan, M.A. Gondal, M.A. Dastageer, S. Akhtar, Single-step synthesis of silicon carbide anchored graphitic carbon nitride nanocomposite photo-catalyst for efficient photoelectrochemical water splitting under visible-light irradiation, Colloids and Surfaces A: Physicochemical and Engineering Aspects. 611 (2021) 125886. https://doi.org/10.1016/j.colsurfa.2020.125886.

[31] Z. Du, P. Sun, K. Wu, X. Zheng, X. Zhang, J. Huang, D. Sun, Y. Zheng, Q. Li, g-C3N4-SiC-Pt for Enhanced Photocatalytic H2 Production from Water under Visible Light Irradiation, Energy Technology. 7 (2019) 1–

10. https://doi.org/10.1002/ente.201900017.

[32] B. Wang, J. Zhang, F. Huang, Enhanced visible light photocatalytic H 2 evolution of metal-free g-C 3 N 4 /SiC heterostructured photocatalysts, Applied Surface Science. 391 (2017) 449–456. https://doi.org/10.1016/j.apsusc.2016.07.056.

[33] M.D. Pirnaci, L. Spitaleri, D. Tenaglia, F. Perricelli, M.E. Fragalà, C. Bongiorno, A. Gulino, Systematic Characterization of Plasma-Etched Trenches on 4H-SiC Wafers, ACS Omega. 6 (2021) 20667–20675. https://doi.org/10.1021/acsomega.1c02905.

[34] G. Mishra, K.M. Parida, S.K. Singh, Facile Fabrication of S-TiO 2 /β-SiC Nanocomposite Photocatalyst for Hydrogen Evolution under Visible Light Irradiation, ACS Sustainable Chemistry & Engineering. 3 (2015) 245–253. https://doi.org/10.1021/sc500570k.

[35] A. Gulino, G.G. Condorelli, P. Mineo, I. Fragalà, An x-ray photoelectron spectra and atomic force microscopy characterization of silica substrates engineered with a covalently assembled siloxane monolayer, Nanotechnology. 16 (2005) 2170–2175. https://doi.org/10.1088/0957-4484/16/10/033.

[36] M.H. Vu, C.C. Nguyen, T. Do, Graphitic Carbon Nitride (g-C 3 N 4) Nanosheets as a Multipurpose Material for Detection of Amines and Solar-Driven Hydrogen Production, ChemPhotoChem. 5 (2021) 466–475. https://doi.org/10.1002/cptc.202000265.

[37] L. Motiei, M. Altman, T. Gupta, F. Lupo, A. Gulino, G. Evmenenko, P. Dutta, M.E. van der Boom, Self-Propagating Assembly of a Molecular-Based Multilayer, Journal of the American Chemical Society. 130 (2008) 8913–8915. https://doi.org/10.1021/ja802470g.

[38] J. Matthew, Surface analysis by Auger and x-ray photoelectron spectroscopy. D. Briggs and J. T. Grant (eds). IMPublications, Chichester, UK and SurfaceSpectra, Manchester, UK, 2003. 900 pp., ISBN 1-901019-04-7, 900 pp, Surface and Interface Analysis. 36 (2004) 1647–1647. https://doi.org/10.1002/sia.2005.

[39] Z. Wu, Y. Li, X. Li, E. Feng, L. Cao, Z. Li, X. Wang, P. Jiang, D. Wang, Acid protonation promoted different crystal phase structure silicon carbide-based carbon nitride composites to enhance the photocatalytic

degradation of dye wastewater, RSC Advances. 13 (2023) 35672–35682. https://doi.org/10.1039/D3RA06438G.

[40] Z. Du, P. Sun, K. Wu, X. Zheng, X. Zhang, J. Huang, D. Sun, Y. Zheng, Q. Li, g-C 3 N 4 -SiC-Pt for Enhanced Photocatalytic H 2 Production from Water under Visible Light Irradiation, Energy Technology. 7 (2019). https://doi.org/10.1002/ente.201900017.

[41] T. Uekert, M.A. Bajada, T. Schubert, C.M. Pichler, E. Reisner, Scalable Photocatalyst Panels for Photoreforming of Plastic, Biomass and Mixed Waste in Flow, ChemSusChem. 14 (2021) 4190–4197. https://doi.org/10.1002/cssc.202002580.

[42] D.T. Li, H. Yu, Y. Huang, Facile H2PdCl4-induced photoreforming of insoluble PET waste for C1-C3 compound production, Frontiers in Chemistry. 11 (2023). https://doi.org/10.3389/fchem.2023.1265556.

[43] E.M.N.T. Edirisooriya, P.S. Senanayake, H.B. Wang, M.R. Talipov, P. Xu, H. Wang, Photo-reforming and degradation of waste plastics under UV and visible light for H2 production using nanocomposite photocatalysts, Journal of Environmental Chemical Engineering. 11 (2023) 109580. https://doi.org/10.1016/j.jece.2023.109580.

[44] D. Jiang, H. Yuan, Z. Liu, Y. Chen, Y. Li, X. Zhang, G. Xue, H. Liu, X. Liu, L. Zhao, W. Zhou, Defect-anchored single-atom-layer Pt clusters on TiO2−x/Ti for efficient hydrogen evolution via photothermal reforming plastics, Applied Catalysis B: Environmental. 339 (2023) 123081. https://doi.org/10.1016/j.apcatb.2023.123081.

[45] S. Bhattacharjee, C. Guo, E. Lam, J.M. Holstein, M. Rangel Pereira, C.M. Pichler, C. Pornrungroj, M. Rahaman, T. Uekert, F. Hollfelder, E. Reisner, Chemoenzymatic Photoreforming: A Sustainable Approach for Solar Fuel Generation from Plastic Feedstocks, Journal of the American Chemical Society. 145 (2023) 20355–20364. https://doi.org/10.1021/jacs.3c05486.

[46] S.H. Paiman, S.F. Md Noor, N. Ngadi, A.H. Nordin, N. Abdullah, Insight into photocatalysis technology as a promising approach to tackle microplastics pollution through degradation and upcycling, Chemical Engineering Journal. 467 (2023) 143534. https://doi.org/10.1016/j.cej.2023.143534.

[47] A.M. Díez, N. Licciardello, Y. V. Kolen´ko, Photocatalytic processes as a potential solution for plastic waste management, Polymer Degradation and Stability. 215 (2023) 110459. https://doi.org/10.1016/j.polymdegradstab.2023.110459.

CHAPTER IX: H_2 production by other plastic materials

CHAPTER IX: H_2 production by other plastic materials

9.SiC-g-C_3N_4-TiCN photocatalysts for the solar photocatalytic H_2 evolution from plastics photoreforming[8]

9.1 Introduction

The photoreforming of other plastic materials was also investigated using the same SiC-g-C_3N_4 (SiC-gCN) composite (with the 1 wt% of graphitic carbon nitride, chosen on the basis of the results showed in the previous chapter) but with the addition of different amounts of titanium carbonitride (TiCN) used as uncommon co-catalyst instead of noble metals. The experimental data demonstrated that the incorporation of small amounts of TiCN into the SiC-gCN system enhanced the separation of charge carriers and improved the interaction between the two components. Furthermore, with the utilization of milder conditions for the plastics pre-treatment (NaOH 2M with ethanol) it was possible to strongly enhance the H_2 production rate through the solar photoreforming of polystyrene (PS), low density polyethylene (PE) and polylactic acid (PLA).

.

[8] Most of the data present in this chapter are present in the manuscript:
"SiC-g-C_3N_4-TiCN photocatalysts for the solar photocatalytic H_2 evolution from plastics photoreforming"
M. T. Armeli Iapichino, *G. Dativo, L. Calantropo, G. Impellizzeri and R. Fiorenza*
Applied Catalysis O: Open ,V.208,September 2025, 207070.

9.2 Photocatalysts synthesis

SiC- 1 wt% of g-C_3N_4 was prepared according to the procedure reported in the ref. [1]. In particular, the SiC powder (Sigma Aldrich, MKCN0364 357,391, β-SiC) was mixed with the right amount of melamine (Thermoscientific, Chemika 99%) to obtain the SiC-1 wt% of g-C_3N_4. The resultant powder was placed in a covered alumina crucible and heated in a muffle at 550 °C for 4 h (10°C/min as heated ramp). In a previous study dealing with the solar photoreforming of PET and BPA using the same experimental conditions of this work [1], we have demonstrated that the 1 wt% of graphitic carbon nitride is the best amount to favour an efficient interaction with the employed silicon carbide.

The SiC-1 wt% g-C_3N_4_TiCN samples were prepared using commercial titanium carbonitride (Ti_2CN, Sigma Aldrich, 518913). In particular, different amounts of TiCN (1 wt%, 5 wt% and 10 wt%) were added to the as-prepared SiC-1wt% g-C_3N_4. The resultant powders were mixed in demineralized water for 1 h under stirring at room temperature. Successively, they were sonicated for 2 h and calcined at 80°C (heating ramp of 10°C/min) for 5 h. The resultant samples are coded as SiC-gCN_xTCN where x is the weight percentage of the titanium carbonitride (Fig.1).

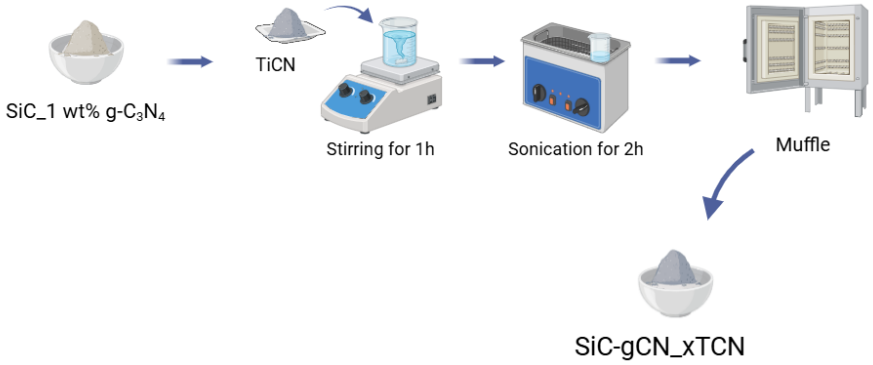

Figure 1 *Photocatalysts preparation.*

9.3 Pretreatment of the sacrificial agents

PLA (from biodegradable glasses), PS (from food dishes) and LDPE (from food packaging) were pre-treated to have a solution of the sacrificial agent [2,3] . Specifically, 30 mg of plastics (previously crushed and transformed in powders of 140–70 mesh), were treated with a solution of 40 mL of H_2O, 10 mL of ethanol and 10 mL of NaOH 2M, kept under stirring for 6 days at 40°C (Fig.2).

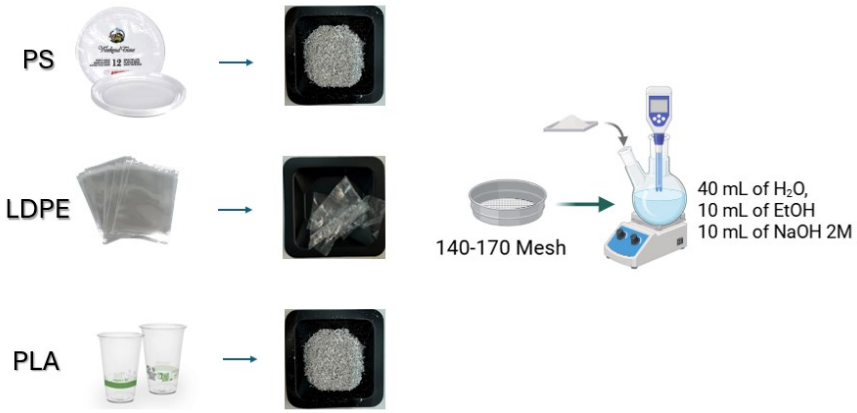

Figure 2 *Pre-treatment of plastic materials.*

9.4 Experimental Set-up

The measurements conducted in this study were performed using the experimental apparatus described in Section 7.1, under the same conditions. The byproducts detection was carried out with a GC-FID (Trace GC, Porapak Q column) coupled with a mass spectrometer (VG quadrupole mass spectrometer). The SEM images were acquired with a ZEISS SUPRA 55 VP equipped with an energy dispersive X-ray (EDX) INCA-Oxford windowless detector.

9.5 H_2 production by solar photoreforming of PLA, LDPE and PS

In the Fig. 3 are reported the obtained H_2 production rates after 5 of simulated solar irradiation for the various plastics photoreforming reactions. Interestingly, for all the plastic substrates, the best sample was the SiC-gCN_5TiCN with the PS photoreforming that led to the highest H_2 production (371 μmol $H_2/g_{cat}·h$).

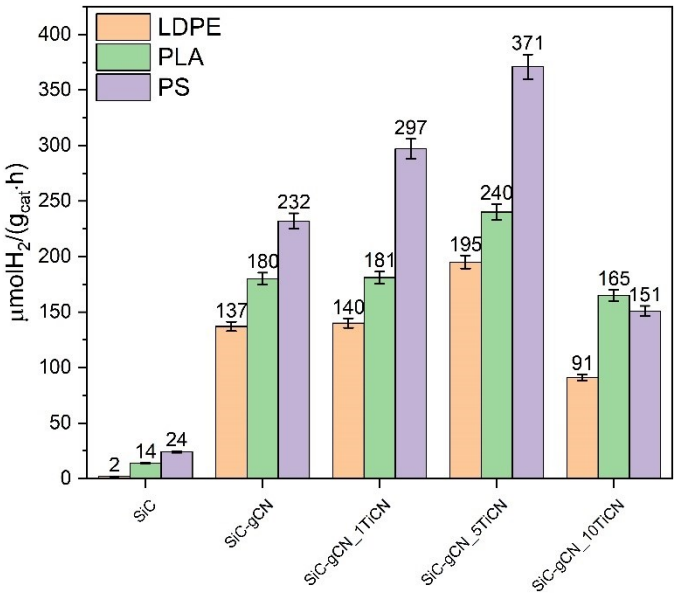

Figure 3 *H_2 production rates obtained during the solar photoreforming of plastic materials for 5 h of irradiation.*

The addition of graphitic carbon nitride allowed to increase the performance of the bare SiC and the further addition of TiCN led a positive effect up to the 10 wt%. The SiC-gCN_10TiCN photocatalyst indeed showed a lower H_2 production rate compared to the other TiCN-containing samples and also to the bare SiC-gCN composite, probably because an excess of TiCN led to cover the surface-active sites of the SiC/g-C_3N_4.

The highest hydrogen production obtained with the PS photoreforming can be explained considering that during the reaction the breakdown of the polymer structure was verified. Furthermore, the alkaline conditions due to the plastics pre-treatments steps, favour the depolymerization of the plastics [4], indeed in the GC-MS measurements the corresponding monomers were detected (Figs. 4-5).

The PS nominally contains an higher content of hydrogen $(C_8H_8)_n$ compared to LDPE $(C_2H_4)_n$ and PLA $(C_3H_4O_2)_n$, therefore the breaking of the polymer chain led to some intermediates (as benzene and toluene detected by GC-MS measurements, (Fig.4), in accordance with the literature[5]) with a continuous evolution of hydrogen. After 5 h of solar irradiation even employing the best photocatalyst (SiC-gCN_5TiCN) the presence of CO_2 was not detected, hence in this case, the photoreforming reaction with the formation of hydrogen and by-products was favoured compared to the photo-oxidation of the formed byproducts [5,6].

Furthermore, at difference to LDPE, the light-induced processes and the interaction of PS with the photocatalyst induced the formation or free radicals generated by the light absorption from the unsaturated chromophoric groups [5,7]. These radicals (generally superoxide and/or hydroxyl radicals) are able to cleavage the chemical bonds in the backbone chain of PS. On the contrary, the LDPE does not have unsaturated chromophores or double bonds in their backbone chain and therefore the formation of free radicals are difficult as well as the breaking of C-H bonds [4].

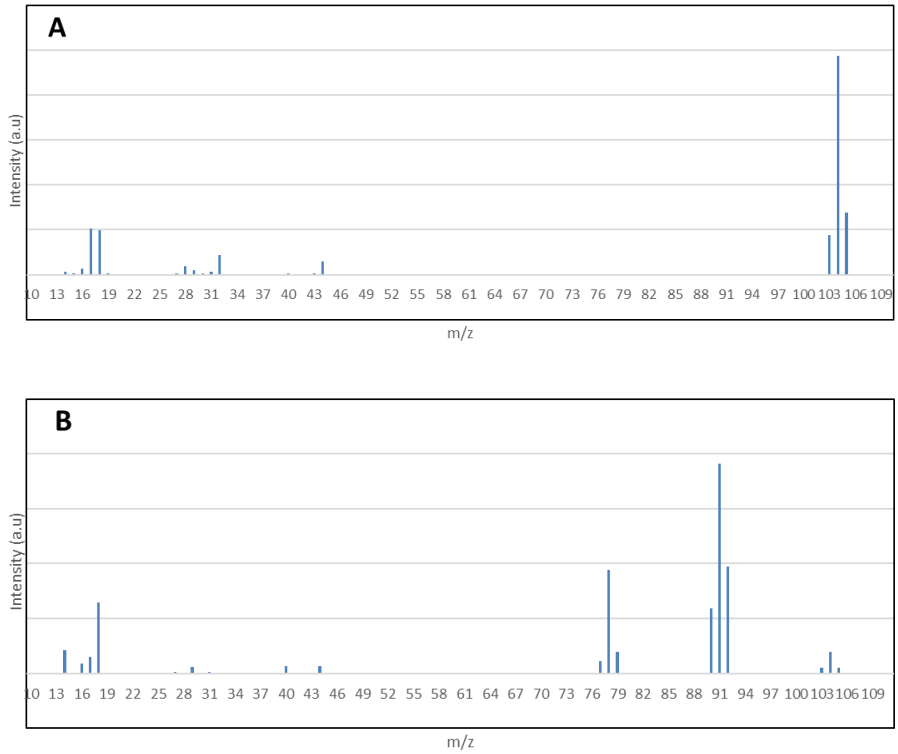

Figure 4 *GC-MS analysis of the products formed during the* ***PS photoreforming*** *employing the SiC-gCN_5TiCN photocatalyst. (A) initial solution after the pre-treatment (before the irradiation), the m/z = 104 identifies the styrene. (B) solution after 5 hours of photoreforming (the catalyst was filtered). It is possible to note the strong decrease of the signal at m/z=104, and the formation of signals at m/z =91 and m/z= 78 associated to the toluene and benzene, respectively. No other m/z signal was detected for m/z >110.*

For these reasons the LDPE photoreforming gave the lowest H_2 production (Fig.3) with no formation of CO_2 and with the detection of other linear C-H compounds (propane and ethane, accordingly to ref. [7], Fig.5).

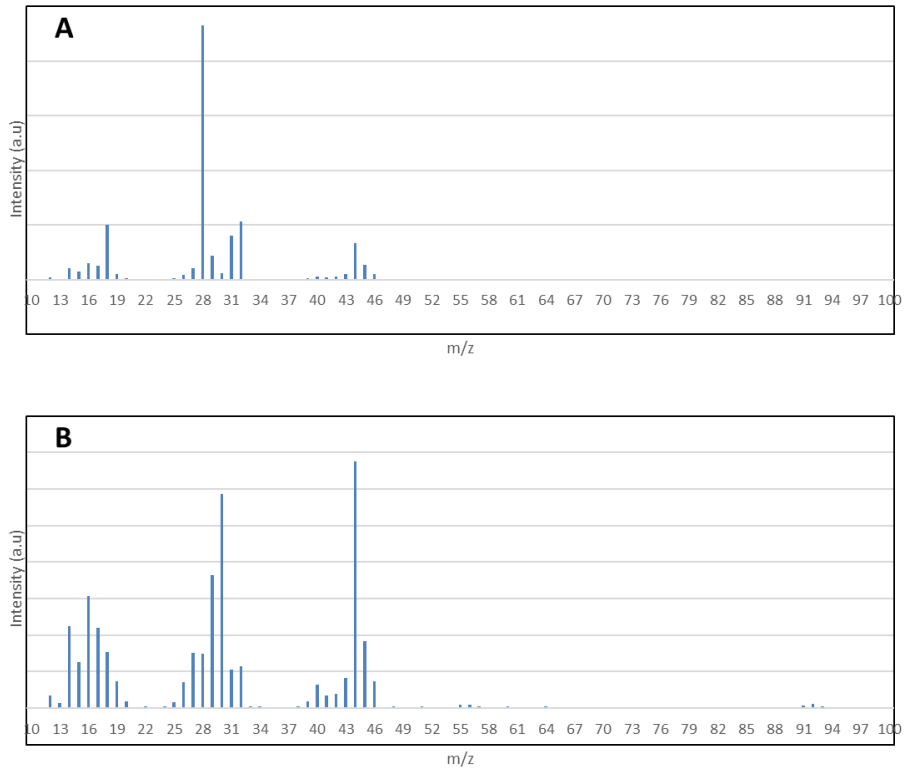

Figure 5 *GC analysis of the products formed during the* ***LDPE photoreforming*** *employing the SiC-gCN_5TiCN photocatalyst. (A) initial solution after the pre-treatment (before the irradiation), the m/z = 28 identifies the ethylene. (B) solution after 5 hours of photoreforming (the catalyst was filtered). It is possible to note the decrease of the signal at m/z=28, and the formation of signals at m/z =30 and m/z= 44 associated to the ethane and propane, respectively. No other m/z signal was detected for m/z >100.*

Conversely, the alkaline hydrolysis of PLA (due to the pre-treatment conditions) led to the formation of lactic acid, that can be further converted into H_2 and CO_2 (reactions a and b) [4]:

$$(a)\ C_3H_4O_2 + H_2O \rightarrow C_3H_6O_3$$

$$(b)\ C_3H_6O_3 + H_2O \rightarrow 3CO_2 + 6H_2$$

During the test with the best performing sample SiC-gCN_5TiCN a H_2/CO_2 ratio of 14.8 was detected, higher than the stoichiometric H_2/CO_2 ratio of 3 (reaction b). This implies that during the photoreforming reaction other intermediates were formed (GC-MS measurements detected, in a measurable concentration, formic acid and acetic acid, as also already reported [4,8], Fig.6). The oxygen present in the structure of PLA facilitates the formation of these small molecules whose parallel photoreforming reactions can be promoted [9,10], with further formation of hydrogen. For these reasons the PLA photoreforming gave a higher H_2 evolution compared to LDPE (Fig.3).

Focusing on the performance of SiC-gCN_5TiCN in the PS solar photoreforming the influence of the plastics pre-treatment conditions was also evaluated (Fig. 7).

The pre-treatment of the plastic materials, carried out to favour their solubilization in the reaction mixture, is also necessary to avoid scattering phenomena during the photoreforming reaction or possible shielding effects caused by plastic particles on the photocatalyst. The reaction mixture in all the photocatalytic tests was indeed made by 40 mL of deionized water and 10 mL of plastics solution (see paragraph 10.2).

As already investigated in a previous work with the SiC-g-C_3N_4 composites, a pH > 7 favours the plastics degradation and an efficient interaction with the generated H^+ and the surface negative charge of the SiC-1%g-C_3N_4 photocatalyst, whereas acidic pH strongly inhibited the H_2 evolution [1]. Furthermore, the strong alkaline conditions (solution of NaOH or KOH 5-10 M) are usually

employed as chemical treatment of the plastics materials to favour their depolymerization [4,11].

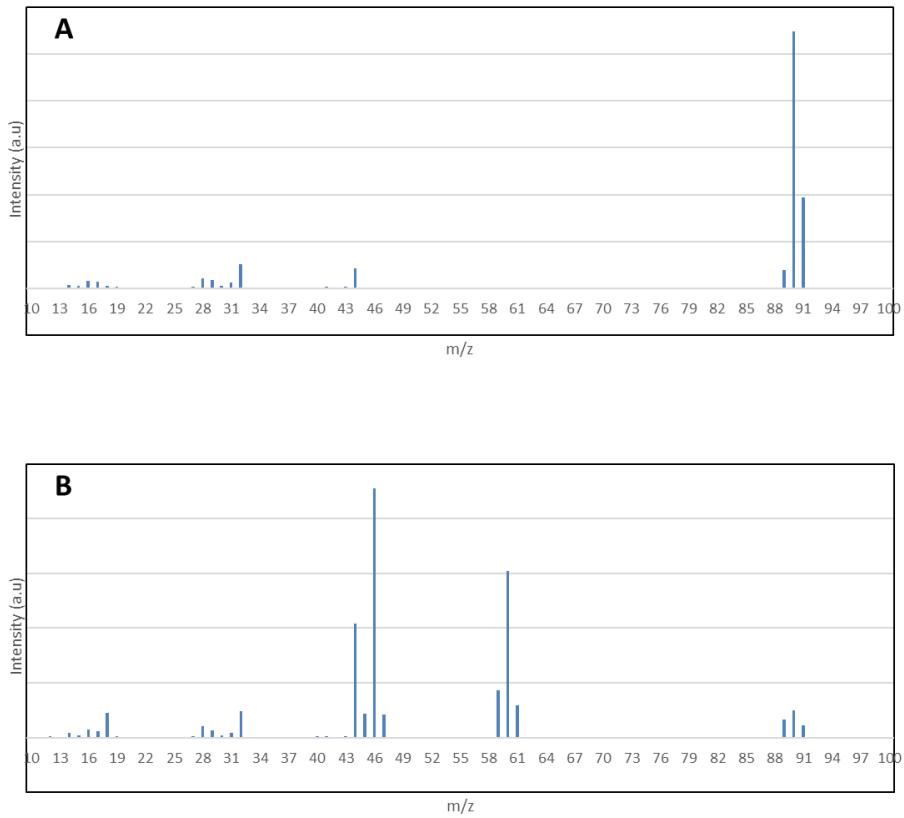

Figure 6 *GC-MS analysis of the products formed during the* ***PLA photoreforming*** *employing the SiC-gCN_5TiCN photocatalyst. (A) initial solution after the pre-treatment (before the irradiation), the m/z = 90 identifies the lactic acid. (B) solution after 5 hours of photoreforming (the catalyst was filtered). It is possible to note the strong decrease of the signal at m/z=90, and the formation of signals at m/z =46 and m/z= 60 associated to the formic acid and acetic acid, respectively. The signal at m/z =44 was due to the formed* CO_2*, verified also by GC-TCD measurement. No other m/z signal was detected for m/z >100.*

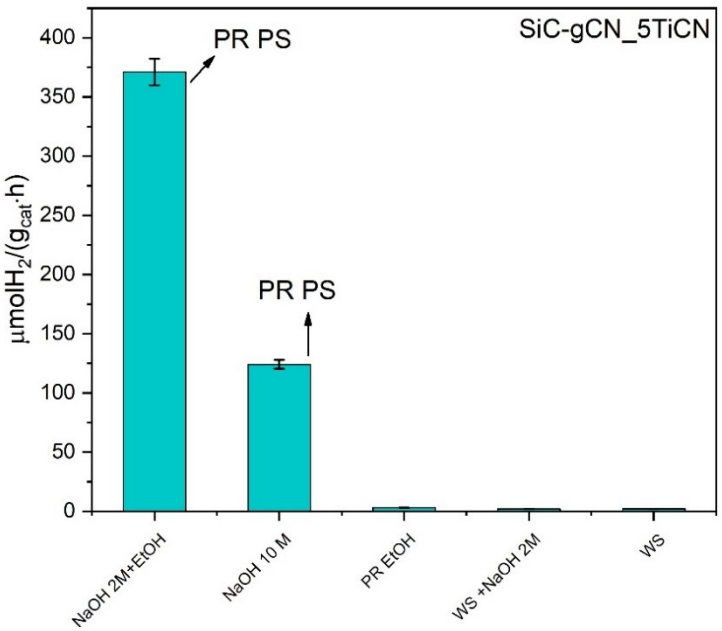

Figure 7 *H_2 production rates obtained during the different pretreatment conditions after 5 h of simulated solar irradiation using the SiC-gCN_5TiCN sample.*

Conversely, in this work it a greener plastics pretreatment methodology was investigated, using a less concentrated basic solution (NaOH 2M) and the addition of ethanol (details in the paragraph 10.2) that favours the plastics solubilization[3,12]. This treatment led to the highest H_2 production in the solar PS photoreforming, with an improvement of about 3 times compared to the same PS pre-treatment but employing a solution of NaOH 10 M without the addition of ethanol (Fig.7). The evolution of H_2 cannot be ascribed to the presence of ethanol, because in the same experimental conditions and using a reaction mixture of 40 mL of deionized water and 10 mL of ethanol, the H_2 production was negligible. Furthermore, the contribution of the overall water splitting (i.e. experiments without sacrificial agents) or of the

solution of NaOH 2M was also not relevant (Fig. 7). This data confirm as the basic pH (for all the plastic photoreforming reactions the pH before and after the 5 h of simulated solar irradiation was 9), necessary for the plastics depolymerization, and the addition of ethanol, that favoured this process, was in our experimental conditions an effective methodology to obtain H_2 exploiting the actions of the plastic monomers molecules as holes scavengers, improving in this way the charge carriers separation.

The photocatalytic stability of the SiC-gCN_5TiCN sample was evaluated performing 5 consecutive runs of the solar PS photoreforming (Fig.8).

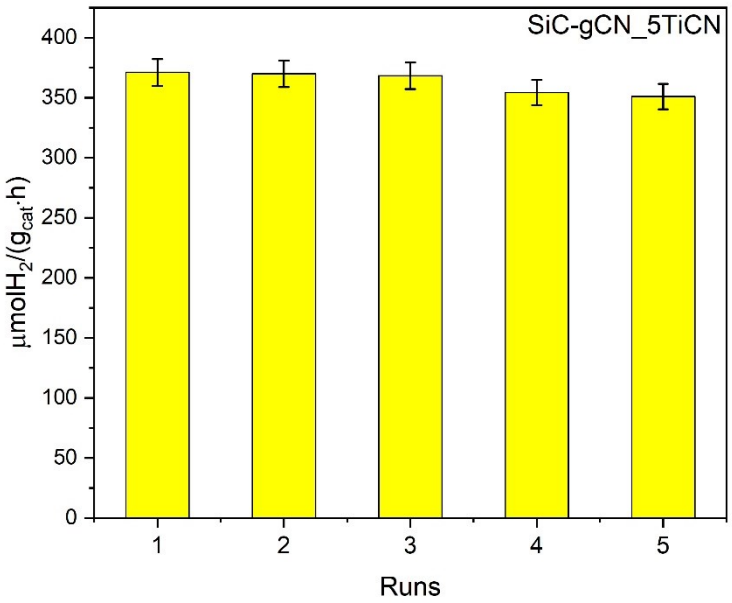

Figure 8 *H_2 production rates obtained during different runs of solar PS photoreforming employing the SiC-gCN_5TiCN sample. Each run was of 5 h of simulated solar irradiation. At the end of each run the catalyst was filtered, dried under vacuum at 80°C and re-used.*

At the end of each run of 5 h of simulated solar irradiation the sample was filtered, dried under vacuum at 80°C and re-used. From the Fig. 8 it is possible to note that the catalyst maintained a good stability with a loss of activity in the fifth run of about only 6%.

9.6 Effect of the plastics pre-treatment conditions

In addition, a chemico-physical pretreatment in acidic condition (as reported in section 4.3.1) was studied for PS-LDPE. In particular, 30 mg of plastics material was placed inside an autoclave in 30 ml of HNO_3 6% w/w and in the muffle furnace at 180°C for 4h with a 10°C/min ramp. As expected, (see previous chapter), the results obtained in acidic condition gave a low H_2 values using the best sample (i.e. SiC-gCN_5TiCN), i.e. 24 $\mu molH_2/g_{cat} \cdot h$ for PS PR and 18 $\mu molH_2/g_{cat} \cdot h$, for LDPE PR. This trend again confirms that an alkaline environment is required, with the SiC-based catalysts, in order to promote this reaction, and the suitable chemical pretreatment is necessary to ensure the polymers breakage. In addition, we carried out a physical pretreatment using 30 mg of PLA in 30 mL of water. The mixture was first put in an autoclave and then heated in a muffle furnace at 130 °C for 2h,10°C/min.

9.7 Samples characterizations

The XRD patterns of the examined samples are reported in the (Fig. 9). The SiC-based composites exhibited diffraction peaks at 2θ = 35.6°, 38.0°, 41.5°, 59.9°, and 65.6° assigned to the cubic 3C-SiC (β-SiC) [13]. The peaks at 2θ = 34.1° and 34.7° were attributed, as reported, to the spontaneous packing fault associated to the SiC growth[14]. In the SiC-gCN and SiC-gCN_5TiCN samples, due to the low amount of g- C_3N_4 (1 wt%) and the good dispersion on the SiC [1,15], no XRD peaks associated to the graphitic carbon nitride were observed. On the contrary, due to the higher amount of TiCN (5 wt%) it is possible to note small signals at 2θ = 36.3° and 60.7° in the SiC-gCN_5TiCN photocatalyst, related to the presence of the Ti_2CN phase [16] in accordance with the commercial powder of TiCN used for the synthesis of the composite (see paragraph 10.1).

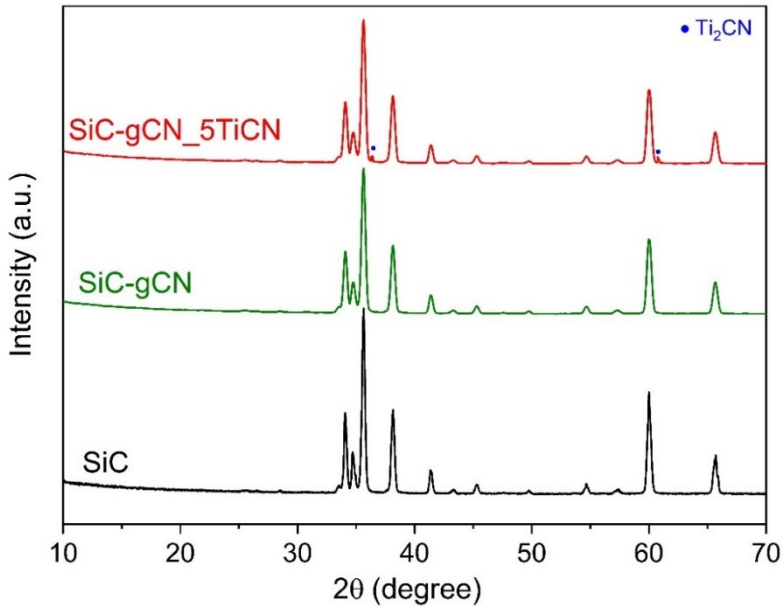

Figure 9 *XRD patterns of the examined photocatalysts.*

The presence of the 3C-SiC phase was confirmed also by the Raman analysis (Fig. 10), with the typical two scattering peaks at wavenumber 782 cm1 and 948 cm1, which correspond to the transverse optical phonon mode (TO) and the longitudinal optical phonon mode (LO) of 3C-SiC, respectively [18,19]. These two bands are present also in the SiC-gCN and SiC-gCN_5TiCN samples, with no other signals related to the gCN and TiCN, probably due to their low amount, high fluorescence of carbon nitride [30], and overlapping with the TO Raman mode of TiCN [18]. However, it is possible to note a Raman red shift for the TO and LO bands of about 5 cm^{-1} for the SiC-gCN and of about 20 cm^{-1} for the SiC-gCN_5TiCN. As reported, this shift is related to the presence of stacking faults and defects in the SiC crystalline structure [25,28]. Therefore, the addition of gCN and especially TiCN caused the presence of defect-induced localized states that can enhance the charge carriers separation efficiency, promoting the photocatalytic activity as already reported for other SiC-based composites [34,35]. Therefore, the higher H_2 production rate of SiC-gCN_5TiCN composite compared to the SiC and SiC-gCN (Fig.3) can be also correlated to the presence of these defect states related to the modification of SiC with the gCN and TiCN.

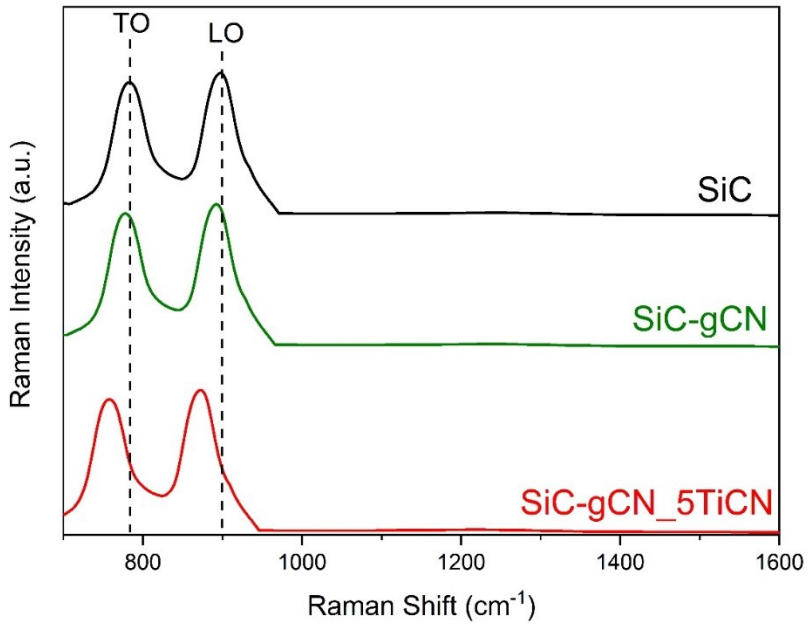

Figure 10 *Raman spectra of the examined samples*.

In the *Table 1* are reported the textural and the optical properties of the examined composites. The addition of graphitic carbon nitride and of progressive amount of titanium carbonitride led to a slight increase of the BET surface area with the consequent decrease of the mean pore diameters and pore volumes (Table 1). The optical properties of the samples were estimated through the UV-Vis DRS spectroscopy and the optical band gap evaluated by plotting the modified Kubelka-Munk function vs hv [17].

Table 3 *Textural and optical features of the examined photocatalyst.*

Samples	BET Surface area (m^2/g)	Mean $Pore_{diameter}$ (nm)	Pore volume (cm^3/g)	Optical band gap (eV)
SiC	17.4	18.6	0.45	2.96
SiC-gCN	20.5	17.4	0.43	2.95
SiC-gCN_1TiCN	21.4	17.1	0.40	2.97
SiC-gCN_5TiCN	21.8	16.9	0.38	3.0
SiC-gCN_10TiCN	22.6	15.8	0.35	3.0

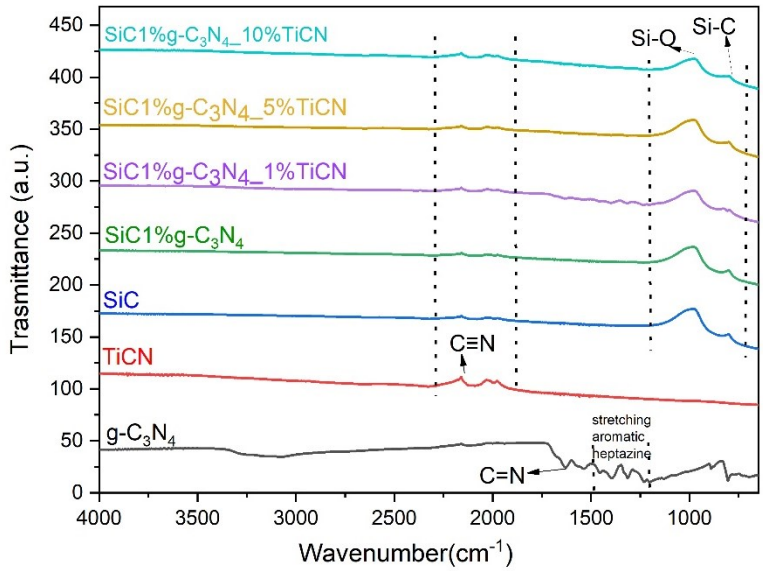

Figure 11 *IR spectra in ATR mode for the examined samples.*

Several characteristic bands can be observed in Fig.11. For the samples SiC 1%g-C_3N_4_1-5-10%TCN, as well as for pure SiC, the band at 858 cm^{-1}, which corresponds to the Si–C stretching vibration, is clearly visible. Another band appears at 1090 cm^{-1}, related to the Si–O stretching vibration, which is mainly due to slight oxidation on the surface of the SiC. Both are typical bands for SiC[18].

In these samples, no clear characteristic bands of graphitic carbon nitride (g-C_3N_4) are observed, probably because the added amount was very small. However, the characteristic peak of TiCN can be observed in the 2100–2300 cm^{-1} range and it is indicative of the cyanide (C≡N) stretching vibrations[19], while peaks in the 700–800 cm^{-1} range correspond to titanium-carbon (Ti–C)[20], but unfortunately they are not entirely clear.

On the other hand, the pure g-C_3N_4 sample shows several typical bands:

- A broad band between 3000 and 3300 cm^{-1}, caused by C–N and N–H stretching vibrations,
- Several bands between 1200 and 1650 cm^{-1}, related to C–N stretching in heterocycles, and
- A band at 808 cm^{-1}, which corresponds to the vibration of s-triazine rings.

In the Fig. 12 are instead reported the photoluminescence spectra (PL) of the examined samples.

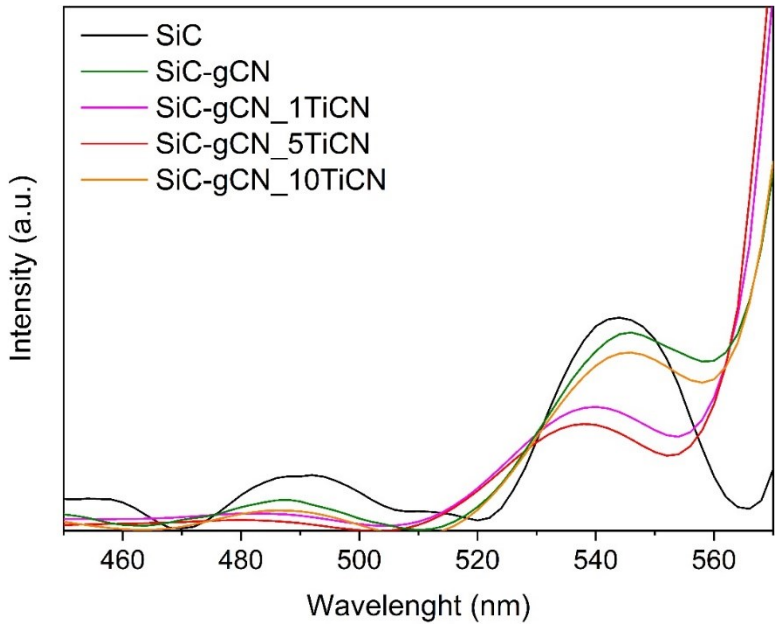

Figure 12 *Photoluminescence spectra of the examined photocatalyst (λ = 300 nm).*

As largely reported, the PL band intensity is correlated to the recombination rate of the charge carriers in a semiconductor, Specifically, lower is the PL intensity lower is the recombination rate[21–23]. The bare SiC showed the highest PL band intensity centred at 489 and 544 nm and they are related to the excitation/recombination phenomena of the e^-/h^+ of SiC-based composites [13,14]. The addition of CN led to a slight decrease of the PL intensity with also a slight red shift. Interestingly, the further addition of TiCN caused a further decrease of the PL bands intensity in order: SiC-gCN_5TiCN > SiC-gCN_1TiCN > SiC-gCN_10TiCN. This trend confirms the photocatalytic behaviour of the examined composites, with the SiC-gCN_5TiCN that was the

best photocatalyst (Fig.3), pointing to as this composition is the optimal one to favour the interaction between the SiC, the g-C_3N_4 and the Ti_2CN leading to increase the charge carrier separation. Consequently, a higher amount (10 wt%) of titanium carbonitride was detrimental for the photoactivity (Fig.3) because in this case the recombination rate was higher than the SiC-gCN_5TiCN (i.e. higher PL band intensity, Fig.12).

The interaction between the carbonitrides and the SiC can be also noted from the SEM-EDX map of the SiC-gCN_5TiCN (Fig. 13) and by the TEM analysis (Fig.14). Indeed, it is possible to note as the TiCN was deposited on SiC-gCN composite.

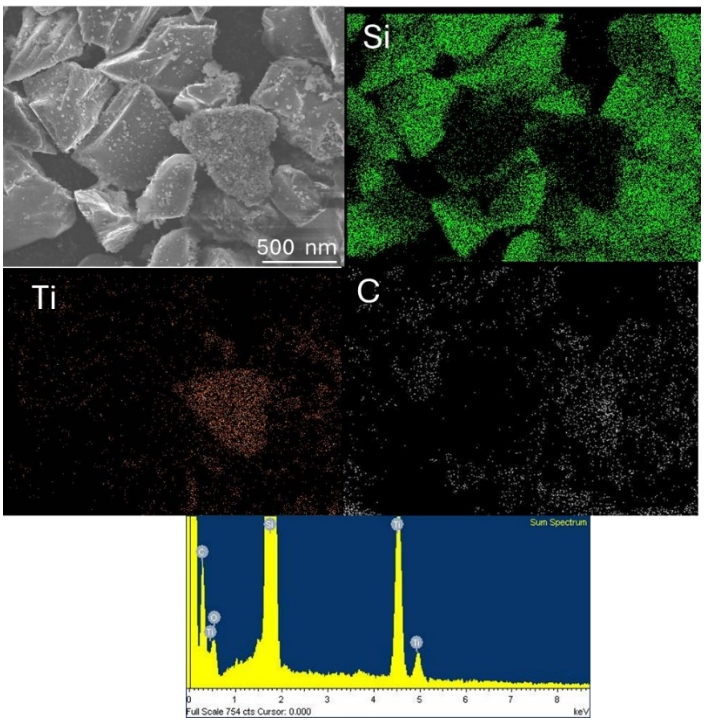

Figure 13 *SEM-EDX image, maps and spectrum of the SiC-gCN_5TiCN sample. Please note that the signal of nitrogen was overlapped with the C and O K-alpha signals. However, the XPS analysis confirmed the presence of nitrogen as well as the oxygen coming from the SiO_x and TiO_2 species.*

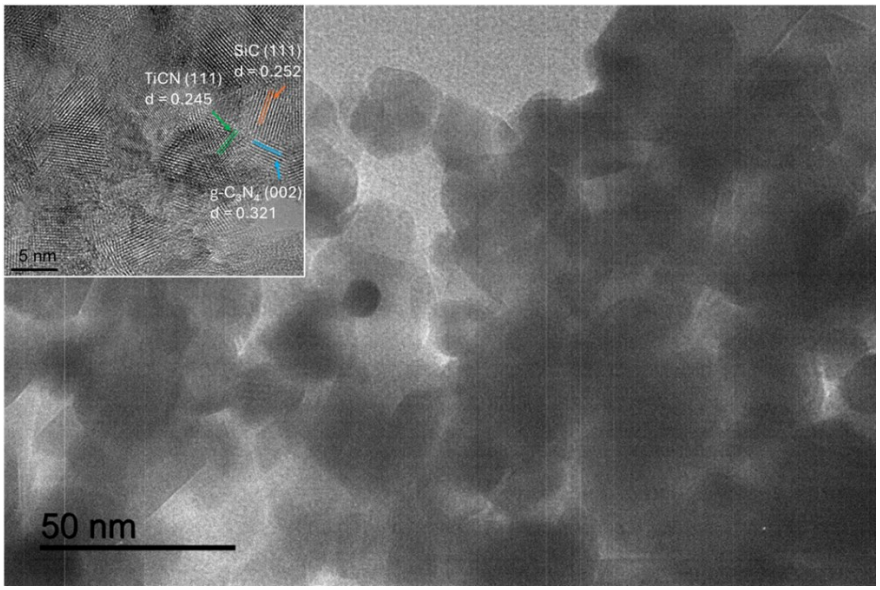

Figure 14 *TEM and HRTEM (inset) images of the SiC-gCN_5TiCN sample. It is possible to observe the formation of interface regions between the SiC-g-C_3N_4 and TiCN particles, as reported for similar composites [1–4]. The measured interplanar crystal spacing distances (nm) are close to the (002) of g-C_3N_4 and (111) of both SiC and TiCN lattice planes. The (111) lattice plane is also the main SiC crystal plan observed by XRD (Fig. 9).*

9.8 Photothermo-catalytic approach

The SiC-gCN_5TiCN showed very good catalytic activity, so to further increase the hydrogen production, it was decided to proceed with a hybrid catalytic approach. A novel photo-thermo-catalytic approach was used (PTC)[24], synergistically coupling thermocatalysis (TC) and photocatalysis (PC), i.e. introducing heat into photocatalytic system or light into thermocatalytic system. PTC has drawn increasing attentions in the very recent years, because it can simultaneously utilize both the UV-VIS irradiation with higher energy to trigger PC and the heating effect of NIR spectrum to provide the demanding endothermic energy for TC[25]. Therefore, compared with sole PC and TC, PTC possesses the following distinct advantages[26]:

- The PTC is characterized by high net energy efficiencies without other external energy sources[27];
- The performance of PTC processes is much higher than a simply linear combination of TC and PC due to the synergistic effect[28];
- In some cases, PTC can effectively refrain the deactivation of the catalyst and increase the selectivity for the desired products[29].

Unfortunately, although the PTC possesses the above advantages, the investigation is still at its early stage and there have been fewer in-depth studies showcasing this novel form of synergistic mechanism[29]. The fundamental mechanisms of PTC can be classified by the heating mode and photo-thermal synergic mode. The heating mode contains local and global heating systems. The

local heating system means that suitable catalysts can efficiently absorb irradiation and partially transform into heat that will be locally released (photo-thermal effect). The global heating system means that the whole reaction medium is heated by external power sources. For this reason, it is possible to distinguish different methodology as: thermal-assisted photocatalysis (TAPC), photoassisted thermocatalysis (PATC), photo-driven thermocatalysis (PDTC) and photo-thermal co-catalysis (PTCC) (Fig.15) [30].

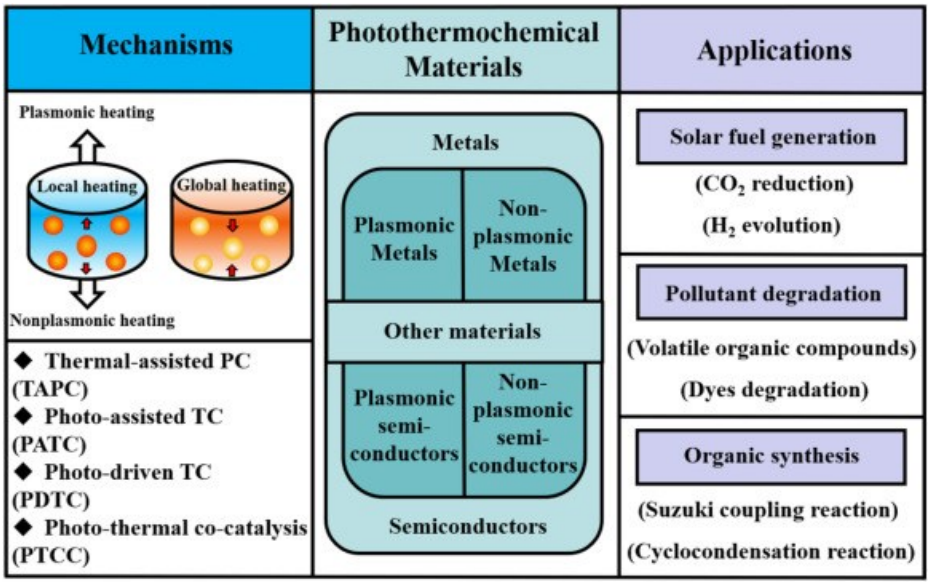

Figure 15 *Summary scheme of the photo-thermo catalysis* [26].

For the reasons outlined above, a thermo-assisted PT experiment was conducted. The experimental setup was similar to the one described in the previous section (paragraph 7.1). In these experiments the thermostat was not employed; however, the temperature due to heating of the solar lamp inside the solar box remained stable at about 60 °C throughout the 5-hours of

irradiation, as confirmed by the hourly monitoring with a thermal imaging camera (Fig.16).

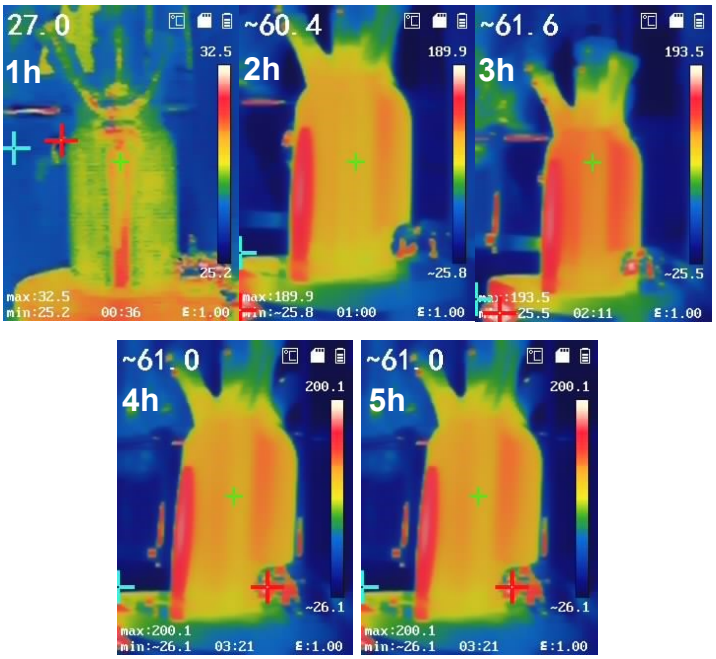

Figure 16 *Temperature control with the infrared thermal camera.*

The use of this hybrid catalysis leads to a significant increase in H_2 production, as shown in the Fig.17, across all three cases. The photothermal approach enables a three-fold increase compared to the photocatalysis alone. Notably, there is a marked improvement in the case of LDPE with similar performance of the photothermo-catalytic reforming of PLA. This is likely due to the contribution of heat, which further facilitates the breaking of C–C bonds, thereby enhancing the H_2 production.

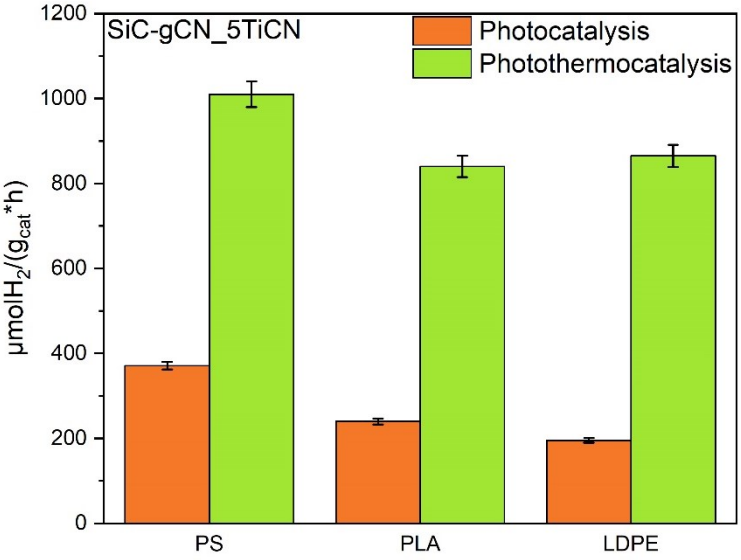

Figure 17 *Comparison of the different catalytic approaches for the plastics photoreforming.*

9.9 Cellulose Photoreforming

The amount of biomass components is approximately 120 × 10^9 T/y[30]. Furthermore, waste natural polymers can also originate from natural sources, such as cellulose and PLA (a biodegradable polymer), and not only from synthetic sources like PS, LDPE, PET, and BPA. Therefore, we aimed to compare these two categories of polymers by applying the same type of pre-treatment, as defined in the section 10.2, using commercial cellulose (Sigma Aldrich crystallinity ≤95%). The photocatalytic set-up chosen is similar to the one described in the section 7.1.

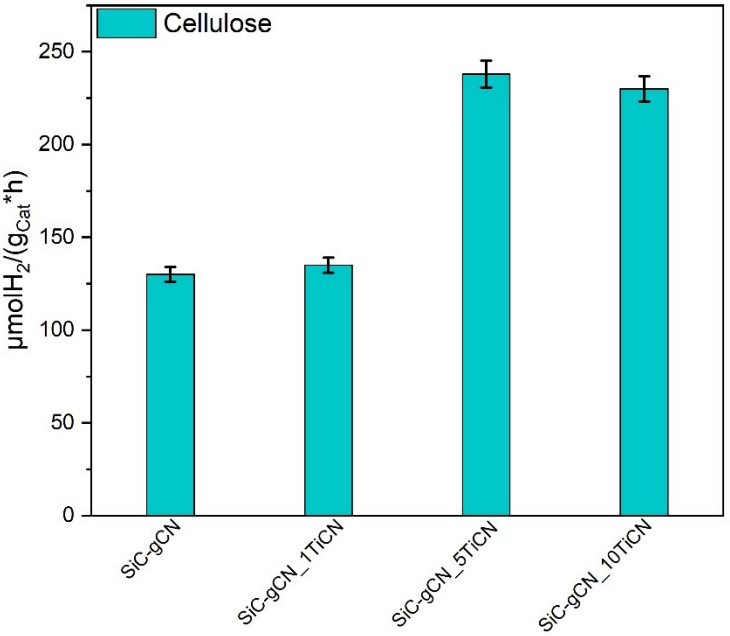

Figure 18 *Cellulose Photoreforming*

Figure 18 shows that also in this case, the highest H_2 production is achieved using SiC-gCN_5TiCN, reaching 238 µmol $H_2/(g_{cat} \cdot h)$ for the cellulose photoreforming (CL PR).

On the other hand, Fig.19 shows the results of photoreforming comparing the different polymers. As seen in the graph, the H_2 production with the best catalyst i.e. SiC-gCN-5TiCN from CL PR (238 µmol $H_2/(g_{cat}\cdot h)$) is lower than PS PR (371 µmol $H_2/(g_{cat}\cdot h)$). This lower yield can be attributed to the highly crystalline structure of cellulose and its dense network of hydrogen bonds, which make it more resistant to degradation[31]. This makes it more difficult to degrade during photoreforming compared to more amorphous or low-density polymers such as polystyrene. Furthermore, cellulose is composed of carbon, hydrogen and oxygen in relatively balanced proportions, but with a lower hydrogen content per unit mass than PS[32]. In contrast, the hydrogen production with the best composite for CL PR and PLA PR is similar (238 and 240 µmol $H_2/ (g_{cat}\cdot h$ respectively). While the hydrogen production for CL PR (240 µmol $H_2/(g_{cat}\cdot h)$ is higher than LDPE PR (195 µmol $H_2/(g_{cat}\cdot h)$. This is probably due to the high degradation rate of PLA with the total photo-oxidation into CO_2 and water that is favoured instead of the formation of byproducts with the release of H_2[33].

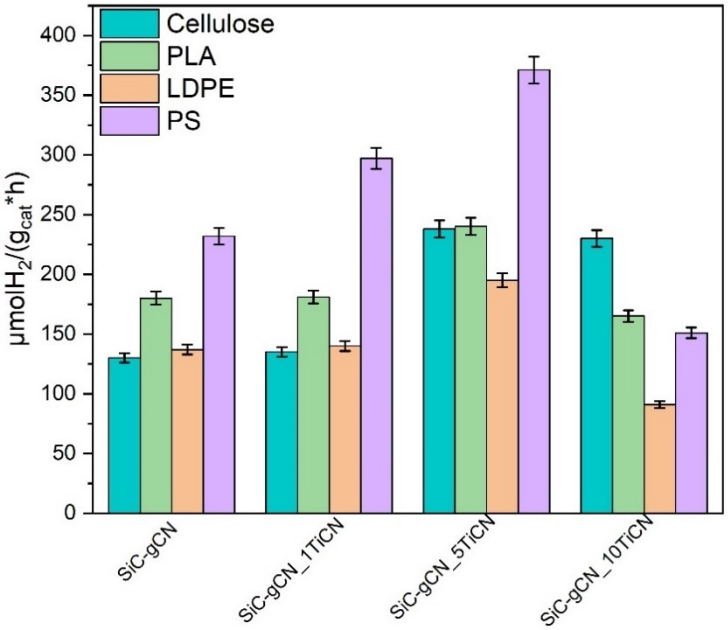

Figure 19 *Comparison between the various polymers photoreforming after 5 h of simulated solar light.*

9.10 Conclusion

The photocatalytic activity of the SiC-gCN_TiCN composite for the photoreforming of both plastic materials and biomass-derived compound as the cellulose showed promising hydrogen production rates. The addition of small amounts of TiCN proved to be highly effective, as it significantly improved the results compared to previous studies and without the use of the noble metals co-catalyst. Moreover, selecting common plastic materials such as plates, tumblers, and food packaging represent a realistic system of common waste that requires a pre-treatment step to obtain H_2 in a waste-to-fuel approach. This step was essential, because it allowed a basic environment necessary for the photoreforming process catalysed by SiC-based compounds, using ethanol as solvent and a much lower concentration (2M) of sodium hydroxide solution instead of more concentrated solution (usually 10 M). This pre-treatment also led to the formation of intermediate products that promote the generation of H_2. Additionally, the results obtained from the hybrid photothermal-catalytic approach suggest a promising future direction, as a significant hydrogen production was achieved by simply increasing the reaction temperature at 60 °C. These milder conditions facilitate also the depolymerization of the plastics therefore boosting up the H_2 formation.

References

[1] M.T.A. Iapichino, R. Fiorenza, V. Patamia, G. Floresta, A. Gulino, M. Condorelli, G. Impellizzeri, G. Compagnini, S. Sciré, H2 production by solar photoreforming of plastic materials using SiC-g-C3N4composites, Catalysis Communications. 187 (2024) 106850. https://doi.org/10.1016/j.catcom.2024.106850.

[2] B. Liu, H. Sun, J.-W. Lee, J. Yang, J. Wang, Y. Li, B. Li, M. Xu, Q. Liao, W. Zhang, D. Han, L. Niu, H. Meng, B.J. Kim, X. Guo, Achieving highly efficient all-polymer solar cells by green-solvent-processing under ambient atmosphere, Energy & Environmental Science. 14 (2021) 4499–4507. https://doi.org/10.1039/D1EE01310F.

[3] T.K. Anh Nguyen, T. Trần-Phú, R. Daiyan, X. Minh Chau Ta, R. Amal, A. Tricoli, From Plastic Waste to Green Hydrogen and Valuable Chemicals Using Sunlight and Water, Angewandte Chemie International Edition. 63 (2024). https://doi.org/10.1002/anie.202401746.

[4] M. Ashraf, N. Ullah, I. Khan, W. Tremel, S. Ahmad, M.N. Tahir, Photoreforming of Waste Polymers for Sustainable Hydrogen Fuel and Chemicals Feedstock: Waste to Energy, Chemical Reviews. 123 (2023) 4443–4509. https://doi.org/10.1021/acs.chemrev.2c00602.

[5] C. Mohanty, A. Samal, J. Kumar, A.K. Behera, R. Das, N. Das, Design and first-principles investigation of step-scheme (S-scheme) g-C3N4/α-MnO2 nanojunction for polystyrene photoreforming into value-added chemicals and hydrogen, International Journal of Hydrogen Energy. 120 (2025) 628–641. https://doi.org/10.1016/j.ijhydene.2025.03.193.

[6] R. Wei, Y. Shi, S. Zhang, X. Diao, Z. Ya, D. Xu, Y. Zheng, C. Yan, K. Cao, Y. Ma, N. Ji, Photocatalytic Upgrading of Plastic Waste into High-Value-Added Chemicals and Fuels: Advances and Perspectives, ACS Sustainable Chemistry & Engineering. 13 (2025) 2615–2632. https://doi.org/10.1021/acssuschemeng.4c09610.

[7] P. Gijsman, G. Meijers, G. Vitarelli, Comparison of the UV-degradation chemistry of polypropylene, polyethylene, polyamide 6 and polybutylene terephthalate, Polymer Degradation and Stability. 65 (1999) 433–441. https://doi.org/10.1016/S0141-3910(99)00033-6.

[8] T. Uekert, H. Kasap, E. Reisner, Photoreforming of Nonrecyclable Plastic Waste over a Carbon Nitride/Nickel Phosphide Catalyst, Journal of the American Chemical Society. 141 (2019) 15201–15210. https://doi.org/10.1021/jacs.9b06872.

[9] Z. Ya, M. Li, D. Xu, H. Wang, S. Zhang, Asymmetric Atomic Pt–B Dual-Site Catalyst for Efficient Photoreforming of Waste Polylactic Acid Plastics in Seawater, ACS Nano. 19 (2025) 16011–16023. https://doi.org/10.1021/acsnano.5c02408.

[10] P. Kumar, H. Zhang, A.G. Yohannes, J. Wang, A. Shayesteh Zeraati, S. Roy, X. Wang, K. Kannimuthu, A.M. Askar, K.A. Miller, K. Ling, M. Adnan, S.-F. Hung, J.-J. Ma, W.-H. Huang, D. Trivedi, M. Molina, H. Zhao, A.A. Martí, A.F.G. Leontowich, G.K.H. Shimizu, D. Sinton, M.M. Adachi, Y.A. Wu, P.M. Ajayan, S. Siahrostami, J. Hu, M.G. Kibria, Isolated iridium oxide sites on modified carbon nitride for photoreforming of plastic derivatives, Nature Communications. 16 (2025) 2862. https://doi.org/10.1038/s41467-025-57999-w.

[11] X. Tang, X. Han, N.H.M. Sulaiman, L. He, X. Zhou, Recent Advances in the Photoreforming of Plastic Waste: Principles, Challenges, and Perspectives, Industrial and Engineering Chemistry Research. 62 (2023) 9032–9045. https://doi.org/10.1021/acs.iecr.3c00809.

[12] S. Ügdüler, K.M. Van Geem, R. Denolf, M. Roosen, N. Mys, K. Ragaert, S. De Meester, Towards closed-loop recycling of multilayer and coloured PET plastic waste by alkaline hydrolysis, Green Chemistry. 22 (2020) 5376–5394. https://doi.org/10.1039/D0GC00894J.

[13] U. Baig, A. Khan, M.A. Gondal, M.A. Dastageer, S. Akhtar, Single-step synthesis of silicon carbide anchored graphitic carbon nitride nanocomposite photo-catalyst for efficient photoelectrochemical water splitting under visible-light irradiation, Colloids and Surfaces A: Physicochemical and Engineering Aspects. 611 (2021) 125886. https://doi.org/10.1016/j.colsurfa.2020.125886.

[14] F. Chang, J. Zheng, X. Wang, Q. Xu, B. Deng, X. Hu, X. Liu, Heterojuncted non-metal binary composites silicon carbide/g-C3N4 with enhanced photocatalytic performance, Materials Science in Semiconductor Processing. 75 (2018) 183–192.

https://doi.org/10.1016/j.mssp.2017.11.043.

[15] M. Xue, J. Han, X. Dai, Y. Ge, Y. Zhang, Z. Hai, Construction of Cu2O ternary composite comprising SiC and g-C3N4 for improved photocatalytic degradation of methyl orange via synergetic Z-scheme effect, Optical Materials. 155 (2024) 115883. https://doi.org/10.1016/j.optmat.2024.115883.

[16] T.-Y. Cho, R. Malik, Y.-W. Kim, K.J. Kim, Electrical and mechanical properties of pressureless sintered SiC-Ti2CN composites, Journal of the European Ceramic Society. 38 (2018) 3064–3072. https://doi.org/10.1016/j.jeurceramsoc.2018.03.040.

[17] P. Makuła, M. Pacia, W. Macyk, How To Correctly Determine the Band Gap Energy of Modified Semiconductor Photocatalysts Based on UV–Vis Spectra, The Journal of Physical Chemistry Letters. 9 (2018) 6814–6817. https://doi.org/10.1021/acs.jpclett.8b02892.

[18] S.A. Grudinkin, S.A. Kukushkin, A. V. Osipov, N.A. Feoktistov, IR spectra of carbon-vacancy clusters in the topochemical transformation of silicon into silicon carbide, Physics of the Solid State. 59 (2017) 2430–2435. https://doi.org/10.1134/S1063783417120186.

[19] P.C.H. Del Castillo, V. Castro-Velázquez, V. Rodríguez-González, Adsorption and photocatalytic-conjugated activity of a chitosan-functionalized titanate coating for the removal of the drug clonazepam from drinking water, Environmental Science and Pollution Research. 32 (2023) 10553–10568. https://doi.org/10.1007/s11356-023-30215-2.

[20] A.H. Rahman, D. Sundeep, C.C. Sastry, J. Krishnaiah, E.K. Varadharaj, Enhanced ballistic and mechanical performance of aluminum nickel phosphorus bronze composites reinforced with TiCN and Y_2O_3 for armored vehicles, Scientific Reports. 15 (2025) 10266. https://doi.org/10.1038/s41598-025-94508-x.

[21] N. Tian, Y. Zhang, X. Li, K. Xiao, X. Du, F. Dong, G.I.N. Waterhouse, T. Zhang, H. Huang, Precursor-reforming protocol to 3D mesoporous g-C 3 N 4 established by ultrathin self-doped nanosheets for superior hydrogen evolution, Nano Energy. 38 (2017) 72–81. https://doi.org/10.1016/j.nanoen.2017.05.038.

[22] Q. Xiao, J. Zhang, C. Xiao, X. Tan, Photocatalytic degradation of

methylene blue over Co3O4/Bi2WO6 composite under visible light irradiation, Catalysis Communications. 9 (2008) 1247–1253. https://doi.org/10.1016/j.catcom.2007.11.011.

[23] X. Zeng, Z. Wang, G. Wang, T.R. Gengenbach, D.T. McCarthy, A. Deletic, J. Yu, X. Zhang, Highly dispersed TiO2 nanocrystals and WO3 nanorods on reduced graphene oxide: Z-scheme photocatalysis system for accelerated photocatalytic water disinfection, Applied Catalysis B: Environmental. 218 (2017) 163–173. https://doi.org/10.1016/j.apcatb.2017.06.055.

[24] C. Song, Z. Wang, Z. Yin, D. Xiao, D. Ma, Principles and applications of photothermal catalysis, Chem Catalysis. 2 (2022) 52–83. https://doi.org/10.1016/j.checat.2021.10.005.

[25] J. Zhang, H. Chen, X. Duan, H. Sun, S. Wang, Photothermal catalysis: From fundamentals to practical applications, Materials Today. 68 (2023) 234–253. https://doi.org/10.1016/j.mattod.2023.06.017.

[26] R. Ma, J. Sun, D.H. Li, J.J. Wei, ScienceDirect Review of synergistic photo-thermo-catalysis : Mechanisms , materials and applications, International Journal of Hydrogen Energy. 45 (2020) 30288–30324. https://doi.org/10.1016/j.ijhydene.2020.08.127.

[27] D. Mateo, J.L. Cerrillo, S. Durini, J. Gascon, Fundamentals and applications of photo-thermal catalysis, Chemical Society Reviews. 50 (2021) 2173–2210. https://doi.org/10.1039/D0CS00357C.

[28] S. Du, X. Bian, Y. Zhao, R. Shi, T. Zhang, Progress and Prospect of Photothermal Catalysis, Chemical Research in Chinese Universities. 38 (2022) 723–734. https://doi.org/10.1007/s40242-022-2039-4.

[29] M. Shi, X. Meng, Photothermal catalysis: From principles to applications, International Journal of Hydrogen Energy. 48 (2023) 34659–34676. https://doi.org/10.1016/j.ijhydene.2023.05.253.

[30] X. Song, X. Shan, H. Xue, X. Li, R. Liu, J. Kong, Z. Zuo, X. Su, Q. Zhang, Y. Yin, Y. Cai, Advances in Photothermal Catalysis: Mechanisms, Materials, and Environmental Applications, ACS Applied Nano Materials. 7 (2024) 26489–26514. https://doi.org/10.1021/acsanm.4c00598.

[31] L. Lan, Y. Shao, Y. Jiao, R. Zhang, C. Hardacre, X. Fan, Systematic

study of H2 production from catalytic photoreforming of cellulose over Pt catalysts supported on TiO2, Chinese Journal of Chemical Engineering. 28 (2020) 2084–2091. https://doi.org/10.1016/j.cjche.2020.03.030.

[32] J. Xu, P. Zhou, C. Zhang, L. Yuan, X. Xiao, L. Dai, K. Huo, Striding the threshold of photocatalytic lignin-first biorefining via a bottom-up approach: from model compounds to realistic lignin, Green Chemistry. 24 (2022) 5351–5378. https://doi.org/10.1039/D2GC01409B.

[33] Y. Miao, Y. Wang, C. Jiang, Y. Zhao, T. Zhang, Photothermal recycling of polylactic acid into H2 and gaseous C1 products via cooperative depolymerization and reforming, Science China Chemistry. (2025) 1–7. https://doi.org/10.1007/s11426-025-2613-3.

[34] J. Wu, Y. Qu, H. Chen, J. Fan, J. Ding, B. Ren, MoSSe/SiC heterojunction with vacancy defect for high-efficiency photocatalytic water splitting, Applied Surface Science. 710 (2025) 164007. https://doi.org/10.1016/j.apsusc.2025.164007.

[35] S.A. Grudinkin, S.A. Kukushkin, A. V. Osipov, N.A. Feoktistov, IR spectra of carbon-vacancy clusters in the topochemical transformation of silicon into silicon carbide, Physics of the Solid State. 59 (2017) 2430–2435.

CHAPTER X: H_2 production by biomass-derived compounds

CHAPTER X: H_2 Production by biomass-derived compounds

10. Carbon Nitride Photocatalysts for Improved H_2 Production in different Water Matrices[9]

10.1 Introduction

g-C_3N_4 based-photocatalysts were prepared from melamine, exfoliating the carbon nitride with a double microwave-assisted thermal treatment. The presence of a small amount of Pt (0.75 wt%) as co-catalyst led to an efficient H_2 production through visible-light glucose photoreforming, also changing the water matrices from ultrapure water to wastewater or seawater. Interestingly, the examined photocatalyst showed higher H_2 evolution in wastewater and in seawater than in ultrapure water in overall water splitting tests (i.e., without the addition of glucose). The photocatalyst demonstrated high stability and reusability in the different water matrices. To increase its applicability, the photocatalyst was also immobilized in film form, while maintaining remarkable photocatalytic activity and showing higher apparent quantum yield at 420 nm (9.5%) compared to the sample in the powder form (3%). The easiness of the synthesis and the effective performance make this approach promising for the development

[9] The data present in this chapter were published in the paper:
"Carbon Nitride photocatalyst for improved H_2 production in different water matrices"
Maria Teresa Armeli Iapichino, M.José Sampaio, C. Gomes Silva, J. Luís Faria, A. Gulino, A.Ferlazzo, E.La Greca, L. F. Liotta, S. Scirè, R. Fiorenza, Chemistry Select V.10, 2025, 23656549

of a new class of visible light driven photocatalysts for the sustainable H_2 production.

10.1 Sample Preparation

The synthesis of bare carbon nitride (referred as GCN) was performed by thermal decomposition of urea (CAS: 57-13-16; Sigma Aldrich) and melamine (CAS: 108-78-1; Sigma Aldrich) as reported elsewhere[1]. Briefly, 2g of melamine or urea was placed in quartz capsule and put in a microwave muffle under static air atmosphere at 550 °C. The resultant material was powdered in a mortar, rinsed with ultrapure water to remove any impurities, filtered and dried overnight at 80 °C. The samples obtained from melamine underwent to a second thermal treatment. The powders were spread in an open crucible, placed in a microwave muffle and treated at 500 °C for 2 h, to carry out the exfoliation of the sample[2]. In the case of urea precursor, the second thermal treatment was not made to avoid the complete degradation of urea[3]. Platinum (nominal 1% wt) was added to GCN by incipient wetness impregnation. In particular, 0,021 g of the platinum precursor (Hexachloroplatinic(IV) acid hexahydrate 99.9%) has been solubilized in 2 mL of water; afterwards, this solution was added drop by drop in a flask containing carbon nitride and treated in an ultrasonic bath for 90 minutes. Then the resultant slurry was dried at 80°C for one night. Subsequently, to reduce the Pt, the sample was placed for 1 hour in an oven under a nitrogen environment and then it was treated with a flow of hydrogen at 200°C for 3 hours and successively cooled under nitrogen. The as-prepared catalysts were coded as Pt_GCN_M (from melamine), and Pt_GCN_U (from Urea) (Fig.1).

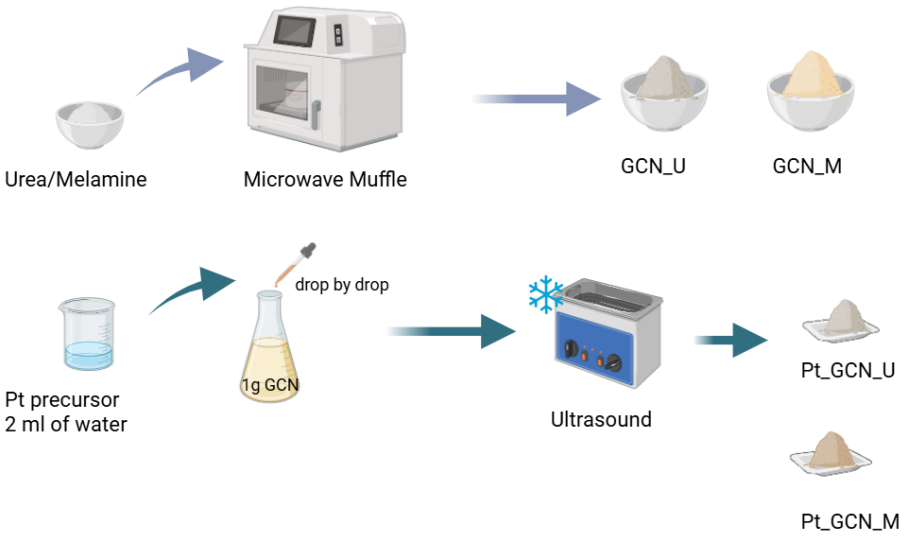

Figure 1 *Steps of photocatalyst preparation.*

10.1.1 Catalyst film preparation

A polymer solution was prepared to anchor the Pt_GCN_M to the substrate i.e. the Polyvinylidene fluoride (PVDF) [3,4]. Briefly, 0.07 g of polyvinylpyrrolidone (PVP) was dissolved in 6.0 mL of N-Methyl-2-pyrrolidone (NMP) via sonication for 3 h at room temperature. Then, 1.07 g of PVDF was added to the solution, stirring at 40ºC for 48 h. The resulting polymeric solution was stored in a glass vial. Several steps were followed to perform the immobilization: 1) the polymeric solution was spread using a knife casting applicator (Elcometer 3580, Warren, MI) to create a PVDF film; 2) about 0.5 g of catalyst was dispersed evenly; 3) the photocatalyst/film system was dipped several times (5 times for periods of 5 min) in distilled water to promote the immobilization of the photocatalyst via phase inversion. Finally, it was stored in a glass box containing ultrapure water until use. The as-prepared catalyst was coded as Film_Pt_GCN_M (Fig.2).

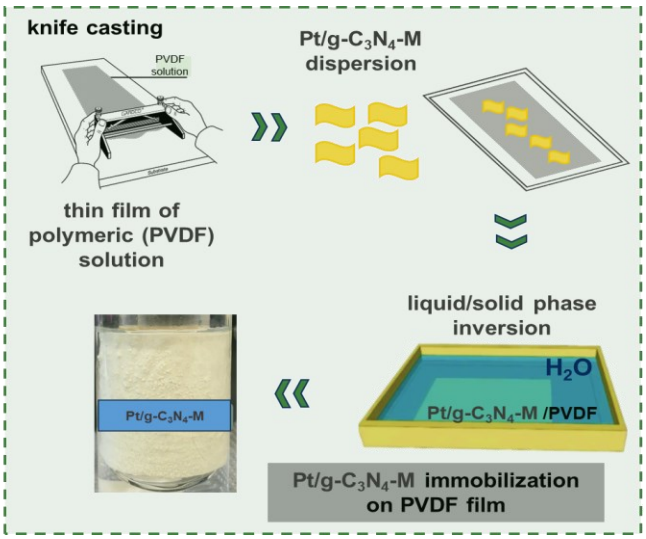

Figure 2 *Film Preparation.*

10.2 Experimental conditions

The mass of photocatalyst was fixed at 50 mg, and it was dispersed in 100 mL of solution with varying concentrations of glucose (0.02 M, 0.05 M, 0.1 M), under stirring, using different water matrices as source of protons. To study the glucose photoreforming reaction in basic and acidic environments, the pH was changed adding a solution 0.1M of NaOH (303126 Panreac) or 0.1M of HNO_3 (7697-37-2 Honewell,Fluka) to obtain a pH>9 or a pH=2, respectively.

10.3 Experimental Set-up

The measurements conducted in this study were performed using the experimental apparatus described in Section 7.2, under the same conditions.

10.4 Effect of g-C_3N_4 precursors

Initially, the performance of the Pt/g-C_3N_4 catalysts obtained from different precursors as melamine (Pt_GCN_M) and urea (Pt_GCN_U) was evaluated by varying the concentration of the glucose used as sacrificial agent. From the Figs.3 A-B, it can be observed that independently to the employed photocatalyst, the H_2 production increased with the glucose concentration, as expected due to the essential role of the sacrificial agent to promote the charge carriers separation and the H_2 formation [5].

Moreover, it is possible to note that the Pt_GCN_M (Fig. 3B) showed a higher H_2 production compared to the Pt_GCN_U (Fig. 3A). This finding is probably ascribed to the employed preparation method. Indeed, the g-C_3N_4 synthetized from melamine was submitted to two treatments (microwave-assisted thermal see the experimental section) to favour its exfoliation, that promoted, as reported, an optimal C/N ratio (around 0.75)[6,7] with a complete thermal polycondensation of melamine, whereas to avoid the complete degradation of urea it was not possible to exfoliate the GCN_U sample[2]. Furthermore, as reported, the exfoliation of g-C_3N_4 to quantum dots or in nanosheet forms drastically improves its piezo-photocatalytic performance due to increased active sites and reduced electrons-holes recombination[8].

A further improvement of the photocatalytic performance of the carbon nitride was obtained with the introduction of vacancies or heteroatoms during the exfoliation process that can lead to defect-rich g-C_3N_4 surfaces[9,10].

Therefore, the exfoliation process of g-C_3N_4 is beneficial also for the photocatalytic H_2 production[11][12] due to the delamination into several layers that facilitates the charge transfers[13].

The preparation of g-C_3N_4 using microwave-assisted heating offers several advantages compared to other reported synthesis methods as it eliminates the need for acid treatments or hard templating techniques with toxic solvents. Moreover, it is more cost-effective compared to the convectional heating due to the faster heating and cooling rates[14].

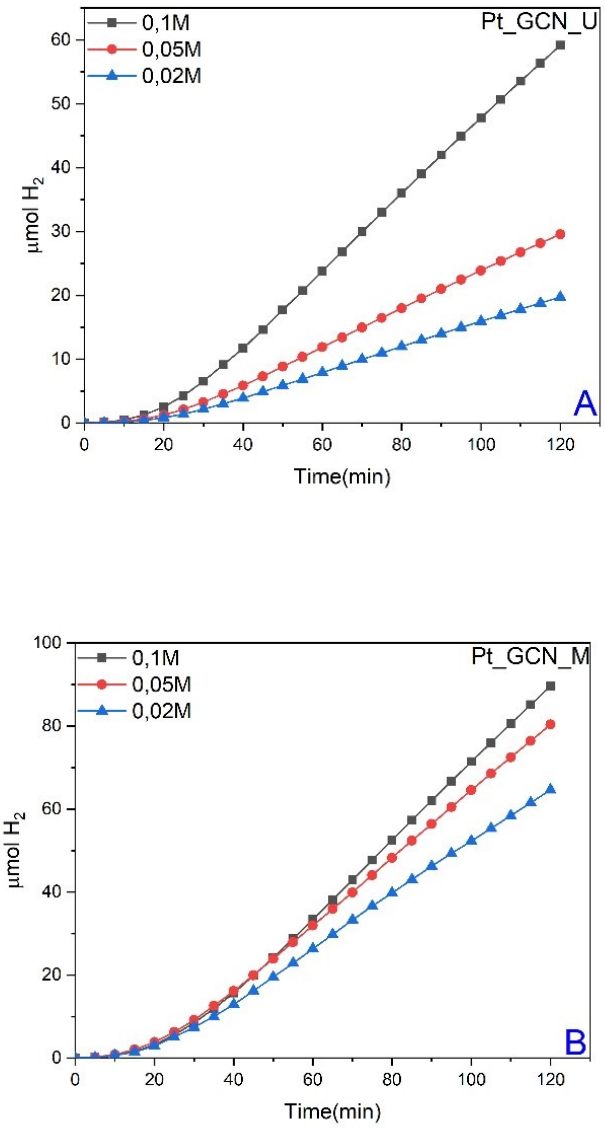

Figure 3 *H_2 evolution from visible light glucose photoreforming using the Pt/g-C_3N_4-based samples: A) Pt_GCN_U; B) Pt_GCN_M*

10.5 Effect of pH in the glucose photoreforming reaction

The photoreforming reaction is driven and influenced by several factors such as the light intensity, the reaction temperature, the employed photocatalyst. Among these, the pH plays a decisive role in the overall reaction results[15]. The presence of a polar, aprotic solvent, for example, can facilitate the desorption products from the photocatalyst surface increasing also the selectivity [16]. Alkaline conditions can suppress the mineralization mechanisms[17] and enhance the holes capture[18].

Fig.4 shows the H_2 production with the Pt_GCN_M photocatalyst at different pH values. The H_2 evolution increased up to 3 times at pH>9 compared to the neutral pH, with almost no production at pH=2. Glucose undergoes to pH-dependent conformational changes, which can affect the photocatalytic reaction. Previous studies have demonstrated that the dissociation of glucose at high pH can increase the glucose absorption. This enhancement is attributed to electrostatic interactions between the substrate and the photocatalyst[15,19].

As a result, there is an improvement in the glucose conversion and the H_2 formation, with a direct correlation between the glucose conversion and the alkalinity of the reaction mixture[15].

As reported, indeed, alkaline pH favours the glucose conversion (≥ 75%) into firstly fructose and after into ascorbic acid, lactic acid, and formic acid with the release of H_2 molecules that further promote the photoreforming reaction[15]. On the contrary, at acidic pH the glucose conversion is quite low (5-7%)[20].

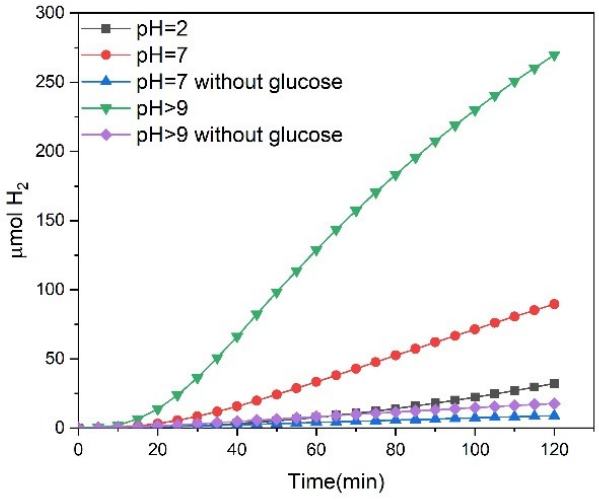

Figure 4 H_2 evolution from visible light glucose photoreforming (0.1 M) at various pH using the Pt_GCN_M sample.

We have evaluated the H_2/CO_2 ratio at both pH=7 and pH>9. At neutral pH, the measured H_2/CO_2 ratio was 0.2, which is much lower than the stoichiometric H_2/CO_2 ratio = 2, accordingly to the following reaction (1):

$$(1)\ C_6H_{12}O_6 + 6H_2O \rightarrow 12H_2 + 6CO_2$$

On the contrary, at pH>9 the H_2/CO_2 ratio was 6, higher than the stoichiometric one. This confirmed that the alkaline environment promoted the formation of intermediates, accordingly to literature for the g-C_3N_4-based photocatalysts (transformation into fructose and after conversion into lactic acid) [21,22] that favoured the evolution of additional H_2 molecules, whereas in acid conditions only the glucose photo-oxidation took place with a greater CO_2 production than H_2.

As expected, the presence of glucose was fundamental to favour the H_2 evolution, indeed in the tests without glucose, even at pH>9, the H_2 production was low (Fig.4).

10.6 Effect of different water matrices

It was also evaluated, for possible scale-up applications, the photocatalytic activity of Pt_GCN_M using different water matrices at pH= 7 *(Fig.5)*.

The tests referred to wastewater (WW) collected at an urban sewage treatment plant located in northern Portugal, while the tests referred to seawater (SW), coming from the Atlantic Ocean (in the Table 1 of the supporting information is reported the chemical analysis of the used WW and SW).

From the Fig.5A it is possible to note that the Pt_GCN_M photocatalyst performs quite well in the seawater and wastewater, providing however a lower H_2 evolution compared to the test with ultrapure water. Probably, in this case the presence of several organic and inorganic species in the SW and WW can hinder the surface-active sites of the photocatalyst. As expected, in the tests without glucose (overall water splitting tests) the production of H_2 was lower compared to the tests with glucose, but in this case the best performance was obtained with the wastewater (Fig.5B). Interestingly, also the H_2 production with the seawater was higher than the tests with ultrapure water (Fig. 5B), pointing to that for the overall water splitting tests these water matrices allowed to obtain an improved H_2 evolution. Indeed, another effect of the presence of inorganic species in the SW and WW, such as nitrates and nitrites, dissolved organic matter and humid acids, when excited by a light source, is the generation of strong reactive species that can act as holes scavengers[23], thus favouring the protons reduction into H_2 by the photoelectrons in the overall water splitting reaction.

Table 4 Chemical analysis of the used WW and SW.

	Wastewater (WW)	Ocean Seawater (SW)
pH	7.45	7.88
Conductivity (mS/cm)	808	48
Turbidity (NTU)	4.60	0.65
Nitrates (mg NO_3^-/L)	<0.819	<0.819
Nitrites (mg NO_2^-/L)	0.01	0.02
Phosphates (mg P/L)	<0.006	<0.006
Total Suspended solids (mg/L)	14	54
Iron (mg/L)	<0.005	<0.005
Nickel (mg/L)	<0.005	<0.005
Chromium (mg/L)	<0.005	<0.005
Cadmium (mg/L)	<0.005	<0.005
Zinc (mg/L)	0.130	0.011
Lead(mg/L)	<0.005	<0.005
Copper (mg/L)	<0.005	<0.005
Cobalt (mg/L)	<0.005	<0.005
Manganese (mg/L)	0.020	<0.005
Sodium (mg/L)	118.75	dilutes 1000x and still remained outside the curve
Magnesium (mg/L)	9.37	1227.00
Calcium(mg/L)	41.32	567.90
Aluminium (mg/L)	0.134	0.023
Boron (mg/L)	0.066	2.655
COD (mgO_2/L)	37	difficult to analyse due to the presence of chlorides
BOD_5 (mgO_2/L)	29	

On the contrary, in the glucose photoreforming tests (Fig. 5A), the presence of glucose guaranteed the consumption of the holes and consequently the presence of these reactive species generated in the SW and WW became detrimental for the H_2 production.

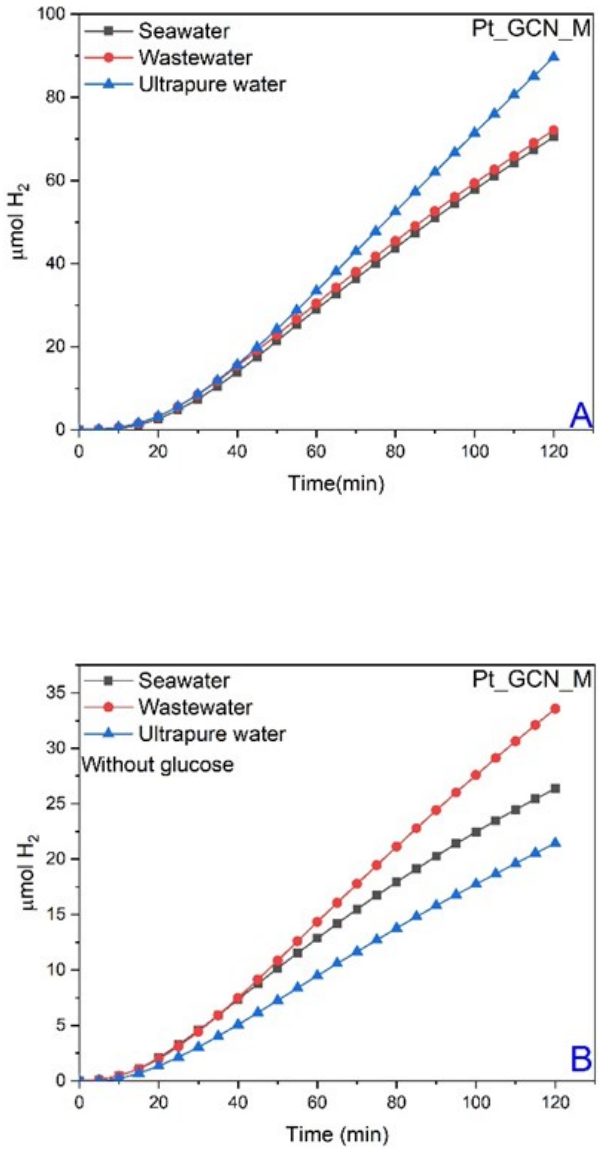

Figure 5 *A) Photocatalytic activity obtained using glucose (0.1M); B) Photocatalytic results obtained in the absence of glucose.*

10.7 Stability and reuse of the photocatalyst

The continuous time-on irradiation tests were carried out on the most active sample, i.e. the Pt_GCN_M catalyst (Fig. 6) examining its photocatalytic behaviour in the visible light glucose photoreforming reaction using the different water matrices. It is possible to note that the photocatalyst, using ultrapure and waste waters did not present any deactivation but remains stable beyond 10 hours of irradiation. On the contrary, in the case of seawater a deactivation of the catalyst occurred after 5 hours of irradiation. This is probably due to high salinity of the SW that can occlude, during the time, the surface of the catalyst leading to a decrease in the light absorption and consequently in the photocatalytic activity[24]. However, in the reuse tests (Figs. 7), where after each runs the catalyst was filtered, washed and dried at 60°C overnight to eliminate the presence of salts, a constant H_2 production was maintained even using the seawater (Fig. 7B).

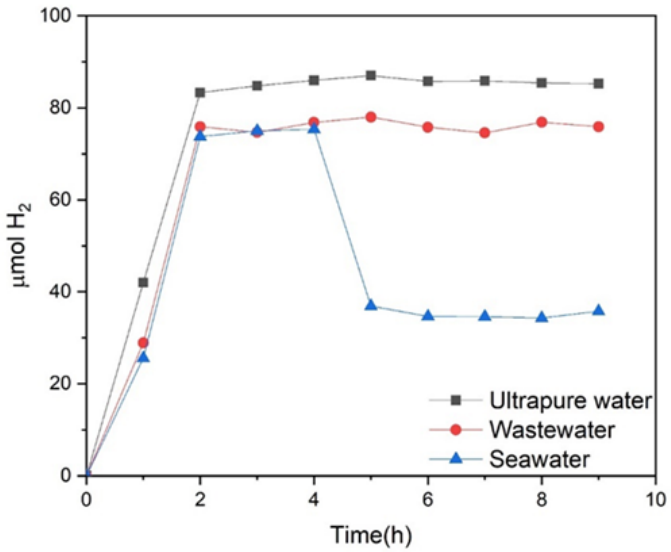

Figure 6 *Catalyst (Pt_GCN_M) performance in different aqueous matrices for the visible light glucose (0.1M) photoreforming at pH=7.*

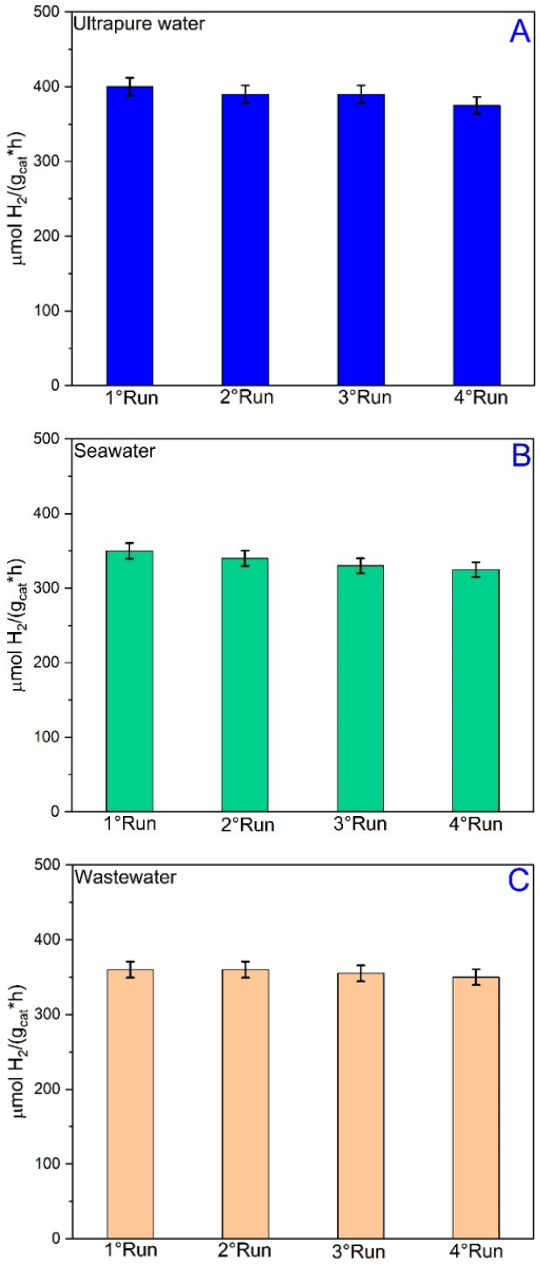

Figure 7 *Catalyst (Pt_GCN_M) reuse tests in different aqueous matrices: A) Ultrapure water; B) Seawater; C) Wastewater. After each run (4 h of irradiation) the catalyst was filtered, dried and re-used.*

In the *Table 1* is reported a comparison between some of the various g-C_3N_4 based photocatalysts investigated in the literature for the visible/solar glucose photoreforming. It is important to underline that a quantitative comparison is very difficult due to the different experimental setups used by the various research groups. However, with the here investigated Pt_GCN_M sample a remarkable H_2 production was obtained considering also the very low amount of Pt added as co-catalyst (*Table 2*). A higher H_2 evolution can be produced preparing ternary compounds with the addition of TiO_2 [25] or with the formation of peculiar composites with rare-earth oxides as the Dysprosium oxide under solar light irradiation[26]. However, this latter approach can limit the possible scale-up applications due to the low availability of the rare-earth oxides.

Table 5 *Visible/solar light-photocatalytic H_2 production by glucose photoreforming of some of the reported g-C_3N_4-based photocatalysts.*

Catalyst	Experimental conditions	Irradiation source	H_2 production ($\mu mol/g_{cat} \cdot h$)	Ref.
0.75 wt% Pt_GCN_M	100 mL of 0.1 M glucose solution in ultrapure water, 50 mg catalyst	4 visible-LED ($\lambda_{exc.}$= 420 nm), 45 mW cm^{-2}, each one)	425	this work
1 wt% Pt/g-C_3N_4	100 mL of 0.1 M glucose aqueous solution, 50 mg catalyst	LED λ_{max} = 440 nm, 580 mW·cm^{-2}	344	[27]
7% wt Pt/ g-C_3N_4 monolith	5 M NaOH aqueous solution (25 mL) containing H_2PtCl_6 and glucose, 25 mg catalyst	300 W Xenon lamp with a 420 nm cut-on filter	4	[28]
5 wt% $Ti_3C_2T_x$/g-C_3N_4	50 mL of 0.2 M glucose aqueous solution, 25 mg catalyst	430 nm LED, 50 mW cm^{-2})	28	[29]
10 wt% g-C_3N_4/1 wt% Pt/TiO_2	100 mL of 0.2M glucose aqueous solution, 50 mg catalyst	LED, 440 nm, 500 mW cm^{-2}	710	[25]
Dy_2O_3/n doped-g-C_3N_4	170 mL of 5 g/L glucose solution, 100 mg catalyst	300 W xenon lamp (λ> 420 nm)	510	[26]

10.8 Pt_GCN_M in film form

The performance of the Pt_GCN_M deposited in film form was also investigated (Fig. 8). Interestingly, the H_2 production in the ultrapure water glucose photoreforming after 2 h of visible irradiation (75 μmol H_2) was only slightly lower compared to the catalysts in powder form (85 μmol H_2) after 2 h of irradiation (Fig.5 A). On the other hand, the H_2 evolution obtained with the seawater and wastewater (Figs. 8B and 8C), is lower compared to the results obtained with the powder catalyst (Fig. 5A). In fact, after 2 h of radiation, 20 and 25 μmol of H_2 were produced in the case of seawater, and wastewater, respectively, that are lower compared to 70 μmol H_2 with SW and 72 μmol H_2 with WW after 2 h of visible irradiation, achieved with the powder catalyst.

The difference in hydrogen production when using the catalyst in powder or film form can be related to the different amount of catalyst really involved in the reaction.

Indeed, in the film form a part of the catalyst was not available to the reactants, being buried inside the bulk of the film, thus negatively affecting the overall catalytic performance. Moreover, both SW and WW contain various organic and inorganic species that rapidly adsorb at the catalyst surface and may occupy the active sites of the catalyst hindering photon activation. This effect should be less pronounced when using powder photocatalyst, as the particles are suspended throughout the solution, with the exposed surface of each particle being fully available for the reaction. Nevertheless, using immobilized photocatalysts overcome technical limitations resulting from the use of powder catalysts, as for example the necessity of steps of filtration or

centrifugation for catalyst reusing. Furthermore, it is possible to better exploit the absorption of the incident visible light. Also, in the film form the photocatalyst exhibited good stability after 3 consecutive runs in all the tested water matrices (Fig.8).

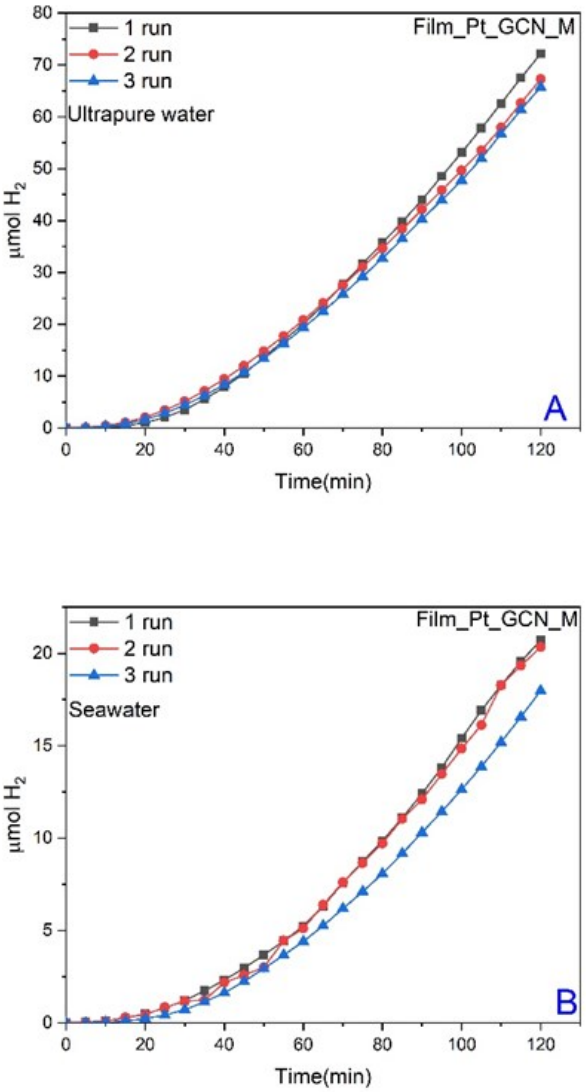

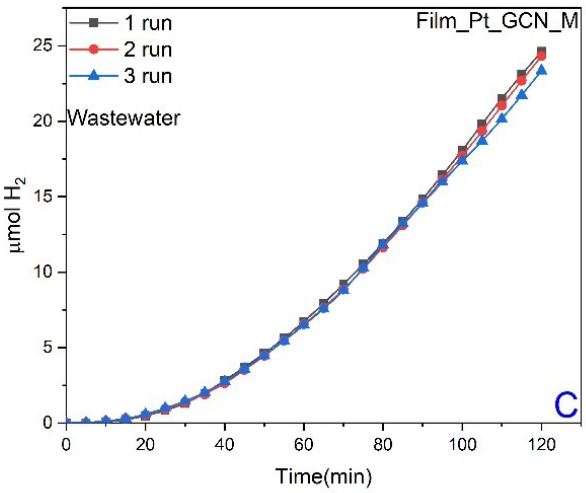

Figure 8 *H_2 evolution from visible light glucose photoreforming (0.1 M) at pH=7 using different water matrices and the Pt-GCN-M in film form. A) Ultrapure water; B) Seawater; C) Wastewater.*

To define the advantages of using immobilized Film_Pt_GCN_M, the apparent quantum efficiency (AQE)[30] at 420 nm was calculated (equation 1-2) considering the tests in the ultrapure water.

(1) $$AQE = \frac{2\times the\ \text{evolved}\ H_2\ \text{molecules number(Ne)}}{the\ incident\ photos\ number(Np)} * 100$$

(2) $$\mathrm{AQE} = \frac{2\times n\times NA\times h\times c}{A\times I\times t\times \lambda}$$

Where n is the amount of H_2 molecules produced (time in seconds), NA the Avogadro constant (mol^{-1}), h the Plank constant (mJs), c the speed of light in vacuum (ms^{-1}), A the irradiated area (152 cm^2 and 88 cm^2 for Pt_GCN_M powder and Film_Pt_GCN_M, respectively), I (J $s^{-1}cm^{-2}$) the intensity reaching the photocatalysts (I = 139 mW cm^{-2} and I = 90 mW cm^{-2} for powder and immobilized photocatalysts, respectively), and λ (λ_{exc}= 420 nm) the wavelength of the monochromatic LED.

With the use of the immobilized film photocatalyst, a higher AQE (9.5%) was obtained compared to powder photocatalyst (3%). This pointing to the higher efficiency of the photocatalyst in the form of film that could have potentiality for applications in continuous flow systems and large-scale operations. Furthermore, the obtained value of AQE of the Film_Pt_GCN_M is higher compared to values reported in the literature for the other g-C_3N_4-based materials in powder form (in the range 0.5-5%)[31], being only lower respect to the CDots-C_3N_4 sample investigated by *Liu et al.* (AQE of 16% at 420 nm) obtained for the visible-light photocatalytic water splitting reaction[32].

Although the results obtained with the Film_Pt_GCN_M and powder Pt_GCN_M demonstrated promising potential for H_2 production in actual water matrices, further studies are needed to address critical challenges posed by impurities and biological activity in untreated sources such as seawater and wastewater [24,33,34]. The presence of inorganic ions, emerging contaminants and microorganisms in some case can compromise catalyst efficiency and durability by surface fouling, light scattering and charge carrier quenching, in other case, as in the overall water splitting reactions, a limited amount of these species can have beneficial effects acting as holes scavengers.

These findings reinforce the need to develop robust photocatalytic systems alongside selective pre-treatment strategies, while also considering a careful cost–benefit balance to ensure the feasibility of a large-scale photocatalytic implementation for H_2 production.

10.9 Characterizations

The optical, the structural and the surface properties of the best samples were determined by UV-DRS, PL, FTIR, XRD, SEM, TEM, XPS and N_2 physisorption measurements. Moreover, the existing differences between the GCN_M sample after only one thermal treatment (coded as Bulk_GCN_M) and the exfoliated one (GCN_M), namely the carbon nitride used for the deposition of Pt and employed for the photocatalytic tests, were evaluated.

The estimation of the optical band gap (E_g) was carried out by the modified Kubelka-Munk function[35] and the results together with the values of the measured BET surface area are reported in the *Table 3*. The microwave-assisted heating treatments of GCN_M induces exfoliation of the material through a combination of layer-by-layer thermal oxidation and layer splitting. This process, which disrupts the van der Waals and H_2 bonding interactions between layers, results in the formation of thinner plates[34], ultimately leading to an increased surface area of GCN_M compared to the unexfoliated sample, i.e. the Bulk_GCN_M. The obtained surface area values are in accordance with the literature for the carbon nitride -based photocatalysts [36,37].

No substantial variations in the E_g values (*Table 3,* Fig.9), were observed, so this parameter cannot be considered as critical factor for the photocatalytic performance in the examined photoreforming reaction.

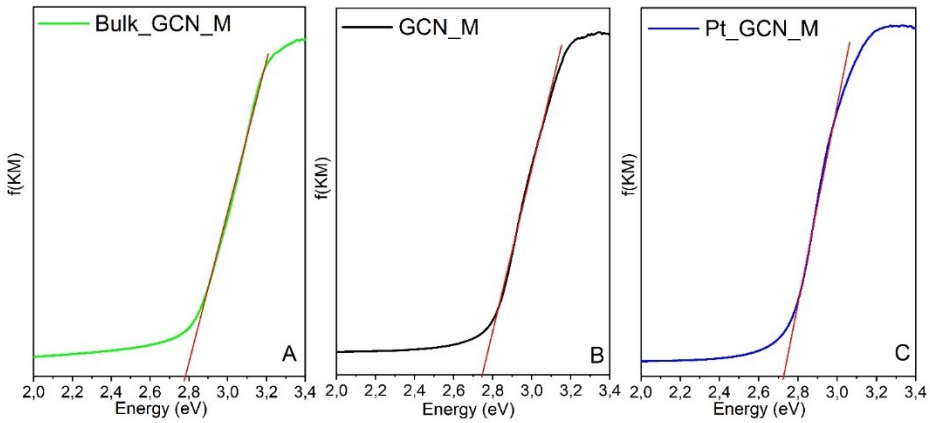

Figure 9 *Evaluation of the optical bandgap of the examined samples by the Kubelka Munk function obtained from the UV-DRS spectra. (A) Bulk_GCN_M; (B) GCN_M; (C) Pt_GCN_M.*

Table 6 *Optical and textural properties of the examined samples.*

Catalyst	Surface area ($m^2\ g^{-1}$)	Band-gap (E_g)
Bulk_GCN_M	8 ± 3	2,77
GCN_M	45± 3	2,75
Pt_GCN_M	46 ± 3	2,74

The broad PL peak observed at 450 nm (Fig.10) is caused by the electrons transfer from the conduction band (CB) to the valence band (VB) of the graphitic carbon nitride[38]. This band is related to the band-band excitation, mostly caused by n-π* electronic transitions involving lone pairs of nitrogen atoms in g-C_3N_4 [39]. The exfoliation treatment led to a decrease of the peak intensity, more evident in the presence of platinum that led also to a slight blue shift. Notably, the sample in the film form showed the lowest PL peak intensity.

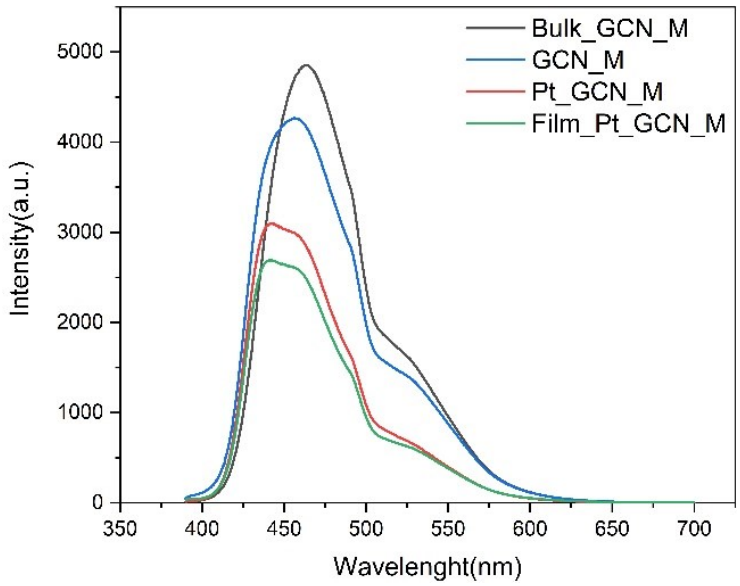

Figure 10 *Photoluminescence spectra of the analysed composites.*

As reported, the lower is the intensity of the PL band, the higher is the charge carriers separation[40]. This pointed to as the exfoliation process, the addition of the Pt co-catalyst and the immobilization in the film form promoted an effective charge carriers separation, thus explaining the higher AQE compared to the sample in powder form.

In order to verify the formation of the carbon nitride, XRD, SEM, TEM and FT-IR analyses were carried out.

From the XRD patterns (Fig.11) it was possible to note that the diffraction peaks at 2θ = 12.9° and 27.4°, related respectively to the crystalline planes (100) and (002) of tetragonal carbon nitride in the graphitic form[41]. The absence of a signal for Pt is due to the low amount of the metal (1 wt% nominal, 0.75 wt% measured by ICP-OES) deposited on the carbon nitride.

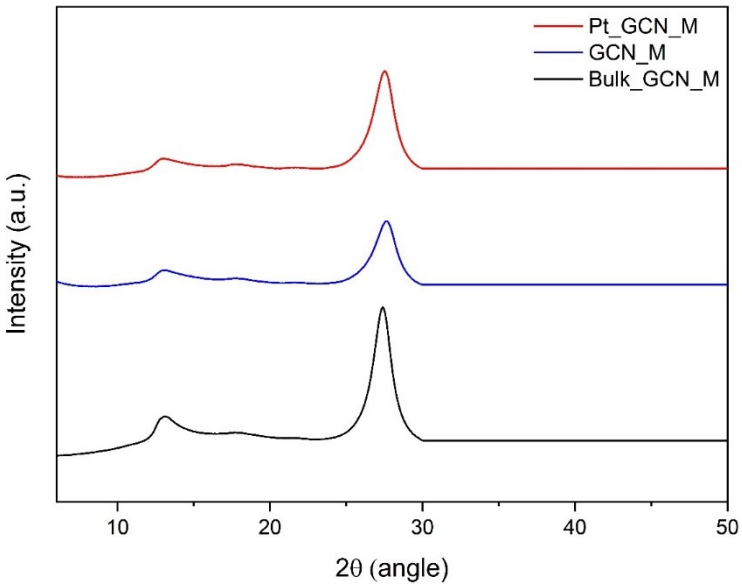

Figure 11 *XRD patterns of the examined samples.*

The morphology of the samples was examined by SEM and TEM measurements and the corresponding images reported in the supporting information (Figs. 12).

The bulk material is constituted by compact aggregates of g-C_3N_4 sheets, which arise from the stacking of multiple layers (Fig. 12a). This stacked structure leads to a material with very low specific surface area (*Table 3*), as well-documented in the literature [34,39,42].

After the bulk material suffers a second thermal treatment. Due to the occurrence of the exfoliation process, it is possible to indicate that the stacking interactions between g-C_3N_4 layers are mainly driven by van der Waals forces and hydrogen bonds, which are unstable at high temperatures. Consequently, the exfoliation process produces thinner nanosheets (Fig. 12b) and leads to a significant increase in the surface area *(Table 3).*

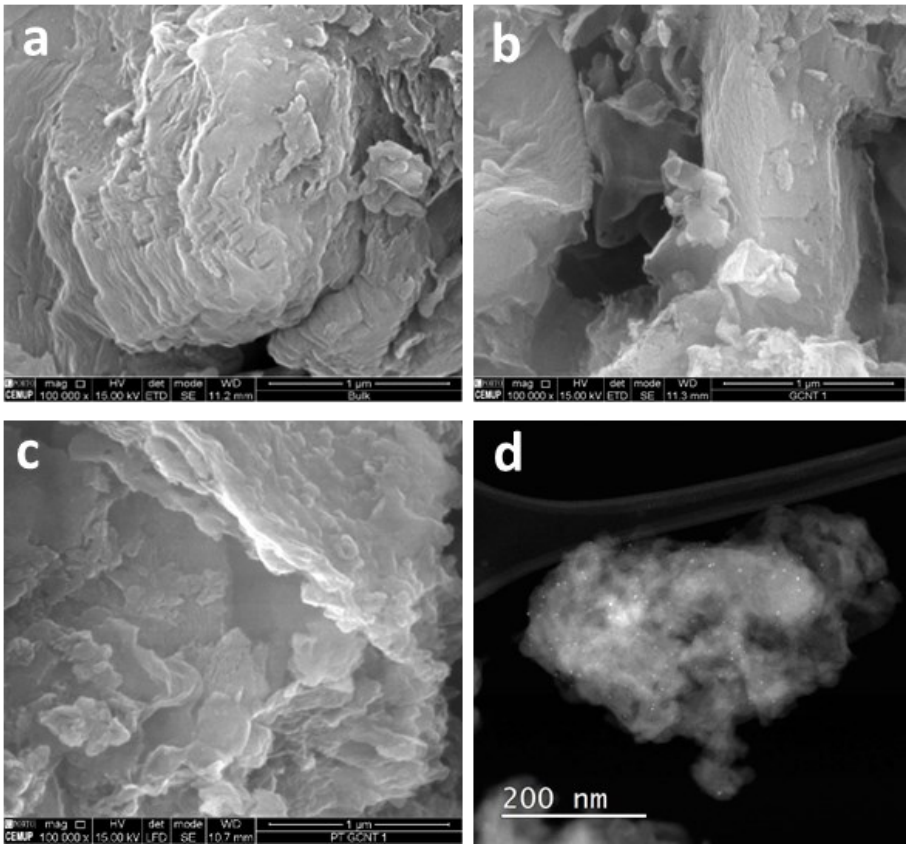

Figure 12 *SEM images of bulk g-C_3N_4 (a), exfoliated g-C_3N_4 (b) and Pt/g-C_3N_4 (c). TEM image of Pt/g-C_3N_4 (d)*

It was also previously reported that the presence of such low loading of Pt nanoparticles doesn't interfere with the morphology and surface area of g-C_3N_4 based photocatalysts (Fig.12c) [31]. Additionally, TEM analysis (Fig.12d) confirms the homogeneous distribution of platinum nanoparticles within the g-C_3N_4 matrix[34]. All the samples in the FTIR spectra (Figs.13) showed a sharp peak at around 805 cm^{-1}, corresponding to tri-s-triazine ring units. A broad band between 3000 and 3500 cm^{-1}, was ascribed to the stretching of amines and amides, overlapping with the stretching of hydroxyl groups of adsorbed water molecules at the catalyst

surface, as reported in the literature[39,42]. The main characteristic peaks of GCN in the range 1210–1530 cm^{-1} are commonly ascribed to stretching vibrations of aromatic heptazine derived from repeating units as well to C-H, O-H, C-O, and C-O-C bonds[43], whereas the C=N amide bond was at 1545 cm^{-1} . The immobilization of GCN powder on the film (Figs.13B-13C) was confirmed by the presence of the bands in the range 1210-1530 cm^{-1} observed in the Film_Pt_GCN_M sample (Fig.13C). It is possible to note a shift of the band at 3141 $cm^{-1}$of Pt_GCN_M to 3389 cm^{-1} of Film_Pt_GCN_M (Fig. 13B), which is related to the higher amount of –OH groups in the film, resulting from the adsorbed water molecules on the Film_Pt_GCN_M surface.

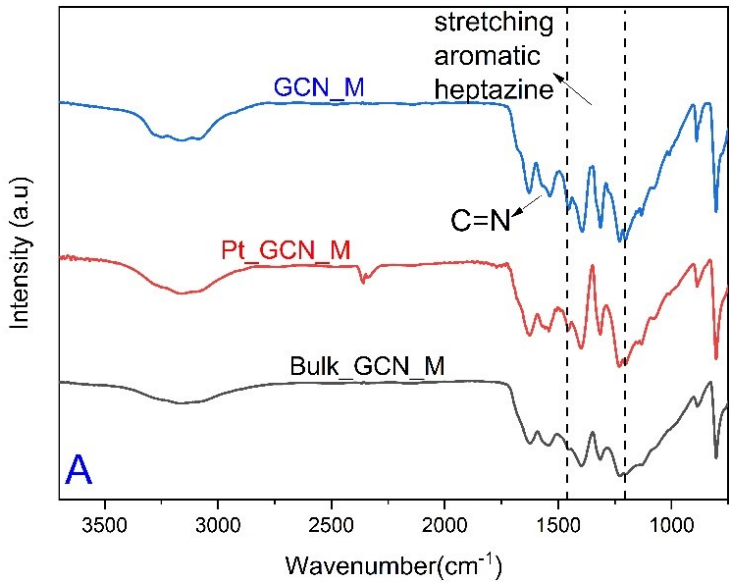

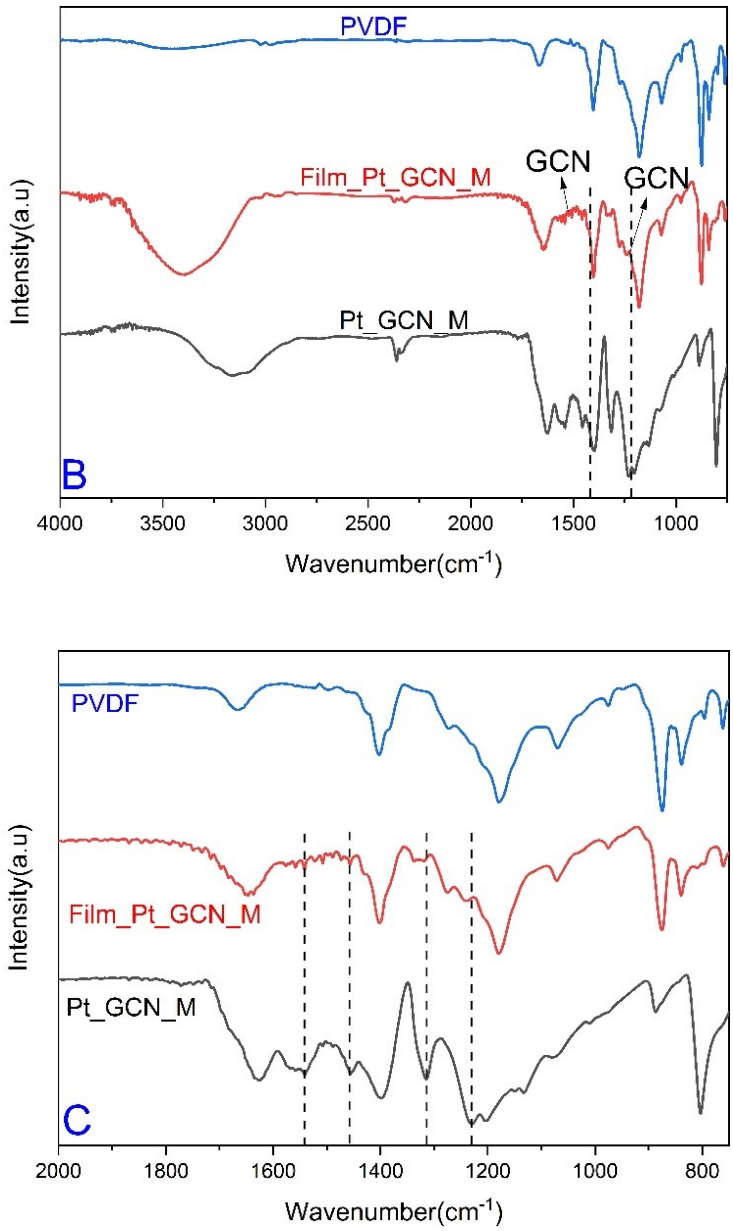

Figure 13 *FT-IR spectra: A) examined samples; B) Comparison between film and powder; C) Zoom in the range of the carbon nitride bands.*

Figure 14A shows the normalized XP spectra of the Bulk_GCN_M GCN_M and Pt_GCN_M samples, in the C1s binding energy region, which always consists of two peaks. According to the already reported literature data on similar systems, the peak at 285.0 eV is due to some hydrocarbons and adventitious carbon[41,44]. The relative intensity of this signal is larger for bulk C_3N_4 while decreases as a consequence of the exfoliation that evidences internal and clean layers. The band at 288.5 eV for bulk C_3N_4 (FWHM = 2.4 eV), consistent with the sp^2 -C=N- bond of the CN heterocycles, narrows after exfoliation (FWHM = 1.6 eV) and moves at 288.3 eV. The addition of Pt does not cause any relevant band broadening variation (FWHM = 1.7 eV) but we noted an additional sizeable shift at 288.2 eV.

Figure 14B illustrates the normalized XP spectra of the same samples, in the N 1s binding energy region. A rather sharp peak at 399.2 eV was observed for Bulk_GCN_M (C=N-C and C_3–N states of the g-C_3N_4) while the exfoliated compound shows a peak at 398.9 eV[41,44]. The addition of Pt resulted in a blue shift of this peak that now appears at 399.6 eV. This observation suggests that the =N- group is now interacting with the platinum.

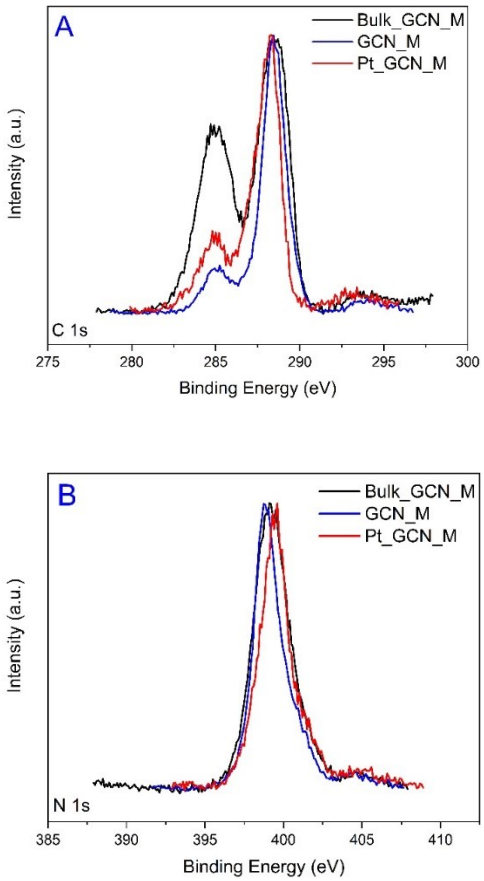

Figure 14 *XPS spectra: A) Al Kα excited XPS of the examined samples in the C 1s binding energy region. B) Al Kα excited XPS of the examined samples in the N 1s binding energy region. The intensities of these spectra were normalized.*

The XPS spectrum of the Pt_GCN_M in the Pt 4f binding energy region is reported in the Fig.15. This spectrum is rather noisy but the two 4f $_{7/2,\ 5/2}$ spin-orbit components are clearly visible at 74.9 and 78.2 eV with a 3.3 eV spin-orbit separation, typically of partially oxidated Pt due to the XPS experimental conditions[45,46]. This observation agrees well with the blue shift observed for N 1s states, upon addition of Pt, since N now donates electrons to Pt in a N-Pt bond interaction.

In summary, the exfoliation of the carbon nitride using melamine as precursor, led to increase the surface area (*Table 2*) compared

to non-exfoliated sample, favouring the deposition of Pt, and consequently the photocatalytic activity. In particular, under visible-light irradiation the Pt_GCN_M showed an efficient H_2 production from the glucose photoreforming also employing different water matrices. The presence of Pt increased the charge carriers separation, further improved by the immobilization through the film form (as stated by PL spectroscopy). The FTIR, and the XRD, stated the successfully formation of the graphitic carbon nitride, whereas the interaction of Pt with the g-C_3N_4 was verified by XPS. The absorption of the visible light led the excitation of the electrons from the valence band to the conduction band of the carbon nitride, with the consequent formation of holes in the valence band. The recombination of e^- and h^+ was efficiently limited by the presence of Pt on the surface of g-C_3N_4. The holes oxided both water and glucose to obtain the necessary protons for the visible-light production of hydrogen, whereas the electrons moved from the conduction band of g-C_3N_4 to the Fermi level of Pt reducing the formed protons to H_2[27,47]. The performance of the examined visible-light driven photocatalyst are promising also for possible scale-up applications.

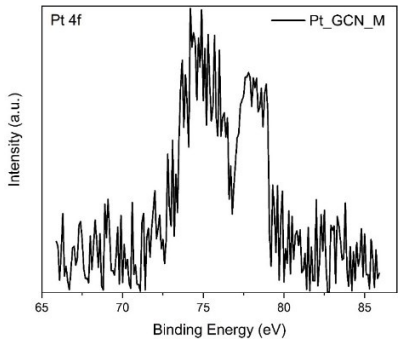

Figure 15 *Al Kα excited XPS of the exfoliated C_3N_4 after the addition of Pt, in the Pt 4f binding energy region.*

10.10 Conclusion

The exfoliation of graphitic carbon nitride (prepared from melamine) with a doble microwave-assisted thermal treatment, followed by the impregnation of Pt as co-catalyst, led to obtain a performing visible-light driven photocatalyst for the H_2 production by glucose photoreforming. The pH was a critical parameter for the H_2 evolution, which was favoured in alkaline conditions. Notably, the photocatalyst showed an effective H_2 production even using wastewater or seawater. Furthermore, in the overall water splitting experiments, the highest H_2 evolution was obtained with wastewater and seawater. The same catalyst immobilized in film form showed an improved apparent quantum yield at 420 nm compared to the powder form, with also a good stability in both the water matrices.

These fascinating preliminary results can be promising for a possible scale up application. In particular, the low bandgap of the photocatalyst (2.74 eV) and the high apparent quantum yield obtained with the film form could be ideal to use this photocatalyst under solar irradiation amplified by a solar concentrator and with a parabolic compound reactor in continuous-flow mode. Moreover, the future tests should be focused on the stability of the film under long-time of solar irradiation and using high volume of seawater and wastewater.

The possibility to use visible light-driven photocatalysts in different form and with various water matrices is an attractive idea to promote the green hydrogen production even in large scale.

References

[1] A. Torres-Pinto, M.J. Sampaio, C.G. Silva, J.L. Faria, A.M.T. Silva, Metal-free carbon nitride photocatalysis with in situ hydrogen peroxide generation for the degradation of aromatic compounds, Applied Catalysis B: Environmental. 252 (2019) 128–137. https://doi.org/10.1016/j.apcatb.2019.03.040.

[2] J.C. Lopes, T. Moniz, M.J. Sampaio, C.G. Silva, M. Rangel, J.L. Faria, Efficient synthesis of imines using carbon nitride as photocatalyst, Catalysis Today. 418 (2023) 114045. https://doi.org/10.1016/j.cattod.2023.114045.

[3] M. Peñas-Garzón, M.J. Sampaio, Y. Manrique, C.G. Silva, J.L. Faria, Enhanced removal of emerging pollutants through visible light-activated carbon nitride materials immobilized over 3D printed structures, Journal of Environmental Chemical Engineering. 11 (2023) 111343. https://doi.org/10.1016/j.jece.2023.111343.

[4] M.J. Sampaio, A.R.L. Ribeiro, C.M.R. Ribeiro, R.A. Borges, M.F. Pedrosa, A.M.T. Silva, C.G. Silva, J.L. Faria, A technological approach using a metal-free immobilized photocatalyst for the removal of pharmaceutical substances from urban wastewaters, Chemical Engineering Journal. 459 (2023) 141617. https://doi.org/10.1016/j.cej.2023.141617.

[5] J. Liu, W. Fu, Y. Liao, J. Fan, Q. Xiang, Recent advances in crystalline carbon nitride for photocatalysis, Journal of Materials Science & Technology. 91 (2021) 224–240. https://doi.org/10.1016/j.jmst.2021.03.017.

[6] Y. Gong, M. Li, Y. Wang, Carbon Nitride in Energy Conversion and Storage: Recent Advances and Future Prospects, ChemSusChem. 8 (2015) 931–946. https://doi.org/10.1002/cssc.201403287.

[7] W. Jiang, W. Luo, J. Wang, M. Zhang, Y. Zhu, Enhancement of catalytic activity and oxidative ability for graphitic carbon nitride, Journal of Photochemistry and Photobiology C: Photochemistry Reviews. 28 (2016) 87–115. https://doi.org/10.1016/j.jphotochemrev.2016.06.001.

[8] J. Wang, Q. Lu, N. Sun, H. Su, P. Chen, J. Wu, Y. Fu, J. Ma, Giant improvement in piezo-photocatalytic capability of colloidal g-C3N4

quantum dots, Progress in Natural Science: Materials International. (2025). https://doi.org/10.1016/j.pnsc.2025.04.005.

[9] S. Peng, X. Ma, J. Tian, C. Du, L. Yang, E. Meng, Y. Zhu, M. Zou, C. Cao, One-Pot Etching Pyrolysis to Defect-Rich Carbon Nanosheets to Construct Multiheteroatom-Coordinated Iron Sites for Efficient Oxygen Reduction, Small. 20 (2024). https://doi.org/10.1002/smll.202310637.

[10] L. Shen, X. Chen, Y. Chen, J. Peng, A. Abbas, J. Wei, C. Yu, J. Li, Y. Li, One-Step Hydrothermal Synthesis of Sulfur Quantum Dots for Photoelectrochemical Catalysis for Dye Degradation, Journal of Electronic Materials. 51 (2022) 3092–3100. https://doi.org/10.1007/s11664-022-09528-4.

[11] J. Pei, H. Li, S. Zhuang, D. Zhang, D. Yu, Recent Advances in g-C3N4 Photocatalysts: A Review of Reaction Parameters, Structure Design and Exfoliation Methods, Catalysts. 13 (2023) 1402. https://doi.org/10.3390/catal13111402.

[12] A.B. Siddique, M.A. Shaheen, A. Abbas, Y. Zaman, A. Ali, M. Naeem-ul-Hassan, J. Iqbal, Photocatalytic and biological efficacy of Carissa macrocarpa fruit extract-mediated one-pot synthesized ternary metal oxide dual S-scheme heterojunction, Journal of Environmental Chemical Engineering. 12 (2024) 112725. https://doi.org/10.1016/j.jece.2024.112725.

[13] F. Cheng, H. Wang, X. Dong, The amphoteric properties of g-C 3 N 4 nanosheets and fabrication of their relevant heterostructure photocatalysts by an electrostatic re-assembly route, Chemical Communications. 51 (2015) 7176–7179. https://doi.org/10.1039/C5CC01035G.

[14] A. Torres-Pinto, C.G. Silva, J.L. Faria, A.M.T. Silva, The effect of precursor selection on the microwave-assisted synthesis of graphitic carbon nitride, Catalysis Today. 424 (2023) 113868. https://doi.org/10.1016/j.cattod.2022.08.010.

[15] U. Nwosu, H. Zhao, M. Kibria, J. Hu, Unlocking Selective Pathways for Glucose Photoreforming by Modulating Reaction Conditions, ACS Sustainable Chemistry & Engineering. 10 (2022) 5867–5874. https://doi.org/10.1021/acssuschemeng.1c08708.

[16] J.C. Colmenares, A. Magdziarz, K. Kurzydlowski, J. Grzonka, O. Chernyayeva, D. Lisovytskiy, Low-temperature ultrasound-promoted synthesis of Cr–TiO2-supported photocatalysts for valorization of glucose and phenol degradation from liquid phase, Applied Catalysis B: Environmental. 134–135 (2013) 136–144. https://doi.org/10.1016/j.apcatb.2013.01.020.

[17] B. Jin, G. Yao, X. Wang, K. Ding, F. Jin, Photocatalytic Oxidation of Glucose into Formate on Nano TiO 2 Catalyst, ACS Sustainable Chemistry & Engineering. 5 (2017) 6377–6381. https://doi.org/https://dx.doi.org/10.1021/acscatal.0c05703?ref=pdf.

[18] M. Zhou, Y. Li, S. Peng, G. Lu, S. Li, Effect of epimerization of d-glucose on photocatalytic hydrogen generation over Pt/TiO2, Catalysis Communications. 18 (2012) 21–25. https://doi.org/10.1016/j.catcom.2011.11.017.

[19] W.-J. Ong, L.-L. Tan, Y.H. Ng, S.-T. Yong, S.-P. Chai, Graphitic Carbon Nitride (g-C_3N_4)-Based Photocatalysts for Artificial Photosynthesis and Environmental Remediation: Are We a Step Closer To Achieving Sustainability, Chemical Reviews. 116 (2016) 7159–7329. https://doi.org/10.1021/acs.chemrev.6b00075.

[20] R. Liu, H. Yin, P. Guo, X. Liu, Z. Yin, Photoreforming Light Alcohols for Value-Added Resources: A Mini Review, Energy Technology. (2024). https://doi.org/10.1002/ente.202301708.

[21] A. Srikhaow, C. Chuaicham, J. Trakulmututa, K. Shu, K. Sasaki, Mg-modified graphitic carbon nitride/converter slag composites as an efficient photocatalyst for sugar conversion, Sustainable Energy & Fuels. 8 (2024) 3065–3076. https://doi.org/10.1039/D4SE00209A.

[22] H. Zhao, X. Wang, X. Wu, J. Wang, N. Zhong, A. Seifitokaldani, S. Larter, M.G. Kibria, J. Hu, Exploration of optimal reaction conditions on lactic acid production from glucose photoreforming over carbon nitride, Resources Chemicals and Materials. 2 (2023) 111–116. https://doi.org/10.1016/j.recm.2023.01.001.

[23] Y.J.O. Asencios, V.A. Machado, Photodegradation of Organic Pollutants in Seawater and Hydrogen Production via Methanol Photoreforming with Hydrated Niobium Pentoxide Catalysts, Sustainable Chemistry. 3 (2022)

172–191. https://doi.org/10.3390/suschem3020012.

[24] M.S. Yesupatham, A. Augustin, N. Agamendran, B. Honnappa, M. Shanmugam, P.J.J. Sagayaraj, G. Thennarasu, N.C. Sagaya Selvam, K. Sekar, Photocatalytic seawater splitting for hydrogen fuel production: impact of seawater components and accelerating reagents on the overall performance, Sustainable Energy & Fuels. 7 (2023) 4727–4757. https://doi.org/10.1039/D3SE00810J.

[25] A.Y. Kurenkova, S.N. Kharina, E.E. Aydakov, E.A. Kozlova, Hydrogen Production from Aqueous Glucose Solutions over g-C3N4/Pt/TiO2 Photocatalysts, Kinetics and Catalysis. 65 (2024) 703–709. https://doi.org/10.1134/S0023158424602353.

[26] X. Jing, Y. Zhang, H. Chang, R. Qiu, W. Yang, H. Xie, W. Wang, M. Zhang, X. Lyu, Q. Liu, X. Wang, J. Crittenden, X. Lyu, Efficient visible light photocatalytic green hydrogen production from Dy2O3 combined with nitrogen-deficient g-C3N4, Journal of Environmental Chemical Engineering. 12 (2024) 113040. https://doi.org/10.1016/j.jece.2024.113040.

[27] S. Kharina, A. Kurenkova, E. Aydakov, D. Mishchenko, E. Gerasimov, A. Saraev, A. Zhurenok, V. Lomakina, E. Kozlova, Activation of g-C3N4 by oxidative treatment for enhanced photocatalytic H2 evolution, Applied Surface Science. 698 (2025) 163074. https://doi.org/10.1016/j.apsusc.2025.163074.

[28] T.-G. Lee, H.-J. Kang, G.A.K.M.R. Bari, J.-W. Park, H.-W. Seo, B.-H. An, H.J. Hwang, Y.-S. Jun, Macroscopic graphitic carbon nitride monolith for efficient hydrogen production by photocatalytic reforming of glucose under sunlight, Chemosphere. 283 (2021) 131174. https://doi.org/10.1016/j.chemosphere.2021.131174.

[29] K.O. Potapenko, D.B. Vasilchenko, A.Y. Kurenkova, A.A. Saraev, D.D. Mishchenko, E.Y. Gerasimov, E.A. Kozlova, Expanding g-C3N4 capabilities for photocatalytic H2 production by modification with Ti3C2Tx MXene, International Journal of Hydrogen Energy. 99 (2025) 291–300. https://doi.org/10.1016/j.ijhydene.2024.12.213.

[30] T.D. Munusamy, S.Y. Chin, M.M.R. Khan, Hydrogen production via photoreforming of wastewater under LED light–driven over

CuO@exfoliated g–C_3N_4 nanoheterojunction, Chemosphere. 301 (2022) 134649. https://doi.org/10.1016/j.chemosphere.2022.134649.

[31] P. Niu, J. Dai, X. Zhi, Z. Xia, S. Wang, L. Li, Photocatalytic overall water splitting by graphitic carbon nitride, InfoMat. 3 (2021) 931–961. https://doi.org/10.1002/inf2.12219.

[32] J. Liu, Y. Liu, N. Liu, Y. Han, X. Zhang, H. Huang, Y. Lifshitz, S.-T. Lee, J. Zhong, Z. Kang, Metal-free efficient photocatalyst for stable visible water splitting via a two-electron pathway, Science. 347 (2015) 970–974. https://doi.org/10.1126/science.aaa3145.

[33] X. Li, G. Huang, X. Chen, J. Huang, M. Li, J. Yin, Y. Liang, Y. Yao, Y. Li, A review on graphitic carbon nitride (g-C3N4) based hybrid membranes for water and wastewater treatment, Science of The Total Environment. 792 (2021) 148462. https://doi.org/10.1016/j.scitotenv.2021.148462.

[34] A.L. Machado, R.A. Oliveira, G. Dražić, J.C. Lopes, C.G. Silva, J.L. Faria, M.J. Sampaio, Producing hydrogen from biomass and seawater using immobilized carbon nitride photocatalysts, Chemical Engineering Journal Advances. 21 (2025) 100697. https://doi.org/10.1016/j.ceja.2024.100697.

[35] P. Makuła, M. Pacia, W. Macyk, How To Correctly Determine the Band Gap Energy of Modified Semiconductor Photocatalysts Based on UV–Vis Spectra, The Journal of Physical Chemistry Letters. 9 (2018) 6814–6817. https://doi.org/10.1021/acs.jpclett.8b02892.

[36] H. Yang, A. Zhang, J. Ding, R. Hu, Y. Gong, X. Li, L. Chen, P. Chen, X. Tian, Amino modulation on the surface of graphitic carbon nitride for enhanced photocatalytic hydrogen production, Carbon. 219 (2024) 118841. https://doi.org/10.1016/j.carbon.2024.118841.

[37] C.R. Thara, P.S. Walko, B. Mathew, Hydrogen evolution via photocatalytic reforming of biomass with palladium nanoparticles decorated g-C3N4 nanosheets, Renewable Energy. 230 (2024) 120811. https://doi.org/10.1016/j.renene.2024.120811.

[38] R. Jin, S. Hu, J. Gui, D. Liu, A Convenient Method to Prepare Novel Rare Earth Metal Ce-Doped Carbon Nitride with Enhanced Photocatalytic Activity Under Visible Light, Bulletin of the Korean Chemical Society. 36 (2015) 17–23. https://doi.org/10.1002/bkcs.10001.

[39] M.J. Lima, A.M.T. Silva, C.G. Silva, J.L. Faria, Graphitic carbon nitride modified by thermal, chemical and mechanical processes as metal-free photocatalyst for the selective synthesis of benzaldehyde from benzyl alcohol, Journal of Catalysis. 353 (2017) 44–53. https://doi.org/10.1016/j.jcat.2017.06.030.

[40] N. Tian, Y. Zhang, X. Li, K. Xiao, X. Du, F. Dong, G.I.N. Waterhouse, T. Zhang, H. Huang, Precursor-reforming protocol to 3D mesoporous g-C 3 N 4 established by ultrathin self-doped nanosheets for superior hydrogen evolution, Nano Energy. 38 (2017) 72–81. https://doi.org/10.1016/j.nanoen.2017.05.038.

[41] M.T.A. Iapichino, R. Fiorenza, V. Patamia, G. Floresta, A. Gulino, M. Condorelli, G. Impellizzeri, G. Compagnini, S. Sciré, H2 production by solar photoreforming of plastic materials using SiC-g-C3N4composites, Catalysis Communications. 187 (2024) 106850. https://doi.org/10.1016/j.catcom.2024.106850.

[42] M. Pedrosa, M.J. Sampaio, T. Horvat, O.C. Nunes, G. Dražić, A.E. Rodrigues, J.L. Figueiredo, C.G. Silva, A.M.T. Silva, J.L. Faria, Visible-light-induced self-cleaning functional fabrics using graphene oxide/carbon nitride materials, Applied Surface Science. 497 (2019) 143757. https://doi.org/10.1016/j.apsusc.2019.143757.

[43] J. Wen, J. Xie, X. Chen, X. Li, A review on g-C 3 N 4 -based photocatalysts, Applied Surface Science. 391 (2017) 72–123. https://doi.org/10.1016/j.apsusc.2016.07.030.

[44] M.H. Vu, C.C. Nguyen, T. Do, Graphitic Carbon Nitride (g-C 3 N 4) Nanosheets as a Multipurpose Material for Detection of Amines and Solar-Driven Hydrogen Production, ChemPhotoChem. 5 (2021) 466–475. https://doi.org/10.1002/cptc.202000265.

[45] J.-N. Zheng, J.-J. Lv, S.-S. Li, M.-W. Xue, A.-J. Wang, J.-J. Feng, One-pot synthesis of reduced graphene oxide supported hollow Ag@Pt core–shell nanospheres with enhanced electrocatalytic activity for ethylene glycol oxidation, Journal of Materials Chemistry A. 2 (2014) 3445. https://doi.org/10.1039/c3ta13935b.

[46] M.-Y. Yen, C.-C. Teng, M.-C. Hsiao, P.-I. Liu, W.-P. Chuang, C.-C.M. Ma, C.-K. Hsieh, M.-C. Tsai, C.-H. Tsai, Platinum

nanoparticles/graphene composite catalyst as a novel composite counter electrode for high performance dye-sensitized solar cells, Journal of Materials Chemistry. 21 (2011) 12880. https://doi.org/10.1039/c1jm11850a.

[47] M. Moussa, A. Hamrouni, N. Lazaar, M. Ferhi, I. Chérif, H. Lachheb, C.G. Silva, M.J. Sampaio, J.L. Faria, Pt-doped g-C_3N_4 photocatalyst for simultaneous hydrogen production and value-added chemical synthesis under visible light, Photochemical & Photobiological Sciences. 24 (2025) 247–259. https://doi.org/10.1007/s43630-025-00683-1.

CHAPTER XI: Conclusion

CHAPTER XI: Conclusion

Globalisation and industrialisation have resulted in a substantial increase in greenhouse gas emissions, particularly carbon dioxide (CO_2). Moreover, since the beginning of the 21st century, there is a growing request in the global energy demand. As a result, scientific research has increasingly focused on the development of renewable energy sources. Among these, hydrogen is considered a promising energy carrier that could address many of the today challenges.

The main objective of this PhD thesis is the investigation of the production of hydrogen from green organic substrates through a photocatalytic process that is environmentally friendly, using the simulated solar irradiation.

Another important goal was the selection of carbon-based materials, offering a sustainable alternative to the most common photocatalysts usually prepared with the use of critical raw materials defined by the European Union.

Specifically, Chapter 8, entitled ***"H_2 Production by Solar Photoreforming of Plastic Materials Using SiC-g-C_3N_4 Composites,"*** investigates the catalytic performance of the SiC-g-C_3N_4 system by varying the amount of g-C_3N_4 used as a co-catalyst.

The addition of small amounts of carbon nitride to SiC led to a strong interaction between SiC and g-C_3N_4, resulting in a negatively charged surface that enhanced the hydrogen production during the photoreforming of plastic substrates such as PET and monomers like BPA. These sacrificial agents were

selected because they are common waste plastic materials and from their degradation/depolymerization it was possible to obtain hydrogen in a waste-to-fuel approach.

A basic pre-treatment using a concentred sodium hydroxide solution is essential to promote the cleavage of PET and BPA, leading to the formation of intermediates and degradation products. In particular, the detection of intermediates such as ethylene glycol, an alcohol, contributed to a higher hydrogen rate in the solar photoreforming of PET compared to BPA.

To further increase the hydrogen production, the performance of the base SiC-g-C_3N_4 compound was enhanced by incorporating titanium carbonitride, as described in Section 9, entitled ***"SiC-g-C_3N_4-TiCN Photocatalysts for Solar Photocatalytic H_2 Evolution from Plastics Photoreforming."***

The addition of ethanol to a less concentred solution of NaOH during the pre-treatment phase of other plastics such as polystyrene (PS), low-density polyethylene (LDPE), and the biodegradable polymer polylactic acid (PLA) improved the depolymerization of these materials. This led to milder reaction conditions and a higher hydrogen production. The highest hydrogen yield was obtained from the photoreforming of PS using the SiC-1 wt% g-C_3N_4-5 wt% TiCN catalyst. In this case, the interaction between the substrate and the catalyst promoted the formation of free radicals, which were generated by the absorption of light by the unsaturated chromophoric groups.

Moreover, hydrogen production was further improved by adopting a photothermal-catalytic approach. The same experimental setup

was successfully applied to the photoreforming of biomass-derived compounds, such as cellulose.

Section 10, entitled ***"Carbon Nitride Photocatalysts for Improved H_2 Production in Different Water Matrices"***, focused on the photoreforming (PR) of biomass, with glucose selected as the model substrate.

Thanks to the presence of g-C_3N_4, obtained via microwave exfoliation and modified with the addition of very little amount of platinum (Pt), excellent hydrogen production was achieved. A key aspect of this study was the application of the process in different water matrices, such as seawater and wastewater. The catalyst demonstrated good stability and was able to strongly produce hydrogen even in the absence of glucose. Furthermore, the preparation of the catalyst in thin film configuration, led to an strong improvement in the apparent quantum yield.

Overall, the results presented in this thesis shows that the vision of an ecological transition toward a more sustainable future is achievable. By refining current methods and optimally reusing waste materials, significant progress can be made in this direction.

Acknowledgments

At the end of this academic journey, full of experiences and unforgettable moments, I would like to express my gratitude to all the people who made this research possible.

First of all, I would like to thank my supervisor, *Professor Salvatore Scirè*, for his invaluable guidance during these three years. His advice has been essential for the completion of this thesis and for my growth as a researcher. His competence and support made this path much richer and more stimulating.

I also wish to warmly thank my co-supervisor, *Professor Roberto Fiorenza*, for his constant availability and for the support he has offered me both on a scientific and human level. His teachings on writing articles, the patience with which he guided me throughout this journey, his support in times of difficulty and his example of rigour and dedication is a reference point for me, that I will carry with me into the future.

My sincere thanks go to all the members of *the Industrial and Environmental Catalysis group (CIA Lab)*, and to the PhD students Dr. Andrea Stefano Balsamo, Dr. Luca Calantropo, Dr. Giusy Dativo, and Dr. Eleonora La Greca, for their daily help in the laboratory and for the many moments of collaboration that made my work easier.

I am also very grateful to *Dr. Maria Josè Sampaio* and to the entire Catalysis and Materials group at the University of Porto for welcoming me during the six months, I spent in their laboratory, which contributed greatly to this research.

I would also like to thank the other research groups of the University of Catania who contributed to this work. I am grateful to Professor

G. Malandrino's group for the XRD analysis, to Professor A. Gulino's group for the XPS analysis, and to Professor G. Compagnini's group for the photoluminescence analysis. I also wish to thank Dr. G. Impellizzeri's group (CNR-IMM) for the BET analysis.

Finally, I would like to acknowledge two important collaborations: with the research group of Professor A. Licciardello and Dr. E.M. Malannata, and with the research group of Professor A. Rescifina and Professor. G. Floresta, and Dr. V. Patamia.

A very special thank goes to my *Family*, for their constant support and for always believing in me. Their closeness has been my greatest strength.

Curriculum Vitae and Doctoral Activities

Maria Teresa Armeli Iapichino was born in November 24th, 1997, in Catania (Italy). In 2020, she earned her bachelor's degree in industrial chemistry from the University of Catania. She continued her studies at the University of Catania, and in 2022 she obtained her master's degree with honours in *Chemical Sciences* (Industry, Environment, and Cultural Heritage curriculum). In November 2022, she qualified as a professional chemist (Section A) and started his PhD research project in the laboratory of Industrial and Environmental catalysis under the supervision of prof. Salvatore Scirè and Roberto Fiorenza. As part of her PhD program, she spent six months (February 2024 to July 2024) at the Laboratory of Catalysis and Materials, Faculty of Engineering, University of Porto (Portugal), where she gained expertise in the preparation and characterization of carbon nitride (g-C_3N_4)-based materials.

In addition to her technical expertise which includes spectroscopy, gas chromatography, and surface analysis she has also developed soft skills such as problem-solving, teamwork, and effective time management. She is confident in the synthesis of catalytic materials, with a particular interest in renewable energy applications. In addition, she has gained experience with catalyst characterization techniques, photocatalytic systems, and reaction analysis. She is member the Industrial chemistry division of the Italian Chemical Society (SCI) and of the Interdivisional group of Catalysis (GIC) of SCI.

Scientific production

Publications related to the PhD project

- ***Authors*: Maria Teresa Armeli Iapichino,** Roberto Fiorenza, Vincenzo Patamia, Giuseppe Floresta, Antonino Gulino, Marcello Condorelli, Giuliana Impellizzeri, Giuseppe Compagnini, Salvatore Sciré.
  Title: *H_2 production by solar photoreforming of plastic materials using SiC-g-C_3N_4composites.*
  Journal: Catalysis Communications,V.187, 2024, 106850.
  https://doi.org/10.1016/j.catcom.2024.106850

- ***Authors*: Maria Teresa Armeli Iapichino**, Maria José Sampaio, Cláudia Gomes Silva, Joaquim Luís Faria, Antonino Gulino, Angelo Ferlazzo, Eleonora La Greca, Leonarda Francesca Liotta, Salvatore Scirè, Roberto Fiorenza.
  Title: *Carbon Nitride photocatalysts for improved H_2 production in different water matrices.*
  Journal: Chemistry Select, V.10, 2025, e02486
  https://doi.org/10.1002/slct.20250248

- ***Authors:* Maria Teresa Armeli Iapichino**, Giusy Dativo, Luca Calantropo, Giuliana Impellizzeri and Roberto Fiorenza.
  ***Title*:** *SiC-g-C_3N_4-TiCN photocatalysts for the solar photocatalytic H_2 evolution from plastics photoreforming.*
  Journal: Applied Catalysis O: Open, V.208,2025, 207070 https://doi.org/10.1016/j.apcato.2025.207070

- ***Authors***: Stefano Andrea Balsamo, Roberto Fiorenza, **Maria Teresa Armeli Iapichino**, Francisco Javier Lopez-Tenllado, Francisco José Urbano, Salvatore Sciré.
  Title: *H_2 production through glycerol photoreforming using one-pot prepared TiO_2-rGO-Au photocatalysts.*
  Journal: Molecular Catalysis, V.547,2023, 113346
  https://doi.org/10.1016/j.mcat.2023.113346

- ***Authors*:** Enrica Maria Malannata, Alessandro Auditore, Roberto Fiorenza, **Maria Teresa Armeli Iapichino**, Francesca Lo Presti, Nunzio Tuccitto, Antonino Licciardello.
  Title: *Simultaneous H_2 production and water purification with surface-modified nanostructured TiO_2 photoelectrodes*.
  Journal: RSC advances, V.15,2025,18, 14273-14281
  https://doi.org/10.1039/D5RA00251F

- ***Authors*:** Eleonora La Greca, **Maria Teresa Armeli Iapichino**, M. Carmen Herrera Beurnio, Francisco J. Urbano Navarro, Leonarda Francesca Liotta, Salvatore Scirè, Roberto Fiorenza.
  ***Title*:** *Influence of Ni Addition on Au/CeO_2 Photocatalysts for Solar Photocatalytic H_2 Production by Glycerol Photoreforming.*
  Journal: Catalysts, V.15,2025,555
  https://doi.org/10.3390/catal15060555

Publications related to the CO_2 conversion:

- ***Authors**:* Roberto Fiorenza, Chiara Contarino, Vanessa Spanò, **Maria Teresa Armeli Iapichino**, Stefano Andrea Balsamo.
  Title: *Photothermo-catalytic strategies for the CO_2 valorisation using TiO_2-based composites.*
  Journal: Catalysis Today, V.423, 2023, 114251
  https://doi.org/10.1016/j.cattod.2023.114251

- ***Authors**:* Roberto Fiorenza, Luca Calantropo, Eleonora La Greca, Leonarda Francesca Liotta, Antonino Gulino, Angelo Ferlazzo, Maria Grazia Musumeci, Giuseppe Proietto Salanitri, Sabrina Carola Carroccio, Giusy Dativo, **Maria Teresa Armeli Iapichino**, Salvatore Scirè, Giuliana Impellizzeri.
  Title: *Solar-promoted photo-thermal CO_2 methanation on SiC/hydrotalcites-derived catalysts.*
  ***Journal*:** Catalysis Today, V.449,2025,115182
  https://doi.org/10.1016/j.cattod.2024.115182

Other publication:

- ***Authors:*** Erika Saccullo, Giusy Dativo, Rosamaria Lombardo, **Maria Teresa Armeli Iapichino**, Roberto Fiorenza, Vincenzo Patamia, Giuseppe Floresta.
  Title: *Natural antenna molecule in halloysite-kojic acid composite for the solar photocatalytic CO_2 methanation.*
  Journal: Materials Today Chemistry, V.44,2025,102587
  https://doi.org/10.1016/j.mtchem.2025.102587

- ***Authors:*** Erika Saccullo, Vincenzo Patamia, Alessandra Bifarella, Angelo Ferlazzo, Roberto Fiorenza, Luca Spitaleri, Gianfranco Sfuncia, Giuseppe Nicotra, Chiara Zagni, **Maria Teresa Armeli Iapichino**, Antonino Gulino, Giuseppe Floresta, Antonio Rescifina.
  Title: *Conversion of VOC-derived CO_2 into sustainable products with a natural magnetic alginate composite.*
  Journal: International Journal of Biological Macromolecules, V.3034,2025, 140695
  https://doi.org/10.1016/j.ijbiomac.2025.140695

- ***Authors:*** Angelo Ferlazzo, **Maria Teresa Armeli Iapichino**, Giulia Calabrese, Giovanna D'Accurso, Roberto Fiorenza, Venerando Pistarà, Antonino Gulino, Antonio Rescifina, Vincenzo Patamia, Giuseppe Floresta.
  Title: *Nano-Sensors Made of Halloysite and Kojic Acid Metal Complexes for Dopamine Detection.*
  Journal: *Applied Nano Materials, V.8,2025,16736-16747*
  https://doi.org/10.1021/acsanm.5c02759

Conference contributions

Oral communications

- **Maria Teresa Armeli Iapichino,** Roberto Fiorenza, Stefano Andrea Balsamo, Salvatore Scirè
  "*Unconventional photocatalysts for the H_2 production by solar photoreforming"*
  XXIII National Catalysis Congress GIC 2023 "Catalysis as a golden lighthouse for green chemistry and energy related technologies,
  Genoa (Italy),11 to 13 June 2023
  Società Chimica Italiana
  Gruppo Interdivisionale Catalisi

- **Maria Teresa Armeli Iapichino,** Roberto Fiorenza, Salvatore Scirè
  "*Green H_2 production by solar plastics photoreforming using unconventional photocatalysts*"
  Conference of the Sicily and Calabria sections of the Italian Chemical Society,
  Palermo (Italy), 11-12 December 2023

- **Maria Teresa Armeli Iapichino,** Roberto Fiorenza, Salvatore Scirè
  "A comparison between the solar photoreforming of natural and synthetic polymeric derivates for the H_2 production"
  XXVIII Conference Nationality of the Italian Chemical Society,
  Milan (Italy), 28-29 August 2024
  Società Chimica Italiana

- **Maria Teresa Armeli Iapichino**, Salvatore Scirè, Roberto Fiorenza, Joaquim L. Faria and Maria José Sampaio
  "Carbon nitride-based photocatalysts for the hydrogen production using actual water matrices"
  Merck Young Chemists' Symposium 2024,
  Rimini (Italy),13 to15 November 2024
  Young Group of Società Chimica Italiana and National Interuniversity Consortium of Materials Science and Technology

- **Maria Teresa Armeli Iapichino,** Roberto Fiorenza, Salvatore Scirè
  "*Solar photo-reforming of natural and synthetic polymers for H_2 production by carbon-based materials"*
  XXI CIRCC Phd day,
  Ancona (Italy),2-3 April 2025
  Interuniversity Consortium for Chemical Reactivity and Catalysis

- ***Maria Teresa Armeli Iapichino*****,** Roberto Fiorenza, Giusy Dativo, Eleonora La Greca, Luca Calantropo, Salvatore Scirè
  "*Carbon materials for the solar H_2 production by photoreforming"*
  The 3rd International Electronic Conference on Catalysis Science,
  23 to 25 April 2025 online

- ***Maria Teresa Armeli Iapichino*****,** Roberto Fiorenza, Giusy Dativo, Salvatore Scirè
  "*Photoreforming of biomass and plastics-derived materials using carbon-based photocatalysts*"
  XXIII International Conference on Environmental Catalysis,
  Palermo (Italy) 2 to 5 June 2025

- ***Maria Teresa Armeli Iapichino*****,** Roberto Fiorenza, Salvatore Scirè
  "*Carbon-based photocatalysts for H_2 production through natural and artificial polymers photoreforming"*
  16th European Congress on Catalysis (EUROPACAT)
  Trondheim (Norway) 31 August to 5 September 2025
  European Federation of Catalysis Societies (EFCATS)

Poster communications

- **Maria Teresa Armeli Iapichino**, Marta Calà Pizzapilo, Roberto Fiorenza, Stefano Andrea Balsamo, Salvatore Scirè
  "SiC based photocatalysts for the solar H_2 production by photoreforming of sustainable organic substrates"
  XXII Nationality Conference of the Division Industrial Chemistry, Catania (Italy),7-8 November 2022

- **Maria Teresa Armeli Iapichino**, Roberto Fiorenza, Salvatore Scirè
  "H_2 Production by plastics photoreforming using SiC-g-C_3N_4"
  XIV European Congress on Catalysis
  Prague (Czech Republic),26 August to 2 September 2023

- **Maria Teresa Armeli Iapichino**, Roberto Fiorenza, Salvatore Scirè
  "Green H_2 production by solar photoreforming"
  18th International Congress on Catalysis,
  Lyon (France) 14 to 18 July 2024

Schools

1. ***School of Industrial Chemistry 2023***
   Società Chimica Italiana
   Divisione Chimica Industriale
   Turin (Italy), 28 May to 1June 2023
2. ***GIC-EFCATS 2025 PhD Winter School***
   Gruppo Interdivisionale di Catalisi
   European federation of catalysis society
   Aquila (Italy), 27 - 31 January 2025
3. ***CO_2 Cat School 2025***
   CNR-ITAE Messina (Italy) 7-11 April 2025
4. **CIG 2025 – Catalisi in Gioco**
   Gruppo Interdivisionale di Catalisi,
   Reggio Calabria (Italy) 17 to 20 September 2025

Courses attended

1. Photochemistry: from basic principles to practical applications
   given by Prof. S. Sortino
2. Paper and Project writing
   held by Prof. Silvia Giordani (School of Chemical Science, DCU – Ireland)